Off-grid PV systems for hydrogen production
From prospection analysis to system control

Martinez Lopez, V.A.

Important note
To cite this publication, please use the final published version (if applicable).
Please check the document version above.

OFF-GRID PV SYSTEMS FOR HYDROGEN PRODUCTION

FROM PROSPECTION ANALYSIS TO SYSTEM CONTROL

OFF-GRID PV SYSTEMS FOR HYDROGEN PRODUCTION

FROM PROSPECTION ANALYSIS TO SYSTEM CONTROL

Dissertation

for the purpose of obtaining the degree of doctor
at Delft University of Technology,
by the authority of the Rector Magnificus prof. dr. ir. T.H.J.J. van der Hagen,
chair of the Board for Doctorates,
to be defended publicly on Monday, 16 September 2024 at 17:30 o'clock

by

Victor Arturo MARTINEZ LOPEZ

Master of Science in Electrical Engineering,
Delft University of Technology, Delft, the Netherlands,
born in Mexico City, Mexico.

This dissertation has been approved by the promotors

Composition of the doctoral committee:

Rector Magnificus,	chairperson
Prof. dr. ir. M. Zeman,	Delft University of Technology, promotor
Prof. dr. ir. O. Isabella	Delft University of Technology, promotor
Dr. H. Ziar,	Delft University of Technology, copromotor

Independent members:

Em. prof. dr. B. Dam	Delft University of Technology
Prof. dr. M. Gibescu	Utrecht University
Prof. ir. C.P.J.W. van Kruijsdijk	Delft University of Technology
Prof. dr. ir. Z. Lukszo	Delft University of Technology
Prof. dr. ir. M. Popov	Delft University of Technology, reserve member

Study nature,
love nature,
stay close to nature.
It will never fail you.

Frank Lloyd Wright

CONTENTS

SUMMARY

Hydrogen is not only the most common element in the universe, but also a versatile molecule which is an option to decarbonize sectors that are not easily electrified or are energy intensive, such as long-distance transport, chemical industry, and metallurgy among others. Hydrogen gas is typically obtained from fossil fuels, and only a small fraction is produced nowadays from electrolysis, or the process of using water and electricity to produce gaseous hydrogen.

If the electricity for powering the electrolysis process comes from renewable sources, the produced gas will have no associated greenhouse emissions. This is the so-called *green* hydrogen, which is the base for decarbonization of carbon intensive industries.

This work investigates the potential of stand-alone green hydrogen production from solar energy, covering the whole design process, from an allocation and feasibility analysis, to system control. To do so, this thesis is separated in two parts. The first part focuses on the preliminary assessment phase of photovoltaic (PV) systems and the solar resource, while the second covers the integration of PV and electrolysis systems finalizing with a control strategy for these systems.

Chapter 2 presents a methodology for analyzing potential sites for PV deployment, including information on the degradation of the site. This provides the designer with additional information beyond the purely technical and economical layers that are typically considered in this type of study. The more degraded a site is, the more suitable it is for deploying new PV projects, avoiding pristine natural areas. This, combined with mitigation measures can minimize the environmental impact of new PV projects.

An analysis of the efficiency loss of PV systems is discussed in Chapter 3. In particular, the efficiency loss caused exclusively by quick variations in irradiance, as a consequence of passing clouds. These abrupt and quick changes affect not only the solar modules, but components downstream, such as the maximum power point tracker. The implemented algorithm might be sensitive to these changes and move the operating point of the PV module away from its maximum power point, leading to energy loss.

Predicting quick changes of irradiance is a topic covered in Chapter 4. Using sky images and artificial intelligence, it is possible to predict ultra-short-term irradiance. The proposed method is an ensemble of models, each trained on a particular sky condition. Because each model is highly specialized, once the sky condition is determined, the model that performs best on each sky type is employed, leading to lower prediction errors, more precise predictions and lower training data needed. Yet, an accurate prediction is a topic for further research.

The integration of PV with hydrogen systems is introduced in Chapter 5, which presents a literature review on integration methods for PV and electrolyzers as well as the main challenges for operating these systems in a variable manner.

Moving to the design phase, Chapter 6 proposes a sizing procedure, based on Particle Swarm Optimization to minimize the energy that cannot be used by the hydrogen

equipment (electrolyzer and compressor), aiming at the maximum energy utilization in the system. Horizontally-placed PV modules provide a good compromise between efficiency, hydrogen production and cost.

Once the system has been designed, Chapter 7 puts together all the topics covered in this dissertation proposing a control strategy for an optimally-sized stand-alone PV electrolyzer systems, without electrical storage. The control is based on prediction of irradaince changes using sky-images. From Chapter 4 it was clear that the prediction using sky images is far from perfect, yet this is needed for control. To solve this problem, the strategy proposed in Chapter 7 relies on information on the uncertainty of the prediction and uses fuzzy logic to account for imperfect predictions. This strategy can effectively smooth power changes without the need of additional storage components.

SAMENVATTING

Waterstof is niet alleen het meest voorkomende element in het universum, maar ook een veelzijdige molecuul dat een optie is om sectoren koolstofvrij te maken dat niet gemakkelijk geëlektrificeerd zijn of energie-intensief zijn, zoals langeafstandvervoer, chemische industrie, metallurgie, enzovoort. Waterstofgas wordt meestal geproduceerd uit fossiele brandstoffen en slechts een klein deel wordt tegenwoordig geproduceerd door elektrolyse, oftewel het proces waarbij water en elektriciteit worden gebruikt om gasvormige waterstof te produceren.

Als de elektriciteit voor het elektrolyseproces afkomstig is van hernieuwbare bronnen, zal het geproduceerde gas geen uitstoot van broeikasgassen hebben. Deze groene waterstof vormt dan de basis voor het koolstofvrij maken van koolstofintensieve industrieën.

Dit proefschrift onderzoekt het potentieel van autonome groene waterstofproductie uit zonne-energie, waarbij het hele ontwerpproces aan bod komt, van een toewijzings- en haalbaarheidsanalyse tot de systeemcontrole. Om dit te kunnen doen, is dit proefschrift opgedeeld in twee delen. Het eerste deel richt zich op de voorbereidende beoordelingsfase van fotovoltaïsche (PV) systemen en de zonne-energiebron, terwijl het tweede deel de integratie van PV- en elektrolysesystemen behandelt en eindigt met een controlestrategie voor deze systemen.

Hoofdstuk 2 presenteert een methodologie voor het analyseren van potentiële locaties voor het plaatsen van PV, inclusief informatie over de degradatie van de locatie. Dit geeft de ontwerper extra informatie die verder gaat dan de puur technische en economische lagen die meestal worden meegenomen in dit soort studies. Hoe meer een locatie is gedegradeerd, hoe geschikter deze is voor het plaatsen van nieuwe PV-projecten, waarbij intacte natuurgebieden worden gespaard. In combinatie met mitigatiemaatregelen kan dit de milieu-impact van nieuwe PV-projecten minimaliseren.

Een analyse van het rendementsverlies van PV-systemen wordt besproken in Hoofdstuk 3. Vooral het rendementsverlies dat uitsluitend wordt veroorzaakt door snelle veranderingen in de instraling als gevolg van passerende wolken. Deze abrupte en snelle veranderingen beïnvloeden niet de zonnepanelen, maar componenten verderop in het systeem, namelijk de maximum power point tracker. Het geïmplementeerde algoritme kan gevoelig zijn voor deze veranderingen en het operationele punt van de PV-module van zijn maximale vermogenspunt verwijderen, wat tot energieverlies leidt.

Het voorspellen van de snelle veranderingen in instraling is een onderwerp dat behandeld wordt in Hoofdstuk 4. Met behulp van hemelbeelden en kunstmatige intelligentie is het mogelijk om de instraling op ultrakorte termijn te voorspellen. De voorgestelde methode is een ensemble van modellen, elk getraind op een specifieke hemelconditie. Omdat elk model zeer gespecialiseerd is, wordt na het bepalen van de hemelconditie het model gebruikt dat het beste werkt voor elk type hemel, wat leidt tot lagere voorspellingsfouten, preciezere voorspellingen en minder trainingsgegevens nodig. Toch is een

nauwkeurige voorspelling een onderwerp voor verder onderzoek.

De integratie van fotovoltaïsche systemen met waterstofsystemen wordt geïntroduceerd in Hoofdstuk 5, waarin een literatuuroverzicht wordt gegeven van integratiemethoden voor fotovoltaïsche systemen en elektrolyse-installaties, evenals de belangrijkste uitdagingen om deze systemen op een variabele manier te laten werken.

In de ontwerpfase wordt in Hoofdstuk 6 een dimensioneringsprocedure voorgesteld op basis van Particle Swarm Optimization om de energie die niet kan worden gebruikt door de waterstofapparatuur (elektrolyse en compressor) te minimaliseren, met als doel een maximaal energiegebruik in het systeem. Horizontaal geplaatste zonnepanelen bieden een goed evenwicht tussen rendement, waterstofproductie en kosten.

Nadat het systeem is ontworpen, worden in Hoofdstuk 7 alle onderwerpen uit dit proefschrift samengevoegd en wordt een regelstrategie voorgesteld voor een optimaal gedimensioneerd zelfstandig PV elektrolysesysteem, zonder elektrische opslag. De controle is gebaseerd op voorspelling van instralingsveranderingen met behulp van hemelbeelden. In Hoofdstuk 4 werd duidelijk dat de voorspelling met behulp van hemelbeelden verre van perfect is, terwijl dit wel nodig is voor de controle. Om dit probleem op te lossen vertrouwt de in Hoofdstuk 7 voorgestelde strategie op informatie over de onzekerheid van de voorspelling en maakt gebruik van fuzzy logic om rekening te houden met imperfecte voorspellingen. Deze strategie kan vermogensveranderingen effectief egaliseren zonder dat er extra opslagcomponenten nodig zijn.

1

INTRODUCTION

E ARTH is the home of at least 74,962 species of vertebrates, 1,480,351 species of invertebrates, 425,035 species of plants, and 172,946 species of protists and fungi [1][1] as well as more than 8,000 million people [2]. All these living creatures need water, food, and shelter, needs that are fulfilled by the ecosystems they live in. It is undeniable that ecosystems provide food, purify the air, prevent flooding, supply compounds for medicine, represent an important part of communities cultural identity, inspire art, improve mental health, among other Nature Contributions to People (NCP) [3]. If Nature provide such valuable services to people, why have humans degraded 70% of the world's land [4] and caused a 10-year global temperature increase of 1.1 °C [5]? As a consequence 28% of identified species is threatened with extinction[2] [1] and 46% of the world's population is affected by the loss of the services that ecosystems provide [5]. As an example, clearing of mangroves along the coasts, results in a loss on the ability of that ecosystem to protect a coastal town against a severe storm. In other words the Nature Contribution to People *Natural hazard impact reduction* is lost [3].

A possible answer might be on the energy that people uses for their daily activities. As of 2019, the world consumed 418 EJ of it, mainly from coal, oil, natural gas and electricity [6]. Figure 1.1 shows the world energy consumption in 2021. [7].

The majority was used in transport and industry [6, 7]. Oil represents the highest source of final energy consumed worldwide, mainly used for transport. Electricity supplied almost 20% of the final consumption of world energy [6]. The energy consumption resulted in 33 Gigatons of carbon dioxide emitted to the atmosphere [8]. These emissions are partly responsible for bringing the increment of the world's temperature closer to 1.5 °C with respect to pre-industrial levels[3].

---

[1]These numbers represent only the *identified* species, the real number might be considerably higher.
[2]The IUCN has only analyzed 7% of the total number of described species. 28% of this 7% is threatened.
[3]An increment in global temperature of 1.5 °C increases considerable the risk of extreme weather events, impacts negatively human health with the spread of heat-related ailments and diseases and, leads to ecosystem degradation and biodiversity loss, among other. These risks are interconnected and trigger cascaded effects [5].
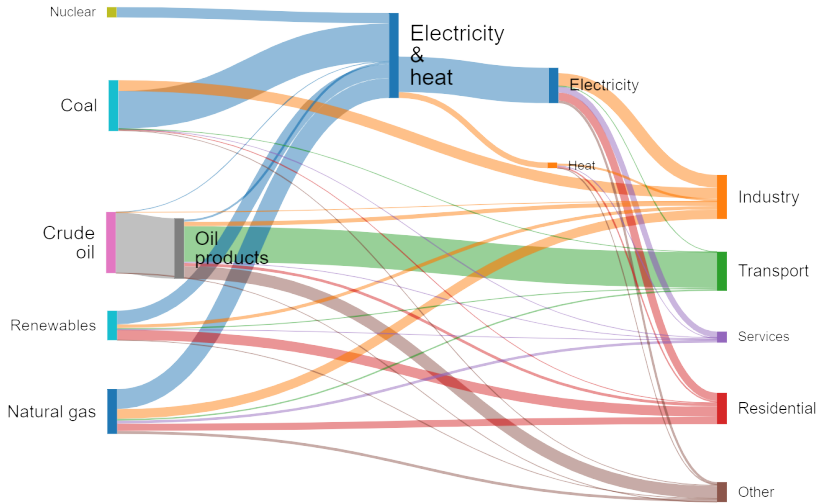
Figure 1.1: World energy flows in 2021 from primary sources (left) to final consumption (right). With information from [7]. The category *Heat* refers to the deliberate generation of heat for its use in the final consumption sectors and not the heat production as a result of inefficiency. The categories *Coal* and *Crude oil* cluster other products not included here for clarity. The category *Renewables* includes hydro, geothermal, solar, wind, ocean, biofuels, municipal and industrial waste. The category *Other* includes agriculture, fishing and other uses. A full description of the categories can be found in [7]

Economic growth[4] caused the major increase of CO_2 emissions from 2018 to 2019 [8]. Which might explain why recently the terms *sustainable growth* and *green growth* have been used to define an economy which makes sure that the environment can provide the resources needed to maintain the life style and quality of life of people [9]. However, these terms imply an economy can grow infinitely in a world with finite natural resources, which is not possible [10]. In contrast, the term *sustainable development* (usually used as synonym of *sustainable growth*) entails an economy which does not grow, but, the quality of life of people improves [10].

In an attempt to bring together the environment, society and economics towards a sustainable development which would eradicate poverty and ensure a healthy planet by 2030, the United Nations proposed a set of 17 Sustainable Development Goals (SDG) under the lemma *leave no-one behind* [11]. These goals are not independent but are interconnected. For example, access to electricity (SDG 7: "Affordable and clean energy") in schools improves learning conditions (through lighting, and educational equipment), leading to better education (SDG 4: "Quality education"). The same applies to health facilities. This, combined with access to clean cooking solutions, lead to an improvement in people's health (SDG 3: "Good health and well-being") [12]. Development of

---

[4] Economic growth affected the increase in emissions in two ways. First, during 2018 the economy slowed down preventing the implementation of cleaner power generating technologies, leading to increased emissions. Secondly, During 2019, the economy started to grow again, demanding more energy, with more associated emissions [8].

renewable energy technology, which is also an important part of SDG 7, helps reduce greenhouse emissions, contributing to limiting the world temperature increase (SDG 13: "Climate Action"). Universal access to electricity also contributes to SDG 5 ("Gender equality") and SDG 8 ("Decent work and economic growth") [12].

Unfortunately, only 15% of the SDGs are on track and a non-negligible number have experienced regression (37%) [13]. Additionally, adverse effects of climate change such as water scarcity and security, severe weather and, extreme heat events, lead to hunger, diseases and increased mortality imposing an even greater risk and challenge for achieving the SDGs[5]. Part of this problem might be a worldview where humans are superior to other creatures and, because of this, have claimed ownership of the land and its resources [14]. This anthropocentric and egoistic worldview, along with the advancement of technology, modifies the relationship between humans and nature. Instead of co-existing, people are allowed to exploit the land without questioning whether by doing that they could damage other species, or even other people [14, 15]. The connection with Nature diminishes as urbanization increases. This limits people's knowledge on Nature along with the benefits and services that it provides to them [3]. This is relevant because there is urgent need to change the relationship between people and Nature to prevent further ecosystem deterioration, land degradation and biodiversity loss, which ultimately, also affect people [13]. Failure to do so and to reduce emissions will result in a temperature overshoot beyond the 1.5 °C [5, 16]. Bringing the temperature down would need an economic investment greater than what was spent on oil consumption during 2022, and it would rely on carbon capture technology, which so far has been inefficient and is not fully developed [16].

Fortunately, "just" changing people's behavior can be benefit for the planet. The International Energy Agency's Scenario for Net Zero Emissions in 2050[5], considers that 12% of the reduction in CO_2 emissions of the energy sector by 2050 are emissions that can be avoided through behavioral change[17]. On top of that, renewable energy (wind and solar) helps mitigate 25% of the emissions [16]. These technologies are mainly implemented in the electricity sector, still heating and transportation do not yet benefit from renewable energy sources [13]. For these, and other hard-to-decarbonize sectors, such as long distance transport, chemical, iron and steel industries, hydrogen produced from clean sources can be a solution to reduce their emissions [17, 18]. This gas can be produced from renewable electricity (*green hydrogen*) and used directly in fuel cells to produce electricity or combined with (captured) carbon dioxide to form synthetic hydrocarbons to be used as fuels, or with nitrogen to produce ammonia (to be used as fertilizer or fuel) [19]. Its very high specific energy opens the door for international hydrogen trade [19] with benefit for developing countries, rich in renewable-energy [18, 19]. This hydrogen trade goes beyond simple export-import from developing to industrialized countries. Hydrogen can boost the energy transition for the local hydrogen producers, facilitate knowledge exchange and bring potential political stability [18]. Furthermore, hydrogen plays an important role in the net-zero emission scenarios of the International Energy Agency (IEA) and the International Renewable Energy Agency (IRENA). The latter indicates that 10% of the carbon emissions in 2050 will be abated by imple-

---

[5]*Net Zero* does not mean that there will be no CO_2 emissions by 2050; rather, these emissions will be offset with carbon sinks (natural or artificial).

1

menting hydrogen technologies [20], while the former is more conservative indicating that only 4% of the emissions by 2050 will be tackled with hydrogen [16].

1.1. MAIN CHALLENGES AND OUTLINE OF THIS WORK

The limited capacity of the electric grid can hinder the installation of new grid-connected projects, including those that generate green hydrogen from electricity. In the Netherlands, for example, more than half of the country has grid congestion problems [21]. In this respect, off-grid systems could help to relief stress on the electric grid [22], benefit local communities and facilitate the success of policies and climate goals [22]. Off-grid systems also play an important role in facilitating universal access to electricity [12]. The systems analyzed in this work are water electrolyzers powered by off-grid photovoltaic (PV) solar energy. Their goal is to produce green hydrogen.

One of the challenges of photovoltaic-electrolyzer systems is the intermittency and variability of the solar irradiance. The first one, caused by the day and night cycles, cannot be avoided without electric storage, combination with other technologies or grid support. The second is mainly caused by passing clouds, and, in contrast to the intermittency of solar resource, mitigation of variability does not necessarily require electric storage.

Understanding PV systems and the solar resource (Part I) is essential to the design and control of PV-hydrogen systems (Part II).

As with many human-made projects, even with good intentions, a PV power plant will affect the land on which it is installed. Therefore during the prospection analysis, when it is still easy and cheap to make decisions, the best location for developing a PV project should consider already a minimum impact to the land along a reasonable solar irradiance and other technical requirements (Chapter 2).

Clouds moving in front of and away from the sun impact the available irradiance and affect the efficiency of PV systems (Chapter 3). The clouds movement and prediction of these events (Chapter 4) is a very challenging task, even in the very short term (from seconds to maximum 30 minutes) using artificial intelligence and images from the sky. However, this very-short term forecasting is the backbone of many control systems.

Powering an electrolyzer with solar energy requires to know the available water electrolyzer technologies and the alternatives to couple them with PV, as well as the effects of irradiance variability and intermittency on the solar-powered electrolysis systems (Chapter 5). This allows a proper sizing of the PV system aiming at maximizing the conversion of solar energy to hydrogen (Chapter 6).

Finally, the control of a properly-sized, stand-alone and battery-less PV-hydrogen system involves the forecasting of irradiance changes and acknowledging that the prediction has a certain degree of uncertainty. Chapter 7 answers the question about how to deal with these uncertainty and the lack of storage.

1.2. MAIN CONTRIBUTION TO THE FIELD

This work contributes to SDG 7, "Affordable and clean energy". Its purpose is to determine the technical feasibility of stand-alone battery-less PV-electrolyzer systems for hydrogen production. It aims at a low environmental impact of these systems and high

conversion efficiency from sunlight to molecules. The main scientific contributions expressed in this thesis are:

- A methodology to help the identification of potential sites for land-based PV systems prioritizing a minimum environmental impact.

- Quantification of the losses that irradiance variability causes, due to an incorrect operation of the Perturb & Observe maximum power point tracking algorithm.

- A method to forecast irradiance in the very short term using sky images and artificial intelligence.

- A sizing methodology for stand-alone PV-electrolyzer systems that reduces the amount of unused energy.

- A control strategy to minimize the effects of changing irradiance without relying on electric storage.

I

SOLAR RESOURCE & PV SYSTEMS

A good understanding of the solar resource is essential to the design of PV-electrolyzer systems. The spatial distribution of the available irradiance on a country determines in great measure where a project can be deployed, while the intra-hour fluctuations have an impact on the design of the control of the whole installation. In terms of spatial planning, the information of the solar irradiance is combined with information on urbanization, segmentation, distance to infrastructure among others to facilitate the decision on the location of a future PV system. Chapter 2 presents a map of the Netherlands with the results of such analysis putting emphasis on reducing the environmental footprint of the future project. Chapters 3 and 4 highlight the changing nature of solar irradiance in the very short term. A consequence of these fluctuations is a reduction of the efficiency of the system. In particular, Chapter 3 quantifies the losses of the Perturb & Observe maximum power point tracking algorithm. Passing clouds cause the intra-hour fluctuations of irradiance. For this reason it could be convenient to include information on the clouds into an irradiance forecasting system. In Chapter 4, an image of the sky is used to classify the sky condition and predict the irradiance on a very-short temporal scale (20 minutes ahead). This part focuses fully on PV systems, but establishes the basis for the integration with hydrogen in Part II.

Artwork of the opposite page by L. E. Lopez Castro

2

MINIMIZING ENVIRONMENTAL IMPACT OF PV AT AN EARLY PROJECT STATE

From the very beginning of the world,
the other species were a lifeboat for the people.
Now we must be theirs.

Robin Wall Kimmerer

N ATURE provides for people not only food, water, medicine, and fuels but also protection against weather and biological events, climate regulation, and pollination, among others. It even stimulates psychological well-being and artistic inspiration [23]. Yet, human activities have modified around 70% of the original land cover in the world [24], reducing the long-term ability of Nature to provide these beneficial resources. Such reduction is called *land degradation* [4, 24]. It is estimated that, as of 2019, at least one fifth of Earth's land has lost this ability, affecting nearly two in five people on the planet [24].

At the same time, in 2022, the global photovoltaic (PV) generation broke a record of 1300 TWh, implying an increase of 26% in one year [25]. National targets in renewable energy generation fuel this growth. In 2021, 109 countries have mentioned renewable power targets in their National Determined Contributions (NDC) to the Paris Agreement [26], and PV generation is expected to reach 8300 TWh in 2030 to meet the Net Zero Emissions scenario of the International Energy Agency [25]. As a result of the Russia-Ukraine

conflict, the European renewable energy generation target became stricter, shifting from 40% to 45% by 2030 and almost doubling the installed PV capacity in just three years [27]. In the Netherlands, the National Climate Agreement establishes an onshore renewable generation (combined wind and solar) of 35 TWh by 2030 [28], and doubling this amount by 2050 [29].

Installing ground-based PV systems to meet the energy goals can raise a *Green on Green conflict* meaning installing *green* energy projects on *green* (natural) areas [30], especially because the installation contributes to land degradation. During construction, when most of the impact occurs, the soil is compacted and graded, and the native vegetation is removed, resulting in soil erosion. The project also fragments the landscape, preventing the movement of species and their genes, leading ultimately to biodiversity loss, and its operation requires water and potentially toxic substances [31]. The reduction in the albedo of the site, caused by the presence of the solar panels, influences the microclimate in the PV park location [32, 33] . Additionally, solar panels cause shading on the ground beneath, potentially affecting plant growth and biological processes in the soil, such as the decomposition of biological matter [34]. All these interventions can further facilitate the presence of invasive species. For example, the methods used to control native vegetation in solar installations in the United States influence the presence of invasive grasses [35].

Is there enough space to deploy the needed PV capacity without further contributing to land degradation? The energy density of PV systems ranges between 0.032 TWh/km^2 for rooftop systems to 0.087 TWh/km^2 for utility-scale systems [36]. Taking the Netherlands as an example, the land area of the country is 39450.53 km^2 [37]. This means that only 1% of the country's land is needed to meet the energy goals for 2030. The scenarios for 2050 (around 70 TWh, and even 200 TWh inland electricity generation) can be met, covering 80% of the rooftops with solar modules [29]. However, policies for rooftop systems [29], the load-bearing capacity of roofs [38], owner perceptions [39], fire safety concerns [40], and restrictions on monumental buildings [41] can discourage the deployment of these systems, resulting in additional land demand. Moreover, some studies [42, 43] claim that the needed land to cover 100% of a country's energy demand (considering not only electricity but also transport, heating and energy used in other countries to supply their needs) requires considerably more land, reaching in some cases more than the country's extension [43].

One way to deal with the potential clashing criteria (including the *green on green* conflict) for locating or siting a PV project, is to consider different perspectives as the framework proposed by Stremke [44]. This framework classifies the criteria for a project into four categories: sustainable-technical, environmental, socio-cultural, and economical.

The existing literature on solar project siting includes, in the sustainable-technical category, the solar resource [45–51], terrain slope [45, 47–52], site visibility [49], site elevation [49, 52] and landslide risk [51]. The environmental category is defined in terms of exclusion areas and includes water bodies [47–50], land use [45, 46, 49, 52], nesting sites and agriculture lands [47], protected natural areas, forests, areas with high vegetation cover [45, 48–51]. Within the socio-cultural category are recreation areas [45, 47, 51], site visibility [49], heritage areas and historic monuments [45–47, 49]. These criteria are typ-

ically considered as exclusion areas. Finally, the proximity to roads and transportation networks [45–52], the proximity to grid infrastructure [45, 47–49, 51, 52], houses and urban areas [45, 48, 50], and energy use centers [49] belong to the economic category.

One of the main problems with existing siting methodologies is that the environmental category is restricted to exclusion areas with high environment [47–50] or heritage value [49]. However, the environmental evaluation *outside* these regions is not considered. While solar plant developers have strategies to mitigate the environmental damage, these are mainly based on relocation of species in the construction site and are applied once the site has been chosen. One of the main problems with this approach is that the strategies target only selected species and have potentially low success rates [32]. One way to reduce the environmental footprint of solar parks is to install them in degraded lands [31, 32].

The purpose of our study is to tackle the problem of existing siting methodologies regarding the environmental impact outside exclusion areas. We relied on the Analytic Hierarchy Process [53] and the Compatibility Index [54, 55] to develop a suitability map for locating solar PV projects. We applied our methodology to the Netherlands, considering technical, economic, and environmental categories.

2.1. RESULTS

2.1.1. COMPATIBILITY MAP OF THE NETHERLANDS

The environmental assessment layer is based on the Compatibility Index [54, 55], as described in the Methods section 2.3.1. The Compatibility Index does not return a metric of the environmental impact but indicates the land degradation. Highly degraded sites are more *compatible* with the development of new projects as the damage to the land is less [54, 55]. Figure 2.1 shows the output of our method. Figure 2.1a shows the Compatibility Index of the Netherlands, while Figure 2.1b shows the full suitability map (discussed in Section 2.1.2). As expected, the most compatible sites are clustered around highly developed areas, such as cities or major roads, where the degradation is highest.

To validate the map, we evaluated the Compatibility Index of areas that are usually considered as exclusion areas due to their high environmental value. These areas are defined in the Natura2000 network [56, 57], the National Ecological Network [58], the National Parks of the Netherlands [59], the National Landscapes of the Netherlands [60] and areas of geological interest in the Netherlands [61].

Figure 2.2 illustrates the validation of the Compatibility Index. Figure 2.2a shows the distribution and the cumulative function of the Compatibility Index of these exclusion areas. The cumulative function shows that approximately 80% of the points within the exclusion areas fall into the incompatible and low compatibility regions. Why are there still significant points in exclusion areas with Medium Compatibility Indices, as the histogram shows? An analysis of the bands in the medium compatibility region shows these are mainly rural areas. The value of the *Green* module (see Section 2.3.1) pushes the Compatibility Index up. However, the most relevant feature of these bands is that they correspond to the National Landscapes exclusion area. This indicates that the criteria behind it are not fully based on environmental reasons. Note that the Compatibility In-
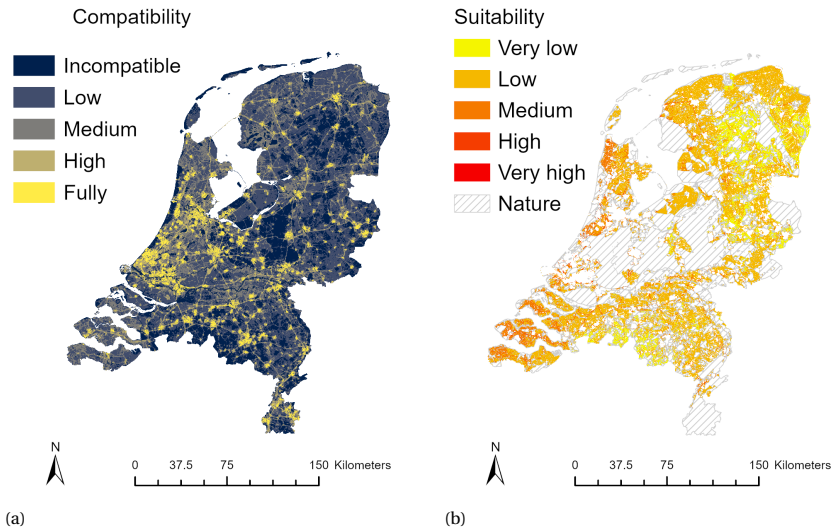
Figure 2.1: (a) Compatibility map of the Netherlands, and (b) Suitability map of the country. The suitability map uses the Compatibility Index as one of its inputs. To show the available land for new ground-based PV projects, the exlusion areas and buildings were removed from the Suitability map. In both cases, the pixel size is 90 × 90 m.

dex itself does not define exclusion areas and, because of its non-binary nature (i.e. it defines a *gradient* of values, rather than a go-no go criterion) [55] even pristine areas have a Compatibility Index value. However, these areas are expected to be less compatible (low Compatibility Index values).

Conversely, highly urbanized areas are expected to be more compatible with PV installations as the degradation is high. Figure 2.2b compares the distributions of the Compatibility Index in the five urbanization categories. The areas with very strong urbanization levels have, on average, the highest Compatibility Indices, which validates the fact that urban areas, which are highly degraded, are more compatible with new solar projects. The fact that an area is regarded as highly urbanized does not imply that every pixel in that area is compatible. The distribution of the "Very strong" urbanization level of Figure 2.2b confirms this, as the whiskers extend towards low Compatibility Indices in urban areas. These correspond to urban parks or green areas. At the same time, Figure 2.2b also confirms that rural regions, characterized by the lack of urbanization, are, in general, less compatible with new projects.

2.1.2. SUITABILITY MAP OF THE NETHERLANDS

The Compatibility Index map by itself is not enough to do a full evaluation of the potential sites for installing new PV systems [54, 55]. Still, it helps in including the environmental category during the prospection phase of PV plants.

To develop the suitability map, we first analyzed 936 existing and planned PV plants in the Netherlands, excluding residential rooftops. The company ROM3D kindly provided these data [62]. We set, in Table 2.4, seven criteria clustered in three main categories,
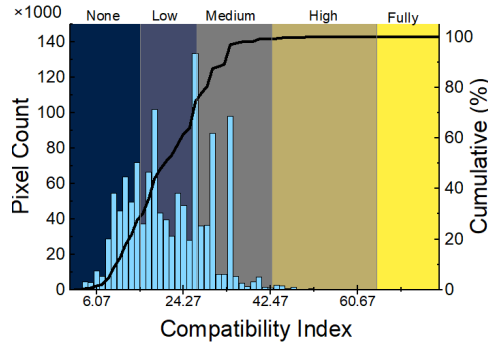
(a)
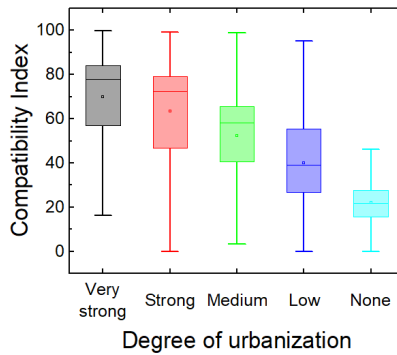
(b)

Figure 2.2: (a) Distribution of Compatibility Indices inside exclusion areas. The color bands show the Compatibility Index categories used in the map of Figure 2.1a. (b) Compatibility Index distribution per urbanization level. Highly urbanized regions have the highest Compatibility Indices, as expected. The outliers are not shown for clarity. Some of the outliers even reach values close to zero in the "Very strong" and "Medium" categories.

technical, environmental, and economic, to determine the priority for siting of the existing PV plants. At each PV plant location, we extracted the criteria value and plotted the distributions in Figure 2.3.

From the distribution and statistics of the criteria, it is possible to set weights that can be applied to the AHP methodology. In this way, the weights are well-posed and not subjective. However, such a method will yield a suitability map that reflects the current status, which does not necessarily encompass the importance of the environmental category (see Section 2.3.2). We proposed a different weighting scheme giving more importance to the Compatibility Index and ran a suitability study of potential sites for the location of PV projects. For this study, we considered only open areas (i.e., cities and other regions with high building densities were excluded) located outside the excluded areas defined before (Natura2000 network, Nature Network, National Parks, National landscapes, and Geological interests). After the exclusion, the available land is only 13 311.31 km^2, which corresponds to 38.4% of the land area of the country. Figure
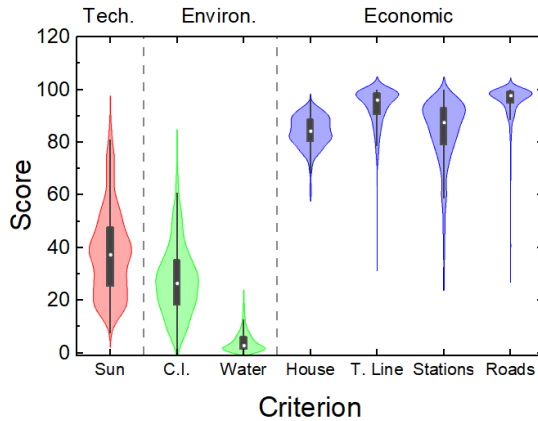
Figure 2.3: Score of siting criteria of the existing PV plants in the Netherlands (see Table 2.4). The colors of each violin plot correspond to a category (also distinguished from the dashed lines). "Tech." and "Environ." stand for "technical" and "environmental", respectively. Note that the minimum value for the score is zero. The plotting software applies smoothing to the violin plot, which would extend below zero. For this reason, for some criteria, the graph appears trimmed at zero.

2.1b shows the Suitability map of the Netherlands. Of the 936 existing and planned new installations, only 475 fall into this region.

The suitability map, combined with the specific PV yield (in kWh/kW_p, obtained from SolarGis [63]), along with Figure 2.5 facilitates answering the question *is there e-nough space to meet the energy requirements?* The final piece of the puzzle is the spe-cific PV power. To obtain this number, we intersected the information from the ROM3D dataset with the solar parks identified in the *Basisregistratie Topografie* (BRT) (see the Methods section 2.3 for a broader description of this dataset) resulting in 417 intersected projects, analyzed in Figure 2.4. Figure 2.4a shows the specific power (in kW/m^2) of these 417 installed and planned PV projects in the Netherlands. To consider the uncertainty in the specific PV power, we considered three values, the mean capacity (0.1 kW/m^2), the upper limit (0.3 kW/m^2), located at three standard deviations from the mean, and the lower limit (2.5 W/m^2) corresponding to the minimum value of the dataset. The reason for the minimum value, instead of three standard deviations below the mean, is that the resulting value would be located below zero.

We binned the suitability index into 64 bins. Then we multiplied the mean specific PV yield (1045.54 kWh/kW_p, obtained from the average value of the solar resource layer [63] of the ideal areas) with the specific PV capacity and the area covered by each suitability bin to obtain cumulative functions of the energy of the non-excluded areas (Figure 2.1b) per suitability bin (Figure 2.5a). This figure shows the minimum suitability index value needed to meet the 35 TWh energy requirement. Every pixel with a suitability index above the minimum should be covered with PV to meet the energy requirements. Fig-ure 2.5b translates this in terms of a percentage of the area of the non-excluded regions (Figure 2.1b).

The suitable areas are mainly composed of grass and croplands. These areas are also
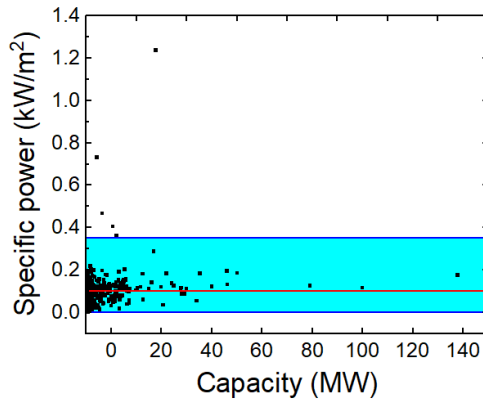
(a)
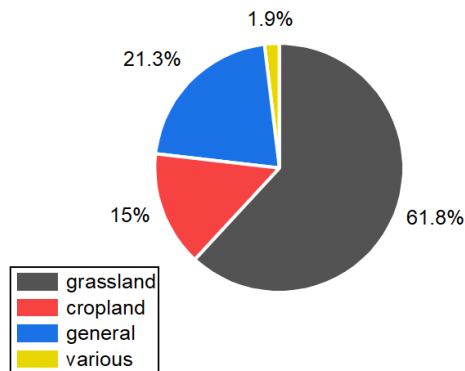
(b)

Figure 2.4: Analysis of existing and planned PV systems in the Netherlands. (a) Specific power (kW/m^2) of the planned and installed PV projects in the Netherlands ($n = 417$, obtained from intersectin ROM3D data with BRT's solar park land type.). The red line represents the mean value. The upper limit is at 3 standard deviations, and the lower is at the minimum value of all the points. (b) Type of land where the systems are installed ($n = 781$, obtained from intersection between ROM3D dataset and the land type (all fields) layer of BRT). The group "general" describes sites that do not have a particular purpose or definition, while the group "various" clusters eight subcategories which do not contribute significantly to the total.

2
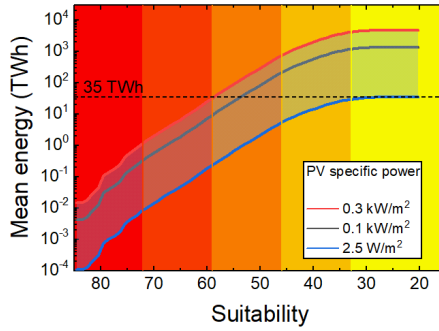
(a)
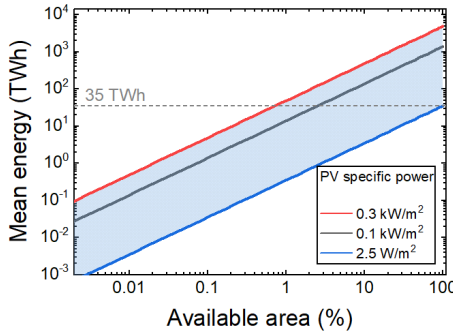
(b)
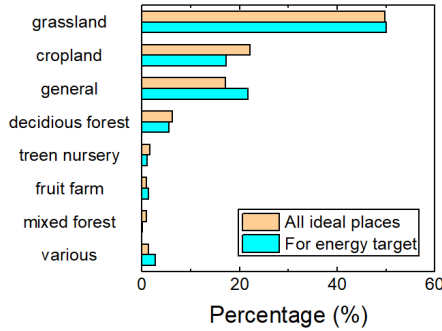
(c)

Figure 2.5: (a) Suitability threshold on the ideal areas to meet the energy target of 35 TWh. Note that the Suitability is displayed in *decreasing* order to facilitate the interpretation of this graph. The colors of the bands correspond to each suitability level as in Figure 2.1b. (b) The required area of ideal regions to meet the energy target of 35 TWh. (c) Land type composition of the suitable areas. The orange bars show the composition of all the pixels in the suitable region, and the blue, the composition of the pixels within the suitable areas needed to meet the 35 TWh generation target.

the preferred type of land where PV systems in the Netherlands are currently installed (Figure 2.4b). The blue bars of Figure 2.5c indicate the composition of those pixels, inside the suitable region, needed to meet the energy generation target of 35 TWh.

The group "various" clusters eight subcategories (*deciduous forest, orchard, tree nursery, basalt block/quarrying, fruit farm, fallow, dune, railway*). These items were grouped for readability and minimal contribution to the total (only 15 of the 781 analyzed projects belong to this group). The "general" type of land describes land without a particular purpose.

2.2. DISCUSSION

Siting of PV projects typically includes an environmental constraint as exclusion areas. The consequence is that potentially susceptible areas, which are not considered within the exclusion, are mapped as "available" for deployment. For example, in California, USA, some solar projects are installed close to, albeit not inside, protected areas. Yet, they still affect the protected environment because the "natural" boundaries of the protection area might extend well beyond its administrative borders [64]. For instance, the borders of protected areas do not account for the migration of species, the interrelation among them, or the threats to biodiversity linked to factors outside their limits [65]. In Europe, in the Netherlands, a study for a potential deterioration ban policy focused on areas outside the protected region defined by the Natura 2000 network (a network of protected sites with high biodiversity [56]) found unprotected sensitive zones, especially on sandy soils, which are highly valuable for conservation efforts [66]. For these reasons, the exclusion area approach might be insufficient to account for the environmental impact of utility-scale solar projects. Our approach aims to solve this problem because it does not result in a binary output but a gradient of suitable places, including the environmental category of areas outside the exclusion areas. Note that the suitability index does not indicate whether or not a site should be installed in a certain area. Rather, it gives extra information to the decision-maker about the condition of it.

Almost one-half of the projects planned and installed in the Netherlands are included in the ideal zones. The rest is distributed in the proximity of urban areas (273 projects) and inside areas considered here as "exclusion areas" (190 projects). Most projects installed in exclusion areas are on either the Geological Values (103 projects) or Landscape Values (105 projects) exclusion areas. Note that some regions belong to both categories. The protection goals of these areas do not specifically target nature conservation, although it is included. This might justify the presence of so many projects inside their boundaries. The three remaining exclusion areas still have projects installed therein (Natura 2000 (3 projects), Netherlands Nature Network (7 projects), and National Parks (1 project)). An important consideration is that the restricted zones might include developed areas (including building clusters), which might justify the presence of solar projects within their boundaries. This suggests that the definition of protected areas is vague, possibly affecting their effectiveness in preserving nature and increasing the possibility for that region to lose its status as a protection area [67].

Installing PV systems on degraded lands minimizes the impact on the land. For instance, the solar association SolarPower Europe proposed guidelines to deploy new solar PV projects, prioritizing degraded lands [68]. In the same direction, the Dutch govern-

ment, released in 2019 the so-called "Solar ladder" (*zonneladder*, in Dutch) to manage the space for developing solar projects [69]. This policy is a non-normative order of preference for installing new solar projects. It prioritizes the combined use of the spaces to avoid land conflict. Unlike the solar ladder, the guidelines of SolarPower Europe are not an order of preference but a recommendation for site selection based on the type of land where the project will be deployed on. It focuses on artificial or intervened places and avoids nature-valuable areas such as forests, wetlands, and water bodies *unless* artificially created or manipulated [68].

Our results show that the mean Compatibility Index of PV plants in the Netherlands is at the border between medium and low compatibility, indicating that the land where they are installed has a considerable degree of environmental importance (is not fully degraded). More importantly, 45% of the land has higher Compatibility Indices, offering better opportunities to deploy PV systems, minimizing the impact on land. A potential explanation for the choice of these places might be the strong focus that the existing PV projects put on the economic category (Figure 2.3), even above the solar resource and environmental ones. This does not mean that developers disregard the environmental impact but highlights one drawback of relying solely on exclusion areas, which was the main reason for developing the Compatibility Index [54, 55]. Because of the logic used to build the Compatibility Index, these guidelines and policies can be easily followed without (or in combination with) explicit exclusion areas.

Solar PV energy worldwide is mostly installed on agricultural, followed by arid, land [64, 70]. In the Netherlands, the projects follow the same trend, prioritizing grass and croplands (Figure 2.4b). This type of land covers most of the territory of places outside the exclusion areas and cities (Figure 2.5c). The required space to meet the energy generation goals for the country is only 2% of the non-excluded region, which is equivalent to fully covering an area larger than the municipality of Amsterdam, the capital of the Netherlands with PV. If land use is completely dedicated to PV, the space needed to deploy this capacity, is not a problem. However, from Figure 2.5c, we see that, to meet the energy goals, the PV systems *must* also be installed on croplands and even forests if all the PV capacity were to be installed in non-excluded areas. Agrivoltaics offer a potential solution to this problem, either spreading the PV system over a wider area (crop-centered approach), changing the crops below for shade-tolerant species (energy-centered approach), or using dead spaces between the crops. PV systems can also be installed in parcels where animals graze, providing shade to the animals in exchange for effortless vegetation management [71]. Ecovoltaics focus on providing suitable conditions for improving the ecological services of a place [72]. For instance, the uneven distribution of light and rainfall that the PV panels create on the land can potentially increase the biodiversity of the site [72, 73]. These activities can work better when the land is already degraded, contributing to land restoration. In this respect, our approach can help to identify the potentially suitable areas, as a first step, and locally, apply the eco- or agrivoltaic principles.

Our work derived a suitability map of the Netherlands considering the technical, economic, and environmental categories. Avoiding further land degradation is the main focus of the environmental category. This was quantified with a modified version of the Compatibility Index. Our modified version avoids the use of historical data, which sim-

plifies the analysis. Combining the Compatibility Index, with economic, solar potential and the location of the PV plants in the Netherlands, we found that the existing projects strongly focused on the economic aspect, even above the solar potential and the land degradation given by the Compatibility Index. Is there enough land space to meet the energy goals for 2030 with only PV?, yes, if every pixel with a suitability index above 40 has PV installed on it. This is translated as occupying nearly 2% of all the non-excluded areas, which include not only grass and croplands but also forests. This highlights that even though we aimed to provide information on the minimum impact on the land, a smart combination of land use and additional mitigation measures should be taken during the design of a PV project. Our methodology, unlike traditional siting methods, does not rely on exclusion areas for dealing with the environmental category. It can provide information on the environmental impact even outside these regions, which can be combined with the already defined no-go zones to have a clearer evaluation of the suitability of future PV projects.

2.2.1. LIMITATIONS
Our present work does not consider PV on water. Following the premise that natural areas should have a low Compatibility Index, we assigned a Compatibility Index of zero to inland waters. This is a point for improvement as artificial waters could be considered "degraded" and available for floating projects [68].
Note that the exclusion areas we defined in our analysis include the geological and geological values. These areas are not necessarily considered as nature protection zones. They focus on regions that have geological or cultural interests, but indirectly they also consider nature areas. For this reason, they were included in the analysis. Although, by doing so, we created a more restrictive scenario. This map was developed for its use in the Netherlands. Its use worldwide would require minor adaptation depending on the local information. While the topographic information is typically available in other locations, the dataset needed for the "Green" module might not be readily available. The "Green" module was obtained from the *Gray & Green map* of the Netherlands. The procedure for obtaining the map can be found in Ref [74]. In our suitability map, the terrain slope was not considered because the country is mostly flat. If the model is applied elsewhere, this technical limitation should be addressed.

The maps shown in this work are intended for prospection analysis to identify high-potential zones. The final selection of a site depends on more factors, including social or business strategy considerations that are not included in this map.

2.3. METHODS
2.3.1. THE COMPATIBILITY INDEX
To quantify the environmental impact of solar projects we followed the Compatibility Index approach proposed by Stoms, *et al.* [54, 55].
The Compatibility Index is a measure of degradation of a site. It is based on the premise that the environmental value of a place reduces as it becomes degraded. Hence, highly degraded sites, with little to no ecological value, are more *compatible* with new projects, as opposed to pristine sites which are *incompatible* with new developments [54, 55]. The

original model measures the degradation in terms of native cover removal and fragmentation of the habitat and it was designed and tested in the California desert [55].

We used ArcGIS Pro software, version 3.0.3 to perform the calculations. Each pixel in the map has a resolution of 90×90 m.

Note that the authors of the original study [54, 55] recognize that the Compatibility Index is not a full environmental assessment, but rather an initial guide for siting solar projects and minimizing their environmental damage.

Fragmentation module

The fragmentation module determines to what extent human-created line-wise interventions divide a habitat [55]. Each pixel on the map receives a score ranging from zero to 100 depending on their line density. The line density is the total length of lines inside a circle (search area) around a map pixel, divided by the area of such circle [75]. The fragmentation module considers the line density of four features: roads, railways, waterways and, transmission lines. The data sources are the *Basisregistratie Topography (BRT) TOPNL10*, with topographic information of the country, Open Street Map (OSM), mapping the waterways and the infrastructure of the electric grid operator, Tennet. Since each line represents a different feature (e.g. a street, a highway, a railway, etc.), a weight was applied to consider these differences following the original calculation of [55]. The line density was calculated for each of these features in every pixel. The pixel score is the maximum fragmentation score of the four features [55]. Table 2.1 shows the origin of the data used and the applied weights to calculate the fragmentation score.

Native cover removal module

The native cover removal module models the damage to the environment in terms of loss of vegetation. This loss can be quantified from the present land use since cities, buildings, mines, landfills, etc. are quantified as highly degraded areas [55].

For our calculation of the native cover removal, we relied on two databases, the BRT and the *Basisregistratie Gewasparcelen (BRP)*, with information on crop areas. The first database includes information on land use, and the second allows a fine selection of agricultural areas.

For each type of land use we applied the weights proposed in [55] and scaled them depending on the level of urbanization (Table 2.2). The level of urbanization is defined as the number of houses within a circle with a radius of 1 km and then categorized into five classes where each class has the same number of inhabitants [76] and obtained from the neighborhood information database of the Dutch Central Office of Statistics [77].

The sum of all the weights in a pixel is the native cover score, ranging from zero to 100.

Green module

The green module considers the amount of vegetation in a pixel. The basic layer is the "Green and Gray" map of the *Klimaateffectatlas* [74], which contains information on the amount of "green" (percentage of trees and grass) and "gray" (stones, asphalt, etc) per neighborhood [74]. While this map gives information on the percentage of green in each pixel that can be directly used as a score (or weight), some regions of the country are not mapped. For this reason, we complemented the information with the large-scale

2

Database	Data provider	Data	Data features	Weight
BRT 2022 (TOPNL10)	PDOK	Roads	General	1
			Highways	9
			Main road	6
			Landstripe	6
			Conveyor	6
			Regional road	4
			Local road	3
			Street	1
			Ferry connection	0
		Railroads	All	5
BRP		Waterways	Artificial	5
			Basin	
			Blocked	
			Boom	
			Canal	
			Construction	
			Ditch	
			Depth_line	
			Delerict_canal	
			Ditch	
			Drain	
			Lock_gate	
			Security_lock	
			Weir	
Tennet	Tennet	Transmission lines	Overhead	1
			Underground	

Table 2.1: Data sources and weights applied for the calculation of the Fragmentation module.

topography (BGT, in Dutch) map of the Netherlands. Table 2.3 shows the databases and features from the BGT used to calculate the Green score. The BGT database does not include a percentage value. The score was calculated by normalizing the area using Equation 2.1. The final score is the combination of the Green and Gray map with the databases of the BGT. Water bodies, obtained from the BRT database, were assigned a Compatibility Index value of zero.

2.3.2. ANALYTICAL HIERARCHY PROCESS (AHP)

The Analytical Hierarchy Process (AHP) is a method to assist in the decision-making of problems involving multiple decision criteria. It is based on a pairwise comparison of the criteria, which assigns a relative weight between the two (e.g., "Criterion A is three times more important than Criterion B"). This pairwise comparison is expressed as a table. The value of each column element, divided by the column total and averaged over all the rows, gives the relative weight of each criterion to each other [53].

Based on the analysis of the literature [45–52], we proposed seven criteria grouped into three categories. The technical criterion is the solar potential in the Netherlands obtained from SolarGIS [63]. The economic category includes the distance to roads, train stations, and transmission lines obtained from the BRT and Tennet databases. The house price (from the CBS neighborhood information) was used as an indicator of the land price.

The weights given to each category are based on two scenarios. The first scenario considers the value of each criterion at the location of existing and planned PV plants in the Netherlands (Table 2.4). ROM3D (*Zon Op Kaart, peildatum* 27-march-2023) kindly provided the data of the plants' location [62]. The mean of each criterion, normalized by the sum of the means of all criteria, is the weight of a particular criterion.

The second scenario strongly focuses on environmental category. A pairwise comparison matrix (Table 2.5) was done for the economic category. The other two categories have one (Technical category) or two (Environmental category) members, so no pairwise matrix is needed. Table 2.6 shows the applied weights for the environment scenario. The column labeled "Relative weight" is the weight of each criterion against each other within the same category. The "Final weight" column is the absolute weight of each criterion and the one applied for calculating the Suitability score. This final weight results from multiplying the relative weight with the importance of each category.

We applied a weighted sum using the final weights of each scenario to calculate the suitability index. The value of the criteria is normalized (X_n) with Equation 2.2 if the values of the criterion x are represented as (max(x) $\rightarrow$$\rightarrow$less suitable and 0$\rightarrow$more suitable). This happens, for example, in the green module. The non-normalized quantities represent a fraction of green within a pixel. However, a 100% pixel (fully green) is not suitable; hence, the normalization needs to be reversed. For the normalization quantities that do not need to be reversed, Equation 2.1 was applied.

$$X_n = \frac{\max(x) - x}{\max(n) - \min(n)} \tag{2.1}$$

$$X_n = \frac{x - \min(x)}{\max(n) - \min(n)} \tag{2.2}$$

2

Table 2.2: Weights used to calculate the native cover removal

Feature	Very strong urban- ization	Strong urban- ization	Medium urban- ization	Low urban- ization	No urban- ization
No data	0	0	0	0	0
Mixed forest	0	0	0	0	0
Coniferous forest	0	0	0	0	0
Deciduous forest	0	0	0	0	0
Willow	0	0	0	0	0
Cotton wood	0	0	0	0	0
Shrubland area	0	0	0	0	0
Railroad	0	0	0	0	0
Sand	0	0	0	0	0
Dune	0	0	0	0	0
Basalt blocks	8	8	8	1	1
Jetty	70	70	57	8	8
Fruit farm	70	70	57	8	1
Orchard	70	70	57	8	1
Nursery	100	70	57	8	1
Cropland	70	70	57	8	1
Graveyard with forest	57	57	8	1	1
Graveyard	70	70	57	8	1
Fallow	N/A	N/A	70	57	8
Built-up area	100	100	70	57	8
Other	100	100	70	57	8
Grassland	0	0	0	0	0
Farmland	70	70	57	8	1
Fallow land	N/D	70	57	8	1
Grassland	70	70	57	8	1
Nature terrain	0	0	0	0	0
Other	N/D	0	0	0	0

2

Table 2.3: Data source and features used to calculate the Green module

Database	Feature	
	Dune	
	Dune: Closed dune vegetation	
	Dune: Open dune vegetation	
	Mixed forest	
	Grassland other	
	Green areas	
	Green area: ground covers	
	Green area: forest plantation	
	Green area: grasses and herbaceous plants	
	Green area: shrubs	
BGT_begroeid	Green area: plants	
	Green area: shrub roses	Heather
	Wooded bank	
	Salt marsh	
	Deciduous forest	
	Deciduous forest: willow and coppice	
	Swamp	
	Coniferous forest	
	Reed land	
	Bushes	
	Sand	
BGT_onbegroeid	Sand: beach and shoreline	
	Sand: sand drift	

Table 2.4: Weights obtained from the existing PV locations

Category	Importance	Criterion	Weight
Technical	8.77%	Solar resource	0.0877
Environmental	7.39%	Compatibility Index	0.0648
		Distance to water	0.0091
Economic	83.84%	Distance to roads	0.2242
		Distance to train stations	0.1974
		Distance to transmission lines	0.2183
		House price	0.1985

2

Table 2.5: Pairwise comparison matrix for the economic category of the environmental scenario

	Roads	Stations	House price	Transmission lines
Roads	1	3	1/3	1/2
Stations	1/3	1	1/7	1/5
House price	3	7	1	3
Transmission lines	2	5	1/3	1

Table 2.6: Weights applied to the environmental scenario

Category	Importance	Criterion	Relative weight	Final Weight
Technical	20%	Solar resource	1	0.2
Environmental	60%	Compatibility Index	0.9	0.54
		Distance to water	0.1	0.06
Economic	20%	Distance to roads	0.159	0.0318
		Distance to train stations	0.059	0.0118
		Distance to transmission lines	0.256	0.0512
		House price	0.526	0.1052

3

EFFECT OF IRRADIANCE VARIABILITY ON PV SYSTEMS

Nature's music is never over.
Her silences are pauses, not conclusions.

Mary Webb

I N 2021, the world generated 821 TWh of electricity from solar PV. This considerable growth of PV generation of 23% is still not enough to meet the growing goals of 24% yearly in order to reach the 6970 TWh of solar generation in 2030. Because of this, additional efforts are needed to increase PV production worldwide [78].

A wafer-to-system analysis [79] shows that most of the energy losses occur at a cell level. The commercial crystalline silicon solar cells have efficiencies reaching 25% [80] while commercial modules have an average efficiency of 20.4% at Standard Test Conditions (STC) [80]. The rest of the losses in the PV system efficiency chain are related to the weather conditions of the site such as the irradiance, temperature and light spectrum effects [79]. Finally, the Balance-of-System components, which support the PV modules, also contribute to losses. Of these, the power converter accounts for the majority of the losses [79].

Based on this analysis, there are several options for increasing the PV system efficiency. Multi junctions can boost the efficiency of PV cells. For example, using perovskites with silicon can boost the cell's efficiency up to 31.25% [81]. At a module level, improving the module's performance under partial shading conditions also leads to an increase in efficiency. A novel way to achieve this is by reconnecting blocks of cells of the PV module in series or parallel depending on the shading pattern of the module [82]. Moving to the system domain, switching from simple converter topologies such as the

buck or boost converters, with efficiencies ranging around 97%, to more advanced designs that employ soft switching techniques, also leads to better efficiency. In addition, the way that different converters are connected in the system opens a window of opportunity for efficiency improvement [83]. The power extracted from PV modules can be maximized by employing maximum power point trackers (MPPT). Their algorithms act upon the power converter to ensure that the PV module delivers the highest possible power, increasing the system's efficiency [83].

Multiple techniques can be found to deal with this topic that span over different degrees of complexity, efficiency, and objectives. For an overview of the MPPT methods, the reader is referred to the work of Karami et al. [84], with a classification of 40 MPPT methods into five categories based on their operating principle. Many other literature reviews list MPPT methods (e.g., [85, 86]). In addition, in many of these, the Perturb-and-Observe is one of the first to appear.

This algorithm is one of the most widely used techniques for a PV module's maximum power point (MPP) tracking [86]. The reason behind its popularity is the simplicity of its logic [87]. It is so simple that it can be implemented in a very accessible embedded board such as the Arduino Nano [86] or even without a microcontroller by means of an analog circuit [84, 86, 88]. The algorithm applies a small voltage *Perturbation* to modify the module's operating point. Then, it *Observes* the resultant power. Depending on the sign of the power change, the next voltage perturbation will either increase the voltage or reduce it. In this way, the operating point will climb along the power-voltage (P-V) curve towards the maximum power point. Under constant irradiance and steady-state operation, the operating power will constantly swing around the theoretical maximum power point. With variable irradiance, the P–V curve of the module is continuously changing. Hence, the operating point occurs on different curves at each perturbation. This causes a potential problem for the algorithm that can become *confused*, setting an operating point different than the MPP and thereby leading to energy loss [85, 87, 89].

Figure 3.1 shows an example. Suppose that the algorithm starts at the maximum power point of the bottom P-V curve (marked with a diamond). The perturbation is positive and the observed power (with no irradiance change) is supposed to be lower, which, in turn, should result in the algorithm decreasing the voltage. Nonetheless, because the irradiance starts to increase, the observed power is now on another P-V curve with a higher value than before. In this scenario, if the irradiance keeps on increasing, the algorithm keeps on increasing the voltage as well. This confusion results in the tracking drifting away from the MPP of every curve and continues until the observed power is lower than the previous. At that moment, the algorithm operates correctly and starts climbing back to the MPP (even with the still increasing irradiance).

The P&O algorithm has two parameters that define its operation and can be tuned for optimization. The first is the sampling time, T_a. It determines how often a perturbation will be made. The second is the amplitude of the perturbation given by the voltage step ΔV. This parameter specifies the magnitude of the change in power that the module experiences (ΔP) [89]. The magnitude of the resultant power as a consequence of a voltage perturbation, its direction (increasing vs. decreasing voltage steps) as well as the power change caused by irradiance (ΔP_G) determine whether the algorithm will track in the correct direction or not [89, 90]. When the algorithm is decreasing the voltage to

Figure 3.1: Example of the P&O confusion when the irradiance increases. The circles indicate the tracking points. The 'x' denotes the maximum power point at each P–V curve, and the diamond marks the starting point.

reach the MPPT, it will not be confused if Equation (3.1) is fulfilled [89, 90]:

$$|\Delta P| < |\Delta P_G|. \tag{3.1}$$

When the algorithm increases the voltage to reach the MPPT, the inequality of Equation (3.1) is reversed [90].

The method presented here corresponds to the most basic version of the P&O algorithm, where the sampling time and perturbation step are fixed. There are many modifications to this algorithm that aim to improve its performance but maintain the basic operating principle. Many of these improvements to the basic P&O algorithm are based on dynamically changing the algorithm's parameters [90]. For example, the perturbation step is larger during the hill-climbing process but then reduced in size when the algorithm reaches the MPP leading to increased tracking speed and small steady-state oscillations [84]. We analyzed the P&O algorithm because of its simplicity and widespread use. Without losing generalization, we will only focus on the most basic form of the P&O algorithm.

3.1. IRRADIANCE VARIABILITY

"Variability" describes how often a quantity changes in time. High variability indicates frequent and significant changes, while low variability is linked to gradual changes.

When describing the Global Horizontal Irradiance (GHI), irradiance with high variability in a given period will exhibit high *dispersion*. Because of this, the standard deviation, as a measure of dispersion, is used to quantify irradiance variability.

Variability is more evident when considering the *differences* between two consecutive irradiance measurements. These differences are close to zero for gradual changes,

hence low *dispersion*. The first variability metric, V, is then a measure of the dispersion of the changes in irradiance within a certain period. Mathematically, $V = \sigma(\Delta G)$, where G represents the measured irradiance (GHI).

To remove the effect of day–night cycles and allow the study of variation caused by clouds, the clearness index k_t (3.2) can be used [91]. It relates the measured irradiance G against the modeled irradiance at the top of the atmosphere (extraterrestrial irradiance, G_{ext}) [92]:

$$k_t = \frac{G}{G_{ext}} \tag{3.2}$$

If extraterrestrial irradiance in (3.2) is replaced with the clear-sky irradiance, the clear-sky index k_c is obtained. The clear-sky irradiance models the irradiance measured on a horizontal surface on Earth on a cloudless clear day. To obtain such irradiance, in this work we employed the ESRA model [93]. This index has the same advantages of removing daily cycles and allowing for studying the changes caused by clouds [94].

Following the same logic as for $\sigma(\Delta G)$, variability of irradiance can be described by means of the differences of k_t or k_c by using $V = \sigma(\Delta k_t)$ or $V = \sigma(\Delta k_c)$.

Changes in irradiance can also be quantified in terms of ramps. In other words, how deep the rate of change of irradiance in a period Δt is. Thus, the ramps are defined as (3.3)

$$r = \frac{\Delta G}{\Delta t} \tag{3.3}$$

Since ramps are changes, the standard deviation method is also used for quantifying irradiance variability: $V = \sigma(r)$. As discussed above, irradiance with high variability exhibits large changes in a short time and hence higher ramps. The maximum value of the ramps is then used to describe the irradiance variability ($V = \max(r)$). In addition, following the same logic, the mean ramp, instead of the maximum, is studied as an irradiance variability metric (i.e., $V = \mu(r)$).

Finally, the Variability Index (VI) describes the variability of irradiance as a ratio of the length of the ramps of the measured irradiance with the clear-sky irradiance as seen in (3.4) [95]

$$VI = \frac{\sum \sqrt{\Delta G^2 + \Delta t^2}}{\sum \sqrt{\Delta G_{clear}^2 + \Delta t^2}} \tag{3.4}$$

3.2. PREVIOUS ANALYSES OF P&O UNDER VARIABLE IRRADIANCE

In the study of the P&O performance in changing irradiance, it is worth mentioning the European standard EN50530 for testing the overall efficiency (tracking and converter) of PV inverters [96]. It defines a triangular-like test signal with increasing slopes (from 0.5 to 50 W/m^2/s) and then repeated at a higher base irradiance and with slopes varying from 10 to 100 W/m^2/s. The sequence is used to simulate changes in irradiance.

In [97], the EN50530 was used to compare the performance of the P&O and the incremental conductance algorithms. The efficiency of P&O is lower at low irradiation and slow irradiance changes but lowest with abrupt changes and low irradiance. The reported average efficiency is 98.3%. The EN50530 standard was also used in [98] to compare different P&O methods. The fixed-step (where the magnitude of the voltage perturbations is constant) version of the P&O was used as a reference and multiple versions of the algorithm with variable steps (where the voltage perturbations are not constant while tracking) were tested. Variable-step versions of the P&O provide an improvement in the performance of the algorithm (e.g., [99]).

The performance of the P&O can also be studied using real conditions as done in [88]. The authors ran the algorithm under different sky conditions. The lowest efficiency for the P&O was 96.5% under partly cloudy skies.

Other studies focused on optimizing the parameters of the P&O algorithm—in particular, the magnitude of the perturbation and the time between perturbations. This leads to conditions for avoiding the algorithm from being confused [89], or expressions that relate the efficiency with the perturbation size [100].

The efficiency of the MPPT system consists of two parts: the hardware efficiency and the tracking efficiency of the algorithm [84]. While most of the previous works focus on the total system efficiency, we focused only on the tracking efficiency of the algorithm and studied the algorithm's efficiency when operating at real irradiance. Our assumptions of an ideal converter and uniform irradiance provide the best-operating conditions for the algorithm. Hence, by quantifying the variability of solar irradiance, we can determine the inevitable loss of efficiency of the algorithm's logic.

To achieve this objective, we present the methodology used for our study in Section 3.3. The results of Section 3.4 present our observations regarding the relationship between the algorithm efficiency and irradiance variability, the effect of the tuning parameters of the algorithm, and the influence of the PV module's tilt. We provide an extensive discussion of the results in Section 3.5 before giving our conclusions in Section 3.6.

3.3. METHODOLOGY

The P&O algorithm performs voltage perturbations with a sampling time (T_a) less than 1 s. Hence, the use of data in the minute range results in rates of irradiance changes that are too slow to yield any conclusion. The larger the data time step, the smoother the rates of change in irradiance. This occurs partly due to the averaging typically performed by the data acquisition systems. For this reason, we used 3-second sampled irradiance data of Oahu, Hawaii from NREL [101]. This dataset is one of the few with such high temporal resolution containing the three components of irradiance: Global Horizontal Irradiance (GHI), Direct Normal Irradiance (DNI), and Diffuse Horizontal Irradiance (DHI). We used these quantities to calculate the irradiance impinging on the same plane as the PV module using Equation (3.5):

$$G = G_{dir} + G_{diff} + G_{ref} \tag{3.5}$$

The direct component (G_{dir}) is calculated from the measured DNI and the angle between the Sun and the vector normal to the module. We used the isotropic sky model

approach to translate the measured DHI to the plane of the module and calculate the diffuse component (G_{diff}). For the reflected component (G_{ref}), we assumed a constant value for the albedo of 0.2. We will refer to the plane-of-module irradiance simply as "irradiance".

Since the irradiance does not change instantaneously but in a ramping way, we used linear interpolation to connect two consecutive data points with a ramp. Each new point is separated by the sampling time (T_a). At every point, we used the approach proposed by [102], based on the well-known single diode model to obtain power–voltage (P–V) curves. The module is treated as ideal, thus neglecting series and parallel resistances [102]. We used the datasheet of the front side of a 400 W Trina Solar DUOMAX Twin module for fitting the model. Except for Section 3.4.3, the simulation considered a single, horizontally placed module, uniform irradiance (i.e., no partial shading), and free horizon (i.e., no obstacles in the surroundings). The ambient temperature was kept constant at 25 °C. With this, we ensure that all effects are due to irradiance changes only. For all the interpolated datasets, the P&O algorithm was run to find the maximum power point at each step. To improve our analysis, we only considered irradiance values above 20 W/m^2 that occurred when the elevation of the Sun was greater than 5°.

The baseline sampling time (T_a) of the P&O was set at 50 ms and a voltage step (ΔV) of 0.3 V.

In reality, the power converter performs the MPPT algorithm. However, we decided to consider this component ideal. Then, the sampling time and voltage step are used to simulate the algorithm directly on the P–V curve of the module. We ensure that the algorithm operates under the most favorable conditions by neglecting the power converter and assuming uniform irradiance on the (ideal) module. This allows us to compute the efficiency losses of the logic of the algorithm caused exclusively by irradiance variability.

Since the P&O algorithm swings around the MPP, the efficiency cannot be calculated with a unique power point. Instead, we considered the efficiency as a ratio of energies for a given time period (3.6) as done by [97]:

$$\eta_{MPP} = \frac{\int_0^{T_M} P_{op}}{\int_0^{T_M} P_{MPP}} \tag{3.6}$$

where P_{op} is the power output of the module operating under the P&O algorithm at a particular moment. P_{MPP} is the theoretical maximum power point of the module at the same P–V curve. The integrating interval T_M was set at 3-s and 1 min.

The variability of solar irradiance is related to the variance of the measured irradiance, and its quantifiers are mainly based on the standard deviation of differences between measured points. An extended description of the used quantifiers was presented in Section 3.1. The period used for irradiance variability calculations was set at 1 min, using the 3-s sampled data.

3.4. RESULTS

Here, we present a statistical analysis of the efficiency loss of the logic of the P&O algorithm when it operates under changing irradiance. First, the results explore the relationship between variability and efficiency of the algorithm. Based on the observations,

a model that quantifies such a relation is presented. We then move to determine the effects of the tuning parameters before presenting an analysis of the influence of the module tilt. Unless explicitly mentioned in the next sections, the term *efficiency* pertains to the efficiency of the algorithm.

3.4.1. IMPACT OF IRRADIANCE VARIABILITY ON THE EFFICIENCY OF THE ALGORITHM

The efficiency of the P&O algorithm is not constant. It experiences sudden drops when the irradiance changes. The depth and frequency of the efficiency drops lead to dispersion in the obtained efficiency values. In other words, scattered efficiency values indicate a deeper efficiency decrease. The dispersion can be easily quantified using the standard deviation of the efficiency, $\sigma(\eta_{MPP})$. We related this to the standard deviation of the changes in irradiance, $\sigma(\Delta G)$, as a measure of variability. Figure 3.2 shows that higher irradiance variability corresponds to higher efficiency dispersion indicating a relation between the two.

Figure 3.2: Daily dispersion of differences in irradiance, $\sigma(\Delta G)$, causes increased daily dispersion of the calculated efficiency, $\sigma(\eta_{MPP})$, for 100 randomly selected days. Two outliers were removed for clarity.

Although Figure 3.2 shows some impact of irradiance variability on efficiency, a Pearson correlation analysis shows a minimal linear correlation between the 1 minute irradiance variability and the 1 minute efficiency with all variability metrics ($\bar{r} = -0.45$). Note that this correlation is against the 1 minute efficiency values and not with the standard deviation of efficiency. A single variability value is not linked to a single efficiency value but many. Because of this, no clear trend can be derived.

To reduce the scattering of the data and obtain a better insight into the effect of irradiance variability on the algorithm's efficiency, the data were grouped into 50 irradiance variability bins. At every bin, efficiency was averaged as well as the irradiance variability (given by $\sigma(\Delta G)$) corresponding to each bin. With this binning approach, we found that the average efficiency $\bar{\eta}_{MPP}$ is related to the mean of irradiance variability, $\overline{\sigma(\Delta G)}$,

through the quadratic expression (3.7):

$$\bar{\eta}_{MPP} = p_1 \bar{V}^2 + p_2 \bar{V} + p_3 \tag{3.7}$$
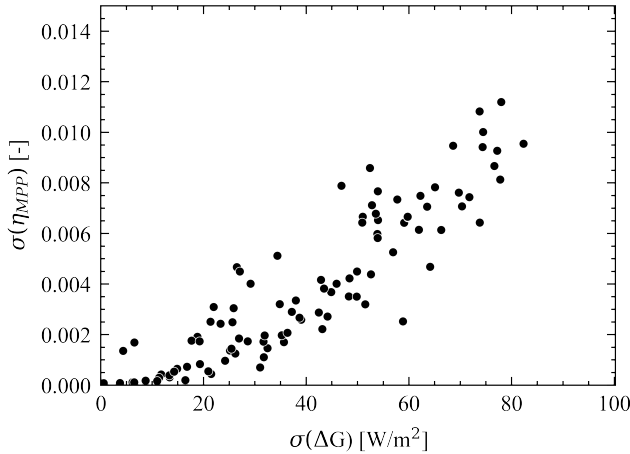
where $\bar{V} = \overline{\sigma(\Delta G)}$. The values for the coefficients p_1, p_2, and p_3 can be found in Appendix A.

The proposed model is illustrated in Figure 3.3. When binning is applied, the model accurately describes the relationship between efficiency and irradiance variability.

Although $\sigma(\Delta G)$ was used as a metric for irradiance variability, other metrics exist to describe irradiance variability, namely,

- Standard deviation of changes of the clearness index;

- Standard deviation of changes of the clear-sky index;

- Standard deviation of ramps;

- Maximum ramp;

- Variability Index.

These were extensively detailed in Section 3.1. To explore the validity of our model for other metrics, we repeated the analysis for the metrics mentioned above, finding that the model can be applied to all of them. This is not unexpected as the studied variability metrics are strongly linearly correlated with each other, with Pearson correlation coefficients exceeding 0.8.
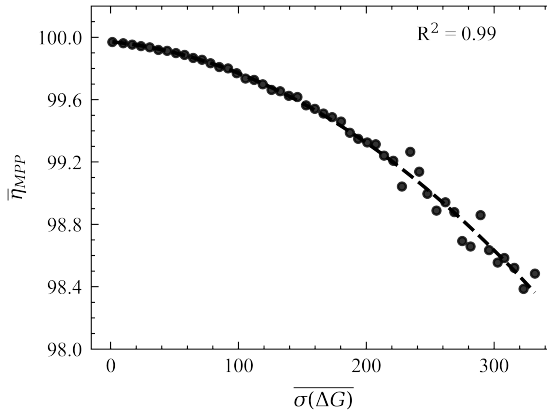
Figure 3.3: Drop of the binned average efficiency, $\bar{\eta}_{MPP}$, of the P&O algorithm as a function of the mean irradiance variability in each bin, $\overline{\sigma(\Delta G)}$. The coefficient of determination (R^2) is included in the graph to indicate the goodness of fit. Other variability metrics can also be fitted with the model. The fitting parameters are given in Appendix A.

3.4.2. SENSITIVITY OF THE P&O PARAMETERS

We selected 1 h of data at the same timestamp (12:00 p.m. to 1:00 p.m. local time, Oahu, Hawaii) with different irradiance variability. For each hour chosen, we modified the sampling time, T_a, logarithmically between 0.1 and 1000 ms and ΔV linearly from 0.1 to 3% of the open circuit voltage of the module at Standard Test Conditions ($V_{oc(STC)}$). Figure 3.4a shows the results of this analysis on an hour with low irradiance variability in contrast to an hour with high irradiance variability as in Figure 3.4b. Under stable irradiance, T_a does not have a significant impact on the P&O performance, and the efficiency loss is mainly determined by ΔV (Figure 3.4a). With variable irradiance, T_a plays an important role. As both parameters influence the efficiency loss under varying conditions, a poorly tuned algorithm with slower sampling time in combination with significant voltage perturbation can experience losses of up to 2% (Figure 3.4b).
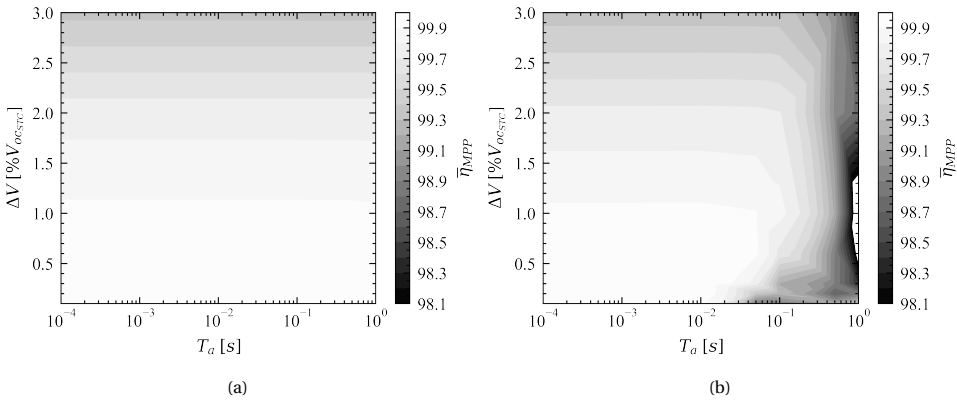
Figure 3.4: Sensitivity of the P&O algorithm efficiency, η_{MPP}, to its parameters under (**a**) clear skies, and (**b**) variable irradiance.

3.4.3. IMPACT OF THE MODULE TILT

So far, our analysis was focused on a horizontally placed module. For a tilted module, the efficiency loss is more significant near the tilt angle of the module that maximizes the annual irradiance ("optimal angle"). More direct irradiance reaches an optimally tilted module than a horizontal one. This implies that a cloud blocking the Sun will cause a more profound reduction of the available irradiance to the module, increasing the effect of variability. To support this argument, we simulated a module placed horizontally and then gradually increased its tilt in steps of 5° until vertically placed. One randomly-selected highly variable day served as the input for all the angles. The simulation followed the procedure explained in Section 3.3. Figure 3.5 shows the dispersion of the P&O algorithm efficiency as the tilt angle increases. The dispersion of efficiency, linked to a more considerable efficiency loss, is higher near the optimal angle for this day. As the module is tilted away from the optimal angle, the direct irradiance exhibits lower peaks. This is linked to lower efficiency losses.
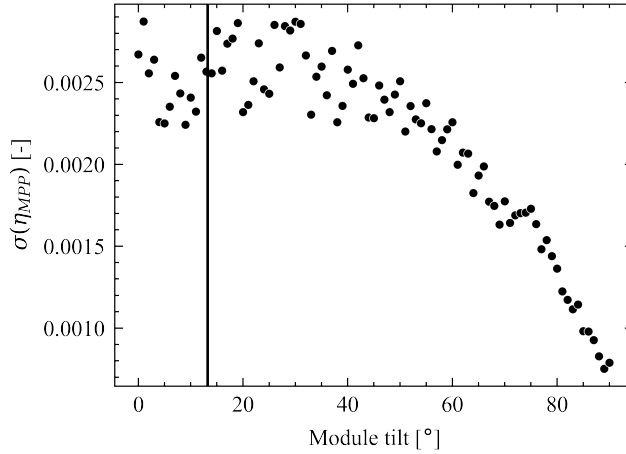
Figure 3.5: Impact of the module tilt on the daily efficiency for one randomly selected day. For the studied location, the optimal tilt angle is 13.23°, marked with the vertical line.

3.5. DISCUSSION

We hypothesized that moments with significant changes in irradiance experience the lowest algorithm efficiency. Then, it should be possible to draw a relation between irradiance variability and efficiency. This, curiously, is not a linear relation and also not a simple task to relate the two quantities. Figure 3.2 only indicates that efficiency data become more spread as the variability of irradiance increases. However, from Figure 3.2, it is not possible to quantify the efficiency loss. In other words, Figure 3.2 gives only an indication of the existence of a relation between irradiance variability and efficiency. It is only after the binned efficiency analysis (Figure 3.3) that we can establish a comprehensive connection between irradiance variability and algorithm efficiency.

When the algorithm gets confused, the operating point will drift away from the MPP. The amount of divergent points depends on the steepness of the irradiance ramp. For shallow ramps of solar irradiance, this drift occurs in one or two points before the algorithm swings back again towards the correct operation. Thus, the impact on efficiency can be neglected. This is not true for steep ramps. Under such conditions, the algorithm diverges during more points, causing substantial drops in the instantaneous efficiency (We observed instantaneous efficiency values dropping as low as 80%). Furthermore, after the algorithm has diverged, it needs additional steps to climb back towards the MPP.

The P&O algorithm's efficiency also depends on its tuning parameters. We observed that, on clear days (Figure 3.4a), the efficiency drops with large voltage steps. This is in line with the remarks of other authors who observed that increasing the perturbation step leads to better dynamic performance, as the MPP is reached faster, but with the disadvantage of a poor steady state tracking due to the swinging around the MPP [103]. Interestingly, when optimizing the perturbation step, some authors have found voltage perturbations that exceed 2% of their module's V_{oc} [100, 104]. In contrast, we observed that the highest dynamic efficiency for clear and highly variable days is obtained with

lower voltage steps. For practical MPPTs, the voltage perturbation is below 1% [90].

Regarding the sampling time (T_a), values found in the literature range from 0.05 s to 0.1 s (1–20 Hz) [90, 100, 105]. Even when these parameters were optimized considering the response of the PV module and the power converter [104], the losses caused by variability only become significant. This is clear from Figure 3.4b. The range of T_a approached the right half of the figure where efficiency is lower, especially combined with small perturbation steps.

The efficiency values for the P&O algorithm given in the literature span over a broad range. Some of the efficiency values are as low as 62.63% for a test under EN50530 with low irradiance and small perturbation step [106]. Under real conditions, the reported mean efficiency of the algorithm was 98.3% [97]. In [88], and the authors determined that the efficiency under partly cloudy days was 96.5%, while, for a clear day, it was 98.7%.

One possible reason for the large discrepancy in the efficiency values is the integration period that different authors consider for their calculations. All these studies (including the present work) use Equation (3.6) for the calculation of efficiency. However, the integrating period ranges from a full day to a few seconds.

An additional contribution of this work is the analysis of the impact of the PV module tilt on efficiency. From Figure 3.5, we see that the scattering of the efficiency reduces as the module is placed more vertically. This is because the variability of irradiance decreases as the module's tilt angle becomes larger. The maximum variability coincides with the optimal angle of the module. Therefore, we can expect a greater efficiency loss at an optimal angle than a horizontally placed module and even greater in comparison with a vertical one. For example, from the data used to obtain Figure 3.5, we can calculate the irradiance variability $\sigma(\Delta G)$. Using Figure 3.3, at an optimal angle, the MPPT efficiency is close to 99.90%. We gain 0.02% in tracking efficiency just by placing the module horizontal, and 0.09% for the vertical case.

Another issue worth mentioning is that, in all previous studies, there is a power converter involved, either in simulation or experimental. This can also be a potential reason for the lower values obtained in the literature with respect to our results. The hardware imposes limitations in the study of the logic of the algorithm as the dynamics of the converter, combined with the PV module, determine the optimal parameters of the P&O algorithm [89, 104, 105]. Additionally, the hardware imposes limitations regarding how fast the PV module can react to a duty cycle change [103, 107], which is related to the maximum sampling frequency that can be used for the perturbations [108]. The resolution of the analog-to-digital converters of the control system and the sensitivity of the sensors imposes constraints on the minimum step size that can be employed [104].

In [97], the authors attributed extremely low values of efficiency observed (<95%) during real conditions to poor performance on the converter. In our simulations, we also observed such behavior (efficiency dropping as low as 80%), which suggests that the hardware is not the only one responsible for large drops in irradiance but the logic of the algorithm itself.

Although Figures 3.4a,b show an idealized situation, in practice, these values could not be reached due to hardware limitations. The importance of our study relies on the fact that the logic of a well-tuned algorithm, under the most favorable conditions for the algorithm (not considering any power electronics and no partial shading), causes a

systematic efficiency loss that, on a monthly basis, can reach up to 0.1% due to variable irradiance. This represents a production reduction of approximately 1 h per month at the selected site.

3.6. Conclusions

We studied the relation of irradiance variability to the efficiency of the P&O MPP tracking algorithm. We found a connection between the binned efficiency and irradiance variability that a second-order polynomial can describe. The confusion of the P&O algorithm depends on the ramps caused by irradiance variability. The divergence of the algorithm results in a systematic decrease in efficiency that can account for up to 0.1% on a monthly average. A wrong choice of the algorithm's parameters and the module tilt significantly impacts the efficiency on highly variable days. Our study opens the possibility for an efficiency analysis in different locations around the globe with the sole input of global horizontal irradiance as well as to compare newer and more advanced algorithms. A considerable amount of resources is spent on increasing the efficiency of solar cells. As single-junction solar cells are reaching the theoretical limit, even small improvements in efficiency are regarded as a success. The loss caused by irradiance variability in one of the most used MPPT algorithms is on the same order of magnitude as the cell's efficiency improvement, highlighting the importance of properly tuning the algorithm to its operation under rapidly changing weather conditions.

Including this loss into the PV systems analysis can help to reduce uncertainty in energy yield caused by irradiance variability and facilitate the growth of PV for meeting the generations' goals of the Net Zero Scenarios set in 2030.

4

ULTRA-SHORT-TERM IRRADIANCE FORECASTING

A cloud is made of billows upon billows that look like clouds...

Benoit Mandelbrot

Clouds influence the irradiance from the Sun as it travels through the atmosphere with their shape, size, and constitution [109]. One of the most obvious effects is that they block the sunlight, reducing the available Sun power reaching the ground. They can also cause the opposite: increasing (or *enhancing*) the irradiance above the theoretical irradiance at the top of the atmosphere [109, 110], caused by scattering inside the cloud [111] which leads to an increase in the diffuse irradiance [110]. Cloud enhancement, for example, can cause blowing of fuses (leading to production loss), overloading of the inverters (leading to efficiency loss) [112] or underestimation of maximum Photovoltaic (PV) production [113]. Therefore, the movement of clouds in front of the Sun produces fluctuations in the solar irradiance available for PV production. These fluctuations occur even in the sub-minute range, negatively affecting the PV systems in the form of significant PV power ramps which impose a challenge to grid operators [114], and the variability of solar irradiance affect the maximum power point trackers' operation resulting in efficiency loss [115].

Irradiance forecasting is a method to alleviate some of the challenges of variations caused by moving clouds. It is applied in the operation of PV systems with benefits such as increasing battery lifetimes of PV systems that incorporate them [116], and it has proven to be a crucial requirement of grid operations with high renewable energy penetration [117].

In the very short term, defined by a time horizon from seconds to maximum 30 minutes [118], images from the sky provide valuable information such as cloud identification (e.g., [119]), cloud classification (e.g., [120]), and cloud tracking (e.g., [121]). Such sky images are obtained with an All-Sky Imager (ASI) (a camera equipped with a fish-eye lens facing the sky) which takes a picture of the sky in a particular location. This has the advantage of retrieving higher resolution information on the site than satellite images (which cover a broader area), ceilometers, and radars (which have lower local resolution) [122].

The core idea behind predicting irradiance using sky images is to 1) identify clouds, 2) determine how they are moving, and 3) assess whether they will obstruct the Sun [121, 123–127]. Additional information (or features) can be given to the model to improve the prediction. For example, in [124], the authors included not only the cloud pixels and their movement but also identified the cloud edges and corners related to the cloud type and the pixel intensity of the clear and cloudy pixels.

Convolutional Neural Networks (CNNs) can automatically detect these features [128] and can be used to perform irradiance forecasting, such as SUNSET [129, 130], SolarNet [131] and ECLIPSE [132]. SUNSET is a CNN that receives a sequence of sky images and historical PV power production to forecast a 15-minute horizon [129, 130]. In highly variable moments, the model predicts the average output PV power in the prediction horizon [130]. SolarNet follows a different approach, as it was designed to predict over a wide range of time horizons using 6 CNNs trained for different forecasting horizons and a single sky image as input. It can predict up to 60 minutes with a 10-minute resolution [131].

The prediction of irradiance ramps can be done by predicting the future position of the cloud pixels and determining whether or not these pixels will block the Sun [132, 133]. ECLIPSE uses this approach to predict up to 10 minutes with a resolution of 2 minutes, and it tackles specifically the prediction of important irradiance ramps. It achieves this by combining temporal information (using a sequence of images) along with spacial information (location of the clouds and the Sun) [132].

CNNs are not the only architecture for implementing sky image forecasting. Especially when including sequences of images, other Artificial Intelligence (AI) architectures such as Long Short-Term Memory (LSTM) or Recurrent Neural Network (RNN) can also compete and even outperform CNNs [134–138]. Nevertheless, a CNN has a relatively simpler architecture than LSTM or RNN [139] and the improvement in the error reduction that the former offer is marginal (around 2%) on forecasting horizons greater than 10 minutes [135, 138]. In some cases, the CNN can even perform better than the networks incorporating temporal information [138].

In general, sky-image-based forecasting methods outperform persistence models in many sky conditions, although their performance for ramp detection is still one of the main challenges and an ongoing research topic [136]. This holds even for models based on artificial intelligence, as they tend to output a smooth prediction of irradiance that effectively misses steep ramps [134, 135, 137] or they predict an average of the output [130, 135]. Additionally, the output from AI models tends to lag from the actual measurements [135]. Even more, deep learning models models are sensitive to weather conditions [137, 139].

To tackle these problems, hybrid models have been proposed. Some combine image processing techniques to extract the evaluating features and then feed them to an LSTM which performs the forecast. This model can solve the problem with time alignment and detect some ramps [127].

AI-based hybrid models can also be created by training different models to cover various scenarios. One of these is based on implementing a classifier for four cloud types. Then four different models are trained using Support Vector Regression and Multiple Linear Regressor. The final prediction is made by determining the prevailing cloud type on a sky image and then applying the corresponding model to that cloud type [126]. The authors claim an improvement in the error not only with respect to the persistence model but also to models based on Artificial Neural Network (ANN)'s [126].

The classification can also be done in terms of time. This is achieved by training the same model aiming at different forecasting horizons and then combining their output using a linear combination [140]. This strategy is also useful to deal with models which have many inputs, such as images and irradiance measurements. In this case, the time resolution of the data can have different sampling times. The use of different models and combining their output (ensemble learning) can help to deal with these situations [141] or facilitate training with fewer data by using transfer learning [142].

The purpose of this work is therefore to develop a mixed model based on sky images (Sections 4.1.1), a sky classifier (Section 4.1.3), and a CNN (Section 4.1.4).

As opposed to ensemble learning techniques, which are also based on classification, our model does not combine the output of different models but uses the output of a specialized model on a particular sky class which leads to a reduction in the prediction error (Sections 4.2 and 4.3).

4.1. MODEL STRUCTURE

Our model consists of three main modules: image processing, sky classifier, and artificial intelligence. Figure 4.1a illustrate the structure of the model. The model receives a sky image and a clear-sky index (defined in Section 4.1.3) and the coordinates of the Sun in the image. The image is manipulated to obtain the cloud cover (Figure 4.1b). Using this and the clear-sky index it is classified in one of five categories. The image is then fed, along with the clear-sky index to one of the five CNNs trained for the particular class the image belongs to. The output is a minute resolution of the Global Horizontal Irradiance (GHI) over the next 20 minutes.

4.1.1. IMAGE PROCESSING MODULE

The image processing module processes the images that will serve as input to the classifier. After the processing, the Cloud Cover, the clear-sky index and the position of the Sun within the image are obtained.

CLOUD IDENTIFICATION

A digital color image (such as that captured by an ASI) is a discrete representation of the intensity of the light impinging upon the sensor of the camera [143]. The *color* of the digital image is obtained by superimposing a checkered pattern where three filters
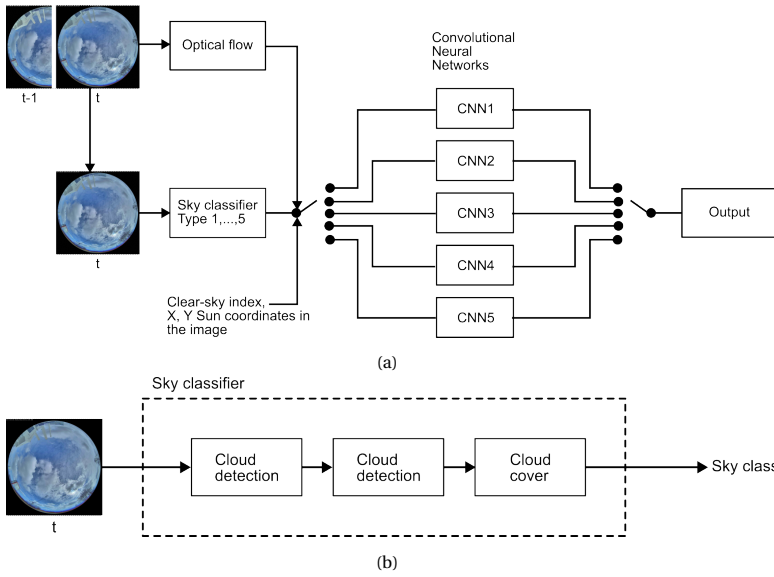
Figure 4.1: (a) Overview of the prediction model. (b) Detail of the sky classifier module.

(red, green and blue) are embedded (Bayer pattern) [144] to the sensor or having three separate red, green and blue sensors [143, 144]. The reason for these three colors is that the model used to represent each pixel in the image defines them as primary colors and is called the Red-Green-Blue (RGB) model [143]. Using the RGB model results in a 3D representation of an image where each matrix dimension represents one primary color [143, 144].

The color channels of a sky image can be used to identify clouds (cloud segmentation). On a clear day when looking at the sky, it appears blue. If, at this instant, a sky image is taken, the value of the blue pixels will be higher than the Red pixels, assuming that our image is mapped in the RGB color space. On the contrary, a cloud-covered sky image will have a greater count of red pixels, making the clouds appear white or gray [120]. Using this fact, the clouds can be detected by using a ratio (e.g., [145]) or a difference (e.g., [120]) between the image's red and blue channels and then establishing a threshold above which the pixels will be classified as clouds while the rest as sky. A combination between the difference and ratio of the red and blue channels can also be used to establish such threshold. This is the case of the Normalized Blue-Red Ratio (nBRR) which is defined in Equation 4.1.

$$nBRR = \frac{Blue - Red}{Blue + Red} \tag{4.1}$$

The problem with the thresholding method is that it fails to detect very thin clouds, has a large misclassification rate due to the overlap of the pixel distribution between clear and cloudy conditions, and performs poorly on pixels located around the sun [119,

146].
The fact that partially cloudy, overcast, and clear days exhibit different nBRR pixel distributions can improve classification accuracy.

The nBRR pixels of partly cloudy images exhibit a bimodal distribution, while this feature disappears on overcast and clear-sky images. The bimodality can be identified from the standard deviation of the histograms [146]. Depending on the sky condition, the thresholding technique can be adapted for partially cloudy (bimodal distribution), partially or clear-sky images (unimodal distrution) [146]. This is the core idea behind the Hybrid Thresholding Algorithm (HYTA), which achieves an overall accuracy of 88.53%. However, HYTA excludes sun pixels, because very few sun pixels, can shift the whole histogram due to their large intensity. For this reason, the improved algorithm version, HYTA+ [119], was developed. This method adds another classification step by first determining whether a cloud covers the sun. Following the logic of the HYTA, the algorithm of [147] is based on sun coverage identification and sky condition classification. We build upon this model because of its simplicity and accuracy. Our implementation of the algorithm [147] is explained below.

1. Sun identification: Determines whether the sun is blocked or not.

    (a) Identification of the sun. Equation 4.2 returns the coordinates (in pixels) of the sun in the image based on the position of the sun in the sky described by its azimuth (A) and altitude (a) (in degrees). It is based on the projection of the sky dome on a plane [148]. Once the sun is identified, the image is cropped, considering a radius of 200 pixels around the sun's coordinates

$$X_{\text{sun}} = X_{\text{center}} + R_{\text{image}} \times \sin(A)\cos(a)$$
$$Y_{\text{sun}} = Y_{\text{center}} + R_{\text{image}} \times \cos(A)\cos(a)$$

(4.2)

    (b) Obtaining the sun coverage ratio. The cropped image is converted to grayscale. The sun is detected by identifying very bright and white pixels with a value exceeding 210. The value of 210 is the minimum average pixel intensity of the region around the sun of 150 clear-sky images [147] (Note: the maximum pixel value of a grayscale image is 255). Then, the ratio of white pixels in the whole image is calculated. The sun is clear if at least 95% of the pixels of the cropped image are white [147].

2. If the sun is blocked:

    (a) Apply a fixed threshold of 0.6 on the Red/Blue ratio to identify the clouds.

3. If the sun is *not* blocked:

    (a) Determine if there are cloudy pixels in the image. The original work [147] set a fixed threshold of 0.6 on the pixel intensity of the image, excluding 200 pixels around the Sun. We decided to apply the average of the normalized Blue-Red Ratio (Equation 4.1). Our threshold value was set at 0.45, which corresponds to the 75$^{\text{th}}$ percentile of the pixel values of 100 partially cloudy days. This means that values above 0.45 will be classified as clear. Figure

(a)

(b)
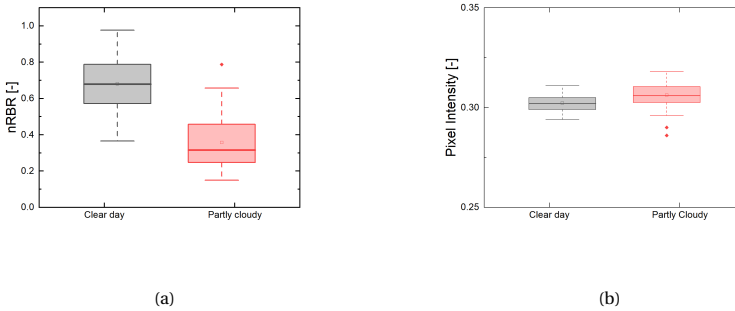
Figure 4.2: Statistics of 100 clear-sky images and 100 partly cloudy images.(a) Mean pixel value using the nBRR and (b) Pixel intensity using the Blue-Red ratio as in [147]. Note that with the pixel intensity, there is a greater overlap between clear day and partially cloudy images.

4.2 shows the statistics of both figures. Using the average of the nBRR (with the sun blocked as in [147]) results in lower overlapping than using the original pixel intensity of the Blue-Red ratio. Our chosen value ensures that most of the clear-sky images are correctly classified, albeit sacrificing accuracy for the partly cloudy days which statistically is 25% of the evaluated images. Despite this considerable large value, a visual inspection of the images suggest that the misclassified images show small clouds, not covering the sun, and a deep blue sky, which is acceptable for the clear-sky classification. Lowering the threshold to the minimum of the observed clear-sky images, results in worst classification as completely overcast where the sun is visible (foggy conditions, for example), can be misclassified as clear-skies.

(b) For images classified as partly cloudy, apply superpixel segmentation method following the approach of [149]. The superpixel segmentation method is, as the name implies, a segmentation strategy that will aggregate pixels with similar characteristics of brightness, texture, and contour smoothness into blocks called *superpixels*[150]. The superpixels offer a segmentation that is closer to how a human would segment the same image manually [150]. The superpixel segmentation method proposed in [149] essentially obtains a global threshold to separate clouds from sky for the whole image using the Otsu algorithm, which is an automated method for finding the optimal threshold. It is based on the fact that the pixels of high-contrast grayscale images have a bimodal distribution. Thanks to this fact, two classes can be created based on the humps of the bimodal distribution. The Otsu thresholding iterates over the image histogram and in each pass separates these two classes by evaluating the probability of each class and its variance, which are dependent on the threshold. The optimal threshold will maximize the variance between both classes [151].

After the global threshold is obtained, the cloud detection algorithm applies superpixel segmentation to the image. For each superpixel, a local thresh-

old is obtained and then compared against the global threshold. This allows establishing a decision on the threshold that should be applied to each super-pixel. By doing this, the identification of clouds is performed *per superpixel* instead of globally. Hence a more accurate identification is achieved [149].

The cloud cover is the count of cloudy pixels to the total image pixels. It is important to mention that we masked the pixels of the image corresponding to the horizon to avoid counting these objects as clouds. We also considered only images with a sun elevation higher than 10° over the horizon. Some examples of cloud identification can be found in B.1.

4.1.2. Optical Flow

The cloud motion is incorporated by calculating a dense optical flow. This tool allows the tracking of pixels between two consecutive images by calculating the displacement of pixels (or group of pixels) between two consecutive images [152]. In particular, we applied the Farneback method [153]. This method approximates the pixel intensity of a greyscale image as a quadratic polynomial. Then, it assumes that the consecutive image is described by the same polynomial function but displaced by a *displacement vector field*. The Farneback algorithm aims to retrieve this displacement vector for every pixel [153].

This algorithm is implemented in the Python package OpenCV as the function `calcOpticalFlowFarneback` and returns the displacement vector for every pixel in terms of magnitude and angle [154].

The optical flow has been applied to irradiance forecasting by first determining the full displacement vector field and then finding an equivalent vector which describes the motion of the main cloud block near the Sun. This can be later related with the direct normal irradiance to predict occlusions of the Sun [155].

4.1.3. Sky classifier

The sky-classifier is built upon the cloud cover retrieved from an instantaneous sky image and the clear sky index obtained simultaneously. To recall, the clear-sky index is an adimensional number relating the measured GHI (GHI_m) against the GHI obtained from a clear-sky model GHI_0 at any instant. Mathematically, it is expressed as in Equation 4.3. The clear-sky index removes the seasonal variation of irradiance, allowing for an analysis for the changes in irradiance caused by clouds ([156]).

$$k_c = \frac{\text{GHI}_m}{\text{GHI}_0} \tag{4.3}$$

For this reason, we hypothesized that there should be an almost linear relation between the cloud cover and the clear-sky index (i.e. the larger the cloud cover, the lower the clear-sky index). Figure 4.3a shows the scatter plot of the clear-sky index and the cloud cover for our dataset. From this image the hypothesized relation cannot be verified.

Pfister, et al. [109] described the relation between the cloud cover, the irradiance, and the clear-sky index. In their results, two bands, or clusters can be observed: The first

(a)   (b)
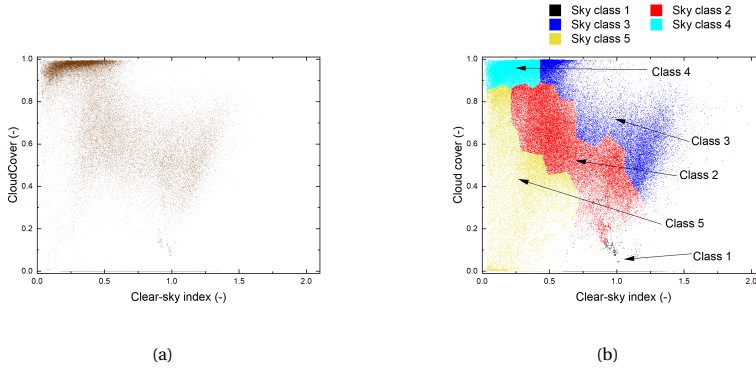
Figure 4.3: (a) Scatter data from instantaneous clear-sky index and cloud cover. (b) Classified dataset. Observe that there are some data points with very high clear-sky index values. Although it is not unexpected to have values of the clear-sky index exceeding unity (due to cloud enhancement), extreme values (close to two) correspond to a mismatch between the clear-sky index model and the measurements. This occurs mainly in the early morning or late evening.

occurs at very high clear-sky indices spreading over a wide range of cloud cover, and the second one at very low clear-sky indices scattered from cloud cover values between 40 and 100% [109]. These bands are not identifiable in our dataset (Figure 4.3a). The potential reasons for these differences are how they processed the irradiance data. In both works, 1-minute data was used; however, in the work of Pfister, et al.[109], the average of 1-second measurements over the minute is taken, while in our work, we took a single irradiance measurement that coincides with the instant that the sky-image is taken. Our approach results in measurements with higher variability (hence, the scattering observed in Figure 4.3a). Nevertheless, with this strategy, we do not include events that are not captured by the camera at that instant. For example, at a particular moment, a sky image might show a clear sun. However, in the course of the minute between images, the sun might have been obscured. By averaging the 60 s of the minute, this information is incorrectly assigned to the unobscured image.

Since we do not observe clusters of data, we applied K-means (50 clusters) and then manually grouped these clusters together to obtain a final classification consisting of five classes. The logic for the cluster strategy is as follows:

- Class 1: *clear-sky* images (high clear-sky index, very low cloud cover)

- Class 2: *partly cloudy* images following an almost linear relation of the clear-sky index and cloud cover.

- Class 3: *overcast days with high irradiance* (high cloud cover, high clear-sky index). This group includes the overirradiance phenomenon.

- Class 4: *overcast* images (Very low clear sky-index, very high cloud cover)

- Class 5: *Partly clear skies with sun obscured* images (low cloud cover, low clear-sky index)

Figure 4.3b shows the resulting clusters after the classification logic.

4.1.4. ARTIFICIAL INTELLIGENCE MODULE

The last module of the model is the one that makes the prediction. It implements a CNN, which processes a low-resolution, color sky image merged with the optical flow information at every pixel, resulting in a 64 × 64 pixels image with five channels. The first three channels of the image correspond to the red, green, and blue channels, respectively. The last two channels map the magnitude of the pixels' velocity (channel 4) and their direction (channel 5) obtained from the optical flow. The architecture of this network is a convolutional neural network with only one convolutional step, which processes the image. Then, the output is flattened to a one-dimensional vector and concatenated with the auxiliary input data: the X and Y coordinates of the Sun's position on the image and the clear-sky index. The auxiliary data combined with the flattened image is fed to a three-layer neural network. The output is a vector containing the 20-minute ahead clear-sky predictions.

This architecture is trained 6 times: one considering the whole dataset (reference) and one time per sky class. In short, the full pipeline of the model is

1. Get sky-image

2. Using the image processing module, obtain: cloud cover, clear-sky index and position of the Sun in the image.

3. Obtain the class of the image.

4. Use the CNN model trained on the sky-image class to get the final prediction

4.2. RESULTS AND DISCUSSION

The data set used in this study contains sky images taken using a CMS Shreder ASI-16/50 All Sky Imager located at the monitoring station of the Photovoltaic Materials and Devices. The irradiance was measured with a silicon-based pyranometer provided by the manufacturer of the sky camera. The full dataset contains data from 29-03-2021 until 24-02-2022. For training purposes, we used a reduced sample of this dataset containing 80 000 randomly sampled sky images with their associated irradiance values and with a sun elevation higher than 10° above the horizon. The distribution of the dataset can be found in B.2, Figure B.6. The clear-sky index was calculated using the python pvlib function `clearsky` with the *solis* model [157]. A reference model, hereafter called "full model", was trained to study the potential improvement of the classifier. This model has the same architecture of each CNNs used in the classifier but is trained with a random sample of 64 000 data points containing data from all classes. The rest of the data points are used for testing the model's performance hyperparameter tuning was performed for any of the models, as the study's main goal is to obtain a comparison of the advantages of the classifier. Each model was trained for 20 epochs using the mean squared error as the loss function. It is worth mentioning that the architectures of all models remain the same.

The models for each class were trained using a sample that contains the same amount of data points regardless of the class (9536 datapoints). Similarly, as the reference model, each model was trained for 20 epochs with no hyperparameter tuning.

Figure 4.4 shows the forecast skill defined in Equation 4.4 [135], where $\text{RMSE}_{\text{eval}}$ is the Root Mean Squared Error (RMSE) of the model under evaluation and $\text{RMSE}_{\text{baseline}}$ is the RMSE of the baseline model (either the model trained with the whole dataset (Full model) or the persistence model). Figure 4.4a compares both, the full model (model trained with the whole dataset) and the classified models against the smart persistence model, which assumes that the clear-sky index will remain constant throughout the forecast horizon. Note that in Class 4 (overcast) the persistence model performs better than the full and classified models, and in Class 5 (mainly overcast with patches of blue), the smart persistence model performs better than the classified model. The classified model is the best option for predicting Class 1 (clear skies), while the full model is the best option for predicting classes 2, 3, and 5 as seen in Figure 4.4b.

$$FS = \frac{\text{RMSE}_{\text{baseline}} - \text{RMSE}_{\text{eval}}}{\text{RMSE}_{\text{baseline}}} \times 100 \qquad (4.4)$$

(a)　　　　　　　　　　　　　　　　　(b)
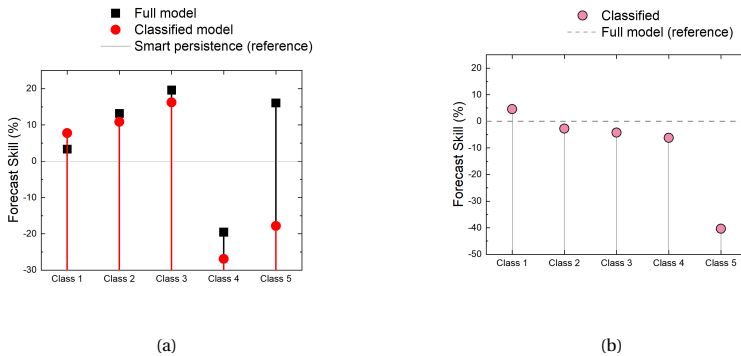
Figure 4.4: Forecast skill per class using the RMSE. (a) Performance per class of the classified and the full models (model trained with the full dataset) against the smart persistence model. The forecast skill of the smart persistence is zero, and is marked with a solid line. (b) Performance of the classifier against the full model (model trained with the full dataset). The forecast skill of the full model is zero because it is the reference in this particular case. It is marked with a dashed line.

With the results of Figure 4.4, it is evident that the full model outperforms the classified model in almost every class. The performance of the classified and the Full model are very similar, with a slight improvement in classes 2 and 3. The full model exhibits a larger scattering between the expected and the predicted values (Figure 4.5), while in the classified model, the points are more clustered. Because of this, the full model has more points close to the perfect prediction line resulting in lower error, especially in large clear-sky indices. We can conclude that the full model is more *accurate*, but the classified model is more *precise* in classes 1, 2, and 3 (Figures 4.5a, 4.5b, and 4.5c).

The classified model fails on classes 4 and 5 (Figure 4.4a, 4.5d, and 4.5e), and the smart persistence model is, by far, the best option for predicting overcast days (Class 4)

(a)

(b)

(c)

(d)

(e)

(f)
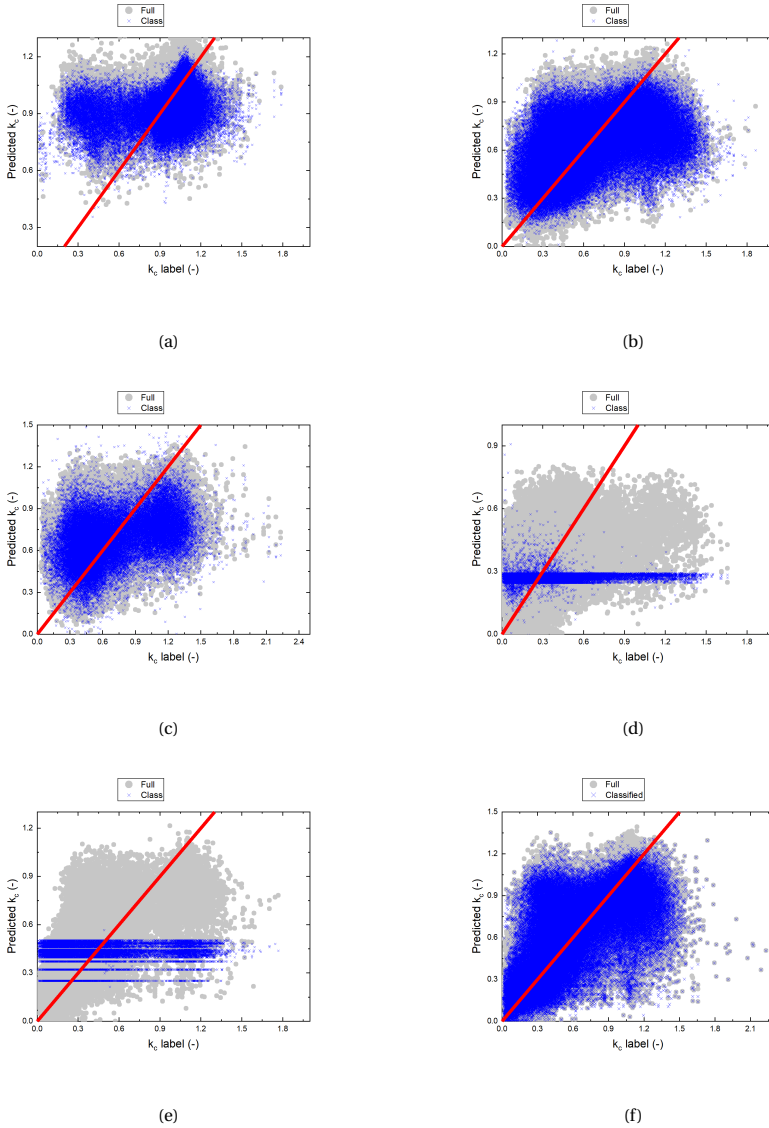
Figure 4.5: Comparison of the predicted and expected value between each class's full and classified models. (a) Class 1, (b) Class 2, (c) Class3, (d) Class 4, (e) Class 5, and (f) an application of the classifier on the whole dataset, where Class 1 was predicted with a class 1 CNN, classes 2,3 and 5 with the full model and Class 4 with the smart persistence model. The prediction on the same dataset with the full model is also shown. The red line on all graphs indicates a perfect prediction. Points above the red line indicate that the model overestimates the labeled value and points below the red label indicate that the model underestimates the labeled value.

(Figure 4.4a).

Figure 4.6 shows the evolution of the RMSE as the forecast horizon increases. The
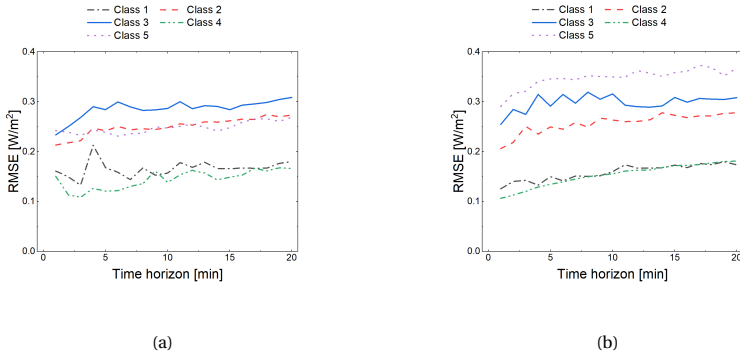
Figure 4.6: RMSE as a function of the prediction horizon for (a) the reference model performing in each class, and (b) the classified model.

error increases as the forecast horizon increases, as expected. For the full model (Figure 4.6a), the increase of the error is minimal, while for the classified model, it is more evident (Figure 4.6b). The models tend to ignore the changes in irradiance, and minimize the error along the whole prediction horizon. For this same reason, the classified model fails in classes 4 and 5, as the model predicts always the same value (Figure 4.5d and 4.5e).

Figure 4.7 shows the application of the model to predict the Global Horizontal Irradiance (GHI). Multiplying the model's output with the modeled clear-sky gives the value of the GHI. During the clear part of the day, the classified model outputs a smoother prediction closer to the measured GHI. In the variable part of the day, both models predict a trend rather than the actual value of irradiance, and neither of them captures the peaks and valleys of the measured irradiance. The Figure also shows the moments where the classified model failed (Class 5, in both cases).

The use of the optical flow to incorporate temporal information of the cloud movement did not show any improvement. There was no difference in the training error of the reference model with and without the optical flow. This suggests that the optical flow does not provide useful information to the model and can be ruled out as a predictor.

One potential explanation for this, is that the optical flow used in this work (the Farnneback method [153]) tracks the movement of *pixels*. But this does not necessarily implies that it tracks the *clouds*. The Farnneback method may provide too much information that the models interpret as noise. Another potential reason for the poor performance of the optical flow is that clouds do not move as a block, but they also change, which is not captured by the optical flow method. This makes the correlation between past images and future measurements a difficult task [133]. Nevertheless, although including the temporal information of clouds in forecasting models leads to improved prediction accuracy as proved by [135] and [136], this improvement is marginal and might not justify the extra effort needed for such an improvement.

Despite an overall higher performance of the full model, our approach has the advantage of improving the prediction by combining different models. The results presented
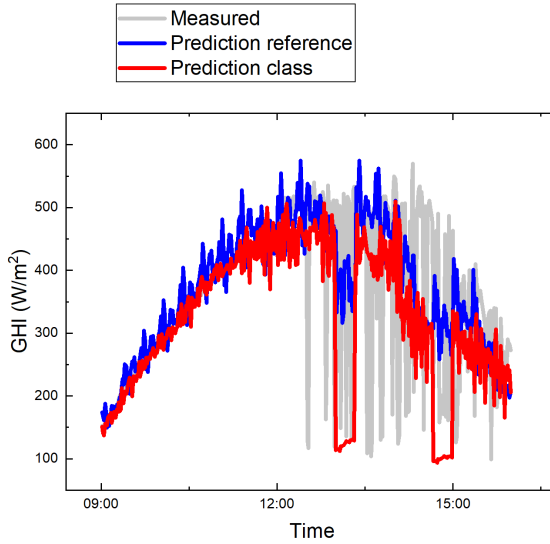
Figure 4.7: Example of 1 day with prediction using the classification model and the reference model. The measurements for such a day are also included as a guide. Note that both models have difficulties during the variable part of the day.

here assumed that the prediction module is the same for the five classes, but the classifier approach can also be combined with different models. For example, use the classified model for Class 1, the reference model for Classes 2, 3, and 5, and the smart persistence for Class 4.

Figure 4.5f shows an example of such an ensemble. When the predicted instant corresponds to Class 1, the predictor is the specialized CNN of Class 1. When it corresponds to classes 2, 3, and 5 the predictor is the full model. The predictor is the smart persistence model for instants that correspond to Class 4. This strategy reduces the error by 2.05% with respect to the full model. Although the improvement is not large, it proves that using specialized systems for different sky classes reduces the prediction error. This opens the possibility of implementing other prediction algorithms even better than our full model for a particular class, while using the classifier concept.

Note that, except for classes 4 and 5, the performance of the full and classified models is considerably close. Even if the full model outperforms the classified model, this could be acceptable, considering that the amount of data to train the classified networks is only a fraction of the data needed for the full model (around 14% per class, 42% for classes 1,2, and 3, 70% for the five classes). Naturally, increasing the number of training examples also helps the prediction accuracy of the classified model.

Our model (both the reference and classifier) still suffers from limitations regarding the prediction of ramps. This phenomenon is not particular to our model, but is present in many prediction models using sky images [130, 135–137].

Improving the accuracy of predictions directly impacts applying these methods to

control PV systems. Grid operators impose restrictions on the ramp rate (i.e., they impose a limit on the rate of change in the plant's output power) [116, 140, 158, 159] that are typically handled with energy storage systems [116, 158]. Incorporating prediction can help in reducing the size of electric storage [159], increasing its lifetime with proper control [116] or even eliminating [140, 158, 159] it, which has a direct effect on the cost of the system [116]. However, these benefits are only achieved if the prediction accuracy is high. Otherwise, it might be detrimental as the curtailed power is higher because of an incorrect prediction or a larger energy storage system is needed to compensate for the inaccuracy.

4.3. CONCLUSION

We presented a model for minutely predicting the clear-sky index in a 20-minute horizon. Our model is based on sky images, a sky classifier, and a convolutional neural network. The reference model has a superior performance than the classified model. The classified model outperforms the reference model in Class 1 with a forecast skill of 5%, while the difference between the classified and reference is small for most of the classes. The classified model fails in overcast and mostly overcast days and partially clouded moments still represent a challenge for both models when the smart persistence model outperforms the most complex artificial intelligence models. The extra effort needed to classify the sky conditions and train more models is justified because using specialized models per sky class can yield better accuracy than a universal one for all classes.

4
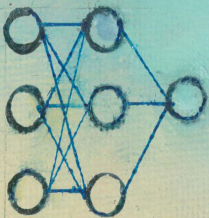
II

PV-HYDROGEN SYSTEMS: DESIGN & CONTROL

The second part of this work focuses on the coupling of PV systems with water electrolyzers for the production of green hydrogen. Part I discussed the variable nature of solar irradiance. In this respect, Chapter 5 centers the attention on whether water electrolyzers are suitable for operation with such fluctuating power and which configurations are available to realize PV-hydrogen systems. Chapter 6 moves up into the design phase of PV-electrolyzer systems with a sizing methodology of the PV plant powering an electrolyzer. It uses three indicators that serve as objective functions for an optimization problem solved with the Particle Swarm Optimization algorithm aiming at ensure a maximum transfer of energy from sunlight to hydrogen, or reducing the hydrogen cost. Finally, Chapter 7 proposes a control strategy that smooths the power of a PV system powering an electrolyzer. This strategy is based on active curtailment using forecasting and fuzzy logic. The control system was deployed in a hardware-in-the-loop emulator of the whole system, effectively putting together all the pieces presented in this dissertation.

Artwork of the opposite page by L. E. Lopez Castro

5

DYNAMICS OF WATER ELECTROLYZERS

.

The sun, with all those planets revolving around it...
can still ripen a bunch of grapes as if it had nothing else in the universe to do.

Galileo Galilei

Hydrogen production with electricity is now in the spotlight as the world moves towards 2050 with net-zero emissions. This gas is so important in this energy transition that the International Energy Agency (IEA) has included it in its Net Zero Emission roadmap as playing a critical role [16]. To mention a few figures, it is expected that by 2030 the world will see 15 million hydrogen cars, and by 2050 the shipping industry will depend on hydrogen as its dominant fuel [16].

Nowadays, most of the hydrogen in the world is produced by Steam Methane Reforming (SMR), which consists of processing natural gas or coal with water vapor at elevated temperatures and pressure over nickel-alumina catalysts. The result is hydrogen gas and CO [160]. This process is CO2 intensive (grey hydrogen). Thus, if this method is to be used, a great effort must be focused on reducing the carbon footprint of grey hydrogen by using carbon sequestration (blue hydrogen) [160].

A better alternative is water electrolysis. The process will be explained in detail in the following sections. If the electricity source for electrolysis comes from renewable energy, the produced hydrogen will have no associated CO2 emissions (green hydrogen). Currently, electrolysis accounts only for 2% of the hydrogen production in the world,

while most of it is a by-product of the chlor-alkali process [161]. Of all the processes primarily aiming at producing hydrogen, only 0.1% of all the hydrogen comes from water electrolysis as this technology still faces higher costs; further, the amount of electricity needed to turn from grey to green hydrogen is enormous, reaching the Terawatt-hour range [161] easily.

Many large-scale green hydrogen projects are being announced, such as a 150 million EUR investment project in Spain started in 2021 to power a 20 MW electrolyzer with solar energy. The produced hydrogen will be used as feedstock for ammonia production [162]. This highlights the importance of renewable hydrogen production in the near future. This is even enhanced by the fact that key oil-producing countries are also investing in hydrogen. A 5 billion USD project has been recently announced in Saudi Arabia, one of the leading oil producers in the world, to produce hydrogen entirely from renewable sources. It is expected that by 2030, the cost of hydrogen produced by this project will be lower than that of fossil-based production methods [163], which account for 830 million tons of CO2 emitted per year [161].

The International Energy Agency (IEA) has compiled a database with large-scale electrolysis projects [164]. Fig. 5.1a shows the worldwide distribution of operational and under construction projects that will produce hydrogen powered exclusively from renewable sources (i.e. they do not depend on the grid nor are supporting the grid to absorb an excess of renewable production). The main renewable sources to produce the electricity for hydrogen production is onshore wind and solar PV as seen in Fig. 5.1c.

These projects and roadmaps highlight the importance that hydrogen is experiencing during this energy transition. Successful integration of electrolyzers with the grid and highly variable renewable energy depends on the knowledge of the response of the electrolyzer plant to quick changes. This work provides extensive insight into the dynamic operation of low-temperature water electrolyzers, focusing on their integration with PV systems. Section 5.1 provides the general background on water electrolysis and low-temperature electrolyzer technologies. Section 5.2 presents the dynamics of water electrolyzers, diving into the fast electrical response and the slower changes caused by temperature and pressure. The integration with solar energy is discussed in Section 5.3. This section contains all issues related to a dynamic operation, including lifetime concerns, and the conclusion is given in Section 5.4.

We want to highlight that our work focuses on the production of hydrogen as raw material and not on hydrogen for grid balancing or micro-grid applications as it is beyond our research goal. Although we included a brief discussion of the costs, an in-depth discussion is also outside of the scope as this topic might even deserve a literature review on its own.

5.1. WATER ELECTROLYSIS

Water electrolysis is an electrochemical process in which *electricity* (electro-) is used to *split* (-lysis) water molecules into dissolved oxygen and hydrogen. Concretely, this electrochemical process involves reduction-oxidation (redox) chemical reactions. Electrons will be produced (*ox*idation) at one *anode* and consumed (*red*uction) at the *cathode*.

The reactions occurring at each electrode will depend on whether the electrolyte is acidic or alkaline. They are summarized in Table 5.1.
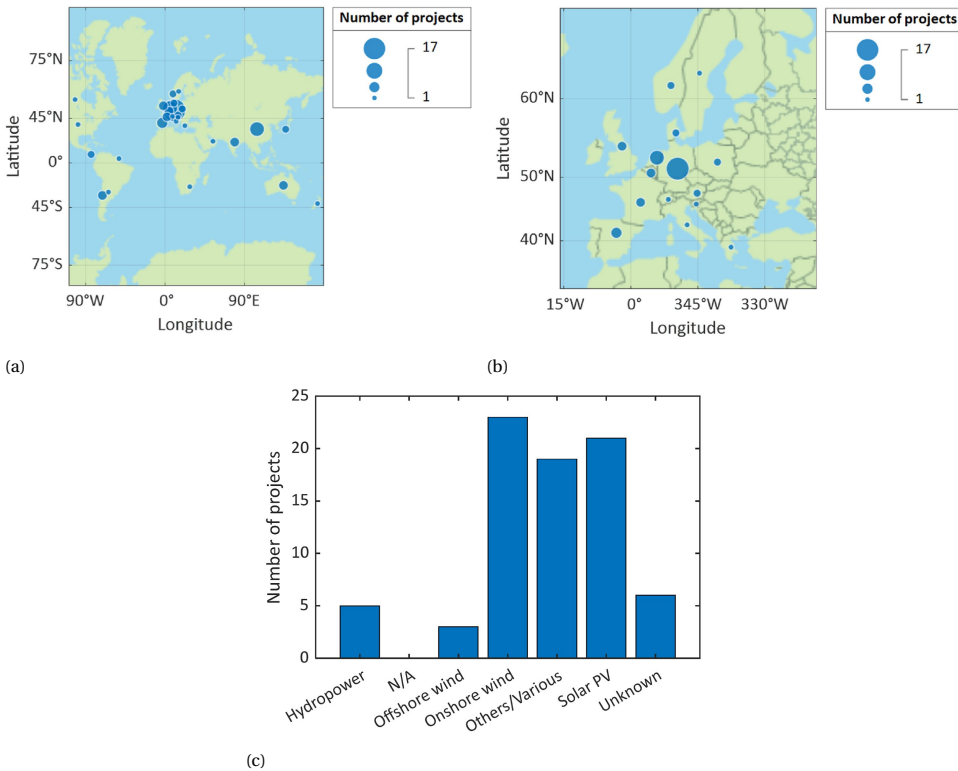
Figure 5.1: (a) Worldwide distribution of electrolysis projects for hydrogen production. All these projects are either operational or under construction and are powered from dedicated renewable sources. (b) Zoom over Europe. (c) Renewable sources that power the electrolysis projects. With data from Ref. [164].

Regardless of the electrolyte type, the overall reaction of water electrolysis can be written as

$$2H_2O(l) \rightarrow 2H_2(g) + O_2(g) \tag{5.1}$$

so for each two *moles* or molecules of water, the same amount of hydrogen and half this amount of oxygen is produced [166]. The addition "(g)" or "(l)" indicates that the products or reactants are in the gas or liquid phase, respectively.

Water electrolysis does not occur spontaneously for temperatures below 2250 °C [167]. It needs to be supplied with additional energy in the form of electricity and heat. The enthalpy of reaction is the change in enthalpy between reactants and products. When the products hydrogen and oxygen are produced in the gas-phase, this reads per mole of water ΔH in $[kJ/\text{mol}]$ [167]:

$$\Delta H = \Delta G + T\Delta S \tag{5.2}$$

The enthalpy of reaction ΔH is associated with the entropy change of the environment and $T\Delta S$ with that of the system, the reactants and products in this case. The

Alkaline	Cathode	$2H_2O(l) + 2e^- \rightarrow H_2(g) + 2OH^-$
	Anode	$4OH^- \rightarrow 2H_2O(l) + O_2(g) + 4e^-$
Acidic	Cathode	$2H^+ + 2e^- \rightarrow H_2(g)$
	Anode	$2H_2O(l) \rightarrow 4H^+ + O_2(g) + 4e^-$

Table 5.1: Reactions at electrodes depending on the electrolyte type. (With information from [165])

entropy of the reaction products, the gases oxygen and hydrogen, is higher than those of the liquid reactants, so $\Delta S > 0$.

The difference $-\Delta G$ is therefore associated with the overall entropy change. A spontaneous process is associated with an increase in entropy so that $\Delta G < 0$. Electrolysis is a non-spontaneous process, which requires work to be performed so that $\Delta G > 0$. The Gibbs free energy of reaction, ΔG, represents the maximum amount of work that can be performed by the energy released in the reaction in case $\Delta G < 0$ [167]. At standard conditions the change in Gibbs free energy is $\Delta G^0 = -237.2 \text{kJ/mol}$. This work may be supplied by applying a potential $E^0 = \Delta G^0/2F \approx 1.229\text{V}$, called the standard electrode potential which is temperature dependent, as seen in Equation 5.3 [168].

Thermodynamically, at least 1.229 V must be applied for reaction of Equation 5.1 to proceed [167].

With ΔG and ΔS both positive, the enthalpy of reaction is also positive, indicating an endothermic reaction. When additional heat surpassing $T\Delta S$ is supplied, cooling as avoided and the overall process becomes exothermic. Therefore, at potential equal to the thermoneutral voltage $E_{tn} = \Delta H/2F \approx 1.48$ V, there is no net heat production or consumption. Owing to energy losses due to resistance and irreversibility in the reaction, in practice usually a higher voltage is applied and the process will release heat [165], [166], [167]. These 'overpotentials' have different origins and are considered in more detail in Section 5.2.1.

$$E^0 = 1.5184 - 1.5421 \times 10^{-3} T + 9.523 \times 10^{-5} T \ln T + 9.85 \times 10^{-8} T^2 \qquad (5.3)$$

5.1.1. WATER ELECTROLYZER TECHNOLOGIES

Hydrogen can be produced at an industrial scale by applying the fundamentals of water electrolysis to large-scale electrolyzers. To do this, two technologies for low-temperature water electrolysis are commercially available and developed at industrial scales: alkaline and PEM. The AEM is the third low-temperature electrolysis technology and is still under development with only a few commercial products available.

ALKALINE ELECTROLYZER

Alkaline electrolyzers are the most mature electrolysis technology. The reactions are taking place in an alkaline electrolyte, so the equations of Table 5.1 (Alkaline row) are occurring.

The basic construction is shown in Figure 5.2a.

The electrodes, typically made of nickel or coated with Raney nickel as a catalyst at the cathode, are immersed in an *alkaline* solution (potassium or sodium hydroxide) with a typical concentration of 30 wt% and separated by a porous separator [167, 169]. A mesh
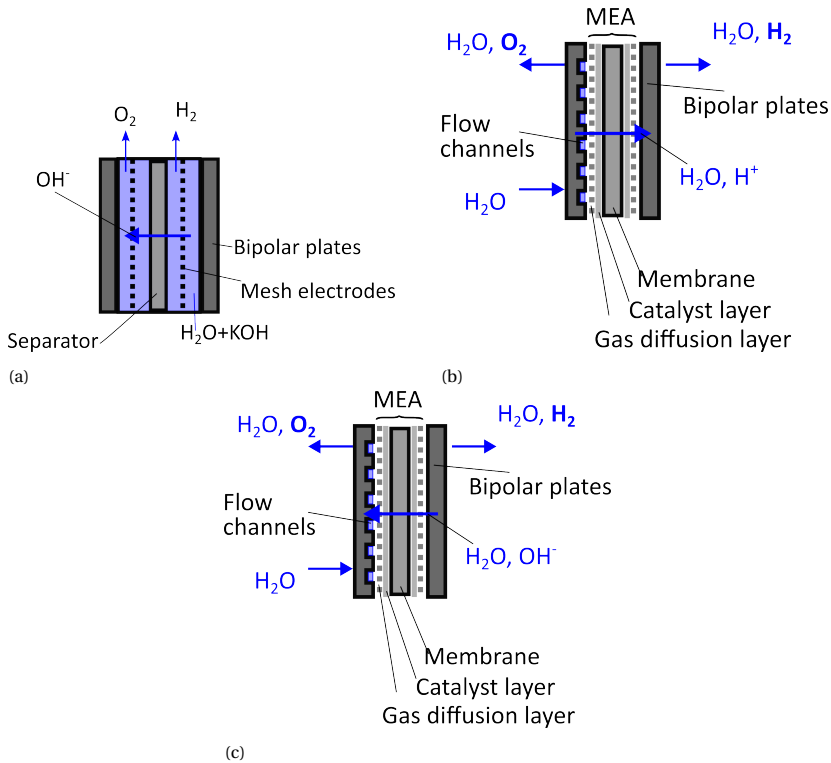
Figure 5.2: (a) Construction and operation of an alkaline water electrolyzer. The electrodes and separator are immersed in an alkaline solution. The separator prevents the recombination of hydrogen and oxygen, which could lead to an explosion. At the same time, it allows the transport of OH^- ions needed to complete the reaction. Traditionally, a small gap (a few millimeters) existed between the electrodes and the separator, now usually removed in the zero-gap configuration where the electrodes are placed touching the separator. Electricity is supplied using the bipolar plates. (b) Construction and operation of a PEM water electrolyzer. The water is fed through the flow channels, which also help remove oxygen. Hydrogen H^+ ions and water molecules are transported through the Membrane-Electrode Assembly. This single-unit component consists of the porous electrodes, a catalyst layer, and the membrane. The electricity is supplied through the bipolar plates. (c) Construction and operation of an AEM water electrolyzer. Note that the construction is the same as the PEM electrolyzer. The main difference lays in the membrane. While PEM allows the movement of hydrogen H^+ ions, AEM allows the movement of hydroxyl ions, in the same way as the alkaline technology.

construction of the electrodes facilitates the removal of bubbles. The separator, which in the past was made of toxic asbestos but now is replaced by other materials such as a mixture of zirconium dioxide and polysulfone under the commercial name of Zirfon™, helps to keep the hydrogen and oxygen gases apart, preventing the formation of a dangerous combination of them [167]. This separator, however, must allow the transport of OH^- ions for the reaction to take place [167, 169]. Adding this separator increases the cell's ionic resistance and facilitates the attachment of bubbles to it, leading to an increased electrical resistance caused by them [170]. If a gap exists between the electrodes and the separator, in this space bubbles will accumulate. The gap will influence how

bubbles are aggregated, creating void spaces where no reaction occurs, thus, affecting the ohmic losses [170–173].

The freely moving bubbles impact the conductivity of the electrolyte by forcing the ions to take longer paths to reach the electrodes [173]. To overcome this problem, the electrodes can also be placed in the zero-gap configuration. Here, the electrodes are placed in direct contact with the separator. Although this helps to reduce the resistance caused by bubbles, it introduces other challenges for the separator, which needs to be well engineered to avoid gas crossover [167, 174].

The alkaline technology consumes between 47 kWh and 66 kWh of electricity to produce 1 kg of hydrogen. In terms of percentage, this is equivalent to 50-68% (with respect to the lower, heating value of hydrogen, LHV=33.33 kWh/kg) [175].

PROTON EXCHANGE MEMBRANE (PEM) ELECTROLYZER

An improvement to the alkaline technology was made in the era of the Gemini space program when a solid membrane replaced the liquid electrolyte of the fuel cells [176]. This new technology consists of a solid electrolyte that facilitates the use of the zero-gap configuration. The solid electrolyte is a thin polymer membrane that allows the conduction of ions [167, 177]. Hence the name Polymer Electrolyte Membrane (PEM). Other names for this technology are Proton Exchange Membrane or Solid Polymer Electrolyte [177]. The material Nafion™, developed by DuPont, is one of the most well-known materials for the membrane [167, 178]. The presence of H^+ ions in the membrane causes it to be a very acidic medium that can corrode the elements in contact with it, namely, electrodes and catalyst layers [167]. The solution to prevent corrosion is using robust but often scarce materials in the electrodes and catalysts such as platinum and ruthenium, which result in elevated costs [167]. The reactions taking place in a PEM electrolyzer are described in Table 5.1 (Acidic row).

Another property of the membrane is its thickness. With 50 to 300 μm thickness, some design choices must be made. On the one hand, the membrane's thickness is related to this component's resistance. The thinner the membrane is, the lower the resistance. On the other hand, if a high-pressure operation is desired, the membrane must be thicker to prevent gas crossover and improve safety and Faraday efficiency [179]. An intermediate (catalyst) layer is introduced to facilitate the reaction. A gas diffusion layer is the last layer of this stack, which is pressed together to form a single unit called Membrane-Electrode Assembly or MEA [167] (see Figure 5.2b). The gas diffusion layer not only allows water into the cathode and facilitates the extraction of gases but also provides strength, allows compression, transports heat, and protects the catalysts from fluid flows.

In contact with the MEA are the bipolar plates where current is applied. They also contain flow channels to feed the water and facilitate the extraction of gases [167] (see Figure 5.2b). The bipolar plates also allow the connection of cells in series, forming a bipolar configuration. One plate receives the two terminals (hence the name), the positive of one cell and the negative of the next.

For industrial size units (around 1 MW), this technology and the alkaline have similar efficiencies (50-68% with respect to the LHV) [175]. The advantage of the PEM technology lays in a broader operating spectrum. While the minimum operating limit for the

alkaline technology is set at 20% of its nominal capacity, PEM can go as low as 5%. On the other extreme, PEM, can operate beyond the nominal capacity, which is not possible for alkaline electrolyzers [175]. Another advantage of PEM is the ability to operate at higher current densities up to 2 A/m^2 (alkaline technology operates at a maximum of 0.8 A/m^2) [175]. This is translated in improved hydrogen production.

Anion Exchange Membrane (AEM) Electrolyzer

Anion-Exchange Membrane (AEM) electrolysis is an emerging technology that exploits the advantages of PEM electrolysis but operates in alkaline conditions. Hence, the reactions driving the process are also the alkaline row of Table 5.1.

Because of the alkaline environment, AEM does not need scarce materials such as iridium or platinum [174]. The AEM electrolyzer construction is similar to the PEM: a membrane sandwiched between two electrodes (see Figure 5.2c). The membrane allows the transport of hydroxyl-ions (OH$^-$) while keeping the product gases (hydrogen and oxygen) separated [180]. The difference with the alkaline technology is the separator. In the AEL, this is a porous material, while in AEM, the membrane is not. The membrane allows only the conduction of the OH$^-$ ions and in the porous separator, these travel through the pores of the material [174]. The AEM electrolyzer can be fed pure, demineralized water as with PEM. However, the system's performance is poor due to the low availability of hydroxyl ions in the membrane [180], and it can lead to electrode degradation if fed exclusively to the anode [180, 181]. A solution is to add an electrolyte, such as KOH, as done in AEL. The concentration of the electrolyte (typically 30% wt in AEL) can be reduced to 3 to 10% wt [181].

AEM is still a developing technology with chemical, mechanical and thermal stability challenges that ultimately lead to durability problems [174]. Research is also being conducted on membrane design, membrane-electrode assembly (MEA) construction, and electrocatalysts materials [174, 181].

Despite still being in the developing phase, there are already commercial products based on AEM, such as the electrolyzers produced by HydroLite [182] or Enapter [183].

AEM still has lower efficiency than that of alkaline or PEM (67%, based on LHV for a unit size of a few kW) and combines characteristics of both. It can operate with the same maximum current density as a PEM (2 A/m^2) but cannot exceed the nominal capacity (same as alkaline technology) [175].

5.2. Dynamics of water electrolysis

The dynamic behavior impacts the development of control strategies for gas production. The stack's response depends on several factors, including water intake, temperature, and bubbles. Further, as these parameters are time-changing, the modeling can become very complex, making it unsuitable for control applications or very simplistic ignoring the time-varying parameters [184].

5.2.1. The voltage-current (I-V) characteristic

The starting point for understanding the operation of an electrolyzer is to recognize its polarization characteristics (I–V curve). In other words, how the voltage of the electrolyzer changes with the applied current under steady-state conditions. The voltage

of an electrolysis cell (E_{cell}) is the sum of the reversible voltage and so-called overpotentials:

$$E_{\text{cell}} = E_{\text{rev}} + \eta_{\text{act,an}} + |\eta_{\text{act,cat}}| + \eta_{\text{ohm}} \tag{5.4}$$

The reversible potential, $E_{\text{rev}} = 1.23$ V at standard conditions, depends on pressure, temperature, and local reactant and product concentrations through the Nernst equation [166].

The extra voltage (overpotential) imposed by η_{act} and η_{ohm} constitute losses and depend on the applied current. The activation overpotentials (η_{act}) on the cathode (cat) and anode (an) appear as a result of additional potential needed to overcome the barrier imposed by a peak of potential energy before the reactants can be transformed into products at the desired rate [177, 185]. Both electrodes have different activation barriers and a logarithmic dependence on the applied current density j [177]. The equation describing the overpotential as a function of the applied current is the concentration-dependent Butler-Volmer equation which is fundamental in electrochemistry [185, 186].

$$j = j_0 \left(\frac{c_{\text{red}}}{c_{\text{red,0}}} \exp\left(\frac{\alpha F}{RT} \eta_{\text{act}} \right) - \frac{c_{\text{ox}}}{c_{\text{ox,0}}} \exp\left(\frac{-(1-\alpha)F}{RT} \eta_{\text{act}} \right) \right) \tag{5.5}$$

The term j_0 is the exchange current density and is the magnitude of the equal anodic and cathodic currents at an electrode when there is no net current. Even in this situation, reduction and oxidation reactions occur, and the exchange current density gives their current density [177, 185]. The local concentrations c_{red} and c_{ox} of reductant and oxidant at the electrode surface can often be assumed to be equal to their equilibrium or bulk concentrations and , respectively. For example, for the cathodic hydrogen evolution reaction (HER), the oxidant water and reductant hydroxide both appear in such large quantities that their variation can be neglected. Note that at the cathode the current density and activation overpotential $\eta_{\text{act,cat}}$ are taken to be negative,the absolute value is taken in Equation 5.4.

The coefficient α (charge transfer coefficient, or symmetry factor) is related to the shape of the activation energy barrier. For a single electron-transfer step it has a value between 0 and 1, although practical effective values may exceed unity [187].

At the anode, Equation 5.5 can be simplified into Equation 5.6 (when $\alpha = 0.5$ and $\frac{c_{\text{red}}}{c_{\text{red,0}}} = \frac{c_{\text{ox}}}{c_{\text{ox,0}}} = 1$ [188, 189].

$$\eta_{\text{act}} = b \, \text{asinh}\left(\frac{j}{2j_0} \right) \tag{5.6}$$

Where the Tafel slope is defined as $b = \frac{RT}{\alpha F}$. Or into the Tafel equation 5.7 if the applied current density is large [166].

$$\eta_{\text{act}} = b \ln\left(\frac{j}{j_0} \right) + b \ln\left(\frac{c_{\text{red,0}}}{c_{\text{red}}} \right) \tag{5.7}$$

The second term here is the concentration-overpotential due to a reduced concentration of reductants. At the anode, depending on the rate-determining step in the reaction, and in agreement with the reactions in 5.1, the reductant concentration c_{red} can be
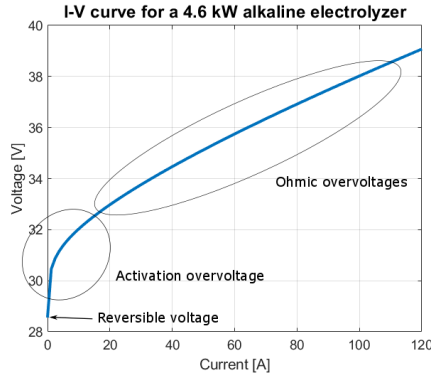
Figure 5.3: Example of an I–V curve of a 4.6 kW alkaline electrolyzer. The effects of the overpotentials are shown. I–V curve obtained with data from Ref. [194].

that of hydroxide ions. Usually, the mass transfer is sufficiently fast so this concentration deviates little from the bulk concentration $c_{red,0}$. At relatively low electrolyte concentrations well below 1 M [190] or in the absence of mixing of anolyte and catholyte [190–192] can this reactant depletion be observed.

Besides the activation overpotential, when current flows through the cell, it will also encounter resistive effects that increase the cell's voltage; thus, an ohmic overpotential (η_{ohm}) will appear. For a layer of electrolyte of thickness l with effective conductivity κ_{eff} Ohm's law and Pouillet's law combine to give $\eta_{ohm} = jl/\kappa_{eff}$. An alkaline water electrolyzer diaphragm can be characterized by a porosity ϵ, denoting the volume fraction of electrolyte, and tortuosity τ, denoting the average ionic path length over the shortest path length. The conductivity of the electrolyte, which strongly increases with increasing temperature, is decreased because of these effects to give $\kappa_{eff} = \kappa_0 \epsilon/\tau$. For the popular Zirfon-Perl diaphragm $\epsilon \approx 0.5$ and $\tau \approx 1.5 - 3$, or even higher if you take into account the additional path-length introduced by zero-gap electrodes and the presence of bubbles [190]. For a PEM electrolyzer, the resistivity of the membrane depends strongly on its water content and temperature [193].

The typical current-voltage (I–V) curve or static characteristic of the electrolyzer is shown in Fig. 5.3.

The I–V curve can also be reproduced by an empirical model relating the current density (defined as the current, I per unit area, A), of which the model proposed by Ulleberg [195] for an alkaline electrolyzer (Equation 5.8) is one of the most widely used because it allows an easy fit to any technology (with the parameters r_x, t_x and s) and include the effect of temperature (T) on the I–V curve.

$$E_{cell} = E_{rev} + \frac{r_1 + r_2 T}{A} I + s \log\left(\frac{t_1 + \frac{t_2}{T} + \frac{t_3}{T^2}}{A} I + 1 \right)$$ (5.8)

The thermal model is based on a lumped thermal capacitance C_t as seen in Equations 5.9, 5.10, 5.11 [195] with N_c the number of cells of the electrolyzer and R_t the thermal resistance of the cell [195].
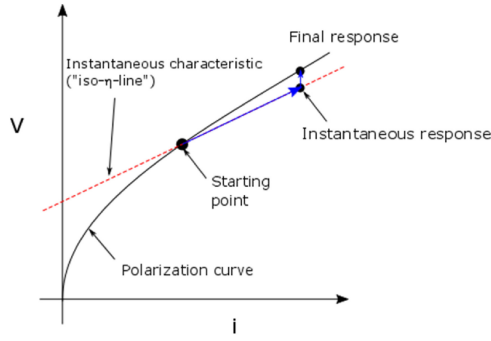
Figure 5.4: The path on the I–V plane after a step response. The instantaneous characteristic marks all the possible points where the immediate response can occur from the current starting point. Adapted from Ref. [197].

$$C_t \frac{dT}{dt} = \dot{Q}_{\text{gen}} - \dot{Q}_{\text{loss}} \tag{5.9}$$

$$\dot{Q}_{\text{gen}} = N_c (E_{\text{cell}} - E_{\text{tn}}) I \tag{5.10}$$

$$\dot{Q}_{\text{loss}} = \frac{1}{R_t} (T - T_{\text{amb}}) \tag{5.11}$$

5.2.2. Electrical dynamic response

The voltage evolution occurs in two phases when a current step is applied to a PEM cell. First, an immediate response will set the response along the instantaneous characteristic curve (called "iso-η-line") [196], which is different from the I–V polarization curve. This first response will often lie outside the polarization curve. After this initial response, a dynamic response will move this initial point towards the I–V curve [196, 197]. The full path is illustrated in Fig. 5.4.

The dynamic response is highly non-linear [197, 198]. In fact, it can take an 8th order transfer function to accurately reproduce the actual voltage response of a device [198]. With a simplification, three time-constants can be identified. Two of which are extremely fast and resolve in approximately 13 ms and one main time-constant of approximately 1 s [197, 198].

The dynamic phase will also depend on [197].

- The direction of the step

- They type of step (voltage, current, or power)

- The magnitude of the step

The initial response of a large downward voltage step can be a negative current. During this negative overshoot, the current is reversed, and its magnitude depends on the
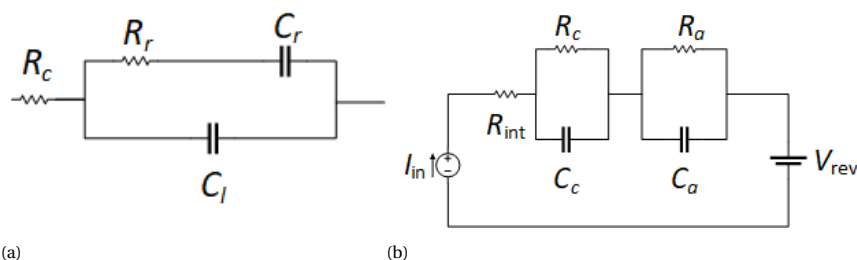
Figure 5.5: (a) Randles circuit. Rc represents the resistance of the electrolyte. The electrical double layer is represented by C_l, while R_r and C_r form an equivalent impedance modeling the speed of the reaction. Adapted from Ref. [200]. (b) Equivalent circuit with two RC networks, one for each electrode. R_{int} represents the ohmic losses and V_{rev} the reversible voltage. Adapted from Ref. [202]. These circuits can be applied to PEM, AEM or AEL.

ohmic losses. The lower the losses, typically associated with thinner membranes, the higher the current reversal [197]. Similar behavior occurs in AEM cells, but the current reversal and overshoot can reach a considerable magnitude (almost $2\,A/cm^2$ in both directions) with high voltage steps (2.1 V–0 V) [199].

The electrolyzer dynamics can be represented using an equivalent circuit model that characterizes the behavior of fast-occurring reactions at an electrode. It models the electrical double layer as a capacitor. In parallel, a resistance in series with a second capacitor characterizes the speed of the reaction. The parallel branch is connected in series with a resistor simulating the resistance of the electrolyte. This circuit, called *Randles equivalent circuit* [200], is illustrated in Fig. 5.5a. A modified version of the Randles circuit, which is often found in literature, is shown in Fig. 5.5b. Each of the two R–C branches represent one electrode [194, 201, 202].

The capacitors can be replaced with non-ideal capacitors modeled as Warburg impedances [203, 204], to model the losses caused by reactants consumed or products not being quickly removed, or Constant Phase Elements to model the uneven distribution of current in the electrodes [201, 203]. The circuit can also be simplified by ignoring the capacitors and introducing controlled voltage sources [194, 205–207] or diodes [208–210] to approximate the response of the I–V curve.

The electrical response of an electrolyzer can be explained using Fig. 5.4, Fig. 5.5. Suppose that the electrolyzer is operating at the point marked as "starting point" in Fig. 5.4 at steady state, so there is no current flowing through the capacitors of Fig. 5.5b. Upon applying a current step, the current will flow immediately through the resistors of Fig. 5.5b causing an instantaneous increase in the electrolyzer's voltage leading to the point marked as "instantaneous response" of Fig. 5.4. The capacitors will begin charging causing the drift of the operating point towards the point marked as "Final response" in Fig. 5.4 [196].

As the initial response of the cell is exceptionally rapid, its voltage response can be approximated as a first-order system [190, 205]. The voltage response of a 12.25 cm2 PEM cell (H-TEC Energy Systems) to a current step followed the exponential approximation typical of first-order systems [205]. The steady-state was reached in approximately

4 s. For an alkaline cell, the behavior exhibits a similar trend. The voltage response $E(t)$ of an electrolyzer cell is an exponential function of the form 5.12 [202]:

$$E(t) = (E_0 - E_\infty) \exp\left(-\frac{t}{\tau}\right) + E_\infty \tag{5.12}$$

The terms E_0 and E_∞ represent the starting and steady-state voltage, respectively.

For alkaline cells, the first-order behavior can be attributed to bubbles. While describing the effect of bubbles under a zero-gap configuration, Haverkort and Rajaei [190] found a response time of approximately $\tau \approx 10$ s, whose behavior is also characterized by an exponential (Equation 5.12. This is associated with the build-up of an additional resistance tentatively attributed to the formation of bubbles. After introducing a small gap between the electrode and the separator, the additional resistance and associated voltage appearing over the mentioned response time, disappeared.

Faster dynamics remains, related to the capacitance of electric double layer (EDL). The supporting information of [190] shows for a single small alkaline cell an associated time-scale of around 1 min at a very low current density of 1 mA/cm^2; decreasing to a fraction of a second for higher current densities [191].

A longer time scale can be associated with diffusion processes. In a porous diaphragm, without any flow through it, half of the current can be transported by diffusion in steady-state. But for steady-state concentration profiles to develop it takes a time of the order of $l^2/4D_a$, with l the diaphragm thickness and D_a the effective medium ambipolar salt diffusion coefficient [191].

Even longer time-scales are associated with changes in the electrolyte concentration. Operation at a significant fraction of the limiting current density gives rise to concentration differences between anolyte and catholyte. When these are not re-combined effectively, depletion of hydroxide at the anode may over time cause an increase in concentration and ohmic overpotential [190–192]. In the absence of flows, the time-scale associated with this is $lV/4AD_a$, with V the combined anolyte and catholyte volume and A the electrode area. For the small single cell studied in Ref. [191] this time-scale was of the order of an hour, but it can be substantially more, including the volume of the piping, manifolds and gas-liquid separators. On a time frame ranging from hours to months, the voltage of an electrolysis cell starts to rise considerably. This voltage rise begins approximately 30 min after the start-up and might continue for months. The cause is attributed to the hydrogen absorption in the electrodes and their oxidation [211].

Moving to a larger scale, the dynamic response of 40 kW PEM and alkaline electrolyzers was studied experimentally in Ref. [212] by applying power steps from 25% to 50%, 75% and 100% (ramp-up) and from 100% to 75%, 50% and 25% (ramp-down) and measuring the electrolyzer's current. The objective was to determine the suitability of both technologies to operate under these conditions. Part of the experiment consisted of quantifying the initial response time when the electrolyzer needs to start responding and reach 1% of the maximum current after a change in the set-point. For the measured electrolyzers, it was determined to be 13 ms and 19 ms for PEMEL (Proton OnSite, 40 kW, three stacks) and AEL (Teledyne Technologies, 40 kW, 75 cells, one stack), respectively. This value is influenced by other components such as power electronics of the power supply that also need time to react [212]. Both electrolyzers required less than 0.2 s to

reach more than 90% of the final current value (*settling time*). The settling time is influenced by the step size and the direction of the ramp. A more significant step will result in a slower response [212]. The authors report that the measurements were taken only for 0.2 s due to equipment limitations.

The ramp rate was also calculated as the ratio of the percentage of the maximum current per second. PEMEL have slightly higher ramp rates than alkaline electrolyzers, meaning that they can reach the maximum current in less time [212].

5.2.3. INFLUENCE OF TEMPERATURE AND PRESSURE

Temperature has an impact on the electrolyzer's voltage. As temperature increases, the activation overvoltages tend to be higher as the Tafel slope is also higher (see Equation 5.7). However, for low overvoltages, temperature also causes a rise in the exchange current density j_0 which, in turn, reduces the activation losses [185]. Higher temperature also results in lower resistive losses [179, 213, 214] as well as lower reversible voltage [168] (see Sections 5.1 and 5.2.1). The benefits of lower ohmic losses overcome the negative influence of temperature [185]. For this reason, temperature is considered to impact the electrolyzer's voltage positively [179]. This influence on the electrolyzer's voltage affects the electrolyzer's efficiency. At lower temperatures, the demanded power to produce hydrogen is higher [215] (lower efficiency).

Temperature also influences the operating voltage and the gas purity (HTO, Hydrogen -To-Oxygen) [213] as the diffusivity and solubility of the produced gases depend on temperature. Sanchez, et al. [213] found that the HTO content increased around 4% with only a 5% temperature increment.

On the other hand, pressure has a minor effect on the polarization curve of alkaline electrolyzers than that of temperature. Even a deviation of 10% from the pressure reference results in a negligible effect on the voltage [213]. This is not the case for the gas cross-over. A pressure difference between the cathode and the anode further enhances the convective transport of gas through the separator. Since the permeability of Zirfon™ (commonly used for separators in alkaline electrolyzers) is higher than Nafion™ (the most used membrane material for PEM), AELs are more susceptible to pressure gradients between cathode and anode. Even when operating at equal pressures in AELs, the control valves can create a slight pressure gradient contributing to gas cross-over [216]. In fact, the HTO can rise by 2% with a pressure increment of 10% [213].

The performance of AEM with pressure is worse than PEM but better than AEL [59]. It lowers the Faraday efficiency and has a minor effect on the ion conductivity of the membrane. This causes a slight increase in its resistance, with a consequent increase in the cell's voltage which is limited to 11 mV when the applied current is 1 A/cm^2 [217]. The pressurized operation, like PEM and AEL, impacts the gas crossover. The hydrogen permeation flux from cathode to anode increases linearly with pressure, and the HTO reached dangerous levels at low currents (0.1 A/cm^2) and high pressure (8.5 bar) [217].

Temperature and pressure influence the operating conditions of electrolyzers. According to Ogumerem and Pistikopoulos [218], the dynamic behavior of the electrolyzer is dominated by the temperature. While developing a control strategy for a simulated PEMEL, the voltage immediately follows the step after a current change but then decays slowly as the temperature increases. Colbertado, et al. [219] reached a similar conclusion

for a 12-cell, 160 cm^2, simulated PEMEL, although their observations did not include the voltage evolution in time, only the temperature. In terms of power consumption, stepping down from a higher power and temperature setting to a lower power is more beneficial than the opposite [215]. This does not mean that the electrolyzer cannot shift to the new power point, but the efficiency (which is temperature dependent and higher at higher temperatures) will be reduced as the temperature rises to the new set point [215].

Pressurized operation improves the ramp rate of alkaline electrolyzers. The ramp rate is limited to keep the gas volume inside the cells always within controllable limits by ensuring that the gases are adequately vented. High pressure facilitates the expulsion of gases leading to higher ramp rates than atmospheric-pressure operation [220]. However, this benefit can only be achieved once the pressure set-point has been reached. During a cold-start, the leading cause of delay is pressure build-up. Additionally, if the electrolyzer goes into standby mode, the pressure needs to be maintained [220].

The gas cross-over increment with temperature and pressure can have severe consequences as the lower explosive limits (3.8% mol H$_2$ at 80 °C and 1 atm for a 15 kW alkaline electrolyzer) can be exceeded [213].

5.3. OPERATING UNDER VARYING CONDITIONS

There are two ways of starting the operation of an electrolyzer. Suppose the electrolyzer is off, cold, and depressurized (for example, at the beginning of a day or after a long period when it is not being used). In that case, the system needs to be warmed up before it can start producing hydrogen. This is called a cold-start. Another situation is a short interruption where pressure and temperature and pressure can be maintained, and the production can continue without delays. This is a warm-start [212].

The steps that are needed during the cold-start are illustrated in Table 5.2:

Step	Process	PEM [221]	Alkaline [220]	AEM [222]
1	Booting the control unit	0.5 min	N/D	N/D
2	Purging pipes	2-10 min	25 min	N/D
3	Ramping up to full power	3 min	10 min	25 min

Table 5.2: Cold-start sequence. The times for the PEM electrolyzer are based on a Proton OnSite C10, 60 kW nominal power [221]. The alkaline electrolyzer times are reported for a 24 kW pressurized (12 bar) unit [220]. Step 2, involves removing the air in the piping system [221] or, in the case of the alkaline unit, injecting nitrogen to remove residual hydrogen in them [220]. The AEL electrolyzer data is published by ENAPTER [222]. The ramping up time for all technologies includes the necessary time to build up the hydrogen pressure.

The first consequence of variable power is that this process is interrupted if the system cannot reach the minimum operating pressure within a specific time range after start-up. This is illustrated with a Proton OnSite HOGEN RE40, PEM electrolyzer. This unit will interrupt the process if the operating pressure of 14 bar is not reached within 30 s [223]. In order to prevent this, a minimum operating load is set (34% of nominal power for the previous example [223]. This minimum load is well above the minimum load required when operating under normal conditions (7.6% of nominal power for PEM [223], 18% for alkaline [220], and up to 60% for AEM technology [222]. As a result, due to the minimum load requirement along with the relatively long time that is needed for a

cold-start, the maximum number of times the system can be stopped and restarted in a day is limited [220, 222].

The ramping rate indicates how fast can the electrolyzer react upon a change in power. The PEM technology has power ramps in the range of 10%/s [224] (change in power of 10% of the current operating set point) to +50%/s and -40%/s [221, 225]. Alkaline technology has ramp rates of 0.3%/s [226], 2.5 kW/s or 308 kW/s [220]. For AEM the ramping up rate is +0.47%/s (ramping up) and a faster ramping down rate up to -10%/s [222]. In general, electrolyzers can react faster to down-ramps than up-ramps. Based on the discussion of Section 5.2.3, and the observations of [220], the slowest variables (pressure, gas venting, temperature) along with the control system impose the limits on the ramp rate, rather than the electrical capability of the stack to manage the power changes. Limiting the ramping of the electrolyzer has little effect on the levelized energy cost, as long as these are constrained to a minimum of 15% of the rated power. If the ramps are restricted to shallower levels, the impact on the cost becomes significant [227].

For a PV system, the ramping rate is between +0.098%/s and -0.078%/s [226] which is slower than the rate at which electrolyzers can respond. Note that the ramping values were originally reported per minute and converted to per second for consistency. However, measured ramps in the per second scale can reach considerable higher values, which are not reflected in a per minute analysis. In this respect, PEM has proven to be able also extreme ramping events managing to respond upon +80% and -100% change in power within 1 second [221]. The fast reaction times of large-scale electrolyzers make them very attractive for grid frequency support and can play a role in future energy systems, marked by the absence of rotational inertia [225, 228]. In fact, the two main low-temperature technologies, AEL and PEM have received approval for their use as ultra-fast ancilliary services [175].

5.3.1. COUPLING WITH SOLAR ENERGY

PV energy is becoming an attractive option for powering electrolyzers. This can be seen in Figure 5.6a. While at first, onshore wind was the preferred technology, in the last years PV is becoming the preferred technology. It does not need to substitute wind power, but can also coexist (Figure 6(a), group "Others/Various"). Figure 5.6b shows the efficiency of solar modules used in literature during the past 10 years, as well as the record efficiency for modules with different cell technology [229].

To evaluate a solar-powered hydrogen project, the Solar-To-Hydrogen efficiency is introduced. It is defined as the ratio of the generated hydrogen to the needed irradiance to produce such amount (Equation 5.13) [248].

$$STH = \frac{\dot{h}_2 \times \Delta G}{S \times A} \tag{5.13}$$

The numerator term converts the flow of hydrogen ($\dot{h}_2$ in mol/s) into energy. The denominator indicates the amount of irradiance (S, in W/m^2) that the module area (A, in m^2) receives. The STH is a non-dimensional number relating hydrogen energy and solar energy.

Fig. 5.7 shows the evolution of the STH reported in the reviewed literature over the last ten years.

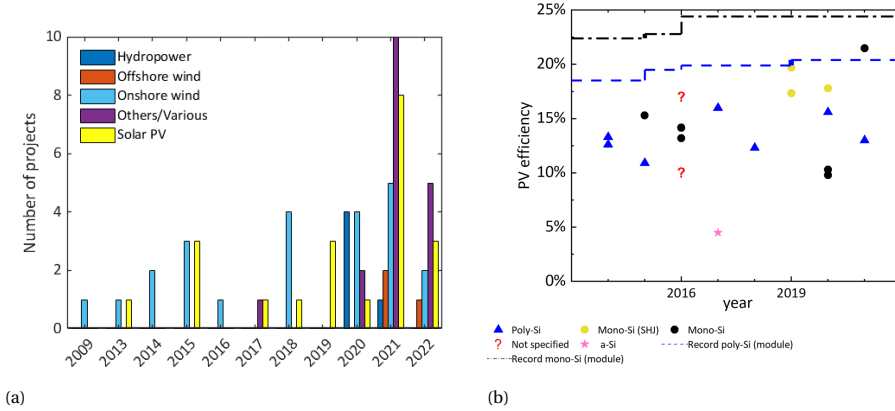(a)   (b)

Figure 5.6: Renewable technologies used to drive large-scale electrolysis projects for hydrogen production worldwide. With data from Ref. [164]. (b) Efficiency of the PV module reported in literature classified per technology [[223, 230–247]. The dashed and dash-dot lines indicates the record efficiency for a poly-si and mono-si module, respectively [229].

The coupling factor (or coupling efficiency) defines the ratio of the PV module used relating the operating power ($P_{pv} = I_{pv} \times V_{pv}$) against the maximum power (P_{mpp}) of the module at a particular instant (Equation 5.14) [257].

$$\text{CF} = \frac{I_{\text{PV}} \times V_{\text{PV}}}{P_{\text{mpp}}} \tag{5.14}$$

The coupling factor is also an non-dimensional number with values ranging between zero (no coupling) to one (operating power is at the maximum power point of the module) [257].

DIRECT-COUPLING SYSTEMS

The simplest way to integrate a PV system with an electrolyzer is to connect the PV array directly to the electrolyzer. This is possible as both devices work with direct current. Fig. 5.8a shows a schematic of this configuration. In the directly coupled systems, the operating point is right at the intersection of the I–V curves of the PV array and the electrolyzer, as seen in Fig. 5.8b. In practice, the system operates away from the MPP of the PV because the polarization curve of the two devices is not well matched. These systems need to be optimized in such a way that the I–V curves of both components are close to the MPP of the PV module. This optimization can be based on setting the MPP of the PV close to the region of operation of the electrolyzer with higher probability of occurrence [258]. Then, the number of series-connected electrolyzer cells, as well as the configuration series-parallel of the solar cells, both curves can get closer to the MPP [252, 258].

Direct-coupling systems have minimum control capabilities, limited to a simple ON-OFF control in case of the electrolyzer operating below the safety threshold or exceeding its nominal capacity [232, 259]. However, the directly coupled system can be optimized by dynamically changing the connection of the electrolyzer cells. Using an external contactor or switch, the number of electrolyzer cells can be incremented or reduced. This
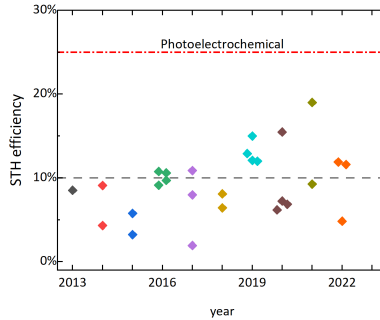
Figure 5.7: Solar-To-Hydrogen efficiency per year as reported in literature [223, 230–238, 240–247, 249–254]. The dashed line marks the limit above which the STH becomes economically feasible [255]. The dashed-dot line with the legend "Photoelectrochemical" indicates the target of the Department of Energy of the USA for a photoelectrochemical devices [256]. Although it is a different technology than the one addressed in this work, it provides a point of comparison as there is no specific target for the STH of a PV-hydrogen system.
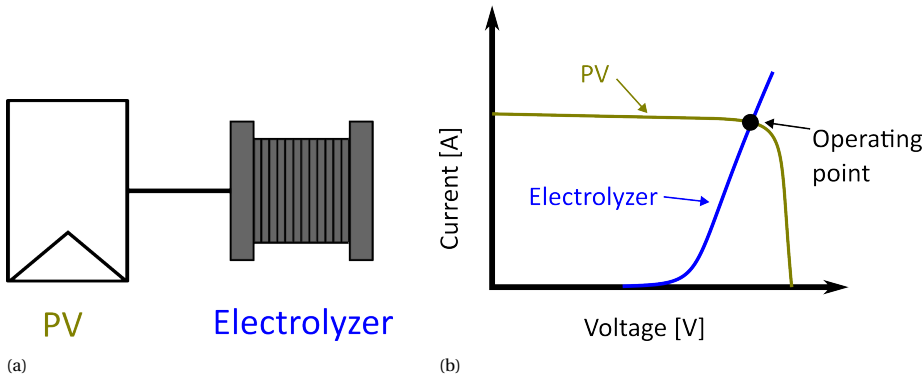
Figure 5.8: Direct coupling of PV and electrolyzer (a). The operating point is the intersection of the I–V curves of the two components (b).

adds another level of control, facilitating the matching of the electrolyzer to the MPP of the PV module. This operating strategy is essentially a "discrete MPPT" which increases the coupling factor 5.14 [234, 260].

In general, directly-coupled systems have lower efficiency that their DC-DC-coupled counterparts [232, 260, 261]. The directly-coupled system can boost its coupling efficiency up to 99% if the discrete MPPT strategy described above is used [260].

COUPLING WITH ELECTRONIC CONVERTER

The PV and electrolyzer can be decoupled so each component operates at different regions of their I–V curve. In this way, the PV modules can operate at maximum power point with the consequence that the electrolyzer will also operate at this maximum power, limited only by the efficiency of the converter [251]. Note that the efficiency of the converter is different from the coupling efficiency. In these systems, the coupling effi-
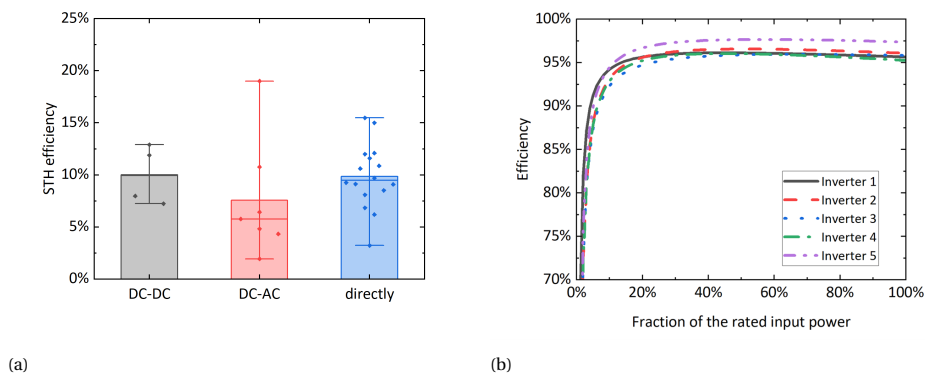
Figure 5.9: (a) Comparison of the STH obtained with different coupling types as reported in literature [223, 230–238, 240–247, 249–254]. Note that battery-assisted systems always use an electronic converter. (b) Five random examples taken from the library of the System Advisor Model [262] showing the efficiency at different operating loads of commercially available inverters for PV applications.
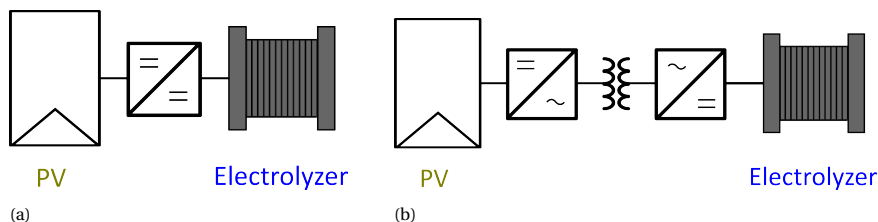
Figure 5.10: Coupling PV with electrolyzer using power converters. (a) Coupling using DC-DC conversion. Depending on the system, more than one DC-DC converted might be present [260], and (b), coupling using DC-AC-DC conversion. This configuration needs a transformer to accommodate for different voltage levels [259, 260].

ciency is virtually 100% as the converters implement a maximum power point tracker that forces the PV to deliver the maximum power. The electronic converter also has an efficiency of its own (Fig. 5.9b), and it degrades considerably if operated at a lower load than its nominal rating [232]. This efficiency affects the Solar-To-Hydrogen efficiency [261] which can be seen in Fig. 5.9a.

Direct coupling systems are best suited in systems where the PV and the electrolysis systems share the same physical location. Indirect coupling (using an electronic converter) allows to cover both scenarios: same physical location or the case where there's a considerable distance between both systems.

In the latter, To transport the electricity from PV to the electrolyzer, either a high-voltage DC transmission system (with the consequence that a series of DC-DC converters are needed (Fig. 5.10a)) or a traditional AC system (with the need of at least one DC-AC conversion stage, a transformer and finally an AC-DC rectifying stage at the electrolyzer side (Fig. 5.10b)) [260].

When DC/DC is used, many converter topologies can be used, which are extensively

reviewed in the work of Guilbert, et al. [263]. In particular, because the voltage of the electrolyzer is smaller than the PV, the traditional buck converter (step-down) converter is an attractive option. Although it suffers from limited conversion range. If the voltage to be stepped-down is considerable, this converter might not work well. Then, an adaptation is needed, which can be achieved by a so-called Quadratic Buck Converter, whose voltage output varies with the square of the duty cycle (instead of linearly as the traditional buck). An additional point is reliability in case of a switch failure. Multi switch configurations, such as the interleaved converters allow for a more reliable operation, Although still have the same operating range limitation as the traditional buck [263].

Battery-assisted electrolysis

Because of the variable and intermittent nature of solar-powered electrolysis, the electrolyzer cannot operate at full capacity for 24 h a day without any backup electric storage or support from the electricity grid. Batteries have the potential to smooth the fluctuations in hydrogen production and enhancing the operating time of an off-grid PV-powered electrolyzer.

There are three main operating methods for the PV-battery-electrolyzer system:

1. The battery supports the electrolyzer in periods where PV is not enough to start the electrolysis process by supplying enough power to operate the electrolyzer at its technical minimum [245, 247, 264].

2. The electrolyzer is operated at a fixed power, which is lower than its nameplate capacity. The battery provides or stores energy as needed to keep the constant operating point of the electrolyzer [247].

3. The electrolyzer operates at a constant set point, which changes daily or seasonally [247, 264, 265].

Whether adding batteries to the electrolysis system is economically feasible or not it is still a matter of discussion. Hybrid systems combining PV and wind or simply curtailing a fraction of the PV production lead to cheaper hydrogen prices and acceptable payback times of 15 years with a hydrogen cost of 4 €/kg, or only 5 years if the cost increases to 7 €/kg [266]. Grid-connected systems without battery support also have lower hydrogen costs (4.22 €/kg) than their off-grid counterparts (around 6 €/kg) [247].

On the other hand, batteries can significantly reduce the size of the components. Koyama [267] argues that with the battery-assisted system, the electrolyzer unit is small, resulting in a reduced amount of investment costs. The savings from the electrolyzer investments are compensated by the installation costs of the battery which can account up to 33.6% of the hydrogen cost [247]. The battery has the potential to increase the amount of hydrogen produced during intermittent periods (such as the day-night cycle) [265]. The hydrogen production can be boosted more than 100% (utilization factor) by adding batteries and has the potential to outperform a PV-wind hybrid system without them by 2.4% [234, 265, 266].

The environmental impact of battery-assisted electrolysis is mainly driven by the production of PV modules and batteries and considerably lower, in terms of greenhouse

emissions than the fossil-fuel based processes. But the need for non-renewable, non-living resources (Abiotic Resource Depletion) results in higher impact that fossil fuel methods. This only points out that other challenges need to be solved besides component sizing and cost reduction [268].

5.3.2. Consequences of variable operation

Changes in solar irradiance or wind speed do not occur instantaneously as in a step but continuously over time (ramp). As these renewable sources are used to power electrolyzers, Lee, et al. [269] determined the effect of current ramp direction and depth on the electrolyzer's efficiency. The efficiency loss is due to the accumulation of gas in the Porous Transport Layers (PTL) that prevents the reactants from reaching the electrodes. The buildup of gas is linked to the current ramps applied to the electrolyzer and depends on the direction of the ramp and its slope. During the ramping process, the gas saturation in the PTL changes linearly, and when the current is kept constant, it changes in a logarithmic way. The gas saturation occurs faster with steep up-ramps, and shallow down-ramps enhance gas removal. Hence, the combination of these two scenarios leads to an improved operation related to the gas response. Further, gas accumulation occurs faster than gas removal. This causes that when the same current is applied twice after a variable operation, the cell voltage will be higher at the second point leading to a lower efficiency [269].

The operating constraints imposed on the electrolysis system will depend on the electrolyzer technology (AEL, PEM or AEM.) Alkaline electrolyzers typically have a partial load operating limit of around 20% of their nominal capacity, while PEMELs offer greater flexibility working at partial loads of 5% of nominal capacity [212, 270]. This allows PEMELs to utilize more energy coming from renewable sources. PEM technology is sometimes argued to benefit from faster ramp speeds. In Ref. [270], the authors considered 10% of nominal power per second for a PEM electrolyzer model, in contrast to 1.67% nominal power per second for their model of an alkaline electrolyzer. These differences do not amount to a significant advantage over the alkaline one in hydrogen production. During periods with low irradiance, the PEM will operate at a low partial load while the alkaline remains off. This additional operating time is not significant in terms of produced hydrogen [270].

At partial load (operation below nominal conditions), the content of hydrogen in oxygen can reach dangerous levels. This is because the hydrogen dissolved in the water or electrolyte is transported to the anode chamber, where oxygen is being evolved. The transport mechanisms are [216].

- Diffusion, as a result of a concentration gradient.

- Convection due to pressure gradients, dissolved gas transport with the ions through the membrane or separator (electro-osmotic drag), and operational strategies (electrolyte mixing, in AEL).

- Supersaturation before the produced gases in dissolved form develop into bubbles.

Gas cross-over increases with pressure and current density; nevertheless, the gas impurity is reduced at higher current densities as the gas production is greater than the permeated gas, so the fraction of the latter in the former is also lower [216].

Mitigation techniques for dealing with the minimum operating power of alkaline electrolyzers include backup electrical storage or using separate units operating in a modular way. Turning off some modules could result in the remaining ones working a higher current densities [271]. Operation strategies can also help reduce gas cross-over and impurities, especially in alkaline technology. Most of the gas cross-over in alkaline electrolysis occurs because the electrolyte from the cathode and the anode is combined in the separator tanks and then recirculated. This electrolyte can be contaminated with gas remains. Hence, using different separator tanks for catholyte and anolyte reduces the gas cross-over, as well as minimizing the recirculation rate. For large electrolysis plants, a constant recirculation rate provides the best strategy [216].

Knowing the time constant of the system can be beneficial in developing operation strategies aiming at improving energy efficiency. The ripple on top of the DC signal causes losses in efficiency [272, 273]. But, if the current is interrupted only for short periods, the effect can be the opposite. Interrupting the current for the duration of the time constant (around 2 ms) reduces the polarization overpotential and helps to keep a constant concentration throughout the electrolyte. Removing the current for short periods also facilitates the expulsion of bubbles, potentially decreasing the resistive losses caused by coverage of the electrodes with bubbles [274].

The electrical response reaches a new set-point in a matter of seconds, but it experiences a slow change caused by temperature affecting the ohmic and activation losses. Energy consumption is higher during the temperature transient leading to an efficiency loss of around 5% [275]. Allidières et al. [275] show that the power density reaches the new set point so fast that the temperature of the stack lags. Energy is lost when the temperature rises again to the corresponding operating point. This results from a suboptimal operating point, as discussed in Section 5.2.3. Their system consists of a 20-cell PEM stack (the size or the power are not specified) with uncontrolled temperature.

The successful deployment of electrolysis plants depends not only on the stack but also on the auxiliary components (Balance-of-Plant) as highlighted by Furfari and Clerici [276]. Even the International Renewable Energy Agency (IRENA) reports that a hydrogen plant designed for variable operation imposes more constraints on the Balance-of-Plant elements than the stack. The configuration of the latter can help in such operation by using smaller units connected in a modular way [277].

The control of the whole plant also relies on the understanding of dynamic response. Although, this work does not aim to discuss the available operation strategies, it was found in at least two works [278, 279] that the misunderstanding of dynamic behavior (at quick and slower scales) can lead to a control system that cannot follow accurately the imposed set-points making the plants unable to follow quick variations imposed by quick changes in renewable power. Other authors have mentioned that ignoring the dynamics of the electrolyzer can lead to considerable efficiency loss [280].

Bifacial modules are an attractive option for boosting hydrogen production of directly coupled PEM electrolyzer systems. Recent experiments show that using a bifacial system, the STH efficiency rises 13% with respect to the monofacial system. This number

can be even improved by using materials that boost the reflectivity of the ground [246].

5.3.3. POTENTIAL IMPACTS OF INTERMITTENCY ON LIFETIME

The estimated lifetime of electrolyzers is a critical issue, especially when operating under variable conditions. For alkaline technology, the lifetime of the stack, based on acceptable efficiency drops, lies between 60 000 and 90 000 h, while for PEM this is lower: 20 000 to 60 000 h [281].

The degradation mechanisms that lead to cell failure are listed in the reviews of [282] (for PEM fuel cells) and [283] (for PEM electrolyzer cells).

A higher voltage or a higher current can be detrimental to the electrolyzer. While high voltages accelerate corrosion, the performance loss is minimal compared to using a high current density [284].

The intermittent operation can result in lifetime benefits. For example, 90 000 h can be translated into 20 years of operation if this is intermittent [281] (considering that 90 000 h are roughly 10 years).

On the other hand, intermittency can also represent a challenge as it can accelerate some degrading mechanisms. For instance, Weiß et al. [285] determined the effect of idle operation where the voltage of the electrolyzer is equal to the open-circuit voltage. They observed an initial improvement of the cell performance after resting periods, where the cell was left at open circuit (10 cycles) followed by performance decrease observed as a higher cell voltage. Mainly, the degradation was related to increased high-frequency resistance due to oxide formed during the open-circuit period. After 700 cycles the high-frequency resistance increased 1.6 times. To overcome this, a voltage of 1.3 V was applied.

When the PEM electrolyzer is switched off, it operates for a short period in reverse mode (i.e., as a fuel cell), consuming the hydrogen and oxygen in the stack immediately after electrolysis is interrupted [286]. During this process, platinum in the cathode electrocatalytic layer is lost as it is transported to the membrane, thus reducing its conductivity [286]. Further, the cathode voltage increases when the electrolyzer is shut down. This voltage increase damages the catalyst causing a reduction of the available area suitable for the reaction [287].

The reverse mode is not a specific characteristic of PEM electrolyzers. As explained by Uchino et al. [288] also alkaline electrolyzers present this behavior when the current is cut. Under this scenario, the dissolved hydrogen and oxygen produced during electrolysis react with the nickel oxide formed at the anode. The reverse current can flow for as long as 100 min.

In AEM, small portions of the catalyst detach from the anode with steep voltage steps. These steps, as with PEM, cause a transitory current reversal, whose magnitude can be considerable (between -100 and -200 mA/cm^2. To put this in context, the cell operated at a maximum current density of 672 mA/cm^2). When the cell is left idle, under open-circuit condition, the membrane becomes dehydrated, leading to increased resistance; hence, even in stand-by conditions, a water flow should be maintained to avoid this situation [199, 289].

Rakousky et al. [284] also investigated the degradation caused by the intermittent operation. To determine that effect, they created a reference test operated at constant

current at both high and low current densities. For the dynamic operation, they applied steps between three current density levels: 0 A/cm^2 to 2 A/cm^2 (high current density) and 1 A/cm^2 (low current density) to 2 A/cm^2. Different intervals of on-off were also used. The cell is stable, with no degradation when operated at 1 A/cm2 continuously. At higher current densities, the lowest degradation rates (16 μV/h) were obtained by operating continuously for 6 h followed by a resting period with no current flowing, for another 6 h. However, more frequent shut-downs lead to a worst degradation rate (50 μV/h). These degradation rate are lower than operating continuously at high current density, which leads to the highest degradation rate of 194 μV/h. High current densities lead to electrode damage, especially passivating the anode [284, 287]. Also, mechanical damage due to bubbles, possible transport of contaminants as more water is consumed [284] and potential damage to the membrane either by forming hotspots [284] or thinning [287]. This last statement is significant as the loss of membrane material has been found to affect industrial-scale electrolyzers with more than 20 000 h of operation. The thinning was attributed to material loss due to a chemical interaction rather than a mechanical process associated with bubbles [290]. Nevertheless, the thinning of the membrane can also be attributed to high temperatures, which can drastically increase the thinning process [291]. Furthermore, the membrane can suffer from puncturing, associated with hotspots appearing. This can destroy the stack because of a dangerous mixture of hydrogen and oxygen in the chambers [292].

Nonetheless, the degradation attributed to intermittency is not entirely clear from an electrochemical point of view. Some studies have found that continuous operation exhibits the same degradation that dynamic operation, so the aging mechanisms cannot be attributed to a highly dynamic process [293]. Degradation might be linked to mechanical stress caused by temperature and pressure variations, and the operation with renewable energy does not necessarily accelerate the aging process [169].

5.4. CONCLUSION AND DISCUSSION

This review presented the integration of electrolyzers with PV systems aiming at green hydrogen production focusing on the three main low-temperature water electrolysis technologies implemented nowadays: alkaline, Proton Exchange Membrane and Anion Exchange Membrane. Water electrolyzers are well suited for integration with variable renewable power as proven by this review and supported by other studies and international certifications. The electrical dynamic response has a minor influence on the electrolysis system and is related to the implementation of control systems. Slower dynamics introduced by temperature and pressure play a more important role in their integration with solar energy. The limitations for the electrolyzers when operating in variable mode, are mainly due to the operating limits of the electrolyzers, especially regarding the minimum operating limit required for safety operation. There is no clear evidence of degradation with a variable operation. Rather, the degradation effects can be caused by improper operation: higher current densities, frequency shut-off and keeping the stack at open-circuit voltage. In this respect, *intermittency* rather than *variability* of the power source play a more relevant role in limiting the integration of electrolyzers with renewable energy.

When powered from PV systems, the solar-to-hydrogen efficiency needs to exceed

10% for a system to be economically feasible. In the last 10 years there have been improvements towards this objective, yet there are still recent studies that fail to meet this goal. One of the potential causes for this is the definition of efficiency itself. Different authors use different definitions from it, ranging from: *solar-to-hydrogen efficiency, MPPT efficiency, Faraday's efficiency* and *energy efficiency*. The latter is also often calculated with either the low or the High Heating value of hydrogen leading to different results. This indicates a lack of standardization and direction on the research lines. This is even marked by the absence of a tangible goal for STH efficiency for PV-hydrogen systems. The goal reported in this work of 25% represent the target of a photoelectrochemical device, but not for PV powered systems. Even if it were the case, the development of PV-hydrogen systems is still very far from this target. Stand-alone systems without storage represent the area where there are more efficiency improvements needed. The coupling efficiency can reach impressive high values close to 99%. In this respect, the improvements in efficiency are linked to the efficiency of the electrolyzer, which is improved by using PEM technology, and the PV system itself. In spite of the advances in the efficiency of PV modules, this still has not fully reached the enough maturity, or cost reduction to be practically implemented. Further, we found only one work discussing bifacial PV systems which could improve the overall PV system efficiency, hence the STH. Research opportunities include focusing on more innovative PV applications besides the typical rack-mounted panels: bifacial PV, agrivoltaics, floating PV, etc. provide new opportunities to explore their integration with hydrogen systems.

Another challenge associated with the variable operation of PV-hydrogen systems is the availability of high-resolution data. Hourly data cannot properly capture the variability of the irradiance, and is only suitable for steady-state analysis. However, for variable operation of electrolyzers, their operation can change in seconds while temperature changes in minutes. Sub-hourly datasets or measurement equipment are better suited for variable operation studies. And with the partial load operation of electrolyzers and converters, the assumption of a constant efficiency of either of them can lead to an overestimation of the produced hydrogen. Simple models that calculate the efficiency as a function of the input power, which are also computationally cheap might help in the simulations of PV-hydrogen systems. Since many works are concerned with optimization, where a complex dynamic model might considerable increase the computation time, the assumption of a constant electrolyzer, or Faraday efficiency becomes attractive.

Battery-assisted electrolysis provides a solution to solar energy intermittency. The drawbacks for this technology is the cost, which is the topic of current research and the environmental issues associated with batteries. For projects in the MW range grid-connected systems are typically considered, which facilitates the continuous operation of the plant and reliable production of hydrogen. For smaller projects, such as refuelling stations, DC-DC systems or even directly coupled systems are well-suited.

With this review the challenges of integration of electrolyzers with solar energy can be identified and tackled, helping to achieve the goals set by international organisations and reaching a net zero emission future.

6

OPTIMIZATION OF PV-ELECTROLYZER SYSTEMS

When you have seen one ant, one bird one tree,
you have not seen them all.

E. O. Wilson

MORE efforts needed is the status of the International Energy Agency tracking report in hydrogen [294]. This means that the deployment of hydrogen with low emissions is still below the expected targets toward the 2050 Net Zero Emissions scenario [294]. Traditional hydrogen generation exceeded 900 Mt_{CO_2} emissions, and only a minority of the total hydrogen produced came from clean sources. While the use of hydrogen diversifies in other sectors beyond refining and chemistry, these two sectors demand more than 90% of the global hydrogen production [294]. Because of the emission-intensive generation methods and the importance of hydrogen in hard-to-decarbonize sectors, such as transport and industry, hydrogen production from electricity and water (electrolysis) is expected to cover around 75% of the clean hydrogen demand worldwide by 2030.

Solar photovoltaic (PV) energy is becoming a preferred option for powering water electrolyzers for hydrogen production with three methods for interconnecting such systems [260]:

Directly-coupled systems. These systems rely on finding an operating point such that the I-V curves of the PV system and that of the electrolyzer intersect at a point that is close to the maximum power point (MPP) of the PV [260]. Direct-coupling

systems can be made more efficient by applying load-management techniques, which consist of dynamically changing the number of electrolyzer stacks connected in parallel using a switch. In this way, a discrete MPP tracker can be implemented reaching coupling efficiencies close to 99% [260]. These systems are also suited for low-power applications (below 1 kW) for their simplicity, safety, and cost [295].

DC-DC coupling. The electrolyzer can also be interfaced with the PV system using a DC-DC converter which decouples the operating point of the PV system from that of the electrolyzer. The PV system can operate at its maximum power point at every instant and does not depend on the component design as with the directly coupled systems [232]. Even when there is one conversion stage that causes power loss, the total efficiency of the system is higher than the static directly coupled system (without load management) mainly because of the deviation from the MPP of the latter at low irradiance [232].

The advantage of using a DC-DC converter is that the performance of the system improves under changing irradiance. A maximum power point tracking algorithm forces the PV modules to deliver, as the name implies, maximum power. However, the algorithm can also drive the electrolyzer into dangerous conditions either above or below the design limits. For this reason, a modified MPP tracking algorithm was proposed in [296], which allows tracking of the MPP under most conditions, but adjusts the set point if the electrolyzer approaches an unsafe operating point.

AC coupling. This configuration is typically used to connect electrolyzers to grid- connected PV systems. The connection is made using an inverter at the output of the PV system and a rectifier at the input of the electrolyzer. Similar to the DC-DC coupling, the AC coupling systems can perform MPPT [260]. For grid-connected systems, transformers are also needed besides the DC-AC-DC conversion, resulting in 4 power processing stages with associated losses [260]. AC conversion can also be used in off-grid PV-electrolysis systems as in [297]. This system needs only two conversion stages (one inverter on the PV side and one rectifier on the electrolyzer side).

Direct coupling systems are well suited for small-scale projects, DC coupling for PV systems located in proximity to the electrolyzer, and AC coupling strategy is adequate for large-scale systems (in the MW range) where the PV production plant is far from the electrolyzer [260].

In all interconnection modalities, optimization must be performed to ensure maximum hydrogen production, minimum cost, and maximum efficiency.

6.0.1. OPTIMIZATION OF PV-ELECTROLYZER SYSTEMS

The sizing of the PV-electrolyzer plant depends on the coupling strategy and is an optimization problem of finding the configuration (in terms of size of PV and EL) that maximizes or minimizes efficiency, hydrogen production, cost, etc.

Directly-coupled systems are typically optimized by choosing an appropriate number of

PV modules, electrolyzer cells, or both and the connection between them (series or parallel). To achieve this, a statistical approach can be employed. The basis of this method is to identify the region in the I-V plane where the MPP of a given PV module occurs frequently and obtain the fraction of the maximum power point current at which the energy density is the highest. Then, the number of series connected electrolyzer cells is tuned such that the system operates in the highest energy density region. This method allows the use of readily available manufacturer data and applies to alkaline and PEM technologies [295]. Additionally, the I-V curve of the PV module can be linearized around the MPP. The resultant expression is a linear equation that relates the maximum power point current and voltage. A similar approach is made for the current of the electrolyzer. These expressions are then expanded by including the number of series and parallel PV modules and electrolyzer cells. When the linearized equations of both components are equated, the number of series and parallel modules and cells for a given temperature are obtained. This system will operate with very high coupling efficiencies regardless of the changing irradiance, as long as the operating temperature is kept at the design parameter [298].

Metaheuristic approaches, which are based on stochasticity and the repetitive evaluation of the objective function [299], are also often used to optimize directly-coupled PV systems. The number of series, parallel PV modules, and series, parallel electrolyzer cells is used as a decision variable. The genetic algorithm [250, 300], the imperialist competitive algorithm [301], and particle swarm optimization [233, 302] have been employed in the past to obtain the best configuration of PV and electrolyzer.

Naturally, an *a posteriori* analysis can also be conducted to study the response of the system to different parameters and find an optimal solution. This is the case for the study of [303] for a combined PV-thermal system. The optimal solution can be found by increasing the number of parallel PV modules and the number of series-connected electrolysis stacks and then analyzing the efficiency.

For DC-DC coupled systems, Gillesen, et al. [265], found the optimal size that minimizes the hydrogen cost for a fictitious power-to-gas installation in Germany powered exclusively by a PV system. The number of alkaline electrolyzer stacks, along with their power, were determined using the mixed-integer linear programming (MILP) method. The system curtails the PV power when it exceeds the maximum power of the electrolyzers. On a second approach, a battery-assisted system was tested using different battery technology. The main conclusion is that the cheaper option is to allow curtailment, at the expense of not producing hydrogen continuously [265].

As with directly-coupled systems, the genetic algorithm appears in literature as an optimization tool, for example, in [250]. The authors used the genetic algorithm to vary the number of PV and electrolyzer cells in series and parallel and obtain optimum solutions defined by four objective functions related to cost and efficiency. For the DC-DC coupled system the topology of the converter was also analyzed finding that the optimum solution is sensitive to the converter topology.

A different approach for sizing the off-grid PV system powering an alkaline electrolyzer was followed in [304] by using the HOMER software to design the PV system and battery bank. They considered the load profile of a glass-producing factory and the solar resource in Algeria, where the project is located. The study resulted in 1 MW$_p$ of fixed-axis

PV with more than 100 batteries. The PV system is fully powering the whole plant, not only the electrolyzer but also the auxiliary systems.

A grid-connected PV system powering a fictitious alkaline electrolyzer plant in Türkiye was studied in [305]. The optimization method was the Generic Optimization algorithm (GenOpt) coupled with the simulation software TRNSYS. The objective was to minimize the electricity withdrawn from the grid by tuning the azimuth and tilt of the PV modules [305]. Setting either the electrolysis technology or the electrolyzer capacity as decision variables also allows minimizing energy taken from the grid and meeting production goals at minimum cost [306].

Piveta et al. [307] used MILP to minimize the cost and CO_2 emissions of a grid-connected PV system that provides electricity to a simulated hydrogen production facility in northeastern Italy. They achieved the optimization objectives by tuning the PV, electrolyzer and storage tanks and using the grid and production targets as constraints. The minimum found Levelized Cost of Hydrogen (LCOH) was 7.8 €/kg_{H_2} for a system supplying hydrogen to a steel plant and a hydrogen refueling station with a 341 kW_p of PV and 89 kW PEM electrolyzer. Similarly, Engstam, *et al.* determined the operating conditions for a grid-connected hydrogen facility in Sweden which minimize the LCOH and CO_2 [308]. The grid model is a multi-country system, and while this model does not aim to sizing, it demonstrates that the LCOH, and carbon emissions are greatly influenced by the operative decisions [308]. For directly coupled systems, the LCOH is a function of the ratio between PV and electrolyzer capacities with a single minimum [309, 310].

Table 6.1 summarizes the selected optimization methods reported in the literature. Note that this list can be considerably expanded for directly coupled systems, as in the literature review of [311].

6.0.2. Relevance of this study

While the literature studies (Table 6.1) have focused on sizing studies, there is a clear gap in the design of stand-alone, DC-DC coupled (indirect coupled) systems. Furthermore, the strategies of direct coupling systems imply that the design of either, or both, components, PV and electrolyzers must be tailor-made for a particular system, because their number of cells and connection are used as decision variables. This prevents the use of readily available components. Grid-connected systems have different optimization objectives and constraints which are also not suitable for stand-alone systems.
The study of Gillesen, et al. [265] is one of the few focusing on readily available components at an industrial scale focusing on indirectly coupled, stand-alone systems.

The purpose of this study is to develop an optimization procedure for a stand-alone PV-alkaline electrolysis system. The output of such procedure is a relative sizing factor, which gives a better insight on the relation between the size of the PV plant and the size of the electrolyzer, as well as the azimuth and tilt of the PV modules, which are often overlooked.
These are typically optimized for the PV production, or decoupled in the optimization process. While the tilt of PV modules is explored in [305] as a decision variable for grid-connected systems and in [312] as an analysis of its effect, these variables have not been used to size off-grid solar-hydrogen systems. In addition, this work considers that the load is not only the electrolyzer but also a compressor, which needs to be also powered

Ref.	Coupling	Optimization tool	Optimization objective	Decision variables
[295]	Direct	Statistical	MPP coupling	series EL & PV cells
[242, 252, 298, 303, 309]		Analytical	Efficiency, MPP coupling, cost	series-parallel EL & PV cells
[233, 241, 300–302]		Metaheuristic	Cost, H_2 production, efficiency, losses	Series-parallel EL & PV cells; EL temperature; water activity
[250]	Direct & indirect	Metaheuristic	Cost, H_2 production, losses; efficiency	Series-parallel EL & PV cells
[312]		Analytical	Cost, efficiency, H_2 production	PV & EL size & capacity
[265]	Indirect	MILP	System cost	EL power & battery type
[305]	Grid	GenOpt	Grid electricity	PV azimuth &tilt
[306–308]		MILP	Cost & CO_2 emissions	PV peak power, EL power, EL technology, Power flows in European countries

Table 6.1: Comprison of optimization methods found in literature. Indirect methods refer to DC-DC coupled systems. *MILP* stands for *Mixed Integer Linear Programming*, *PV* for *photovoltaic*, *EL* for *electrolyzer* and, *GenOpt* for *Generic Optimization*.

by the PV system in a stand-alone system. Using a metaheuristic approach allowing the optimization of complex and diverse objective functions.

The model used, although programmed in MATLAB, can be easily translated into any programming language that supports the Particle Swarm Optimization algorithm (e.g. [313] and [314]).

Determining of the orientation of the PV modules, the focus on a fully autonomous system and the inclusion of a compressor to model the balance-of-plant form the main contributions of the present work.

The rest of this paper is structured as follows. Section 6.1 proposes the system description and models of the electrolyzer and compressor. This is extended in Section 6.2 with the optimization procedure. The results and analysis are discussed in Section 6.3 before closing with the conclusion in Section 6.5.

6.1. SYSTEM MODEL

The studied model consists of an off-grid PV system coupled to an alkaline electrolyzer using a DC-DC converter. A compressor is added as a Balance-of-Plant component. Figure 6.1 illustrates the studied system.
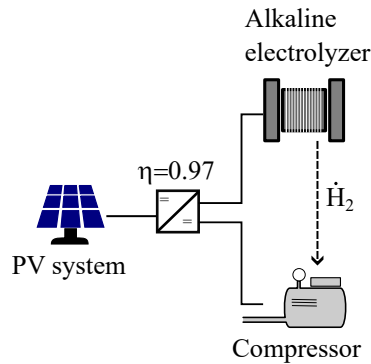

Figure 6.1: Description of the studied system. The solid line represents the electrical connection between components, while the dashed line indicates the flow of hydrogen.

6.1.1. ELECTROLYZER MODEL

The electrolyzer in this work was assumed to be of alkaline technology with a nominal power of 100 kW, and modeled with Ulleberg's model [195]. This model assumes that the total cell voltage is a sum of the reversible voltage and the overvoltage caused by resistive effects and activation of the electrodes.

$$V_{\text{cell}} = V_{\text{rev}} + V_{\text{ohm}} + V_{\text{act}} \tag{6.1}$$

The reversible voltage V_{rev} is the minimum voltage needed to start the decomposition of water. It is related to the change of Gibbs free energy, ΔG, and is a function of temperature. At 25 °C and 1 atm (standard conditions), $\Delta G^0 = 237.2$ kJ/mol, which

is equivalent to V_{rev} =1.229 V [167]. The ohmic losses V_{ohm} represent the losses at the electrolyte, electrodes, and bubbles, while the activation losses, V_{act}, model the overpotential caused by the energy needed to start the reaction. This is often described with the Butler-Volmer equation, or one of its simplifications [177]. The activation overpotential has a logarithmic dependency on the applied current.

Equation 6.2 shows the semi-empirical equation to describe the electrolyzer voltage as a function of the applied current density i (in A/m^2) and the operating temperature (in °C) [195].

$$V_{\text{cell}} = V_{\text{rev}} + ri + s\log(ti + 1) \tag{6.2}$$

The current density normalizes the applied current to the electrolyzer, I, by the cell area (A): $i = I/A$. The terms r and t are coefficients linked to the resistivity of the separator and the exchange current density respectively. The latter is related to the charge transfer between the electrodes in an open circuit condition [315]. Both r and t are temperature (T) dependent, as seen in Equations 6.3 and 6.4. The coefficient s is linked to the Tafel slope. Note that the r_x, t_x, and s terms are fitting parameters [195].

$$r = r_1 + r_2 T \tag{6.3}$$

$$t = t_1 + t_2/T + t_3/T^2 \tag{6.4}$$

The values for the parameters were taken from [316] and shown in Table C.1 of the appendix

Equation 6.2 defines the voltage of a single electrolyzer cell; however, for a stack of cells, it is assumed that all the cells are identical and connected in series. The total voltage of the stack V_{ele} is the number of cells (N_{cells}) multiplied by the voltage of a single cell (V_{cell}). Figure 6.2 shows the simulated I-V curve. Constant temperature of 60°C and 186 series-connected cells were assumed. The reason for this is to simulate an industrial-sized electrolyzer. The I-V model used here is reproduced from [316] where the I-V curve of a small-scale electrolyzer was demonstrated to be scalable to an industrial size with an electrolyzer of 186 cells. This number allows the results to be traceable and comparable.

According to Faraday's law of electrolysis, the hydrogen flow, $\dot{H}_2$, is proportional to the current applied to the electrolyzer, I as in Equation 6.5.

$$\dot{H}_2 = \eta_F \frac{I}{2F} \tag{6.5}$$

The term η_F accounts for the difference between the theoretical rate of production and the real one, and is called the Faraday efficiency. For simplification, $\eta_F = 1$. F is Faraday's constant, indicating the electric charge of one mole of electrons (F = 96485 C/mol).

The alkaline technology cannot operate below 20% of its nominal current to avoid gas crossover from the oxygen to the hydrogen chamber. This, if happens, can result in an unsafe situation [195]. For this reason, whenever the PV power, P_{PV}, is insufficient to meet the minimum power demand of the electrolyzer, P_{min}, the system will be switched off. When the PV power exceeds the nominal power of the electrolyzer, P_{nom} it will be
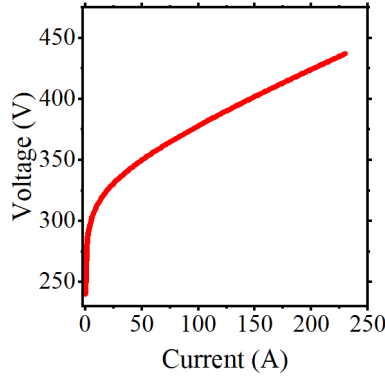
Figure 6.2: Current-Voltage curve of the simulated alkaline electrolyzer.

curtailed to the nominal power of the electrolyzer. The conditions are expressed in Equation 6.6.

$$\begin{cases} P_{\text{ele}} = 0, & P_{\text{PV}} < P_{\text{min}} \\ P_{\text{ele}} = P_{\text{nom}}, & P_{\text{PV}} > P_{\text{nom}} \\ P_{\text{ele}} = P_{\text{PV}}, & \text{otherwise} \end{cases} \tag{6.6}$$

6.1.2. COMPRESSOR MODEL

The compressor is modeled as an isentropic process. The main assumption is that the hydrogen behaves as an ideal gas and there is no heat transfer from the gas to the structure of the compressor or the ambient. From these assumptions and applying the First Law of Thermodynamics, the work (W) needed to compress hydrogen at constant volume is the change of enthalpy (H) of the gas as seen in Equation 6.7. The change of enthalpy can be obtained from the specific heat of hydrogen at constant pressure (C_p), the difference of temperature at the inlet (T_1) and outlet (T_2) of the compressor, and the amount of gas involved (n) [317], [318].

$$W = n\Delta H = nC_p(T_2 - T_1) \tag{6.7}$$

The law of ideal gases is recalled in Equation 6.8. This equation describes the behavior of the amount of gas (n) at given pressure (P), volume (V), or temperature (T). R is the universal gas constant with a value of 8.314 Jmol^{-1}K^{-1}.

$$PV = nRT \tag{6.8}$$

For an isentropic compression process, the entropy remains constant, and the relation between the input and output pressures is given by the Compression Pressure Ratio (CPR) as in Equation 6.9 [319].

$$\mathrm{CPR} = \frac{P_2}{P_1} = \left(\frac{T_2}{T_1}\right)^{\gamma/(\gamma-1)} \tag{6.9}$$

The term γ is the ratio of the specific heats at constant pressure C_p and constant volume C_v (Equation 6.10). The latter can be derived from the former using the fact that the universal gas constant, R, is the difference of both specific heats ($R = C_p - C_v$) [319].

$$\gamma = \frac{C_p}{C_v} \tag{6.10}$$

Under ideal conditions, the electrical power to compress hydrogen (w_c) is the same as the work applied to the gas (Equation 6.7) per unit of time. To consider non-idealities, an efficiency term needs to be considered ($\eta = 0.6$ [303]). Working out Equations 6.7 6.8, 6.9, and 6.10 leads to the expression for the electric power needed by the compressor (Equation 6.11) [303].

$$w_c = C_p \dot{H}_2 \frac{T_1}{\eta} \left(\mathrm{CPR}^{(\gamma-1)/\gamma} - 1\right) \tag{6.11}$$

Note the term $\dot{H}_2$ which is the hydrogen flow in kg/s defined in Equation 6.5. It results from replacing n with $\dot{H}_2$ in Equation 6.8. This allows the calculation of electric *power* instead of *energy*. This model is typically applied in describing PV-hydrogen systems as in [303]. Table C.2 in the appendix shows the used values for the model.

6.1.3. PV MODEL

The production of the PV system was calculated using data from the Royal Meteorological Institute of The Netherlands [320]. This data was collected in 2013 in Cabauw, a small town located in the center of The Netherlands. The dataset contains 1-minute resolution irradiance values including Global Horizontal Irradiance (GHI), Diffuse Horizontal Irradiance (DHI), Direct Normal Irradiance (DNI) and, ambient temperature.

The PV system is assumed to be installed on flat ground, with free horizon. Further, all the PV modules receive the same irradiance, and there is no partial shading either from clouds, self-shading or any other obstacle.

The total irradiance that the PV module receives (G_m) is needed to calculate the instantaneous PV power. G_m is the sum of direct (G_{dir}), diffuse (G_{diff}) and reflected (G_{ref}) irradiance components as seen in Equation 6.12

$$G_m = G_{\mathrm{dir}} + G_{\mathrm{diff}} + G_{\mathrm{ref}} \tag{6.12}$$

The direct irradiance on a tilted surface (PV module) can be obtained from the DNI by calculating the angle of incidence (AOI) between the Sun (described by its altitude in degrees above the horizon, a_s, and its azimuth in degrees starting from the North, A_s) and the normal vector of the PV module (described by the module's tilt, a_m and azimuth A_m) as shown in Equations 6.13 and 6.14 [321].

$$\cos \mathrm{AOI} = \cos a_m \cos a_s \cos(A_m - A_s) + \sin a_m \sin a_s \tag{6.13}$$

$$G_{dir} = DNI \times \cos AOI \tag{6.14}$$

The diffuse irradiance seen by this (tilted) PV module (G_{diff}) was obtained from the DHI considering an isotropic sky model (Equation 6.15) [321].

$$G_{diff} = DHI \times \frac{1 + \sin a_m}{2} \tag{6.15}$$

A tilted module also receives reflected irradiance from the ground which is affected by the albedo (α) of the site. A constant value of the albedo of 0.2 was assumed (Equation 6.16).

$$G_{ref} = DHI \times \alpha \times \frac{1 - \sin a_m}{2} \tag{6.16}$$

The Normal Operating Cell Temperature (NOCT) model accounts for the temperature effect, which models the difference between the temperature of the solar cell (T_m) and the ambient temperature (T_a) as a linear function of the incident irradiance on the PV module (Equation 6.17). [321].

$$T_m - T_a = \frac{T_{NOCT} - 20}{800} G_m \tag{6.17}$$

The term T_{NOCT} in Equation 6.17 refers to the solar cell temperature when the module is exposed to an incident irradiance of 800 W/m^2 and 20 °C ambient temperature with 1 m/s wind speed [322]. This value is given in the datasheet of manufacturers.

Figure 6.1 shows that the PV module is connected to a DC-DC converter. This converter performs maximum power point tracking (MPPT), which implies that, at every instant, the instantaneous PV power is the PV module's maximum power under the instantaneous irradiance. This assumption simplifies the calculation as it does not require knowledge of the module's IV curve. The module's MPP (instantaneous PV power) is then equal to the received irradiance multiplied by the efficiency of the module (given in the module's datasheet) corrected for temperature and irradiance effects and the module's area (Equation 6.18) [321]. At standard test conditions, the maximum power point, P_{mpp}, the open circuit voltage V_{oc}, and the module's efficiency, η, can be obtained from the module manufacturer's datasheet as well as the module's area A_{module} and the deviation of the maximum power point as the temperature changes, α_p. The parameter $n_d = 1.5$ is the ideality factor of the diode. The technical specifications of a Trina Tallmax M 450 W$_p$ module [323] were considered.

$$\eta_{Tm,Gm} = \frac{P_{mpp}}{1000 A_{module}} \left(1 + \frac{0.0258 n_d}{V_{oc}} \times \ln\left(\frac{G_m}{1000}\right)\right) \left(1 + \frac{1}{\eta} \frac{\partial \eta}{\partial T} (T_m - 25)\right)$$
$$\frac{\partial \eta}{\partial T} = \frac{P_{mpp} + \alpha_p (T_m - 25)}{(1000 A_{module})(T_m - 25)} \tag{6.18}$$

The PV power was further reduced by 97% to account for the losses at the DC-DC converter (semi-ideal behavior, considering a constant efficiency of 0.97 over the whole power range. This number was chosen after an analysis with the model proposed in [324]).

6.2. OPTIMIZATION PROCEDURE

The optimization consists on finding the values of the decision variables that minimize the objective function. In this case, the decision variables are the azimuth of the PV modules, their tilt, and the oversize factor (i.e., ratio between the PV system peak power to the nominal power of the electrolyzer). The objective functions are the cost, specific energy use and specific wasted energy, explained in Section 6.2.3. The Particle Swarm Optimization (PSO), (discussed in Section 6.2.1) is the tool used for finding the optimal values. For each iteration of PSO, the following steps are taken:

1. Calculate the theoretical instantaneous power of the PV system without load.

2. Distribute the PV power to the electrolyzer and compressor (discussed in Section 6.2.2.

3. Integrate the instantaneous values over the whole year and calculate the performance indicator (Section 6.2.3) to be optimized (objective function).

The next section explains the aforementioned steps in detail.

6.2.1. PARTICLE SWARM ALGORITHM (PSO)

The Particle Swarm Optimization (PSO) is an algorithm based on the interactions between individuals in flocks of birds or school of fish [325]. It relies on the concept of *particles*, which are associated to solutions of the objective functions [326]. Each individual, or *particle*, is described by its position in the search space (i.e. the possible values for the decision variables) and a velocity, an updatable parameter that controls how fast this particle moves toward the rest of the individuals. Additionally, the particles have a memory of themselves and the rest of the group. This means that a particle keeps a record of the best solution it has found over all the iterations, and also knows the best solution of all the individuals in the swarm [325]. The algorithm starts by creating a population of individuals randomly distributed over the search space, with initial position and velocity. The objective function is calculated for every particle and the individual best and group best parameters for each particle are updated. If a particle finds a solution that is lower than the record of its individual best, it replaces its parameter with the new found solution. The same applies to the group best parameter. The position and velocity parameters of each particle are updated and then, all the particles are again randomly replaced. But, this new placement depends on the previous position, velocity, and individual and group bests. In this way, all the particles begin to move towards the global minimum of the objective function [325, 326].

PSO performs better than other metaheuristic algorithms (genetic algorithm and imperialist competitive algorithm) when optimizing directly-coupled systems. It is faster, finds the optimum in fewer iterations and converge to the global minimum [327].

6.2.2. POWER DISTRIBUTION

As a completely stand-alone system, the PV system (P_{PV}) must provide all the electricity needed to operate the electrolyzer P_{ele} and the compressor P_{comp} as seen in Equation 6.19.

$$P_{PV} = P_{ele} + P_{comp} \tag{6.19}$$

This implies that not all the power of the PV system is available to produce hydrogen. Hydrogen production is proportional to the applied current to the electrolyzer I_{stack} as discussed in Section 6.1.1. The Newton-Raphson method shown in Equation 6.20 was used to calculate this amount.

$$I_{stack_{n+1}} = I_{stack_n} - \frac{f(I_{stack_n})}{f'(I_{stack_n})} \tag{6.20}$$

The subindices $n + 1$ and n are the updated and current values of the current, respectively. As this is an iterative process, the updated value will be used as the current value in the next iteration. Equation 6.21 shows $f(I_{stack})$ which is the function of the electrolyzer current whose root is precisely the current which ensures that the power balance (Equation 6.19) is valid. This equation was obtained from the power of the electrolyzer, calculated as the product of its voltage and current $P_{ele} = V_{ele} \times I_{stack}$. Note that the electrolyzer's voltage (Equation 6.2) is a function of the electrolyzer's current, I_{stack}, hence, P_{ele} is also a function of this variable. The hydrogen flow, which is also dependent on I_{stack} (Equation 6.5), is the link between the electrolyzer and the compressor because the compressor power (Equation 6.11) is governed by the hydrogen flow, and subsequently, by the electrolyzer current. The power balance can be written in terms of I_{stack} because both the electrolyzer and compressor powers can be expressed in terms of the electrolyzer current. Equating the resulting expression to zero leads to Equation 6.21 which is the expression of $f(I_{stack})$. The coefficient 2.016×10^{-3} kg/mol is the molar weight of hydrogen and is included to ensure the match of the units. The term K_1 is defined in Equation 6.22 and it is used to simplify the expressions in Equations 6.21 and 6.23. With the assumptions described in Section 6.1, K_1 is a constant.

$$f(I_{stack}) = \frac{s}{\ln 10} \ln\left(\frac{t}{A} I_{stack} + 1\right) I_{stack} + \frac{r}{A} I_{stack}^2 + \left(\frac{2.016 \times 10^{-3} \times K_1}{2F} + V_{rev}\right) I_{stack} - \frac{P_{PV}}{N_{cells}} \tag{6.21}$$

$$K_1 = \frac{C_p T_1}{\eta} \left(CPR^{(\gamma-1)/\gamma} - 1\right) \tag{6.22}$$

$f'(I_{stack})$ (Equation 6.23) is the derivative of this function with respect to I_{stack}, which is needed in the Newton-Raphson method.

$$f'(I_{stack}) = \frac{s}{\ln 10} \left[\frac{t}{t I_{stack} + A} I_{stack} + \ln\left(\frac{t}{A} I_{stack} + 1\right)\right] + \frac{2r}{A} I_{stack} + \frac{2.016 \times 10^{-3} \times K_1}{2F} + V_{rev} \tag{6.23}$$

6.2.3. Performance indicators

Three performance indicators evaluate the system. These indicators were used also as objective functions.

The *specific energy use* of the system was defined as Equation 6.24. This indicator is a measure of the efficiency of the system, because it relates the energy that could be produced from the PV system ($\int_{\text{year}} P_{\text{PV}}$) to the amount of hydrogen that was actually produced $\int_{\text{year}} \dot{H}_2$. The units are in $\text{kWh/kg}_{\text{H}_2}$.

$$\text{Energy use} = \frac{\int_{\text{year}} P_{\text{PV}}}{\int_{\text{year}} \dot{H}_2} \tag{6.24}$$

A closely related indicator is the *specific wasted energy* and contains two components: the *unused energy* energy and the *curtailed energy*. These indicators arise from the operational limits of the electrolyzer defined in Section 6.1.1. The unused power, P_{unused}, is the power that could be generated from the PV system, but it is not, as a result of the electrolyzer being off due to insufficient power to meet the operating limits. The curtailed power, $P_{\text{curtailed}}$, is defined analogously, as the energy that could be generated from the PV but it is bounded to meet the maximum operating limit of the electrolyzer. The wasted energy is then defined as Equation 6.25.

$$\text{Wasted energy} = \frac{\int_{\text{year}} (P_{\text{unused}} + P_{\text{curtailed}})}{\int_{\text{year}} \dot{H}_2} \tag{6.25}$$

The Levelized Cost of Hydrogen (LCOH) is the third and last indicator. It represents the cost of producing one kilogram of hydrogen (€/kg_{H_2}). Equation 6.26 [328] was used to calculate the LCOH. The numerator is the sum over every year, t, of all the installation costs of the system I_t incurred during the lifetime of the project ($n =25$ years) plus the maintenance and replacement costs, M_t. The denominator is the yearly production of hydrogen H_t. The term $\frac{1}{(1+r)^t}$ is the annuity factor to consider for the future value of the costs and is calculated with the interest rate, $r = 4\%$ (which is in line with the sensitivity analysis carried out by [329]), and the year of the calculation, t. The values used for the calculation of the LCOH are given in the appendix, Table C.3.

$$LCOH = \frac{\sum_{t=0}^{n} \frac{I_t + M_t}{(1+r)^t}}{\sum \frac{H_t}{(1+r)^t}} \tag{6.26}$$

6.3. RESULTS AND DISCUSSION

6.3.1. OPTIMIZATION RESULTS

Two types of PV systems were studied. First, one with all modules oriented at the same azimuth and tilt, and second, a PV system whose half of the modules are flipped 180° in azimuth with respect to the first half, but the tilt is the same for both halves. This second system opens the possibility for the optimization of east-west oriented modules.

Ten runs were carried out for each indicator for each PV system to check for convergence of the optimization procedure. Figures 6.3a and 6.3b show the optimization results for the orientation of the PV modules of single and double orientations, respectively. Figure 6.3c shows the resultant oversize factor for each type of the PV systems as a function of the objective functions.
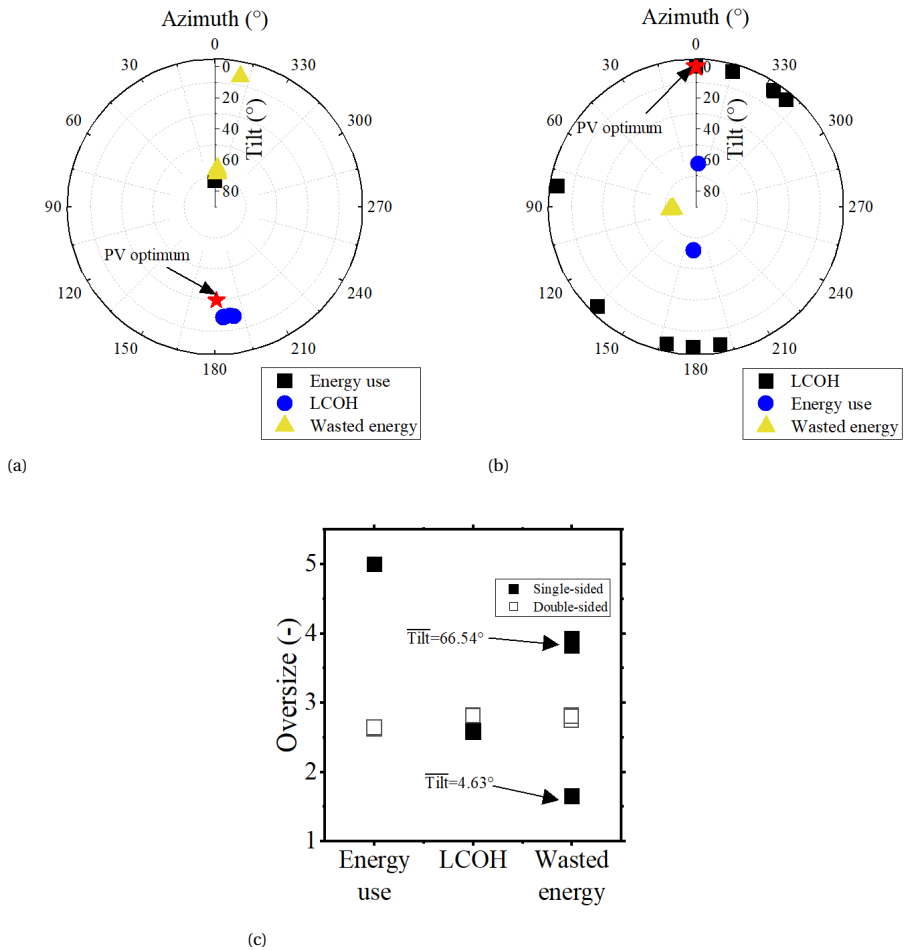
Figure 6.3: Optimization results for orientation and oversize factor. Ten runs were carried out. Each point represents one of the runs. Note that in many cases the points are overlapping, indicating convergence of PSO. (a) Single-sided configuration (All PV modules have the same azimuth and tilt). The orientation that maximizes the yearly PV energy is marked with a star. (b) Double-sided configuration (Half of the PV modules are displaced 180° in azimuth with respect to the first half. All modules share the same tilt). (c) Oversize factor for all indicators and both PV configurations. The arrows that are labeled with $\overline{\text{Tilt}}$ mark the average tilt of the pointed clusters.

From Figure 6.3a it is possible to note that the PSO found that the configurations which minimize the specific energy use are facing north. As a reminder, the PV system is assumed to be installed in The Netherlands, in the northern hemisphere, and the expected best azimuth is facing southwards. Even more remarkable is the fact that the north-facing modules are not horizontal (as would be expected to compensate for the north-facing azimuth). This means that the PV modules are oriented away from the Sun. When looking at Figure 6.3c, this configuration corresponds to the upper limit set for the oversize factor. This is needed to compensate for the fact that the north-facing PV

system harvests only diffuse irradiance. The minimization of the wasted energy with a single orientation also results in north-facing PV modules. Although the oversize factor does not reach its limits. One of the configurations that minimize the wasted energy results in almost horizontal modules, which are associated with a lower oversize factor (Figure 6.3c).

Another interesting observation is that, for single-sided systems, the angle that maximizes the PV production is not the same as the one that optimizes any of the indicators. This is relevant because typically, the PV system is optimized first for maximum energy production; then, the electrolyzer is selected.

Figure 6.3b shows the case of the double-sided configuration. For the energy use, PSO found configurations in the North-South orientation. As opposed to the single-sided version, where all the modules receive only diffuse irradiance, in the double-sided version, half of the PV modules are actually facing south.

To minimize the hydrogen cost with a two-sided system, the modules should be placed horizontally. Under this situation, the azimuth does not play a role anymore (as seen in the wide range of azimuth values for LCOH in Figure 6.3b). This is the only case where the orientation for a particular indicator (LCOH in this case) matches the optimal angle for PV generation. The oversize factor remains almost the same for both configurations (2.58 and 2.82 for single and double-sided, respectively)(Figure 6.3b).

The double-sided analysis was performed to study the possibility of installing the PV modules in an East-West configuration. However, PSO did not find this orientation favorable for any indicator.

The calculation of the indicators of each configuration offers a better insight into the effect of the configurations. The selection of these configurations is based on the results of Figure 6.3 and are, two for minimizing energy use, two for the LCOH (one for each type of PV system), and three for wasted energy (2 single-sided and one double-sided). The used values are given in Table 6.2.

Indicator	PV system	Azimuth (°)	Tilt (°)	O.F.	# PV	Abbreviation
Energy use	single	0.3	73.4	5	1111	Efficiency 1
	double	176.83	62.16	2.63	584	Efficiency 2
LCOH	single	184.5	18.9	2.58	573	LCOH 1
	double	243.07	0.0	2.82	627	LCOH 2
Wasted energy	single	355.98	66.54	3.86	858	Wasted 1
		348.94	4.63	1.65	367	Wasted 1H
	double	95.2	74.66	2.80	622	Wasted 2

Table 6.2: Selected configurations. O.F. stands for "oversize factor" and "#PV" for the number of PV modules

Figure 6.4 shows the value of every indicator for each configuration of Table 6.2. The minimum hydrogen cost is obtained with configuration *LCOH 1*, which is a south-facing, single-sided arrangement. The two-sided configuration did not offer any advantage for the hydrogen cost. But a horizontal placement of the PV modules opens the possibility of reducing energy consumption, and wasted energy while boosting hydrogen production
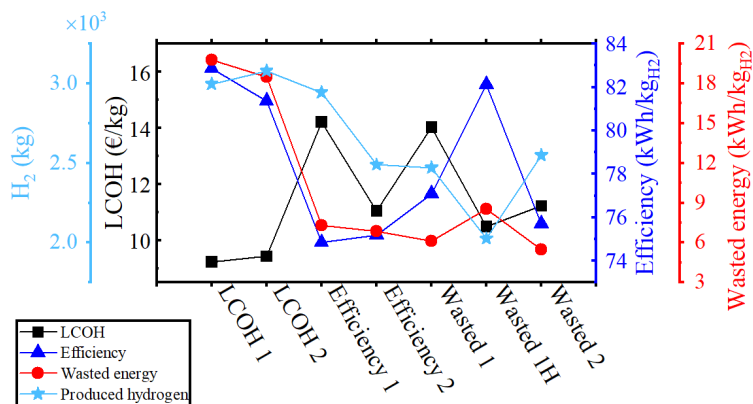
Figure 6.4: Evaluation of the different configurations with every indicator. The abbreviations on the horizontal axis correspond to those mentioned in Table 6.2

with just a small increase in the price. It can be even more attractive because the increase in PV size is not significant.

It is no surprise that the higher costs correspond to the north-facing configurations.

Note that the energy consumption calculated here also considers the curtailed energy. And for this reason, the obtained values are higher than the expected values for energy consumption for alkaline technology, which are in the range of 50 kWh/kg$_{H_2}$ [330].

Authors in [331] found an optimal oversize ratio of 1.4 on average to minimize the hydrogen cost. They compared the performance of 18500 commercial PV modules and perform the optimization with the number of PV modules as a decision variable. In the same direction, the oversize ratio which minimizes the LCOH of a stand-alone PV-hydrogen system located in Townsville, Australia was 1.5 [310], while the oversize factor obtained from this study is around 2.5. One potential reason for this difference can be attributed to the energy needed by the compressor. Another important difference is the geographical location (Algeria [331] and Australia [310]) with a higher irradiance than The Netherlands. The optimal oversize factor changes depending on the capacity factor of the PV plant, linked to the solar resource available per location [309]. Lastly, the fact that the orientation is also taken into account influences the oversize factor compensating for lower generation from the PV system.

The efficiency is sensitive to the tilt of the PV modules, as demonstrated by the results and also reported in [312]. As opposed to [312], whose optimal tilt is 60°, the highest efficiency occurs when the PV modules are vertical. The difference in efficiency values can be attributed to a) location (Rome [312], and The Netherlands (this study)), b) the consideration of the oversize factor and azimuth of the PV modules and c) The sensitivity of PSO to the imposed limits to the oversize factor (see C.1.2).

Albeit the three defined indicators, reliability (expressed with the loss of load probability), economic (net present cost, LCOH, capital recovery factor), and environmental (CO$_2$ emisions and energy emission factor) are other indicators discussed in the litera-

ture for stand-alone hydrogen-based systems [332].

6.3.2. OPERATION AT PARTIAL LOAD

A load duration curve is a tool frequently used in electrical engineering to represent the time (horizontal axis) that a load is expected (vertical axis) [333]. This tool facilitates the description of the operation at partial load of the alkaline electrolyzer. Figure 6.5 shows the partial load duration curve of the electrolyzer when different configurations are used. These figures were obtained by calculating the instantaneous power delivered to the electrolyzer (following the procedure described in Section 6.2.2). This power, with a resolution of minutes, was resampled into hourly values by calculating the average of all powers within an hour. The hourly power values were normalized against the nominal power of the electrolyzer, sorted in descending order, and then plotted. Note that the graphs show an average of every hour. For this reason, the graph shows values below the minimum operating threshold.

Figure 6.5a corresponds to the partial load operation of the electrolyzer when optimized for maximum efficiency (minimum energy use). The inset at the top right shows the portion of the graph when the electrolyzer operates at full load. In all cases, the electrolyzer operated for less than 100 hours at full load. The single-sided, north-facing PV system has a better partial load characteristic than the south-facing PV system operating for an additional 390 hours (inset, lower right corner).

For the configurations optimizing the LCOH, there is little difference in the partial load operation for single-sided and horizontally-placed PV modules. The latter allows the operation for 3 days more than with the former configuration, as seen in Figure 6.5b. Observe that the electrolyzer operates at full-load for more time for the layout that minimizes the LCOH. This results in improved hydrogen production (Figure 6.4).

The layout that minimizes the specific energy use (Figure 6.5a) prioritizes the operation at lower loads rather than the full-load range. In fact, the electrolyzer only operates for a few hours at full capacity. A similar situation occurs with the configuration optimizing the specific wasted energy (Figure 6.5c). The single-sided configuration with an almost horizontal module (*Wasted 1H*) leads to very poor use of the electrolyzer despite being the configuration with the lowest cost among those aiming at reducing the energy spill (wasted energy and energy use) as seen from Figure 6.4.

The utilization of the PV system can be studied by looking at the histograms of the potential production for each configuration. The word *potential* is important because not all of the PV power can be used. As presented in Section 6.2.3, the electrolyzer imposes operative limits, and, whenever the PV power violates these boundaries, it must be curtailed. Figure 6.6 illustrates the distributions of the PV power (P_{PV}). As a reference, the distribution of the GHI at the site is also included (Figure 6.6a). A light blue rectangle marks the regions where the PV power is used by the hydrogen equipment (i.e., electrolyzer and compressor). From Figures 6.6b and 6.6d it is possible to conclude that the PSO algorithm tries to minimize the curtailed energy (values above 112 kW of PV power). In doing so, it allocates more power to the low-production region. The power in this region cannot be used, and despite it being very small, the large occurrence results in more unused than curtailed energy.
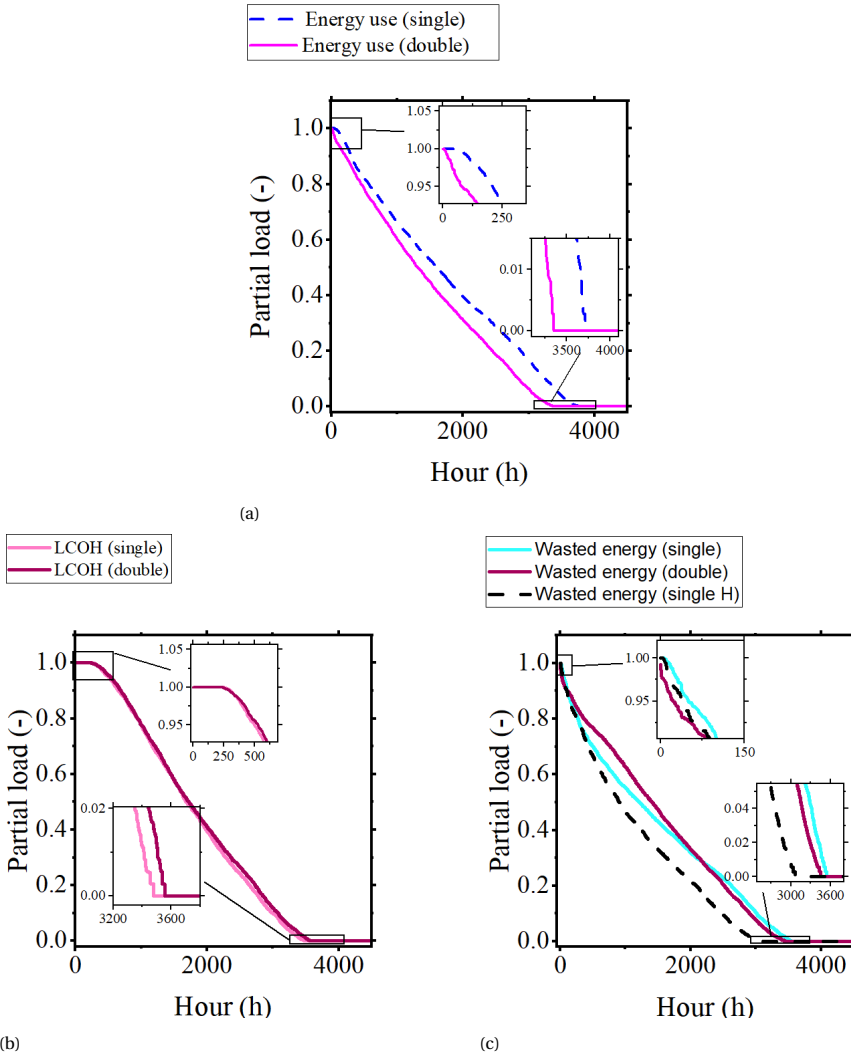
(a)

(b)

(c)

Figure 6.5: Partial load curves for the configurations of Table 6.2. (a) Efficiency (energy use). (b) LCOH. (c) Wasted energy.

The minimum LCOH is achieved with a more aggressive strategy. Figure 6.6c illustrates that, in contrast to the other indicators, the PV layout for minimum LCOH attempts to harvest as much PV power as possible in the operating region of the hydrogen equipment. The trade-off is a considerable amount of curtailed energy.

A different electrolyzer technology, such as Proton-Exchange Membrane (PEM), with a higher dynamic range (from 0-100%) [277], could improve the utilization of the PV power. The optimization for reducing the wasted energy already leads to very little curtailed energy (0.59 kWh/kg$_{H_2}$ with a two-sided configuration). Most of the wasted energy
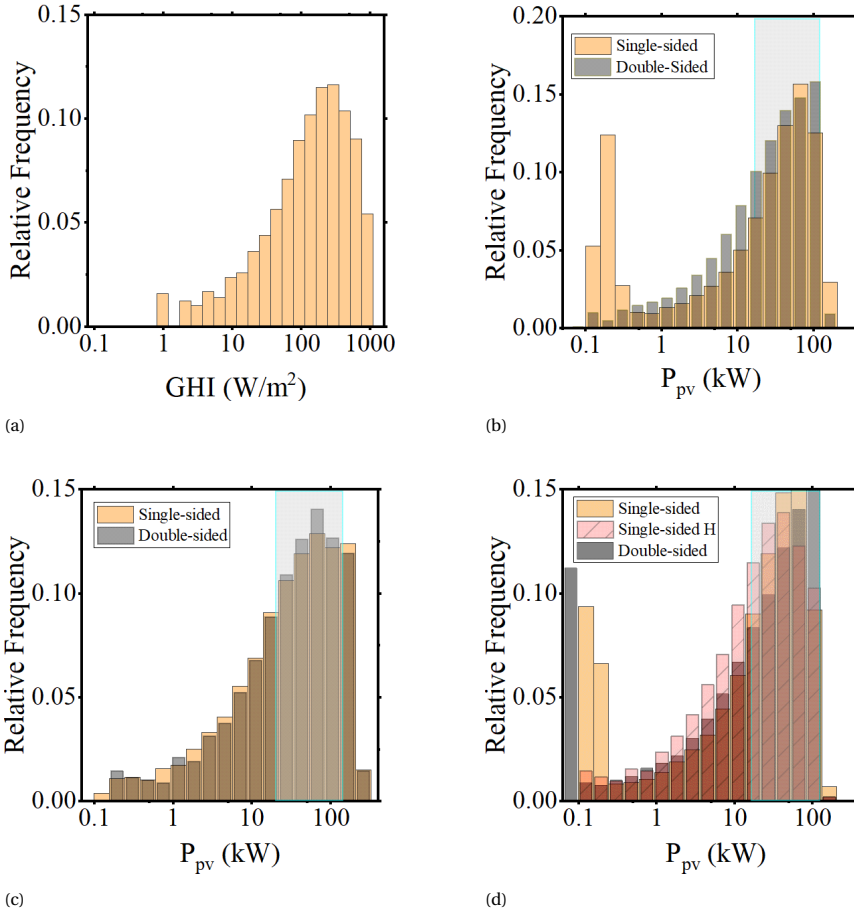
Figure 6.6: Histograms of the potential PV production for configuration optimizing each indicator. (a) Distribution of the GHI at the analyzed site. (b) PV power when the system is optimized for maximum efficiency (minimum energy use). (c) PV power when the system is optimized for minimum LCOH. (d) PV power when the system is optimized for minimum wasted energy. In graphs (b), (c), and (d), the light blue rectangle marks the operating region of the hydrogen equipment (electrolyzer and compressor). Observe that the horizontal axis in all figures is a logarithmic scale.

in this configuration comes from the unused energy (Figure 6.6d) which could be well absorbed by a PEM electrolyzer or multiple smaller units as in [260] or [334].

6.4. SENSITIVITY AND UNCERTAINTY ANALYSIS

6.4.1. UNCERTAINTY ANALYSIS

An uncertainty analysis on the convergence of PSO for each indicator ensures the validity of the presented results. The uncertainty analysis relies on the results from the

ten runs carried out for each indicator, as discussed in Section 6.3 and shown in Figure 6.3. The bootstrap resampling method offers an alternative to recalculating hundreds of new samples and was chosen because the optimization procedure is computationally expensive. The bootstrap uses the original ten optimization runs as the initial sample and allows to easily increase the sample size from 10 to 1000. Recall that the bootstrap is a resampling with replacement method is used to compute population statistics based on a small sample [335]. The median of each sample describes best data. The mean is highly affected by outliers, assumed present in the samples. Then, the 95% confidence interval of the sample medians was calculated.

Indicator	Variable	Median	CI low	CI high
Efficiency single side	Azimuth (°)	0.3701	0.2476	0.4357
	Tilt (°)	73.3787	73.3735	73.4190
	Oversize (-)	5.0000	4.9999	5.0000
Efficiency double side	Azimuth (°)	196.3287	176.7190	356.8274
	Tilt (°)	62.2008	62.1838	62.3933
	Oversize (-)	2.6357	2.6305	2.6390
LCOH single side	Azimuth (°)	184.7602	184.3911	186.3103
	Tilt (°)	18.8621	18.6695	19.0356
	Oversize (-)	2.5777	2.5740	2.5907
LCOH double side	Azimuth (°)	253.5580	157.1478	335.5511
	Tilt (°)	0.0005	0.0000	0.0031
	Oversize (-)	2.8178	2.8148	2.8215
Wasted single side	Azimuth (°)	355.9400	355.6708	356.2193
	Tilt (°)	65.9232	65.5979	67.7439
	Oversize (-)	3.8381	3.8261	3.9005
Wasted double side	Azimuth (°)	95.0952	94.9564	95.4597
	Tilt (°)	74.6581	74.3982	75.1216
	Oversize (-)	2.7984	2.7948	2.8050

Table 6.3: Mean of medians of 1000 bootstrapped samples. "CI low" and "CI high" are the 95% confidence interval for the low and high limits, respectively.

Table 6.3 shows the mean of medians of the 1000 bootstrapped samples. The 95% confidence interval limits are a measure of uncertainty. There is a 95% probability that the true median is found within the confidence interval limits. Note that there are four significant digits to show that, in general, the confidence intervals are tight, indicating that the variables tend to converge to the same value, leading to a stable median. The azimuth has the highest uncertainty, especially in the double-sided efficiency and LCOH. This high uncertainty comes from the fact that for the double-sided efficiency, PSO found two opposite configurations, one pointing north and one south. Although this might seem contradictory, when analyzing the deviations, it is possible to see that the offset is almost 180° (same as the difference between the low and high confidence interval limits for this configuration), and only for a double-sided system, as defined in this work, north-facing and south-facing are equivalent. The other situation with very high uncertainty is the azimuth for the double-sided LCOH. The high dispersion of values can

be explained when looking at the *tilt* for this configuration. It can be stated with very high confidence, that the modules are horizontal, and, under this situation, the azimuth has no influence on the PV output. Omitting these two scenarios, the highest deviation for the azimuth is 1.92° and 2.15° for the tilt. With respect to this last variable, Figure 6.3 shows one value that did not converge to the median. With the uncertainty analysis, it is safe to label this point as an outlier, as it is beyond 1.5 times the interquartile range and has a negligible effect on the position of the sample median. The maximum deviation of the oversize factor is 0.0743. This means that the PV installation will have an uncertainty of ±17 commercial PV modules (450 W).

6.4.2. SENSITIVITY OF THE MODEL PARAMETERS

The modeling parameters influence the PV and hydrogen production calculation, leading to potential deviations of the results if these are chosen incorrectly. To determine the extent of these deviations, a sensitivity analysis was performed changing the site's albedo, the operating temperature, and the compression ratio. For the last two, the obtained configurations only change slightly, while for the albedo, has a more significant effect. Figure 6.7 shows the orientation for single (Figure 6.7a) and double (Figure 6.7b) sided orientations when changing the assumed albedo from 0.2 to 0.5 and 0.8. The results for the oversize are shown in Figures 6.7c (single-sided) and 6.7d (double-sided).

For single-sided systems, the albedo modifies the tilt of PV modules, which is expected, as they harvest more reflected irradiance. This has a consequence on the optimal configurations for LCOH which follows the same trend (more vertical installations), but is negligible for energy consumption and wasted energy. The opposite occurs with the oversize factor. The LCOH remains almost constant, while the oversize for efficiency (energy consumption) and wasted energy decreases dramatically. This can be attributed to the considerably high tilt of the PV modules. Under this situation, they receive more reflected irradiance, even when facing north.

For a double-sided system, the results remain almost the same. Note that, in Figure 6.7b, the efficiency results remain the same, even when there are opposite azimuths. Remember that the modules are back-to-back, making all efficiency results of figure 6.7b equivalent. For the LCOH, two of the three configurations are horizontal making the azimuth of the PV modules irrelevant.

An interesting observation is that with a large albedo (0.8) the configuration for the LCOH changes dramatically, from horizontal to a vertical East-West one with a slight increase in the plant size (Figure 6.7c).

The optimization procedure is also sensitive to the computation parameters, especially to the upper limit imposed on the oversize factor, as this forces PSO to find new configurations. A detailed description can be found in C.1.2.

Figure 6.8 shows the effect of assuming the wrong albedo value for the optimization. The reference orientation was calculated assuming an albedo for 0.2. Then the indicators (energy consumption, wasted energy and LCOH) were calculated using the optimal configuration but using a different albedo, which mean that these systems are suboptimal.

The LCOH of the double-sided system is the most resilient, followed by the single-sided LCOH, which has a positive impact (lower cost at higher albedo). The other indicators
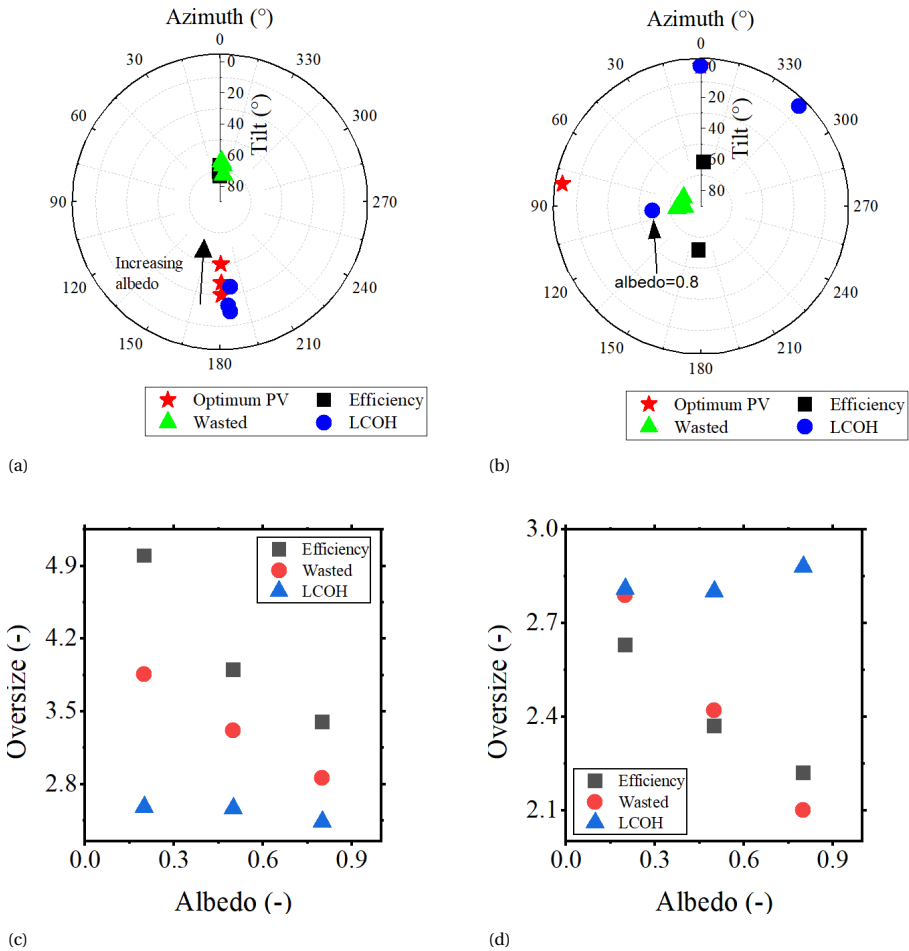
(a)

(b)

(c)

(d)

Figure 6.7: Sensitivity analysis of the albedo modeling parameter. The selected albedo values are 0.2, 0.5 and 0.8 (unitless). (a) PV module orientation of single-sided system. The arrow shows that the optimal tilt for PV production increases with albedo. (b) PV module orientation of a two-sided system. The arrow points a highly tilted east-west orientation. (c) Oversize factor of the single-sided system, and (d) oversize factor of the double-sided system.

are underestimated if the albedo used has a lower value than the real one.

6.4.3. INFLUENCE OF NON-IDEAL FARADAY EFFICIENCY

The system model assumed a Faraday efficiency of 1, which indicates that all the current is used for the generation of hydrogen. In reality, Faraday's efficiency depends on the applied current and the operating temperature [336]. A well-accepted model that describes the Faraday efficiency of an alkaline electrolyzer is Equation 6.27 [195].
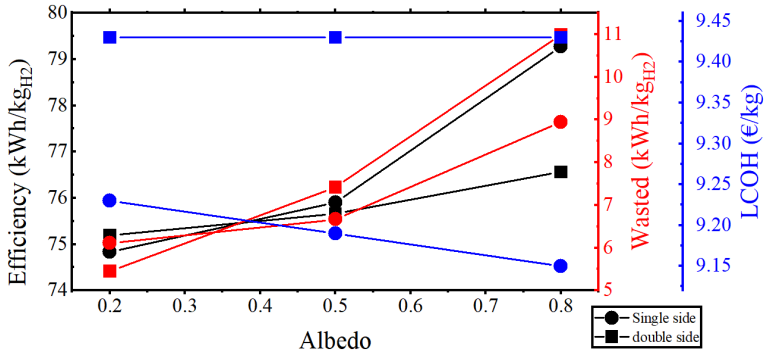
$$\eta_F = \frac{i^2}{f_1 + i^2} f_2 \tag{6.27}$$

Figure 6.8: Effect of the albedo on the indicators. The reference system is optimized for an albedo of 0.2. Then the albedo was changed to 0.5 and 0.8 and the indicators calculated with the optimal system configuration but with these new albedo values. The system was not re-optimized for these values.

Where the coefficients f_1 and f_2 are fitting parameters and are temperature dependent [195, 336].

Figure 6.9a shows that the Faraday efficiency is far from being constant and drops significantly at low electrolyzer powers. Figure 6.9b shows that, with the ideal approach, the production of hydrogen per second (the hydrogen flow, $\dot{H}_2$) is overestimated.

This overestimation has an influence on the power that the compressor needs, which is proportional to the hydrogen flow as discussed in Section 6.1.2, Equation 6.11. When comparing the calculated compressor power under ideal conditions, to the power that the compressor would have needed if the Faraday efficiency was included, assuming that the power of the electrolyzer is the same, the median of the differences in the compressor power is only 0.44 kW, with a maximum of 0.77 kW. These differences are considerably small to influence the presented results and validate the assumption for a negligible influence of Faraday efficiency. This is critical because it facilitates the analytic calculation of the functions used in the Newton-Raphson method (Equations 6.21 and 6.23).

An advantage of this methodology is that it is location-independent. The results presented in this work are based on data from The Netherlands. On locations with higher irradiance, the distribution of the GHI (Figure 6.6a) is expected to have higher relative frequency values on higher irradiance bins. As a consequence, it is possible that the maximum operating limits of the electrolyzer are reached, leading to more wasted energy as a result of more energy being curtailed. With the observations from this study, it can be hypothesized that the oversize factors will be larger for sites with higher irradiance, as the orientation results will probably result in north-facing PV modules (for northern-hemisphere sites) to minimize the specific energy use and specific wasted energy. On the contrary, lower oversize factors are expected to lead to lower LCOH values. This work considered ideal conditions for the PV system (flat ground, open space, uniform irradiance, constant albedo). Under realistic conditions, nearby obstacles change the irradiance seen by the module. The orientation results might change slightly for min-
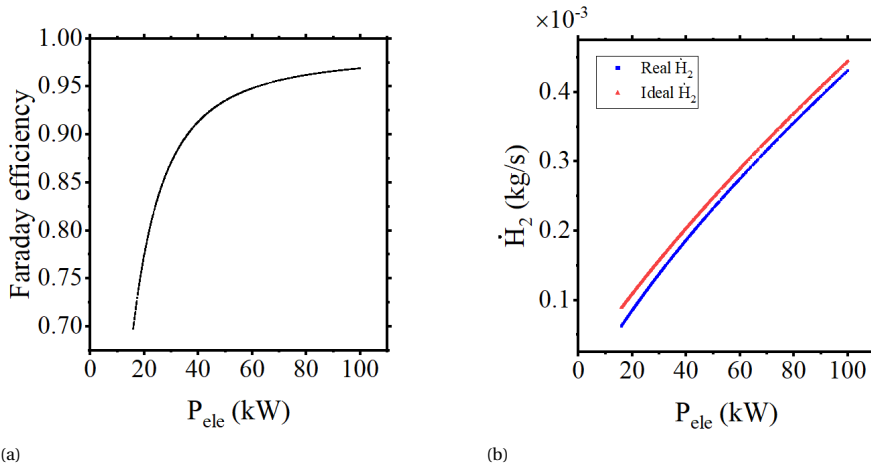
Figure 6.9: Influence of the Faraday efficiency on the hydrogen production. (a) Faraday efficiency with respect to the electrolyzer power, P_{ele}, and (b), a comparison of the ideal hydrogen flow ($\dot{H}_2$) as a function of the electrolyzer power, against the hydrogen flow when the Faraday efficiency is considered.

imizing the LCOH, depending on the horizon profile. However, for specific energy use and wasted energy, they should not change significantly because the orientations are not harvesting all the incoming sunlight (vertical configurations or north-facing configurations).

6.5. Conclusions

This work presented the optimization of a stand-alone PV-electrolyzer system. The system consists of an alkaline electrolyzer and a compressor and is coupled using a DC-DC converter, which forces the PV system to operate always at its MPP. The optimum configuration was defined by three decision variables, namely, azimuth and tilt of the PV modules and the oversize factor. The optimum configuration to minimize energy use, wasted energy, and hydrogen cost, was found using the Particle Swarm Optimization algorithm.

Horizontally-placed modules are an interesting option for improving the usage of the PV system with only a small increase in the hydrogen cost.

The electrolyzer is best utilized in configurations that reduce the LCOH, because it operates more time at full load in comparison with configurations that minimize energy use or wasted energy. These last ones, prioritize longer operating times at very low loads, rather than operation at nominal power.

Although an idealized situation with Faraday's efficiency being 100% was considered, an analysis of a realistic situation when this efficiency is not ideal shows a slight overestimation of hydrogen production. This is translated into an increased compressor power of less than 1 kW that can be considered negligible with respect to the power levels at hand in this work.

With the optimization procedure and analysis this work contributes to the needed ef-

forts for the implementation of green hydrogen systems towards meeting the goals of
the Net Zero Emissions scenarios of 2050.

6

7

OPERATING UNDER UNCERTAINTY. CONTROL OF PV-ELECTROLYZER SYSTEMS

The only thing that makes life possible is permanent, intolerable uncertainty; not knowing what comes next.

Ursula K. Le Guin

RENEWABLE energy has grown significantly in the last years and is expected to cover as much as 38% of the world's electricity mix by 2027 [78]. In particular, solar energy is the most rapidly expanding technology, exceeding the expectations by a 30% [78]. Solar energy is highly variable and, due to passing clouds, it can result in sudden and significant power changes of a PV plant. These changes, often called *ramps* can have consequences on the network to which the plant is connected. For grid-connected systems, these changes might negatively influence the grid voltage and frequency [337]. Furthermore, grid operators often impose limits on the allowed changes of power. For example, Germany and Puerto Rico establish a ramp rate limit of 10%/min [338]. A straightforward solution to power ramps of PV systems is to add electric storage, but this is not a fixed requirement to do power smoothing. This objective can also be fulfilled by curtailing the output PV power during a ramp event. For ramp-up events, this is straightforward, as the power can be curtailed to the current production level and slowly climb to the new maximum power point, thus avoiding a ramp violation. On the other hand, for a ramp-down event, the power will drop immediately if no storage is available. To prevent this,

the power must be slowly curtailed *before* the event [159]. Battery-less smoothing techniques also result in lower levelized costs of electricity, especially when the smoothing requirement is small because the investment costs of batteries exceed the cost of loss of energy due to curtailment. However, this is only true when the prediction of ramps is highly accurate [339]. In the stand-alone case, PV-electrolyzer systems for hydrogen production can be operated with or without batteries. The advantage of battery-assisted electrolysis is a constant operation despite the variations in irradiance, and the production during nighttime [340]. Also, in these systems, curtailment might be the cheapest option for off-grid operation of solar-hydrogen systems [265].

Since battery-less power smoothing relies on short-term forecasting (*nowcasting*), this tool becomes an essential ramp control [140, 159, 341, 342]. As an example, an algorithm of a power management system relies on nowcasting as a first step to perform power smoothing based on signal processing techniques [342]. For PV systems, a method using a sky image facilitates determining whether or not a cloud will (partially) block the sun. This information allows the estimation of the drop in PV power, which determines the active power curtailment needed to smooth the ramp [343]. Also, in this approach, the performance of the smoothing approach depends heavily on the quality of the prediction.

These systems require a high level of prediction accuracy to perform the control [159, 342] which is not achieved in practice. Nowcasting irradiance ramps is a challenging task and even systems with artificial intelligence fail to predict irradiance events in the very short term. While some authors have discussed that knowledge on the accuracy of predictions can improve the control strategies [341], how to include such knowledge is not mentioned. Some strategies to deal with the forecasting inaccuracy include using reinforced learning to adapt the power curtailment even with low-quality predictions [344]. This study tackles the problem of the inherent inaccuracy of ultra-short-term forecasting (nowcasting) when applied to a smoothing technique based on active power curtailment. Its novelty relies on combining the knowledge of the forecasting uncertainty with fuzzy logic to smooth the power from an off-grid PV system feeding an alkaline electrolyzer. An experimental setup validates the control strategy emulating the off-grid PV-electrolyzer system. Section 7.1 describes the models used (Sections 7.1.1 and 7.1.1), while the experimental setup is introduced in Section 7.1.2. The prediction module is presented in (Section 7.1.3) along with the fuzzy logic controller (Section 7.1.3). Section 7.2 reports the results and the discussion before the conclusion, presented in Section 7.3.

7.1. METHODOLOGY

This work proposes a battery-less, uncertainty-based power smoothing technique for a stand-alone PV-electrolyzer system. We validated the operation of our technique with a hardware setup that emulates the system. The emulation of this system requires three domains: a physical domain that emulates the PV system, the electronic converter that controls the PV system, and the electrolyzer, a modeling domain that describes the behavior of the physical domain so it closely represents a real system, and a control domain which supervises and controls the whole system. Figure 7.1 provides an overview of the system, and the corresponding domains. Each of these domains is explained in detail below.
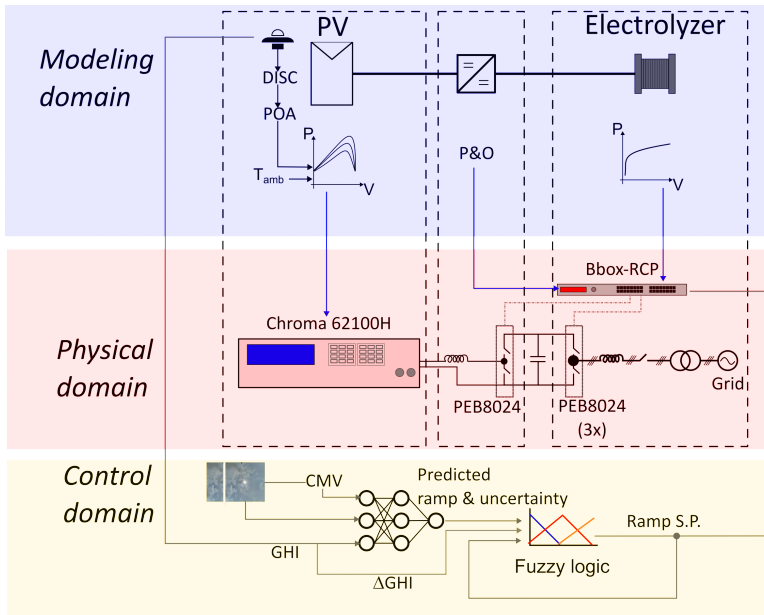
Figure 7.1: Overview of the implemented system. The physical domain consists of a DC power supply (Chroma 62100H), a boost converter, and a three-phase grid-tied inverter built from Imperix PEB8024 half-bridge modules. An FPGA board (Imperix Bbox RCP) controls the switches of the boost converter and of the three-phase inverter. On top of the physical domain, a modeling domain describes how the hardware reproduces the real system signals. The PV model consists of a set of current-voltage curves calculated from measured data using the DISC decomposition model, a transposition model to calculate the Plane-of-Array irradiance, and a two-diode model. The boost converter controlling the PV system performs a modified Perturb-and-Observe (P&O) Maximum Power Point Tracking (MPPT) algorithm. The inverter uses the Power-Voltage curve of the electrolyzer to set its input voltage according to the received power, following the electric behavior of the electrolyzer. The control domain sets the reference points that ultimately perform the power smoothing. It relies on an artificial intelligence module making one-minute ahead predictions of the ramps and the uncertainty associated with such prediction. Its output feeds a fuzzy logic model that outputs the ramp set point, which is sent back to the Bbox-RCP in the physical domain. CMV, GHI and S.P. stand for *Cloud Motion Vector, Global Horizontal Irradiance* and *set point*, respectively

7.1.1. MODELLING DOMAIN

PV MODEL

The emulated PV system consists of 6 PV modules connected in series, with a total peak power of 2700 W. The PV module used as a reference is a TRINA TALLMAX-M 450 [323]. The modules share the same tilt ($a_m = 19°$) and azimuth ($A_s = 185°$). The size and orientation of this system come from an optimization procedure for stand-alone PV hydrogen systems as described in [345]. The model of this system is a set of current-voltage (I-V) curves, one per simulation step, calculated from measured irradiance and ambient temperature. The monitoring station of the Photovoltaic Materials and Devices (PVMD) group of TU Delft (latitude 51.9997°, longitude 4.3689°) recorded the 1-minute Global Horizontal Irradiance (GHI) using a silicon pyranometer on 13-June-2021 (clear day) and 31-July-2021 (variable day).

The calculation of the module's I-V curve at a specific irradiance level requires the knowledge not of the horizontal irradiance, but the irradiance impinging on the PV module (Plane-Of-Array, POA, irradiance), and for this, the direct and diffuse components are needed.

The DISC decomposition model [346] allows the retrieval of the Direct Normal Irradiance (DNI) from the Global Horizontal Irradiance (GHI). The implementation of this model is readily available as a MATLAB function from PV LIB [347]. Equation 7.1 shows the calculation of the Diffuse Horizontal Irradiance (DHI) from the GHI and the sun's elevation angle, a_s [321].

$$\text{DHI} = \text{GHI} - \text{DNI} \cdot \sin(a_s) \tag{7.1}$$

These three quantities allow the calculation of the Plane-of-array irradiance G_{POA}. Equation 7.2 [321] shows the calculation of G_{POA}. Note that it includes the three irradiance components obtained before. The Greek letters ρ and γ correspond to the albedo (assumed constant, with a value of 0.2) and the angle between the sun and the PV module, (calculated by MATLAB PVLIB's function pv_getaoi), respectively.

$$G_{\text{POA}} = \text{DNI} \cdot \cos\gamma + \text{DHI} \cdot \text{SVF} + \rho \cdot \text{GHI} \cdot (1 - \text{SVF}) \tag{7.2}$$

The model assumes an isotropic sky. This assumption implies that the diffuse irradiance is the same across the sky dome and the portion of the sky that the module, tilted at an angle α_m, sees (sky view factor) is simplified as in Equation 7.3 [321].

$$\text{SVF} = \frac{1 + \cos a_m}{2} \tag{7.3}$$

Following the procedure in [348], the plane-or-array irradiance, combined with a two-diode model leads to the calculation of the module's I-V curve at each irradiance point.

ELECTROLYZER MODEL

The electrolyzer is simulated as a power-voltage curve of a fictitious 1280 W, alkaline electrolyzer. This power is 2.1 times smaller than the nominal power of the PV system, following the optimization procedure described in [345].

A current-voltage curve models the electrolyzer. When the current flows through the electrolyzer, its voltage increases as the electrons must overcome energy barriers for the chemical reaction that decomposes water into hydrogen and oxygen molecules. These barriers are the reversible voltage (minimum energy that the reaction needs, considered as 1.229 V) and overvoltages. We consider only the activation overvoltage (energy of the reaction at the electrodes) described by a modified version of the Tafel equation. Equation 7.4 gives the current-voltage characteristic of the electrolyzer [349].

$$I = I_0 \exp\left(\left(\frac{F}{RT}\right)(\frac{V}{n_{\text{cells}}}) + 1.229\right) \tag{7.4}$$

Its parameters are the universal gas constant $R = 8.314 \frac{J}{\text{mol}K}$, Faraday's constant ($F = 9.64 \times 10^4$ C, Temperature ($T = 333.15$ K), exchange current ($I_0 = 1.8 \times 10^{-7}$ A), and

the number of cells in the stack (n_{cells} = 244). This last one was adjusted so the electrolyzer voltage would lay between 300 and 400 V to avoid problems with the protections of the inverter (see Section 7.1.2 for an explanation of the setup). The power of the electrolyzer is the product of its current and voltage. Ten voltage levels were defined, ranging from 300 to 400 V, and at each point, the power was computed using Equation 7.4 multiplied by the corresponding voltage. The voltage of the electrolyzer, as a function of the input power, is derived from these points and implemented in a lookup table. Except for the physical constants, the parameters used in Equation 7.4 are fictitious.

The production of hydrogen ($\dot{h}_2$, mol/s) is proportional to the current, I, flowing through every cell of the electrolyzer (number of cells, n_{cells}) according to Faraday's law of electrolysis (Equation 7.5).

$$\dot{h}_2 = \eta_F \frac{I}{2F} n_{cells} \tag{7.5}$$

The Faraday efficiency, η_F, describes losses caused by the current not flowing through the electrodes (parasitic currents). This phenomenon increases at low current density, i, as described by Equation 7.6 [195].

$$\eta_F = \frac{i^2}{f_1 + i^2} f_2 \tag{7.6}$$

where the fitting parameters are $f_1 = 2 \times 10^4$ A^2/m^4 and $f_2 = 0.985$ (dimensionless) [195].

7.1.2. PHYSICAL DOMAIN (EXPERIMENTAL SETUP)

The experimental setup consists of two main parts. A solar I-V curve emulator and a power electronics module which concurrently performs the MPPT and emulates the electrolyzer's P-V curve. The solar emulator is a Chroma 62100H - 600S DC-power source. Its software allows the reproduction of a PV system I-V curve which can be programmed to change in time [350]. The interface between the electrolyzer and the PV system (output of DC power supply) is a boost converter, responsible for controlling the PV system's output either by performing maximum power point tracking (MPPT) or setting a specific power set point. This converter is connected to a three-phase inverter. Both converters are implemented using Imperix PEB8024 (half-bridge) power modules and power filters [351, 352]. The Imperix Bbox-RCP unit controls the power modules [353]. The control of all the converters can be easily developed using MATLAB Simulink and sent to the Bbox-RCP.

The Perturb & Observe (P&O) maximum power point tracking algorithm extracts the maximum power from the PV system. The modification proposed in [354] allows a deliberate operation of the PV system at a different power point rather than the maximum (i.e. curtailment) with only a small change in the original P&O algorithm. This algorithm drives a boost converter (interface between the PV system and electrolyzer) and is implemented in the Bbox-RCP unit. Varying the voltage of the DC-link between the boost converter and the inverter according to the P-V curve of the electrolyzer allows the emulation of this component. The P-V curve of the electrolyzer is also implemented as a lookup table in the Bbox-RCP unit. Note that although the inverter is connected to the

grid, the system is not a grid-connected system. This connection is there to dissipate the generated power, that in a real system will be consumed by the electrolyzer. **The emulated system is a stand-alone (off-grid) system.**

7.1.3. Control domain

Irradiance prediction module

The irradiance prediction module predicts one-minute-ahead ramps of the global horizontal irradiance (GHI). In this work, a ramp is defined as the percentage of change with respect to the last measured GHI value. Rather than a single value, the model outputs the probability that a certain set of inputs belongs to a ramp class. By doing this, it is possible to retrieve information not only on the most probable ramp that will occur but also a measure of uncertainty of the prediction.

The model is based on neural networks whose input are, a single low-resolution (64 × 64 pixels) sky image centered around the sun, last measured GHI, and cloud motion vector. The sky images were taken using an all-sky imager (CMS-Shreder ASI-16 [355]) equipped with a fisheye lens located at the above-mentioned PVMD group monitoring station. The sky images are taken every minute, along with the global horizontal irradiance (GHI), measured with a silicon pyranometer provided with the sky imager. The high-resolution images are first corrected to remove the fish eye distortion, cropped around the sun (200 × 200 pixels), and then resized to a resolution of 64 × 64 pixels. Using optical flow from two consecutive images it is possible to calculate the cloud motion vector which returns the direction and speed of the main cloud layer and is expressed in cartesian coordinates whose origin is the center of the sky image, which is also the center of the sun.

The Farneback optical flow [153] is an image-processing method that determines the vectors indicating how the pixels of two consecutive images are moving. This preprocessing step returns all the vectors of the pixels moving between two sky images. Since most of the pixels remain static, a histogram of the directions of the vectors will exhibit a bimodal distribution with one mode close to zero and the second indicating the main cloud direction. The mean magnitude of the vectors in this direction is the main cloud speed [356]. In practice, the cloud motion vector is obtained by running a clustering algorithm (k-means) with two clusters of magnitudes and directions obtained from the optical flow. All values smaller than one standard deviation of each vector component are excluded from the clustering (still pixels). The largest of the two cluster centroids obtained through k-means is the cloud motion vector (in pixels per minute) [356].

The neural network comprises two stages: one responsible for the processing of the sky image, and the second which combines the image analysis output with the auxiliary data (GHI, X and Y components of the cloud motion vector). Figure 7.2 shows the architecture of the neural networks. The network responsible for processing the sky image is a ResNet50 implemented in the Keras library [357]. The auxiliary data network is a fully connected network of 3 layers with 64, 32, and 1 neurons, respectively. The first two layers use the Rectified Linear Unit (ReLU) activation function, and the output layer uses a softmax activation function. The training loss is the sparse categorical loss entropy. Note that this is a *classification* problem rather than a *regression* one. As such, the softmax function of the last layer returns the probability that a particular set of inputs belongs to one of the labeled classes. The labeled classes are 20 ramp bins with equal
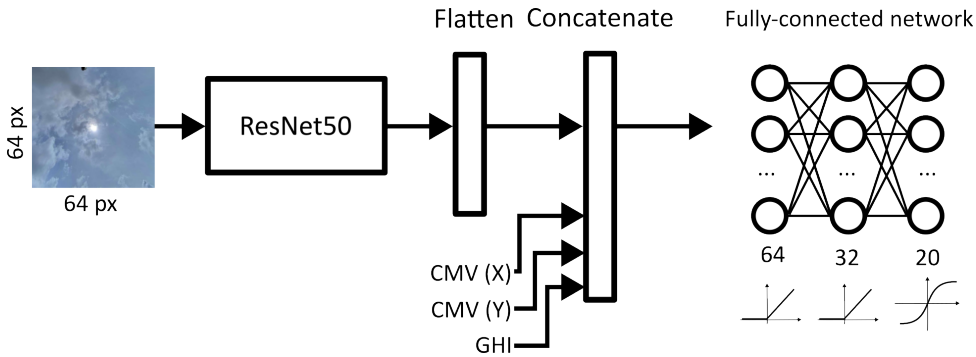
Figure 7.2: Architecture of the prediction module. The acronym "CMV" refers to the cloud motion vector; each component of this vector, X and Y, is a separate input to the model. GHI is the Global Horizontal Irradiance. The fully-connected network has two hidden layers with 64 and 32 neurons with a Rectified Linear Unit (ReLU) as activation function. The output layer consists of 20 neurons (one per bin) with the softmax activation function.

frequency in each bin, which means that the width of the bins is different, but the number of elements is approximately the same. The labels are coded as integers from 1 to 20. The class with the highest probability is the predicted class. Since each class label is linked to a bin, the actual predicted ramp is the center of the bin corresponding to that particular class. A cumulative sum of the probabilities of all the classes allows the determination of the 5th and 95th percentiles; their difference is a measure of uncertainty. These two outputs, the predicted ramp (the bin center of the most probable class) and the uncertainty (the difference between the 5th and 95th percentiles of the cumulative sum of the probabilities of all classes), are inputs to the fuzzy logic control. The training set consists of 27,723 samples and the validation set of 7,431 samples.

FUZZY LOGIC CONTROLLER

Fuzzy logic offers a solution to complex systems by describing them as linguistic variables rather than complicated equations. The relations between the inputs and outputs (already described by linguistic variables) are written using a set of if/then rules. This makes handling the uncertainties and imprecision of the model an easy task. Fuzzy logic as opposed to traditional set theory, relies on the fact that an element can simultaneously (and partially) be a member of more than one set. In other words, its degree of membership to a set is not a binary (yes/no) function, but a continuous one. And this is mapped by a membership function. Membership functions are useful in the *fuzzyfication* step, where a *crisp* variable value is transformed into a *fuzzy* variable. The linguistic variables are also linked to the membership functions in the sense, that a variable "slow" can be described by a particular membership function. The if/then rules describe the relation between the system variables and constitute the implication step of a fuzzy system (e.g. if TEMPERATURE is COLD then SPEED is FAST). These are translated as minimum and maximum operators (equivalent to the intersection and union of the traditional set theory) [358].

Our model used the *Mandami min* implication rule, which is the minimum value of both input and output membership functions. This rule typically results in clipping

the output membership function at the value of the input membership function, evaluated at the crisp input. Converting the fuzzy output back to a crisp number is done by calculating the centroid of the clipped output membership function [358].

The fuzzy control model takes four inputs, every minute: the predicted ramp (from the Prediction Module), the uncertainty of the prediction (from the Prediction module), the last observed change in the Global Horizontal Irradiance (ΔGHI), and the previous slope applied. The output is the slope (given as a percentage of change with respect to the nominal power). This slope defines the power set point sent to the system, every second. Using ΔGHI instead of the Plane-of-array irradiance (G_{POA}) allows a generalization of our approach (ΔGHI is not system dependent as G_{POA}.

Table 7.1 shows the system variables and their corresponding fuzzy descriptors and Figure 7.3a shows the membership functions for all the inputs (Figures 7.3a, 7.3b, 7.3c, and 7.3d) and the output (Figure 7.3e). A description of the fuzzy rules can be found in Appendix D.

Variable name	Linguistic descriptor
Inputs	
ΔGHI	Negative large, Shallow, Positive high
Predicted ramp	Deep down, Shallow, Deep up
Previous slope	Negative big, Zero, Positive big
Uncertainty	Low, High
Output	
Slope	Negative large, Zero, Positive large

Table 7.1: Fuzzy controller variables and their linguistic descriptors

7.2. Results

We used two scenarios to test our control strategy. Figure 7.4 shows the GHI of both scenarios along with the portion of the day considered for the experiments. The first scenario corresponds to a clear day (13-June-2021, Figure 7.4a). The second scenario is a day with high irradiance variability (31-July-2021, Figure 7.4b). The reader must be aware that the results are presented in two time resolutions: the instantaneous, which is 1 s resolution and is the time resolution at which the controller acts. In other words, it sends a power set point every second (see Section 7.1.3). The irradiance and prediction data have a lower time resolution, namely one minute. The downsampling of the 1-second data to 1-minute resolution takes place using the median every 60 s. The median is less sensitive to extreme values, present within the variable scenario, and the mode can either be non-existent or have multiple values, especially with a small sample (60 points). Hence we consider that the median can represent better the 1-minute value.

7.2.1. Ramp prediction

The prediction model has a training accuracy of 19.51% and a validation accuracy of 17.29%. Note that the training dataset is relatively small, which can be one of the causes of the low accuracy. Many of the samples also correspond to images with the sun blocked.
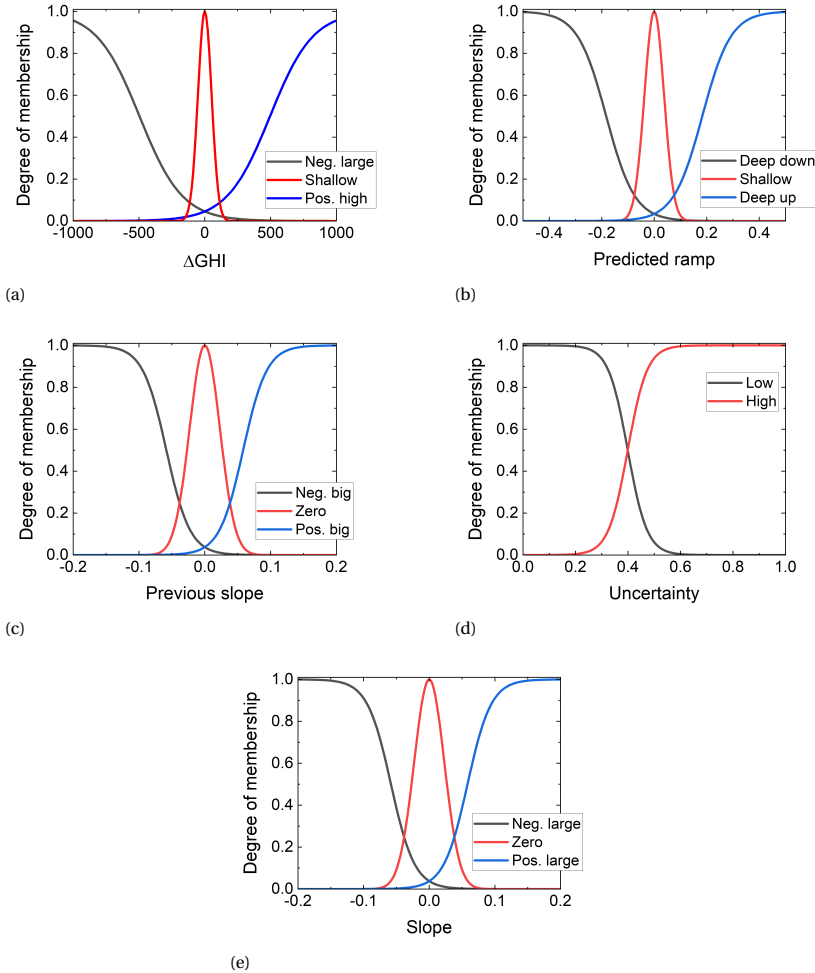
Figure 7.3: Membership functions of the fuzzy logic controller of (a) the irradiance changes, ΔGHI, (b) the predicted ramp, (c) the previous slope. (c) The uncertainty. Note that everything above 0.5 is classified as "high" and everything below 0.3 as "low" uncertainty. The region between these numbers is fuzzy (can be "high" *and* "low". (d) The output slope.

Identifying the sun automatically is almost straightforward, through identifying the brightest pixels on the image [359]. However, when the sun is covered, its location on the image needs to be estimated based on the sun's position in the sky. Although the estimation accurately identifies the sun's position, when the image is cropped around the sun, the estimation error causes the sun not to be centered in the cropped image. The mismatch error on cloudy images is larger because the image is first corrected, and the sun is identified afterward. This can have negative consequences downstream, because the cloud motion vector is estimated from two consecutive *cropped* images, and it assumes that
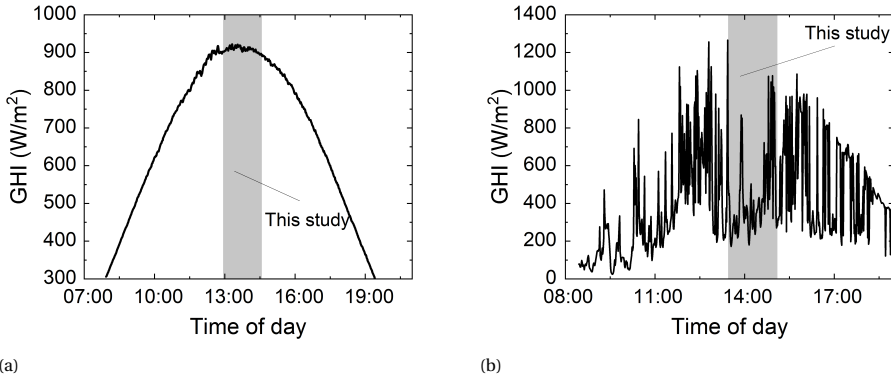
Figure 7.4: Global Horizontal Irradiance of the two used scenarios. (a) a clear day, and (b) a variable day. In both graphs, the shaded area marked as "This study" shows the period used for the experiments.

the sun is in the middle of the image.

The calculation of the cloud motion vector might also be responsible for the low prediction accuracy. It is calculated from the optical flow results followed by a k-means clustering algorithm (see Section 7.1.3). The optical flow returns the apparent movement of *pixels* between two consecutive images. The main assumption is that the difference between the two consecutive images, especially taken one minute apart, is the movement of clouds. Although we applied a smoothing filter on the image to remove noise, the movement of pixels might not entirely correspond to clouds. Changes in the tone of the sky, clouds, objects moving on the scene, and glare, among others, might be identified as moving pixels and can affect the estimation of the cloud motion vector.

Figure 7.5 shows an example of the prediction for the interval used for the clear and variable scenarios shown in Figure 7.4. For the clear scenario (Figure 7.5a), the output is basically a constant that is lower than the measured ramps. Many measured points fall into the uncertainty range, as desired. For the variable case (Figure 7.5b), the discrepancy between the measured and the predicted ramps and the uncertainty is higher. Note that, in Figure 7.5b, the predicted ramp and uncertainty seem to saturate at ±0.4%. This behavior and the constant output of Figure 7.5a might be attributed to the binning method used for training the data (see Section 7.1.3). Each ramp bin has a different width and assigned a number to identify it. Hence the calues that the classifier learns are integers (bin numbers) and not actual ramp values. To retrieve the actual ramp we used the value at the center of each bin as a representative value of the whole bin. The extreme values of this approach are precisely ±0.4%.

Figure 7.6 shows the measured against the predicted ramps for the clear (Figure 7.6a) and the variable (Figure 7.6b) scenarios. Note that the predicted ramps are located only at particular intervals (bin centers) that span over a wide range of measured ramps. Increasing the number of bins can reduce the scattering within each bin and lead to a more accurate prediction.

The prediction result do not need to be accurate because the fuzzy logic will convert
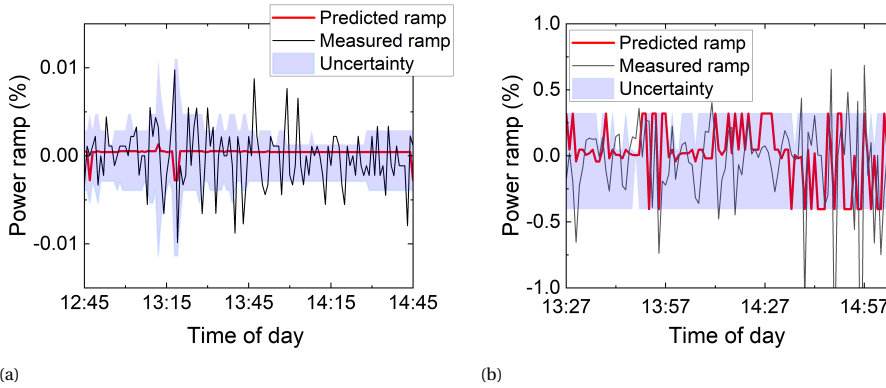
(a)   (b)

Figure 7.5: Example of ramp prediction of (a) the clear scenario and (b) the variable scenario.

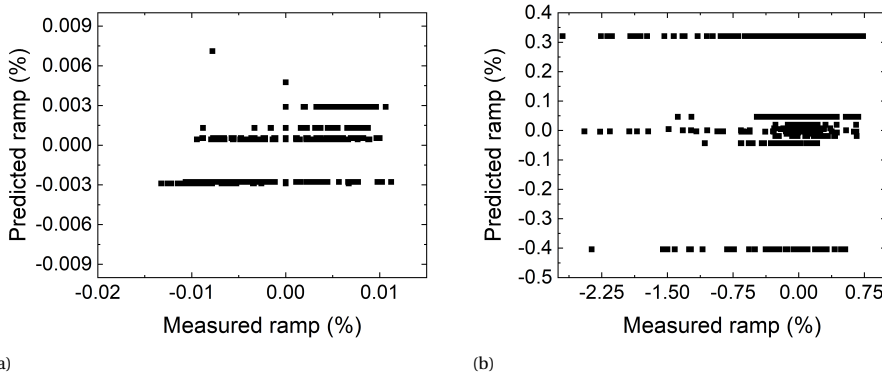(a)   (b)

Figure 7.6: Measured and predicted ramps of (a) the clear scenario and (b) the variable scenario.

these values into a language descriptor (e.g. LOW, LARGE, see Table 7.1) making it able to deal with the imprecision and uncertainty, which is the main goal of this work.

7.2.2. RAMP CONTROL

Figure 7.7 shows the results of applying our proposed approach to the clear scenario. Under clear conditions (Figure 7.7a), our approach always operates in a curtailment condition after the initial system startup. It is worth mentioning, that an initial power drop of 30% was deliberately introduced to avoid problems with the curtailment set point. After this sudden power decrease, the system stabilizes and increases monotonically. For a clear scenario, the ramps are always within the required limits (Figure 7.7b).

Figure 7.8 shows the results for the variable scenario. Similar to the clear scenario, the controller curtails the power most of the time, and under shallow ramps, the controller even keeps the power at a constant level (Figure 7.8a). This results in an evident ramp smoothing, reducing ramp violations (Figure 7.8b) and proving that our approach
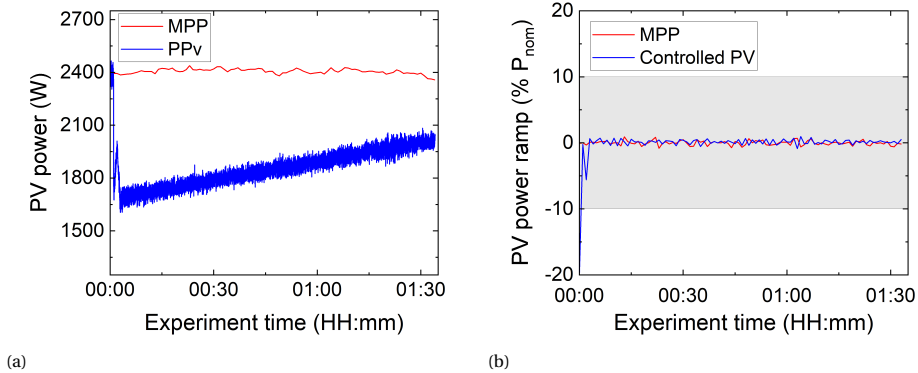
Figure 7.7: Results of the clear scenario with 1 s resolution. (a) Instantaneous PV power (PPv), and (b) one-minute PV power ramps, given as a percentage of the nominal PV power, (P_{nom}. The 10% ramp limit is marked as a red band. Points outside these bands are considered ramp violations.
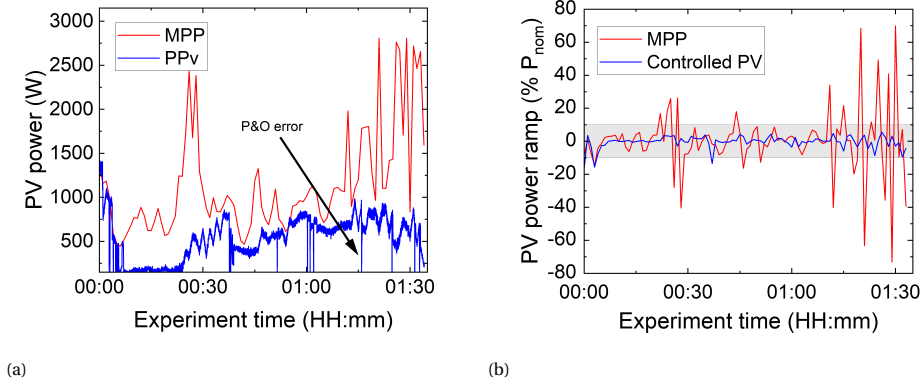

Figure 7.8: Results of the variable scenario with 1 s resolution. (a) Instantaneous PV power. Note the sudden power drops to zero as a result of a failure of the P&O algorithm. An example of these peaks is marked with an arrow ("P&O error"). (b) One-minute PV power ramps, given as a percentage of the nominal PV power, (P_{nom}. The 10% ramp limit is marked as a red band. Points outside these bands are considered ramp violations.

is able to meet the objective.

Figure 7.8a also shows that the P&O algorithm fails under variable conditions. This occurs because the controller sends a power set point higher than the actual MPP. Note that the P&O implemented in this work is a modified version of the traditional P&O. This version tracks MPP in the absence of a power set point. Otherwise, it uses the same P&O logic to track a curtailment set point [354]. If the power set point is larger than the actual MPP, the algorithm will keep reducing the voltage until it reaches the short-circuit condition, attempting to find a point outside the power-voltage curve of the PV module. The sampling time of the P&O algorithm is 5 ms, which explains the sudden drops in the power of Figure 7.8a. A watchdog timer monitors the PV power to detect and correct this
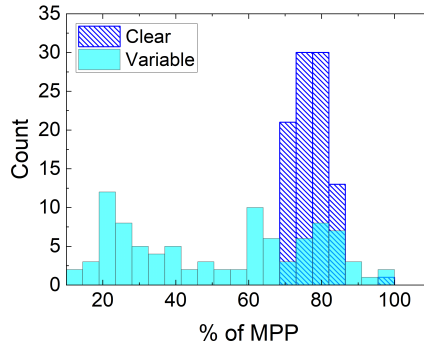
Figure 7.9: Distribution of the operating point of both scenarios. The operating point is given as a percentage of the theoretical maximum power point with 1-minute resolution.

condition. When this timer detects a faulty condition, it removes the power set point, restoring the normal operation of the algorithm. The failure of the P&O is only visible in the 1 s resolution data. It does not affect the power smoothing results. Note that the aggregation method for the downsampling to 1 minute is the median.

Figure 7.9 compares the operating point (as a percentage of the maximum power point) of the 1-minute resolution data of the clear and variable scenarios. While in the clear moments most of the points are centered around 80% of the theoretical MPP, in the variable scenario, the operating points are more distributed and can even get lower than 20% of the theoretical maximum. This stricter control, needed to smooth 1-minute ramps, leads to an energy loss of 53.1% with respect to the theoretical maximum power point. Section 7.2.3 provides an in-depth discussion on how to improve this aspect.

Applying control to a clear day results in unnecessary power curtailment that can go as low as 70% of the theoretical maximum power point (Figure 7.9). The system generates 3.77 kWh during the 100 minutes at its theoretical maximum power point and 2.91 kWh under controlled power. This represents a loss of 22.8% of the potential generated energy. Because of this, for a clear moment, no control action is needed. An ideal controller should be able to (a) avoid any control action in clear conditions or (b) ensure a minimum curtailment. In this sense, the traditional P&O MPP algorithm is more than suitable. Identifying clear moments before they occur is fundamental to applying the traditional P&O during these moments instead of unnecessarily curtailing energy. Our approach is based on one-minute ahead prediction to smooth instantaneous ramps. With a single-prediction value it is impossible to identify clear moments. Using historical data could give an indication of the present conditions. The probability that the sky conditions remain the same in a very short period is very high, so a simple persistence model could be already an improvement for clear moments. A larger forecasting horizon has the drawback that as the prediction horizon increases, so does the prediction uncertainty. This could result in more ramp violations in exchange for higher energy production because it is possible that the controller misapplies the traditional P&O instead of curtailment in a variable situation.
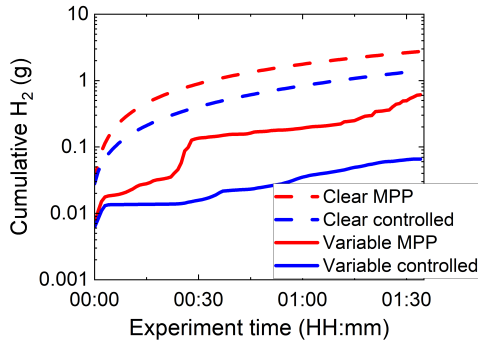
Figure 7.10: Theoretical 1-minute hydrogen generation of the clear and variable scenarios with and without control. Note that the vertical axis has a logarithmic scale. Although the typical unit used for hydrogen is kg, because hydrogen is very light and its production is low, for clarity's sake, the hydrogen generation is expressed in grams (g).

Figure 7.10 shows the effect of our strategy on hydrogen generation. In line with Figure 7.7 and 7.9, the effect of the control strategy on the clear scenario is only a generation reduction, without affecting the generation rate, which remains constant (the hydrogen generation increases linearly with time. Note that the vertical axis is logarithmic). This also occurs with the controlled power of the variable scenario, with the lowest generation. The uncontrolled variable scenario has steep changes. While the electrolyzer can handle these changes in power, other components in the system might have problems with the sudden increase in generation, as they respond slower [340]. Even though this study does not consider the electrolyzer temperature, this variable might determine the hydrogen production efficiency. With steep up ramps, the efficiency might be lower because a higher temperature results in higher efficiency, but the temperature cannot follow the ramps as fast as the changes in the electric set points. Then, the electrolyzer would operate at a higher power with a lower temperature, reducing efficiency.

7.2.3. Limitations of this study and future improvements

Our study assumes that the irradiance remains constant during each minute, changing only at the top of the minute. In reality, irradiance is not discrete. The measurement system takes images every minute, which justifies the time resolution. Additionally, the hardware emulator is limited to 100 I-V curves per simulation block, making time downsampling impractical as only a few minutes could be simulated rather than a full hour. The prediction module and the fuzzy logic controllers can still be optimized. The study aims to prove the concept rather than provide a fully optimized system.

Although the prediction module has a low classification accuracy, the system was designed to deal with imperfect predictions, turning the disadvantage of its low accuracy into a tool for analyzing our solution. Naturally, the prediction module can be improved by increasing the number of training points (nearly 28,000 in this study), the number of classification bins and hyperparameter tuning. The dataset consists of many training examples with the sun covered, which might affect the low accuracy of the algorithm. A

more balanced dataset can also boost the prediction accuracy.

The approach in this work used empirically determined rules based on the observations of the system. Adding more rules can improve the system's performance, but manual tuning might be cumbersome. Switching to a neuro-fuzzy approach where the shape and position of the membership functions and the inference rules can be determined from training data [358], can facilitate the process and improve the system's performance.

The simulation of the electrolyzer assumes a constant operating temperature, which is only true if there is an external control system. This assumption simplifies the system considerably. In reality, without thermal control, the temperature of the electrolyzer depends on the current flowing through the electrolyzer. At the same time, the current force the applied voltage to change because the current-voltage characteristic of the electrolyzer also depends heavily on temperature.

7.3. CONCLUSION

We presented a control strategy for a battery-less stand-alone PV-electrolyzer system to smooth power ramps from the PV system without the need for electrical storage using active power curtailment. This approach typically needs ultra-short-term forecasting to determine the curtailment level. Our control system acknowledges that the prediction is imperfect and incorporates information on the uncertainty to deal with inaccurate predictions using fuzzy logic.

We validated our control strategy with a hardware emulator and prediction from measured data. Using this approach, although it compromises 53% of the potential energy generation, is possible to smooth PV power ramps to a limit of 10% of the PV plant capacity on very high variable moments, and with very imprecise predictions without any storage nor power interruption to the electrolyzer.

7

8

CONCLUSION AND OUTLOOK

8.1. CONCLUSIONS

This work presented the integration of PV systems and electrolyzers for hydrogen production, focusing on stand-alone operation without the backup of electric storage. Part I focused on PV systems covering the design phase (Chapter 2) and operating challenges (Chapters 3 and 4).

In particular Chapter 2 proposes a methodology to identify potential sites for new land-based PV projects. It aims at reducing the land degradation caused by the (potential) new PV projects. During the design (prospection) phase of a new project, the most suitable sites, from an environmental perspective are those where land is highly degraded, identified with the Compatibility Index. This metric can, using the Analytic Hierarchy Process (AHP), be combined with economic and technical factors to determine the suitability of a site. The approach in Chapter 2 puts a strong weight on the Compatibility Index, which means that the environmental aspects dominate the decision of the suitability of a site. The main advantage of using the Compatibility Index in the AHP is that it is independent of whether a specific site is inside, or in the proximity of a nature-protected exclusion area. This leads to a better evaluation of non-protected areas that can still be nature-valuable but not identified as such.

Chapter 3 studies the loss of efficiency of one of the most popular maximum power point tracking algorithms used in the PV industry: the *Perturb&Observe*. This algorithm can work incorrectly with quick variations in irradiance, even under uniform irradiance (i.e. no partial shading), moving the operating point of the PV module away from its maximum power point. This results in momentary power loss (hence efficiency loss). This worsens with improper selection of perturbation step size and sampling time, the tuning parameters of the traditional P&O algorithm. Larger and slower perturbations lead to increased power loss, reaching up to 2% efficiency loss. The efficiency loss of the P&O is independent on the control hardware which will introduce additional power losses.

Chapter 4 presents a method for predicting the clear-sky index on the very short term (20 minutes ahead) using sky images and a convolutional neural network and a sky clas-

sifier. The proposed model consists of five convolutional neural networks trained on a particular set of sky conditions (clear, overcast, partially cloudy, mostly clear with the sun covered and mostly cloudy with the sun visible). Although a universal model is more accurate on all classes, except on clear skies, the classified approach is more precise and has the advantage of requiring less training data. Moreover, a classified approach opens the possibility for combining different models that predict best for each class, for instance, using a specialized network for clear-skies, and a smart persistence for overcast days. The convolutional neural network does not need to be extremely complex to produce accurate results. In fact, a single convolutional layer and a fully-connected network are sufficient to make the predictions. Interestingly, adding information of the movement of pixels using optical flow does not yield improvement on the prediction. One potential reason is that the optical flow detects differences in pixels for two consecutive images. These pixels do not necessary corresponds to clouds. The optical flow also detects changes in hue, shadings, and objects (such as passing birds) as changes between two images. This extra information might only introduce noise in the prediction.

Part II of this thesis focuses on the integration of PV with water electrolyzers. Chapter 5 focuses on the variable operation of water electrolyzers powered by solar energy. All low-temperature electrolyzer technologies, namely alkaline, Proton and Anion Exchange Membranes have a good dynamic response and are well suited for variable operation. The bottlenecks are at the supporting equipment (balance-of-plant) which also deals with slowly-changing variables such as temperature and pressure. Electrically, the electrolyzer has minimum operating limits due to safety, which need to be considered when operating in a non-constant regime, for example, when directly powered by renewable energy sources. The discussion over the accelerated aging of the electrolyzers caused by dynamic operation is still ongoing in the literature.

Of the three coupling methods, stand-alone systems are best suited for small projects such as refuelling stations, while projects in the MW range benefit from grid-connected systems. Battery-assisted electrolysis have higher costs. An economically successful PV-hydrogen project needs to have a solar-to-hydrogen efficiency greater than 10%.

In Chapter 6 the sizing of a PV-electrolyzer-hydrogen compressor system was introduced. The optimization procedure, based on Particle Swarm Optimization, minimizes separately three indicators, namely, energy use, wasted energy and, hydrogen cost. The decision variables for all the indicators are the same: orientation of the PV modules and an oversize factor. The system converts more sunlight to hydrogen with horizontally-placed modules. Although it is not the cheapest option, it results in just a small increase in hydrogen cost. Optimizing for the energy use or wasted energy, results in the electrolyzer not being fully used, which means that the electrolyzer operates more time at a setting lower than its nominal power. In contrast, an electrolyzer functioning at rated power for longer periods leads to minimum hydrogen cost.

Chapter 7 combines the content of the previous chapters to propose a control strategy for a stand-alone PV-electrolyzer system aiming at reducing the abrupt changes in the PV power caused by passing clouds. The novelty of this approach is that it utilizes the fact that the prediction f these ramps, crucial for the control strategy, is imperfect. The prediction uncertainty can be calculated using a probabilistic prediction. A natural way to deal with this uncertainty is through fuzzy logic. The elimination of the electric

storage is achieved by timely curtailing the PV power, using a modified P&O maximum power point tracking algorithm. Although the proposed approach results in very high losses close to 53%, it is able to limit the PV power ramps to a maximum change of 10% of the PV plant's peak power on variable days. Under a cloudless sky, there is no need for curtailment and the PV plant can operate at its maximum power point.

8.2. Outlook

This thesis presents recent advances in powering low-temperature water electrolyzers with solar energy. Based on the results presented in the previous chapters, the following recommendations are put forward.

- Nature's Contributions to People (NCP) can be used as a metric for environmental impact. The NCP have been globally mapped [360] which indicate that it is possible to quantify them. The advantage over the Compatibility Index is the availability of Open Source data [360], and, most importantly, NCP also identifies regions where damage to Nature impacts people. The methodology proposed in this work was tailored specifically for PV systems, but it can be easily applied to other projects, even non-energy related. The weights applied to Analytic Hierarchy Process can be modified depending on the stakeholders' interests, yet the whole process remains the same leading to results that are more suitable for the stakeholders' interests. This, however, needs to be considered carefully to avoid a misuse of information. For example, a developer that assigns a negligible weight to the Compatibility Index and claims that the environmental impact was considered since the design phase.

- Incorporating conservation information into the design phase of a project, could reduce the mitigation actions needed in more advanced stages. This could bring benefits not only in economic terms but also potentially facilitating some aspects of social acceptance of the project.

- The optimization of PV-hydrogen systems should consider a proper optimization objective. This objective, which is typically cost of hydrogen produced, can be selected to minimize also the environmental impact of the installation, in terms of land use change, materials or land degradation. Efficiency cannot be regarded as such indicator, because, as seen in Chapter 4, a system that uses the energy most efficiently, is a very large system, with, potentially, the largest land footprint. Multi-objective optimization can harmonize the conflicts between different objectives with the problem that the output of such method is a *set* of optimal solutions and the selection of the most suitable one, depends on a decision-maker.

- Many control approaches rely on perfect predictions, and very few works tackle the operation under uncertainty. Given the difficulty of getting accurate irradiance predictions, a probabilistic approach gives the decision-maker extra information over the uncertainty of the prediction than point predictions. In this respect, the development of decision tools suited for uncertain conditions might even be more important than improving the forecast accuracy.

8

The results presented here can help with the reduction of greenhouse emissions and aimed to bring attention in the responsibility of engineers and scientists to develop projects that consider their effect on Nature since the design phase. Changing people's point of view regarding their relation with Nature begins with its re-valuation [361], considering that humans are part of the ecosystem, and not owner of it [362, 363] and that all inhabitants of the Earth have an intrinsic value, whether or not they are usable or economically valuable to humans. [362–364]. This change in point of view will lead to a moral obligation to Nature, resulting in concrete rules and actions [361]. These actions, along with a responsible application of technology, could finally slow climate change ensuring a livable 2050, and beyond.

8

A

PARAMETERS OF THE BINNED EFFICIENCY MODEL

Table A.1 shows the fitting parameters of Equation (3.7) for different variability metrics for the Oahu dataset and 3-second data. Note that the offset term, p_3, is always close to 99.9 because the expected algorithm efficiency lies within this range.

Table A.1: Parameters of the binned efficiency model.

Metric	p_1	p_2	p_3	R^2
$\sigma(\Delta G)$	-1.22×10^{-5}	-8.03×10^{-4}	99.97	0.99
$\sigma(\Delta k_t)$	-28.90	0.61	99.95	0.99
$\sigma(\Delta k_c)$	$-19.63.94$	0.33	99.97	0.97
$\sigma(r)$	-2.50×10^{-4}	2.15×10^{-3}	99.92	0.90
$\max(r)$	0	-2.94×10^{-3}	1.00	0.92
VI	0	-2.98×10^{-4}	99.9	0.92

B

CLOUD DETECTION AND DATA DISTRIBUTION FOR IRRADIANCE FORECASTING

B.1. EXAMPLES OF CLOUD DETECTION

This section shows examples of the cloud identification of each class. The examples were taken randomly from the training dataset. In all cases, the images on the left correspond to the image under evaluation. On the right is the cloud identification output. The cloud pixels are highlighted with clear areas. Figures B.1, B.2, B.3, B.4, and B.5 show the examples per class.

B.2. DATASET DISTRIBUTION

Figure B.6 shows the distribution of the dataset in terms of the sun's elevation. As a remainder, the minimum sun elevation that we considered is 10°.
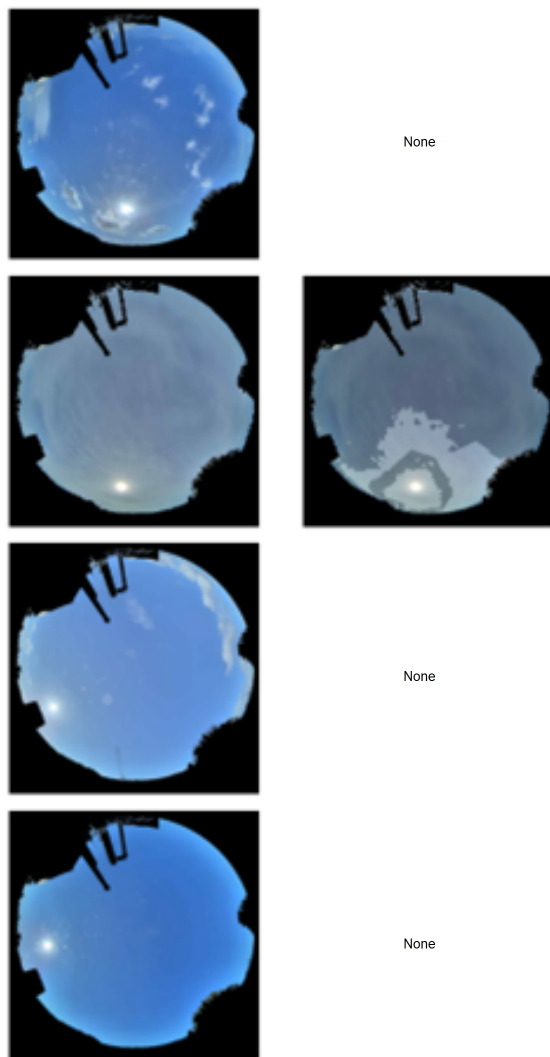
None

None

None

Figure B.1: Random examples of Class 1 cloud identification. The images on the left column are the original images. On the right, the clearer areas identify "Cloud" pixels while the darker are "Not cloud" pixels. The label "None" indicates that there are no clouds identified in that image. Note that the horizon has a mask of black pixels.
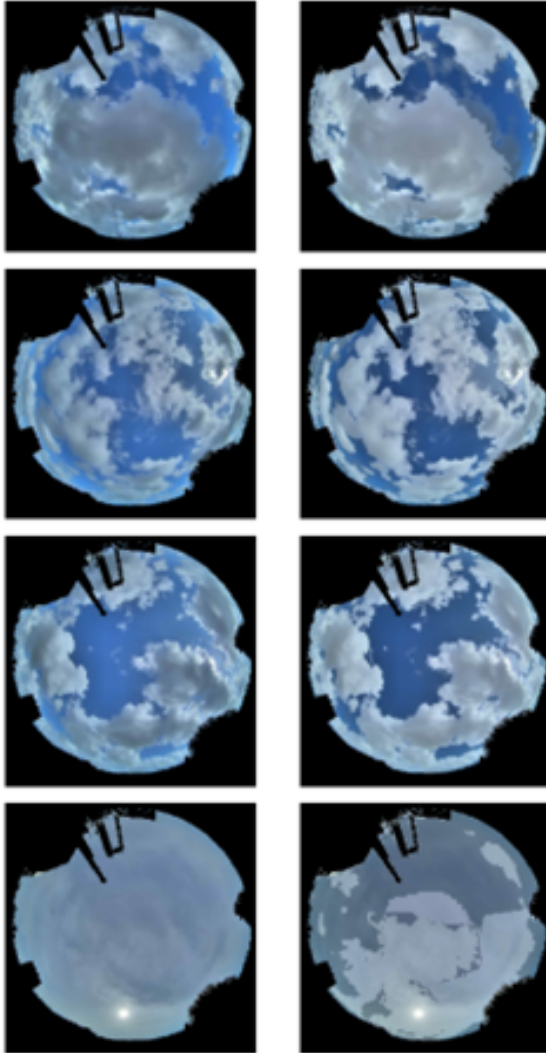
Figure B.2: Random examples of Class 2 cloud identification. The images on the left column are the original images. On the right, the clearer areas identify "Cloud" pixels while the darker are "Not cloud" pixels. Note that the horizon has a mask of black pixels.
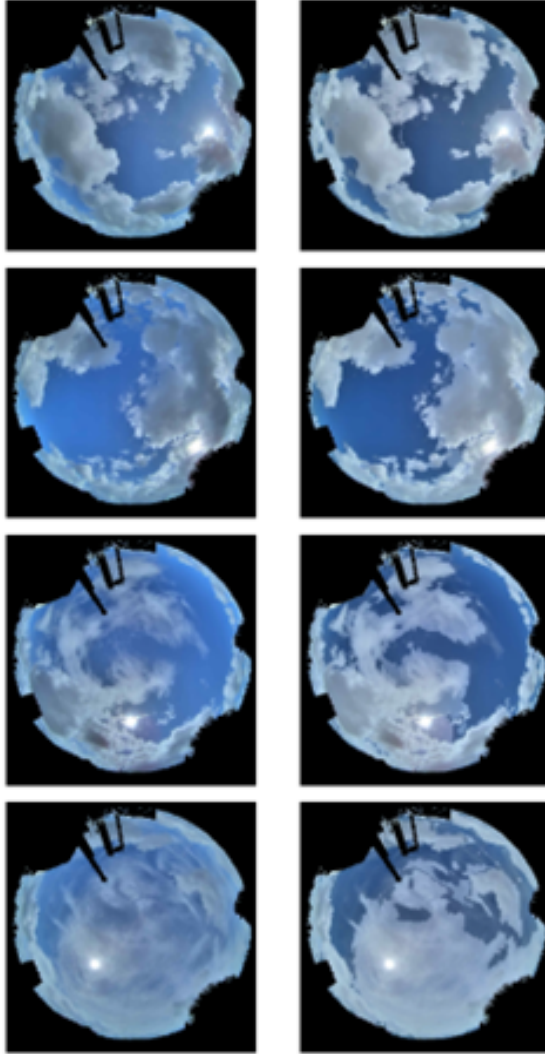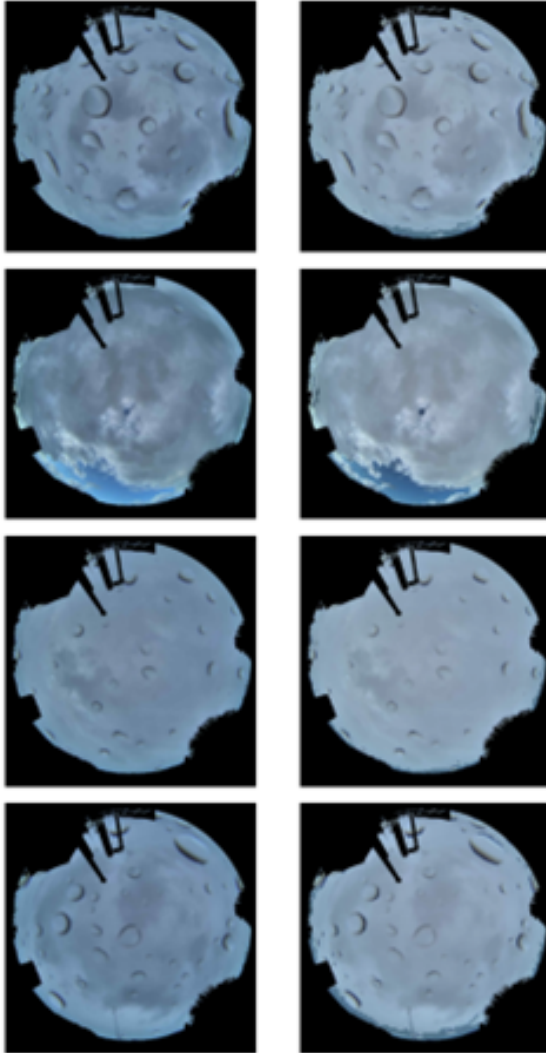
Figure B.3: Random examples of Class 3 cloud identification. The images on the left column are the original images. On the right, the clearer areas identify "Cloud" pixels while the darker are "Not cloud" pixels. Note that the horizon has a mask of black pixels.

Figure B.4: Random examples of Class 4 cloud identification. The images on the left column are the original images. On the right, the clearer areas identify "Cloud" pixels while the darker are "Not cloud" pixels. Note that the horizon has a mask of black pixels.
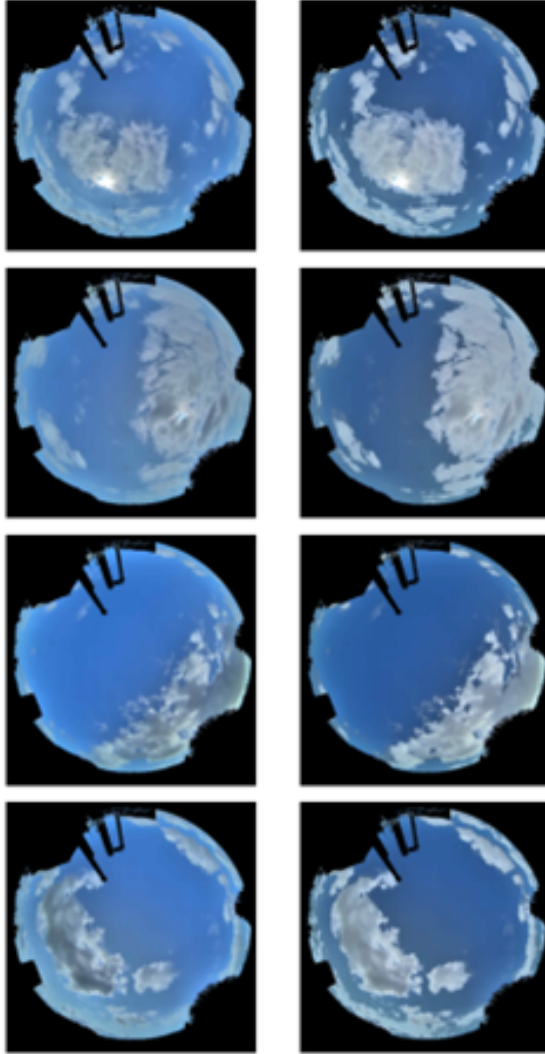
Figure B.5: Random examples of Class 5 cloud identification. The images on the left column are the original images. On the right, the clearer areas identify "Cloud" pixels while the darker are "Not cloud" pixels. Note that the horizon has a mask of black pixels.
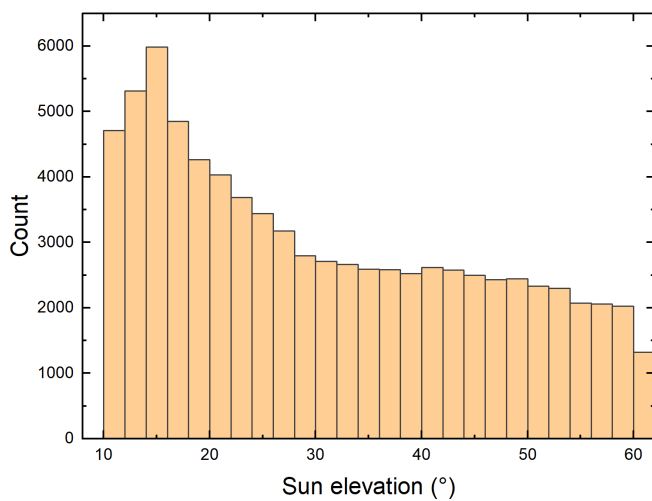
Figure B.6: Distribution of the dataset to the sun's elevation above the horizon.

C

EXTRA ANALYSIS FOR THE OPTIMIZATION OF PV-ELECTROLYZER SYSTEMS

C.1. VALUES FOR THE MODEL PARAMETERS

Parameter	Value
r_1	0.0004296
r_2	-4.153×10^{-7}
s	0.1803
t_1	0.05171
t_2	-2.415
t_3	8134
A	0.2082

Table C.1: Electrolyzer parameters from [316].

Parameter	Value
C_p	14.4 kJ/kgK
T_1	333.15 K / 60°C
η	0.6
CPR	198.0198
γ	1.4058

Table C.2: Parameters of the compressor model.

Concept	Cost
Installation PV	737 €/kW
Maintenance PV	13 €/kW
Installation electrolyzer	600 €/kW
Maintenance electrolyzer	4% installation costs
Electrolyzer replacement	20% installation costs

Table C.3: Parameters used for the calculation of the LCOH with data from [328]

C

C.1.1. CONFIGURATION OF PARTICLE SWARM OPTIMIZATION

The Particle Swarm optimization was implemented using the MATLAB function `particleswarm` with default values. To reduce computational time, the option of parallel computing was used.

The limits for the variables are shown in Table C.4. Note that the limits for the azimuth are negative. This was done to allow the algorithm to discover azimuth angles near the north (0°).

Variable	Min	Max
Azimuth	-45	370
Tilt	0	90
Oversize	0.1	5

Table C.4: Computational parameters of the Particle Swarm Optimization algorithm

C.1.2. SENSITIVITY ANALYSIS FOR PSO PARAMETERS

The azimuth and tilt of the PV modules cannot be modified because they cover a full hemisphere: the azimuth describes a full circle and the tilt one-quarter of it. Combining azimuth and tilt, then a half sphere is obtained. For this, the values are kept fixed. The oversize is the only PSO parameter that can be modified. The sensitivity analysis changes this parameter from 5, 3 and 2. Figure C.1a and C.1b show the sensitivity analysis regarding the orientation of single and double-sided systems respectively. Figures C.1c and C.1d show the sensitivity of the oversize factor for single and double-sided respectively.

The wasted energy and efficiency are the most affected indicators. for single-sided systems, the efficiency will change the orientation dramatically, from north-facing modules with an oversize factor of five, to a south-facing configuration with an oversize factor that does not surpass two. Yet, the efficiency is lower in the south-facing configurations (74 kWh/kg$_{H_2}$, for the north-facing system to 78 kWh/kg$_{H_2}$ for the south-facing ones). The wasted energy tends to allocate more vertical PV modules as the oversize factor limit decreases.

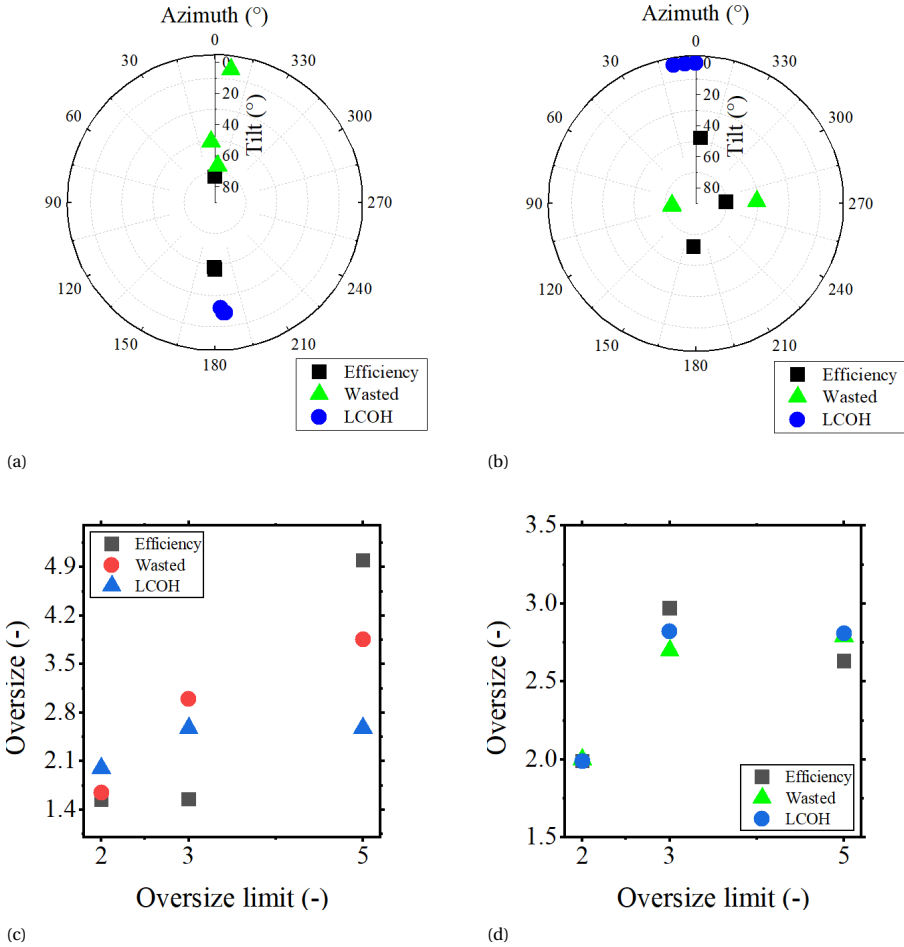For the double-sided system, the indicators need an oversize factor above 2 (Figure C.1d).

Figure C.1: Sensitivity analysis for the higher limit of the oversize factor. The tested values are 2, 3, and 5 (unitless). (a) PV module orientation of the single-sided system. (b) PV module orientation for the double-sided system. (c) Oversize factor for the single-sided system. (c) Oversize factor of the double-sided system. Note that the LCOH converges to the same values as long as it can go beyond an oversize factor of two.

D

FUZZY RULES OF THE UNCERTAINTY-BASED CONTROL OF ELECTROLYZER

1. If *uncertainty* is LOW and *predicted ramp* is DEEP DOWN and *previous slope* is POSITIVE BIG then *slope* is NEGATIVE LARGE.

2. If *uncertainty* is LOW and *predicted ramp* is DEEP DOWN and ΔGHI is NEGATIVE LARGE and *previous slope* is not NEGATIVE BIG then *slope* is ZERO.

3. If *uncertainty* is LOW and *predicted ramp* is DEEP DOWN and ΔGHI is NEGATIVE LARGE and *previous slope* is ZERO then *slope* is ZERO.

4. If *uncertainty* is HIGH and ΔGHI is POSITIVE HIGH and *previous slope* is ZERO then *slope* is POSITIVE LARGE.

5. If *uncertainty* is HIGH and ΔGHI is NEGATIVE LARGE and *previous slope* is ZERO then *slope* is NEGATIVE LARGE.

6. If *uncertainty* is HIGH and ΔGHI is NEGATIVE LARGE and *previous slope* is POSITIVE BIG then *slope* is NEGATIVE LARGE.

7. If *uncertainty* is HIGH and ΔGHI is POSITIVE HIGH and *previous slope* is POSITIVE BIG then *slope* is ZERO.

8. If *uncertainty* is HIGH and ΔGHI is POSITIVE HIGH and *previous slope* is NEGATIVE BIG then *slope* is POSITIVE LARGE.

9. If *uncertainty* is HIGH and ΔGHI is NEGATIVE LARGE and *previous slope* is NEGATIVE BIG then *slope* is POSITIVE LARGE.

10. If *uncertainty* is HIGH and Δ*GHI* is SHALLOW and *previous slope* is NEGATIVE BIG then *slope* is POSITIVE LARGE.

11. If *uncertainty* is HIGH and Δ*GHI* is SHALLOW and *previous slope* is ZERO then *slope* is ZERO.

12. If *uncertainty* is HIGH and Δ*GHI* is SHALLOW and *previous slope* is POSITIVE BIG then *slope* is ZERO.

13. If *uncertainty* is LOW and *predicted ramp* is DEEP DOWN and Δ*GHI* is SHALLOW and *previous slope* is NEGATIVE BIG then *slope* is ZERO.

14. If *uncertainty* is LOW and *predicted ramp* is DEEP DOWN and Δ*GHI* is SHALLOW and *previous slope* is ZERO then *slope* is NEGATIVE LARGE.

15. If *uncertainty* is LOW and *predicted ramp* is DEEP DOWN and Δ*GHI* is POSITIVE HIGH and *previous slope* is NEGATIVE BIG then *slope* is ZERO.

16. If *uncertainty* is LOW and *predicted ramp* is DEEP DOWN and Δ*GHI* is POSITIVE HIGH and *previous slope* is ZERO then *slope* is NEGATIVE LARGE.

17. If *uncertainty* is LOW and *predicted ramp* is SHALLOW and Δ*GHI* is NEGATIVE LARGE then *slope* is ZERO.

18. If *uncertainty* is LOW and *predicted ramp* is SHALLOW and Δ*GHI* is SHALLOW and *previous slope* is NEGATIVE BIG then *slope* is ZERO.

19. If *uncertainty* is LOW and *predicted ramp* is SHALLOW and Δ*GHI* is SHALLOW and *previous slope* is POSITIVE BIG then *slope* is NEGATIVE LARGE.

20. If *uncertainty* is LOW and *predicted ramp* is SHALLOW and Δ*GHI* is SHALLOW and *previous slope* is ZERO then *slope* is ZERO.

21. If *uncertainty* is LOW and *predicted ramp* is SHALLOW and Δ*GHI* is POSITIVE HIGH and *previous slope* is NEGATIVE BIG then *slope* is POSITIVE LARGE.

22. If *uncertainty* is LOW and *predicted ramp* is SHALLOW and Δ*GHI* is POSITIVE HIGH and *previous slope* is ZERO then *slope* is POSITIVE LARGE.

23. If *uncertainty* is LOW and *predicted ramp* is SHALLOW and Δ*GHI* is POSITIVE HIGH and *previous slope* is POSITIVE LARGE then *slope* is ZERO.

24. If *uncertainty* is LOW and *predicted ramp* is DEEP UP and Δ*GHI* is POSITIVE HIGH and *previous slope* is NEGATIVE BIG then *slope* is POSITIVE LARGE.

25. If *uncertainty* is LOW and *predicted ramp* is DEEP UP and Δ*GHI* is POSITIVE HIGH and *previous slope* is ZERO then *slope* is POSITIVE LARGE.

26. If *uncertainty* is LOW and *predicted ramp* is DEEP UP and Δ*GHI* is POSITIVE HIGH and *previous slope* is POSITIVE BIG then *slope* is ZERO.

27. If *uncertainty* is LOW and *predicted ramp* is DEEP UP and ΔGHI is NEGATIVE LARGE and *previous slope* is NEGATIVE BIG then *slope* is POSITIVE LARGE.

28. If *uncertainty* is LOW and *predicted ramp* is DEEP UP and ΔGHI is NEGATIVE LARGE and *previous slope* is ZERO then *slope* is POSITIVE LARGE.

29. If *uncertainty* is LOW and *predicted ramp* is DEEP UP and ΔGHI is NEGATIVE LARGE and *previous slope* is POSITIVE BIG then *slope* is ZERO.

30. If *uncertainty* is LOW and *predicted ramp* is DEEP UP and ΔGHI is SHALLOW and *previous slope* is ZERO then *slope* is ZERO.

31. If *uncertainty* is LOW and *predicted ramp* is DEEP UP and ΔGHI is SHALLOW and *previous slope* is NEGATIVE BIG then *slope* is POSITIVE LARGE.

32. If *uncertainty* is LOW and *predicted ramp* is DEEP DOWN and ΔGHI is SHALLOW and *previous slope* is POSITIVE BIG then *slope* is ZERO.

D

BIBLIOGRAPHY

[1]   International Union for Conservation of Nature. *The IUCN red list of threatened species*. (online). 2023. URL: https://www.iucnredlist.org.

[2]   United Nations. *Global issues: population*. (online). URL: https://www.un.org/en/global-issues/population.

[3]   Kate A. Brauman et al. *Chapter 2.3. Status and Trends -Nature's Contributions to People (NCP)*. Sept. 2021. DOI: 10.5281/zenodo.5519476.

[4]   Lennart Olsson et al. "Chapter 4: Land degradation". In: *Special report on climate change and land*. Ed. by José Manuel Moreno and Carolina Vera. IPCC, 2019.

[5]   IPCC. "Summary for policymakers". In: *Climate Change 2023: Synthesis Report*. Ed. by Core Writing Team, H. Lee, and J. Romero. Contribution of Working Groups I, II and III to the Sixth Assessment Report of the Intergovernmental Panel on Climate Change. IPCC, 2023. DOI: 10.59327/IPCC/AR6-9789291691647.001.

[6]   International Energy Agency. *Key World Energy Statistics 2021*. (online). 2021. URL: https://www.iea.org/reports/key-world-energy-statistics-2021.

[7]   International Energy Agency. *World Energy Balances Highlights*. (online). 2023. URL: https://www.iea.org/data-and-statistics/data-product/world-energy-balances-highlights.

[8]   International Energy Agency. *Global Energy Review*. (online). 2020. URL: https://www.iea.org/reports/global-energy-review-2019.

[9]   Organization for Economic Co-operation and Develoment (OCDE). *Green growth and sustainable development*. (online). 2022.

[10]   Herman E. Daly. "Sustainable Growth: An imposibility theorem". In: *Development* 3,4 (1990), pp. 45–47.

[11]   UN Department of Economic and Social Affairs. *Transforming our world: the 2030 Agenda for Sustainable Development*. (online). 2012. URL: https://sdgs.un.org/2030agenda.

[12]   IEA et al. *Tracking SDG 7: The Energy Progress Report*. Report. 2020.

[13]   United Nations. *The Sustainable Development Goals report Special Edition*. Report. 2023.

[14]   Holmes Rolston III. "World hunger and morality". In: Prentice Hall, Inc., 1996. Chap. Feeding people versus saving nature?

[15]   Lynn White. "The Historical Roots of Our Ecologic Crisis". In: *Science* 155.3767 (1967), pp. 1203–1207. DOI: 10.1126/science.155.3767.1203.

[16] International Energy Agency. *Net Zero Roadmap: A Global Pathway to Keep the 1.5 °C Goal in Reach*. (online). 2023. URL: https://www.iea.org/reports/net-zero-roadmap-a-global-pathway-to-keep-the-15-0c-goal-in-reach.

[17] International Energy Agency. *Tracking Clean Energy Progress 2023*. (online). 2023. URL: https://www.iea.org/reports/tracking-clean-energy-progress-2023.

[18] Smeeta Fokeer et al. *Green Hydrogen for sustainable industrial development*. Report. 2023.

[19] IRENA. *Hydrogen*. Website. 2022. URL: https://www.irena.org/Energy-Transition/Technology/Hydrogen.

[20] IRENA. *Energy transition outlook*. Website. 2022. URL: https://www.irena.org/Energy-Transition/Outlook.

[21] Netbeheer Nederland. *Capaciteitskaart invoeding elektriciteitsnet*. (online). 2024. URL: https://capaciteitskaart.netbeheernederland.nl/.

[22] International Energy Agency. *Empowering people – the role of local energy communities in clean energy transitions*. (online). 2023. URL: https://www.iea.org/commentaries/empowering-people-the-role-of-local-energy-communities-in-clean-energy-transitions.

[23] Sandra Díaz et al. "Assessing nature's contributions to people". In: *Science* 359 (6373 2018), pp. 270–272. DOI: https://10.1126/science.aap8826.

[24] United Nations Convention to Combat Desetification. *The global land outlook, second edition*. Report. 2022.

[25] Piotr Bojek. *IEA - Solar PV*. (online). 2022. URL: https://www.iea.org/energy-system/renewables/solar-pv.

[26] IRENA. *NDCs and renewable energy targets in 2021: Are we in the right path to a climate-safe future?* Abu Dhabi, 2022.

[27] European Comission. *REPowerEU with Clean Energy*. (online). 2022. URL: https://ec.europa.eu/commission/presscorner/detail/en/fs_22_3138.

[28] *National Climate Agreement*. (online). 2019. URL: https://www.klimaatakkoord.nl/.

[29] Robin Quax et al. "Assessment of spatial implications of photovoltaics deployment policies in the Netherlands". In: *Solar Energy* 243 (2022), pp. 381–392. ISSN: 0038-092X. DOI: https://doi.org/10.1016/j.solener.2022.07.048.

[30] Charles R. Warren et al. "'Green On Green': Public perceptions of wind power in Scotland and Ireland". In: *Journal of Environmental Planning and Management* 48.6 (2005), pp. 853–875. DOI: 10.1080/09640560500294376.

[31] Muhammad Tawalbeh et al. "Environmental impacts of solar photovoltaic systems: A critical review of recent progress and future outlook". In: *Science of the total Environment* 759 (2021), p. 143528. DOI: https://doi.org/10.1016/j.scitotenv.2020.143528.

[32] R.R. Hernandez et al. "Environmental impacts of utility-scale solar energy". In: *Renewable and Sustainable Energy Reviews* 29 (2014), pp. 766–779. DOI: https://doi.org/10.1016/j.rser.2013.08.041.

[33] Amalesh Dhar et al. "Perspectives on environmental impacts and a land reclamation strategy for solar and wind energy systems". In: *Science of the total environment* 718 (2020), p. 134602. DOI: https://doi.org/10.1016/j.scitotenv.2019.134602.

[34] Friso van der Zee et al. *Zonneparken natuur en landbouw*. Report. 2019.

[35] Steven M. Grodsky and Rebecca R. Hernandez. "Reduced ecosystem services of desert plants from ground-mounted solar energy development". In: *Nature sustainability* 3 (2020), pp. 1036–1043. DOI: https://doi.org/10.1038/s41893-020-0574-x.

[36] Jonas Kristiansen Nøland et al. "Spatial energy density of large-scale electricity generation from power sources worldwide". In: *Scientific Reports* 12 (2022), p. 21280. DOI: https://doi.org/10.1038/s41598-022-25341-9.

[37] Centraal Bureau voor de Statistiek. *How do we use our land?* (online). 2020. URL: https://longreads.cbs.nl/the-netherlands-in-numbers-2020/how-do-we-use-our-land/.

[38] Xu-Hui He et al. "Mechanical characteristics of a new type of cable-supported photovoltaic module system". In: *Solar Energy* 226 (2021), pp. 408–420. DOI: https://doi.org/10.1016/j.solener.2021.08.065.

[39] Jenny Palm. "Household installation of solar panels – Motives and barriers in a 10-year perspective". In: *Energy Policy* 113 (2018), pp. 1–8. DOI: https://doi.org/10.1016/j.enpol.2017.10.047.

[40] Monireh Aram et al. "A state-of-the-art review of fire safety of photovoltaic systems in buildings". In: *Journal of cleaner Production* 308 (2021), p. 127239. DOI: https://doi.org/10.1016/j.jclepro.2021.127239.

[41] Y. Zhou et al. "A geographic information system-based large scale visibility assessment tool for multi-criteria photovoltaic planning on urban building roofs". In: *Renewable and sustainable energy reviews* 188 (2023), p. 113885. DOI: https://doi.org/10.1016/j.rser.2023.113885.

[42] David J. MacKay. "Solar energy in the context of energy use, energy transportation and energy storage". In: *Philosophical Transactions of the Royal Society A* 371 (2013), p. 20110431. DOI: https://doi.org/10.1098/rsta.2011.0431.

[43] Iñigo Capellán-Pérez, Carlos de Castro, and Iñaki Arto. "Assessing vulnerabilities and limits in the transition to renewable energies: Land requirements under 100% solar energy scenarios". In: *Renewable and Sustainable Energy Reviews* 77 (2017), pp. 760–782. ISSN: 1364-0321. DOI: https://doi.org/10.1016/j.rser.2017.03.137.

[44] S. Stremke. "Sustainable Energy Landscape: Implementing Energy Transition in the Physical Realm". In: *Encyclopedia of Environmental Management*. Ed. by S.V. Jørgensen. United States: CRC Press, 2015. DOI: 10.1081/E-EEM-120053717. URL: www.tandfonline.com/doi/abs/10.1081/E-EEM-120053717.

[45] J. Arán Carrión et al. "Environmental decision-support systems for evaluating the carrying capacity of land areas: Optimal site selection for grid-connected photovoltaic power plants". In: *Renewable and Sustainable Energy Reviews* 12.9 (2008), pp. 2358–2380. DOI: https://doi.org/10.1016/j.rser.2007.06.011.

[46] Yassine Charabi and Adel Gastli. "PV site suitability analysis using GIS-based spatial fuzzy multi-criteria evaluation". In: *Renewable Energy* 36.9 (2011), pp. 2554–2561. DOI: https://doi.org/10.1016/j.renene.2010.10.037.

[47] Justin Brewer et al. "Using GIS analytics and social preference data to evaluate utility-scale solar power site suitability". In: *Renewable Energy* 81 (2015), pp. 825–836. DOI: https://doi.org/10.1016/j.renene.2015.04.017.

[48] Ahmed Alami Merrouni et al. "Large scale PV sites selection by combining GIS and Analytical Hierarchy Process. Case study: Eastern Morocco". In: *Renewable Energy* 119 (2018), pp. 863–873. DOI: https://doi.org/10.1016/j.renene.2017.10.044.

[49] Marina Giamalaki and Theocharis Tsoutsos. "Sustainable siting of solar power installations in Mediterranean using a GIS/AHP approach". In: *Renewable Energy* 141 (2019), pp. 64–75. DOI: https://doi.org/10.1016/j.renene.2019.03.100.

[50] Thomas Finn and Paul McKenzie. "A high-resolution suitability index for solar farm location in complex landscapes". In: *Renewable Energy* 158 (2020), pp. 520–533. DOI: https://doi.org/10.1016/j.renene.2020.05.121.

[51] Hsiao-Wen Wang, Adrienne Dodd, and Yekang Ko. "Resolving the conflict of greens: A GIS-based and participatory least-conflict siting framework for solar energy development in southwest Taiwan". In: *Renewable Energy* 197 (2022), pp. 879–892. DOI: https://doi.org/10.1016/j.renene.2022.07.094.

[52] Djilali Messaoudi et al. "GIS based multi-criteria decision making for solar hydrogen production sites selection in Algeria". In: *International Journal of Hydrogen Energy* 44.60 (2019), pp. 31808–31831. DOI: https://doi.org/10.1016/j.ijhydene.2019.10.099.

[53] R.W. Saaty. "The Analytic Hierarchy Process - What it is and how it is used". In: *Mathematical modelling* 9.3 (1987), pp. 161–176.

[54] David M. Stoms, Stephanie L. Dashiell, and FRank W. Davis. "Sitting solar energy development to minimize biological impacts". In: *Renewable Energy* 57 (2013), pp. 289–298. DOI: https://doi.org/10.1016/j.renene.2013.01.055.

[55] David M. Stoms, Stephanie L. Dashiell, and Frank W. David. *Mapping compatibility to minimize biodiversity impacts of solar energy development in the California Deserts*. Biogeography Lab, University of California Santa Barbara. 2011.

[56] Ministerie van Landbouw, Natuur en Voedselkwaliteit. *Natura 2000*. (online). URL: https://www.natura2000.nl/.

[57] *Dataset: Beschermde Gebieden - Natura 2000 (INSPIRE geharmoniseerd)*. (online). URL: https://www.pdok.nl/introductie/-/article/beschermde-gebieden-natura2000-inspire-geharmoniseerd-.

[58] *Dataset: Natuurnetwerk Nederland (NNN) - Provincies (INSPIRE geharmoniseerd)*. (online). URL: https://www.pdok.nl/introductie/-/article/natuurnetwerk-nederland-nnn-.

[59] *Dataset: Nationale Parken*. (online). URL: https://www.pdok.nl/introductie/-/article/nationale-parken.

[60] *Dataset: Provinciaal Landschapsbeleid - Provincies (INSPIRE geharmoniseerd)*. (online). URL: https://www.pdok.nl/introductie/-/article/provinciaal-landschapsbeleid.

[61] *Dataset: Aardkundige waarden*. (online). URL: https://www.pdok.nl/introductie/-/article/aardkundige-waarden.

[62] ROM3D. *Zon op Kaart*. peildatum 27 maart 2023.

[63] The World Bank. Source: Global Solar Atlas 2.0, Solar resource data: Solargis. 2020.

[64] Rebecca R. Hernandez et al. "Solar energy development impacts on land cover change and protected areas". In: *PNAS* 112 (44 2015), pp. 13579–13584. DOI: https://doi.org/10.1073/pnas.1517656112.

[65] Tsegaye T. Gatiso et al. "Effectiveness of protected areas influenced by socio-economic context". In: *Nature sustainability* 5 (2022), pp. 861–868. DOI: https://doi.org/10.1038/s41893-022-00932-6.

[66] Ministerie van Landbouw, Natuur en Voedselkwaliteit. *Ambtelijke verkenning impact verslechteringsverbod buiten Natura 2000-gebieden van de verordening Natuurherstel*. Report. 2022. URL: https://www.rijksoverheid.nl/documenten/rapporten/2023/04/20/ambtelijke-verkenning-impact-verslechteringsverbod-buiten-natura-2000-gebieden-van-de-verordening-natuurherstel.

[67] Anteneh T. Tesfaw et al. "Land-use and land-cover change shape the sustainability and impacts of protected areas". In: *PNAS* 115 (9 2018), pp. 2084–2089. DOI: https://doi.org/10.1073/pnas.1716462115.

[68] SolarPpower Europe. *Solar, Biodiversity, Land Use. Best practice guidelines*. Report. 2022.

[69] Eric Wiebes. *Beantwoording moties dik-Faber over een zonneladder als nationaal afwegingskader bij inpassing van zonne-energie*. 2019.

[70] L. Kruitwagen et al. "A global inventory of photovoltaic solar energy generating units". In: *Nature* 598 (2021), pp. 604–610. DOI: https://doi.org/10.1038/s41586-021-03957-7.

[71] Rebecca R. Hernandez et al. "Techno-ecological synergies of solar energy for global sustainability". In: *Nature sustainability* 2 (2019), pp. 560–568. DOI: https://doi.org/10.1038/s41893-019-0309-z.

[72]   Matthew A. Sturchio and Alan K. Knapp. "Ecovoltaic principles for a more sustainable ecologically informed solar energy future". In: *Nature ecology & Evolution* (2023). DOI: https://doi.org/10.1038/s41559-023-02174-x.

[73]   Zon in landschap. *EcoCertified solar Parks.* (online). URL: https://zoninlandschap.nl/projecten/i358/ecocertified-solar-parks.

[74]   Klimaateffectatlas. *Basiskaart Groen en Grijs.* (online). URL: https://www.klimaateffectatlas.nl/nl/basiskaart-groen-en-grijs.

[75]   ESRI. *Line Density (Spatial Analyst).* (online). URL: https://pro.arcgis.com/en/pro-app/latest/tool-reference/spatial-analyst/line-density.htm.

[76]   Centraal Bureau voor de Statistiek. *Stedelijkheid (van een gebied).* (online). 2023. URL: https://www.cbs.nl/nl-nl/onze-diensten/methoden/begrippen/stedelijkheid--van-een-gebied--.

[77]   Centraal Bureau voor de Statistiek. *Wijk- en buurtkaart 2022.* (online). 2022. URL: https://www.cbs.nl/nl-nl/dossier/nederland-regionaal/geografische-data/wijk-en-buurtkaart-2022.

[78]   International Energy Agency. *Solar PV.* Tech. rep. International Energy Agency, 2021. URL: https://iea.org/reports/solar-pv.

[79]   Max Mittag et al. "Approach for a Holistic Optimization from Wafer to PV System". In: *2018 IEEE 7th World Conference on Photovoltaic Energy Conversion (WCPEC) (A Joint Conference of 45th IEEE PVSC, 28th PVSEC & 34th EU PVSEC).* 2018, pp. 3194–3199. DOI: 10.1109/PVSC.2018.8547350.

[80]   *Photovoltaics Report.* Tech. rep. Fraunhofer Institute for Solar Energy Systems, 2022. URL: https://www.ise.fraunhofer.de/content/dam/ise/de/documents/publications/studies/Photovoltaics-Report.pdf.

[81]   CSEM-EPFL. *New world records: perovskite-on-silicon-tandem solar cells.* July 2022. URL: https://www.csem.ch/pdf/172336.

[82]   Andres Calcabrini et al. "A fully reconfigurable series-parallel photovoltaic module for higher energy yields in urban environments". In: *Renewable Energy* 179 (2021), pp. 1–11. DOI: 10.1016/j.renene.2021.07.010.

[83]   R Venkateswari and S. Sreejith. "Factors influencing the efficiency of photovoltaic system". In: *Renewable and Sustainable Energy Reviews* 101 (), pp. 376–394. DOI: 10.1016/j.rser.2018.11.012.

[84]   Nabil Karami, Nazih Moubayed, and Rachid Outbib. "General review and classification of different MPPT Techniques". In: *Renewable and Sustainable Energy Reviews* 68 (2017), pp. 1–18. ISSN: 1364-0321. DOI: 10.1016/j.rser.2016.09.132.

[85]   Mojtaba Kordestani et al. "Maximum Power Point Tracker (MPPT) for Photovoltaic Power Systems-A Systematic Literature Review". In: *2018 European Control Conference (ECC).* Limassol,Cyprus, June 2018, pp. 40–45. DOI: 10.23919/ECC.2018.8550117.

[86] Saad Motahhir, Aboubakr El Hammoumi, and Abdelaziz El Ghzizal. "The most used MPPT algorithms: Review and the suitable low-cost embedded board for each algorithm". In: *Journal of Cleaner Production* 246 (2020), p. 118983. ISSN: 0959-6526. DOI: 10.1016/j.jclepro.2019.118983.

[87] Mazen Abdel-Salam, Mohamed-Tharwat El-Mohandes, and Mohamed Goda. "On the Improvements of Perturb-and-Observe-Based MPPT in PV Systems". In: *Modern Maximum Power Point Tracking Techniques for Photovoltaic Energy Systems*. Ed. by Ali M. Eltamaly and Almoataz Y. Abdelaziz. Cham: Springer International Publishing, July 2020, pp. 165–198. ISBN: 978-3-030-05578-3. DOI: 10.1007/978-3-030-05578-3_6.

[88] D. P. Hohm and M. E. Ropp. "Comparative study of maximum power point tracking algorithms". In: *Progress in Photovoltaics: Research and Applications* 11.1 (Nov. 2003), pp. 47–62. DOI: 10.1002/pip.459. eprint: https://onlinelibrary.wiley.com/doi/pdf/10.1002/pip.459.

[89] N. Femia et al. "Optimization of perturb and observe maximum power point tracking method". In: *IEEE Transactions on Power Electronics* 20.4 (July 2005), pp. 963–973. ISSN: 1941-0107. DOI: 10.1109/TPEL.2005.850975.

[90] Dezso Sera et al. "On the Perturb-and-Observe and Incremental Conductance MPPT Methods for PV Systems". In: *IEEE Journal of Photovoltaics* 3.3 (2013), pp. 1070–1078. DOI: 10.1109/JPHOTOV.2013.2261118.

[91] A. Woyte et al. "Quantifying the occurrence and duration of power fluctuations introduced by photovoltaic systems". In: *2003 IEEE Bologna Power Tech Conf.* Bologna, Italy, June 2003, pp. 1–7. DOI: 10.1109/PTC.2003.1304368.

[92] Benjamin Y.H. Liu and Richard C. Jordan. "The interrelationship and characteristic distribution of direct, diffuse and total solar radiation". In: *Solar Energy* 4.3 (July 1960), pp. 1–19. ISSN: 0038-092X. DOI: 10.1016/0038-092X(60)90062-1.

[93] Christelle Rigollier, Olivier Bauer, and Lucien Wald. "On the clear sky model of the ESRA — European Solar Radiation Atlas — with respect to the heliosat method". In: *Solar Energy* 68.1 (Jan. 2000), pp. 33–48. ISSN: 0038-092X. DOI: 10.1016/S0038-092X(99)00055-9.

[94] Matthew Lave, Jan Kleissl, and Joshua Stein. "Chapter 7 - Quantifying and Simulating Solar-Plant Variability Using Irradiance Data". In: *Solar Energy Forecasting and Resource Assessment*. Ed. by Jan Kleissl. Boston: Academic Press, 2013, pp. 149–169. ISBN: 978-0-12-397177-7. DOI: 10.1016/B978-0-12-397177-7.00007-3.

[95] Joshua Stein, Clifford Hansen, and Matthew J Reno. "The variability index: A new and novel metric for quantifying irradiance and PV output variability." In: *World Ren. Energy Forum*. Denver, CO, United States, May 2012, pp. 1–7.

[96] R. Bründlinger et al. "prEN 50530-The new european standard for performance characterisation of PV inverters." In: *24th EU PV conf.* Hamburg, Germany, Sept. 2009, pp. 1–5.

[97]   Kashif Ishaque, Zainal Salam, and George Lauss. "The performance of perturb and observe and incremental conductance maximum power point tracking method under dynamic weather conditions". In: *Applied Energy* 119 (Apr. 2014), pp. 228–236. ISSN: 0306-2619. DOI: 10.1016/j.apenergy.2013.12.054.

[98]   Po-Cheng Chen et al. "A comparative study on maximum power point tracking techniques for photovoltaic generation systems operating under fast changing environments". In: *Solar Energy* 119 (2015), pp. 261–276. DOI: 10.1016/j.solener.2015.07.006.

[99]   Ashish Pandey, Nivedita Dasgupta, and Ashok Kumar Mukerjee. "High-Performance Algorithms for Drift Avoidance and Fast Tracking in Solar MPPT System". In: *IEEE Transactions on Energy Conversion* 23.2 (Apr. 2008), pp. 681–689. DOI: 10.1109/TEC.2007.914201.

[100] Søren Bækhøj Kjær. "Evaluation of the "Hill Climbing" and the "Incremental Conductance" Maximum Power Point Trackers for Photovoltaic Power Systems". In: *IEEE Transactions on Energy Conversion* 27.4 (2012), pp. 922–929. DOI: 10.1109/TEC.2012.2218816.

[101] M. Sengupta and A. Andreas. *Oahu Solar Measurement Grid (1-Year Archive): 3-Second Solar Irradiance; Oahu, Hawaii (Data).* Mar. 2010. URL: http://dx.doi.org/10.5439/1052451.

[102] Filippo Spertino et al. "A method for obtaining the I-V curve of photovoltaic arrays from module voltages and its applications for MPP tracking". In: *Solar Energy* 139 (Dec. 2016), pp. 489–505. ISSN: 0038-092X. DOI: 10.1016/j.solener.2016.10.013.

[103] Hegazy Rezk and Ali M. Eltamaly. "A comprehensive comparison of different MPPT techniques for photovoltaic systems". In: *Solar Energy* 112 (2015), pp. 1–11. DOI: 10.1016/j.solener.2014.11.010.

[104] Vibhu Jately et al. "Experimental Analysis of hill-climbing MPPT algorithms under low irradiance levels". In: *Renewable and Sustainable Energy Reviews* 150 (2021), p. 111467. DOI: 10.1016/j.rser.2021.111467.

[105] Jyri Kivimäki et al. "Revisited Perturbation Frequency Design Guideline for Direct Fixed-Step Maximum Power Point Tracking Algorithms". In: *IEEE Transactions on Industrial Electronics* 64.6 (2017), pp. 4601–4609. DOI: 10.1109/TIE.2017.2674589.

[106] Xingshuo Li et al. "A Comparative Study on Photovoltaic MPPT Algorithms Under EN50530 Dynamic Test Procedure". In: *IEEE Transactions on Power Electronics* 36.4 (2021), pp. 4153–4168. DOI: 10.1109/TPEL.2020.3024211.

[107] Mostefa Kermadi et al. "Assessment of maximum power point trackers performance using direct and indirect control methods". In: *International Transactions on Electrical Energy Systems* 30.10 (2020), e12565. DOI: https://doi.org/10.1002/2050-7038.12565.

[108] Mohammed A. Elgendy, Bashar Zahawi, and David J. Atkinson. "Operating Characteristics of the P&O Algorithm at High Perturbation Frequencies for Standalone PV Systems". In: *IEEE Transactions on Energy Conversion* 30.1 (2015), pp. 189–198. DOI: 10.1109/TEC.2014.2331391.

[109] G. Pfister et al. "Cloud coverage based on all-sky imaging and its impact on surface solar irradiance". In: *Journal of applied meteorology and climatology* 42 (10 2003), pp. 1421–1434.

[110] Christian A. Gueymard. "Cloud and albedo enhancement impacts on solar irradiance using high-frequency measurements from thermopile and photodiode radiometers. Part 1: impacts on global horizontal irradiance". In: *Solar energy* 153 (2017), pp. 755–765.

[111] Zachary K. Pecenak et al. "Simulating irradiance enhancement dependence on cloud optical depth and solar zenith angle". In: *Solar energy* 136 (2016), pp. 675–681.

[112] Lucas Rafael do Nascimento et al. "Extreme solar overirradiance events: occurrence and impacts on utility-scale photovoltaic power plants in Brazil". In: *Solar energy* 186 (2019), pp. 370–381.

[113] Frank P.M. Kreuwel et al. "Analysis of high frequency photovoltaic solar energy fluctuations". In: *Solar Energy* 206 (2020), pp. 381–389.

[114] Andrew Mills et al. "Dark Shadows". In: *IEEE Power and Energy Magazine* 9.3 (2011), pp. 33–41. DOI: 10.1109/MPE.2011.940575.

[115] Victor Arturo Martinez Lopez et al. "Study on the Effect of Irradiance Variability on the Efficiency of the Perturb-and-Observe Maximum Power Point Tracking Algorithm". In: *Energies* 15.20 (2022), p. 7562. DOI: 10.3390/en15207562.

[116] A. Gonzalez-Moreno et al. "A PV ramp-rate control strategy to extend battery lifespan using forecasting". In: *Applied Energy* 323 (2022), p. 119546. DOI: https://doi.org/10.1016/j.apenergy.2022.119546.

[117] Gilles Notton and Cyril Voyant. "Chapter 3 - Forecasting of Intermittent Solar Energy Resource". In: *Advances in Renewable Energies and Power Technologies*. Ed. by Imene Yahyaoui. Elsevier, 2018, pp. 77–114. DOI: https://doi.org/10.1016/B978-0-12-812959-3.00003-4.

[118] Naveen Krishnan, K. Ravi Kumar, and Chandrapal Singh Inda. "How solar radiation forecasting impacts the utilization of solar energy: A critical review". In: *Journal of Cleaner Production* 388 (2023), p. 135860. DOI: https://doi.org/10.1016/j.jclepro.2023.135860.

[119] M. Hasenbalg et al. "Benchmarking of six cloud segmentation algorithms for ground-based all-sky imagers". In: *Solar Energy* 201 (2020), pp. 596–614.

[120] A. Heinle, A. Macke, and A. Srivastav. "Automatic cloud classification of whole sky images". In: *Atmospheric Measurement Techniques* 3.3 (2010), pp. 557–567. DOI: 10.5194/amt-3-557-2010.

[121] S. Quesada-Ruiz et al. "Cloud-tracking methodology for intra-hour DNI forecasting". In: *Solar energy* 102 (2014), pp. 267–275.

[122] Janet E. Shields et al. "Day/night whole sky imagers for 24-h cloud and sky assessment: history and overview". In: *Applied optics* 52 (8 2013), pp. 1605–1616.

[123] M. Caldas and R. Alonso-Suárez. "Very short-term solar irradiance forecast using all-sky imaging and real-time irradiance measurements". In: *Renewable energy* 143 (2019), pp. 1643–1658. DOI: https://doi.org/10.1016/j.renene.2019.05.069.

[124] Chia-Lin Fu and Hsu-Yung Cheng. "Predicting solar irradiance with all-sky image features via regression". In: *Solar energy* 97 (2013), pp. 537–550. DOI: https://doi.org/10.1016/j.solener.2013.09.016.

[125] Hsu-Yung Cheng and Chih-Chang Yu. "Multi-model solar irradiance prediciton based on automatic cloud classification". In: *Energy* 91 (2015), pp. 579–587. DOI: https://doi.org/10.1016/j.energy.2015.08.075.

[126] Yinghao Chu, Hugo T.C. Pedro, and Carlos F.M. Coimbra. "Hybrid intra-hour DNI forecasts with sky image processing enhanced by stochastic learning". In: *Solar energy* 98 (2013), pp. 592–603. DOI: https://doi.org/10.1016/j.solener.2013.10.020.

[127] Ardan Hüseyin Eşlik, Emre Akarslan, and Fatih Onur Hocaoğlu. "Short-term solar radiation forecasting with a novel image processing-based deep learning approach". In: *Renewable Energy* 200 (2022), pp. 1490–1505. DOI: https://doi.org/10.1016/j.renene.2022.10.063.

[128] Ivan Vasilev. *Python deep learning: exploring deep learning techniques and neural network architectures with PyTorch, Keras and TensorFlow*. Birmingham, UK: Packt Publishing, 2019.

[129] Yuchi Sun, Gergely Szűcs, and Adam R. Brandt. "Solar PV output prediction from video streams using convolutional neural networks". In: *Energy & Environmental Science* 11.7 (2018), pp. 1811–1818. ISSN: 1754-5692. DOI: 10.1039/C7EE03420B.

[130] Yuchi Sun, Vignesh Venugopal, and Adam R. Brandt. "Short-term solar power forecast with deep learning: Exploring optimal input and output configuration". In: *Solar Energy* 188 (2019), pp. 730–741. DOI: https://doi.org/10.1016/j.solener.2019.06.041.

[131] C. Feng and J. Zhang. "SolarNet: A sky image-based deep convolutional neural network for intra-hour solar forecasting". In: *Solar Energy* 204 (2020), pp. 71–78. DOI: https://doi.org/10.1016/j.solener.2020.03.083.

[132] Quentin Paletta et al. "ECLIPSE: Envisioning CLoud Induced Perturbations in Solar Energy". In: *Applied Energy* 326 (2022), p. 119924. DOI: https://doi.org/10.1016/j.apenergy.2022.119924.

[133] Zhao Zhen et al. "Deep Learning Based Surface Irradiance Mapping Model for Solar PV Power Forecasting Using Sky Image". In: *IEEE Transactions on Industry Applications* 56.4 (2020), pp. 3385–3396. DOI: 10.1109/TIA.2020.2984617.

[134] J. Zhang et al. "Deep photovoltaic nowcasting". In: *Solar Energy* 176 (2018), pp. 267–276. DOI: https://doi.org/10.1016/j.solener.2018.10.024.

[135] Quentin Paletta, Guillaume Arbod, and Joan Lasenby. "Benchmarking of deep learning irradiance forecasting models from sky images -An in -depth analysis". In: *Solar Energy* 224 (2021), pp. 855–867. DOI: 10.1016/j.solener.2021.05.056.

[136] Stavros-Andreas Logothetis et al. "Benchmarking of solar irradiance nowcast performance derived from all-sky imagers". In: *Renewable Energy* 199 (2022), pp. 246–261.

[137] Stavros-Andreas Logothetis et al. "Solar Irradiance Ramp Forecasting Based on All-Sky Imagers". In: *Energies* 15.17 (2022), p. 6191. DOI: 10.3390/en15176191.

[138] Weicong Kong et al. "Hybrid approaches based on deep whole-sky-image learning to photovoltaic generation forecasting". In: *Applied Energy* 280 (2020), p. 115875. DOI: https://doi.org/10.1016/j.apenergy.2020.115875.

[139] Cong Feng et al. "Convolutional neural networks for intra-hour solar forecasting based on sky image sequences". In: *Applied Energy* 310 (2022), p. 118438. DOI: https://doi.org/10.1016/j.apenergy.2021.118438.

[140] Haoran Wen et al. "Deep Learning Based Multistep Solar Forecasting for PV Ramp-Rate Control Using Sky Images". In: *IEEE Transactions on Industrial Informatics* 17.2 (2021), pp. 1397–1406. DOI: 10.1109/TII.2020.2987916.

[141] Shuo Shan et al. "Ensemble learning based multi-modal intra-hour irradiance forecasting". In: *Energy Conversion and Management* 270 (2022), p. 116206. DOI: https://doi.org/10.1016/j.enconman.2022.116206.

[142] Prajowal Manandhar, Marouane Temimi, and Zeyar Aung. "Short-term solar radiation forecast using total sky imager via transfer learning". In: *Energy Reports* 9 (2023), pp. 819–828. DOI: https://doi.org/10.1016/j.egyr.2022.11.087.

[143] Rafael Gonzalez and Richard Woods. *Digital image processing, global edition*. Pearson Education, Limited, 2017.

[144] Chi-Wah Kok and Wing-Shan Tam. *Digital image interpolation in Matlab*. Wiley-IEEE Press, 2019.

[145] D.W. Slater, C.N. Long, and T.P. Tooman. "Total Sky Imager/Whole Sky Imager cloud fraction comparison". In: *Eleventh ARM Science Team meeting proceedings*. Atlanta, USA, 2001.

[146] Qingyong Li, Weitao Lu, and Jun Yang. "A hybrid thresholding algorithm for cloud detection on ground-based color images". In: *Journal of atmospheric and oceanic technology* 2 (10 2011), pp. 1286–1296.

[147] Huo-Min Zuo et al. "Ten-minute prediction of solar irradiance based on cloud detection and a long short-term memory (LSTM) model". In: *Energy Reports* 8 (2022), pp. 5146–5157.

[148] Alessandro Niccolai and Alfredo Nespoli. "Sun Position Identification in Sky Images for Nowcasting Application". In: *Forecasting* 2.4 (2020), pp. 488–504. DOI: 10.3390/forecast2040026.

[149] Shuang Liu et al. "Automatic cloud detection for All-sky images using super-pixel segmentation". In: *IEEE Geoscience and Remote Sensing Letters* 12.2 (2015), pp. 354–358.

[150] Ren and Malik. "Learning a classification model for segmentation". In: *Proceedings Ninth IEEE International Conference on Computer Vision*. Vol. 1. 2003, pp. 10–17. DOI: 10.1109/ICCV.2003.1238308.

[151] Nobuyuki Otsu. "A Threshold Selection Method from Gray-Level Histograms". In: *IEEE Transactions on Systems, Man, and Cybernetics* 9.1 (1979), pp. 62–66. DOI: 10.1109/TSMC.1979.4310076.

[152] Joel Gibson and Oge Marques. "Optical Flow Fundamentals". In: *Optical Flow and Trajectory Estimation Methods*. Cham: Springer International Publishing, 2016, pp. 1–7. DOI: 10.1007/978-3-319-44941-8_1.

[153] Gunnar Farnebäck. "Two-Frame Motion Estimation Based on Polynomial Expansion". In: *Image Analysis*. Ed. by Josef Bigun and Tomas Gustavsson. Berlin, Heidelberg: Springer Berlin Heidelberg, 2003, pp. 363–370.

[154] OpenCV. *Optical Flow*. URL: https://docs.opencv.org/3.4/d4/dee/tutorial_optical_flow.html.

[155] Youssef Karout et al. "Hybrid intrahour DNI forecast model based on DNI measurements and sky-imaging data". In: *Solar Energy* 249 (2023), pp. 541–558. DOI: https://doi.org/10.1016/j.solener.2022.11.032.

[156] A. Woyte, R. Belmans, and J. Nijs. "Analysing short-time irradiance fluctuations by their characteristic time scales". In: *Proceedings of the 3rd World Conference on Photovoltaic Energy Conversion, 2003*. Vol. 3. Osaka, Japan, 2003, pp. 2290–2293.

[157] William F. Holmgren, Clifford W. Hansen, and Mark A. Mikofski. "pvlib python: a python package for modeling solar energy systems". In: *Journal of Open Source Software* 3 (29 2018), p. 884. DOI: https://doi.org/10.21105/joss.00884.

[158] Xiaoyang Chen, Yang Du, and Huiqing Wen. "Forecasting based power ramp-rate control for PV systems without energy storage". In: *2017 IEEE 3rd International Future Energy Electronics Conference and ECCE Asia (IFEEC 2017 - ECCE Asia)*. 2017, pp. 733–738. DOI: 10.1109/IFEEC.2017.7992130.

[159] Xiaoyang Chen et al. "Forecasting-Based Power Ramp-Rate Control Strategies for Utility-Scale PV Systems". In: *IEEE Transactions on Industrial Electronics* 66.3 (2019), pp. 1862–1871. DOI: 10.1109/TIE.2018.2840490.

[160] National Academy of Engineering (US), National Research Council (US), and Committee on Alternatives and Strategies for Future Hydrogen Production and Use. *The Hydrogen Economy : Opportunities, Costs, Barriers, and R & D Needs*. National Academies Press, 2004.

[161] International Energy Agency. *The future of hydrogen*. 2019. URL: https://www.iea.org/reports/the-future-of-hydrogen.

[162] Liam Stoker. *Iberdrola unveils plans for 'Europe's largest' solar-storage-hydrogen project*. (online). 2020. URL: https://www.pv-tech.org/iberdrola-unveils-plans-for-europes-largest-solar-storage-hydrogen-project/.

[163] Verity Ratcliffe. *Saudi Arabia's Bold Plan to Rule the $700 Billion Hydrogen Market*. (online). URL: https://www.bloomberg.com/news/articles/2021-03-07/saudi-arabia-s-plan-to-rule-700-billion-hydrogen-market.

[164] International Energy Agency. *Hydrogen Production and Infrastructure Projects Database*. (onine). 2021. URL: https://www.iea.org/data-and-statistics/data-product/hydrogen-production-and-infrastructure-projects-database.

[165] Ibrahim Dincer and Calin Zamfirescu. "Chapter 3 - Hydrogen Production by Electrical Energy". In: *Sustainable Hydrogen Production*. Ed. by Ibrahim Dincer and Calin Zamfirescu. Elsevier, 2016, pp. 99–161. DOI: https://doi.org/10.1016/B978-0-12-801563-6.00003-0.

[166] Marie- C. Pera et al. *Electrochemical Components*. Somerset, UNITED STATES: Wiley, 2013.

[167] Sergey A. Grigoriev and Vladimir N. Fateev. "Hydrogen Production by Water Electrolysis". In: *Hydrogen Production Technologies*. John Wiley & Sons, Ltd, 2017. Chap. 6, pp. 231–276.

[168] Rodney L. LeRoy. "The Thermodynamics of Aqueous Water Electrolysis". In: *Journal of The Electrochemical Society* 127.9 (1980), p. 1954. ISSN: 0013-4651. DOI: https://doi.org/10.1149/1.2130044.

[169] Agata Godula-Jopek and Detlef Stolten(eds). *Hydrogen Production : By Electrolysis*. Berlin, GERMANY: John Wiley & Sons, Incorporated, 2015. ISBN: 9783527676521.

[170] S. K. Mazloomi and Nasri Sulaiman. "Influencing factors of water electrolysis electrical efficiency". In: *Renewable and Sustainable Energy Reviews* 16.6 (2012), pp. 4257–4263. ISSN: 1364-0321. DOI: https://doi.org/10.1016/j.rser.2012.03.052.

[171] Ernesto Amores, Jesús Rodríguez, and Christian Carreras. "Influence of operation parameters in the modeling of alkaline water electrolyzers for hydrogen production". In: *International Journal of Hydrogen Energy* 39.25 (2014), pp. 13063–13078. ISSN: 0360-3199. DOI: https://doi.org/10.1016/j.ijhydene.2014.07.001.

[172] N. Nagai et al. "Existence of optimum space between electrodes on hydrogen production by water electrolysis". In: *International Journal of Hydrogen Energy* 28.1 (2003), pp. 35–41. ISSN: 0360-3199. DOI: https://doi.org/10.1016/S0360-3199(02)00027-7.

[173] A. Angulo et al. "Influence of Bubbles on the Energy Conversion Efficiency of Electrochemical Reactors". In: *Joule* 4.3 (2020), pp. 555–579. DOI: https://doi.org/10.1016/j.joule.2020.01.005.

[174] C. Santoro et al. "What is Next in Anion-Exchange Membrane Water Electrolyzers? Bottlenecks, Benefits, and Future". In: *ChemSusChem* 15.8 (2022). DOI: 10.1002/cssc.202200027.

[175] IRENA. *Green Hydrogen Cost Reduction: Scaling up Electrolysers to Meet the 1.5°C Climate Goal*. Report. 2020. URL: www.irena.org/publications.

[176] Marvin Warshay and Paul R Prokpius. *The fuel cell in space: Yesterday, today and tomorrow*. Report. 1989. URL: https://ntrs.nasa.gov/citations/19900002488.

[177] *Solar hydrogen generation : toward a renewable energy future*. New York, NY: Springer, 2008. DOI: https://doi.org/10.1007/978-0-387-72810-0.

[178] Alyssa Sutton. *Nafion: Properties, Structure and Applications*. Hauppauge, UNITED STATES: Nova Science Publishers, Incorporated, 2016. ISBN: 9781634842006.

[179] O. F. Selamet et al. "Effects of operating parameters on the performance of a high-pressure proton exchange membrane electrolyzer". In: *International Journal of Energy Research* 37.5 (2013), pp. 457–467. DOI: https://doi.org/10.1002/er.2942.

[180] C. Li and J. B. Baek. "The promise of hydrogen production from alkaline anion exchange membrane electrolyzers". In: *Nano Energy* 87 (2021). DOI: 10.1016/j.nanoen.2021.106162.

[181] Hamish Andrew Miller et al. "Green hydrogen from anion exchange membrane water electrolysis: a review of recent developments in critical materials and operating conditions". In: *Sustainable Energy & Fuels* 4.5 (2020), pp. 2114–2133. DOI: 10.1039/C9SE01240K. URL: http://dx.doi.org/10.1039/C9SE01240K.

[182] Hydrolite. *Electrolyzer technology AEM and use of hydrogen*. Web Page. (online). URL: https://www.hydrolite-h2.com/aem-electrolyzer-technology/.

[183] Enapter. *Enapter homepage*. Web Page. (online). URL: https://www.enapter.com/.

[184] Alicia Li Jen Keow and Zheng Chen. "Auto-Tuning Control of Proton Exchange Membrane Water Electrolyzer With Self-Assessment and Gain Scheduling". In: *Journal of Dynamic Systems, Measurement, and Control* 143.5 (2021), p. 051009. DOI: https://doi.org/10.1115/1.4049365.

[185] Ryan O'hayre et al. *Fuel cell fundamentals*. John Wiley & Sons, 2016.

[186] Allen J Bard and Larry R Faulkner. *Electrochemical methods: fundamentals and applications*. Second edition. John Wiley & Sons, 2001.

[187] Roger Parsons. "General equations for the kinetics of electrode processes". In: *Transactions of the Faraday Society* 47 (1951), pp. 1332–1344. DOI: 10.1039/tf9514701332.

[188] John Newman and Karen E. Thomas-Alyea. *Electrochemical systems*. John Wiley & Sons, 2012.

[189] Martin Z Bazant. "10.626 Electrochemical energy systems". In: *Massachusetts Institute of Technology: MIT OpenCourseWare, Lecture* (2014).

[190] J.W. Haverkort and H. Rajaei. "Voltage losses in zero-gap alkaline water electrolysis". In: *Journal of Power Sources* 497 (2021), p. 229864. DOI: https://doi.org/10.1016/j.jpowsour.2021.229864.

[191] J.W. Haverkort. "Modeling and Experiments of Binary Electrolytes in the Presence of Diffusion, Migration, and Electro-Osmotic Flow". In: *Physical Review Applied* 14.4 (2020), p. 044047. DOI: 10.1103/PhysRevApplied.14.044047.

[192] J.W. Haverkort and H. Rajaei. "Electro-osmotic flow and the limiting current in alkaline water electrolysis". In: *Journal of Power Sources Advances* 6 (2020), p. 100034. DOI: 10.1016/j.powera.2020.100034.

[193] D.S. Falcão and A.M.F.R. Pinto. "A review on PEM electrolyzer modelling: Guidelines for beginners". In: *Journal of Cleaner Production* 261 (2020), p. 121184. DOI: 10.1016/j.jclepro.2020.121184.

[194] Alfredo Ursúa and Pablo Sanchis. "Static-dynamic modelling of the electrical behaviour of a commercial advanced alkaline water electrolyser". In: *International Journal of Hydrogen Energy* 37.24 (2012), pp. 18598–18614. DOI: 10.1016/j.ijhydene.2012.09.125.

[195] Øystein Ulleberg. "Modeling of advanced alkaline electrolyzers: A system simulation approach". In: *International Journal of Hydrogen Energy* 28.1 (2003), pp. 21–33. DOI: 10.1016/S0360-3199(02)00033-2.

[196] Federico Zenith et al. "Control-oriented modelling and experimental study of the transient response of a high-temperature polymer fuel cell". In: *Journal of Power Sources* 162.1 (2006), pp. 215–227. DOI: 10.1016/j.jpowsour.2006.06.022.

[197] C. Immerz et al. "Understanding electrical under- and overshoots in proton exchange membrane water electrolysis cells". In: *Journal of the Electrochemical Society* 166.15 (2019), F1200–F1208. DOI: 10.1149/2.0881914jes.

[198] Rebah Maamouri et al. "Proton exchange membrane water electrolysis: Modeling for hydrogen flow rate control". In: *International Journal of Hydrogen Energy* 46.11 (2021), pp. 7676–7700. DOI: 10.1016/j.ijhydene.2020.11.276.

[199] Atif Khan Niaz, Jun-Young Park, and Hyung-Tae Lim. "Operational parameters correlated with the long-term stability of anion exchange membrane water electrolyzers". In: *International Journal of Hydrogen Energy* 46.62 (2021), pp. 31550–31562. DOI: 10.1016/j.ijhydene.2021.07.078.

[200] J.E.B. Randles. "Kinetics of rapid electrode reactions". In: *Faraday Discussions* 1 (1947), pp. 11–19. DOI: 10.1039/DF9470100011.

[201] C. Rozain and P. Millet. "Electrochemical characterization of Polymer Electrolyte Membrane Water Electrolysis Cells". In: *Electrochimica Acta* 131 (2014), pp. 160–167. DOI: 10.1016/j.electacta.2014.01.099.

[202] Damien Guilbert and Gianpaolo Vitale. "Dynamic emulation of a PEM electrolyzer by time constant based exponential model". In: *Energies* 12.4 (2019), p. 750. DOI: https://doi.org/10.3390/en12040750.

[203] Jan Van Der Merwe et al. "A study of the loss characteristics of a single cell PEM electrolyser for pure hydrogen production". In: 2013, pp. 668–672. DOI: 10.1109/ICIT.2013.6505751.

[204] C.A. Martinson et al. "Characterisation of a PEM electrolyser using the current interrupt method". In: *International Journal of Hydrogen Energy* 39.36 (2014), pp. 20865–20878. DOI: 10.1016/j.ijhydene.2014.09.153.

[205] Francisco Da Costa Lopes and Edson H. Watanabe. "Experimental and theoretical development of a PEM electrolyzer model applied to energy storage systems". In: 2009, pp. 775–782. DOI: 10.1109/COBEP.2009.5347619.

[206] Ozcan Atlam and Mohan Kolhe. "Equivalent electrical model for a proton exchange membrane (PEM) electrolyser". In: *Energy Conversion and Management* 52.8-9 (2011), pp. 2952–2957. DOI: 10.1016/j.enconman.2011.04.007.

[207] Jaroslaw Milewski, Giulio Guandalini, and Stefano Campanari. "Modeling an alkaline electrolysis cell through reduced-order and loss-estimate approaches". In: *Journal of Power Sources* 269 (2014), pp. 203–211. DOI: 10.1016/j.jpowsour.2014.06.138.

[208] K. Górecki et al. "Modelling and the analysis of the power supply system for the generator of hydrogen". In: *2nd International Congress on Energy Efficiency and Energy Related Materials ENEFM 2014* (2015), pp. 451–457.

[209] Krzysztof Górecki, Paweł Górecki, and Janusz Zarębski. "Electrical model of the alkaline electrolyser dedicated for SPICE". In: *International Journal of Circuit Theory and Applications* 46.5 (2018), pp. 1044–1054. DOI: 10.1002/cta.2459.

[210] Christian Henao et al. "Simulation tool based on a physics model and an electrical analogy for an alkaline electrolyser". In: *Journal of Power Sources* 250 (2014), pp. 58–67. DOI: 10.1016/j.jpowsour.2013.10.086.

[211] R.L. Le Roy et al. "Analysis of Time-Variation Effects in Water Electrolyzers". In: *Journal of the Electrochemical Society* 126.10 (1979), pp. 1674–1682. DOI: 10.1149/1.2128775.

[212] J. Eichman, K. Harrison, and M. Peters. *Novel Electrolyzer Applications: Providing More Than Just Hydrogen.* Report. 2014. DOI: https://doi.org/10.2172/1159377.

[213] Mónica Sánchez et al. "Semi-empirical model and experimental validation for the performance evaluation of a 15 kW alkaline water electrolyzer". In: *International Journal of Hydrogen Energy* 43.45 (2018), pp. 20332–20345. DOI: 10.1016/j.ijhydene.2018.09.029.

[214] Ahyoun Lim et al. "A study on electrode fabrication and operation variables affecting the performance of anion exchange membrane water electrolysis". In: *Journal of Industrial and Engineering Chemistry* 76 (2019), pp. 410–418. DOI: 10.1016/j.jiec.2019.04.007.

[215] Xiaojun Shen et al. "Experimental study on the external electrical thermal and dynamic power characteristics of alkaline water electrolyzer". In: *International Journal of Energy Research* 42.10 (2018), pp. 3244–3257. DOI: 10.1002/er.4076.

[216] P. Trinke et al. "Hydrogen crossover in PEM and alkalinewater electrolysis: Mechanisms, direct comparison and mitigation strategies". In: *Journal of the Electrochemical Society* 165.7 (2018), F502–F513. DOI: 10.1149/2.0541807jes.

[217] Hiroshi Ito et al. "Pressurized operation of anion exchange membrane water electrolysis". In: *Electrochimica Acta* 297 (2019), pp. 188–196. DOI: 10.1016/j.electacta.2018.11.077.

[218] Gerald S. Ogumerem and Efstratios N. Pistikopoulos. "Dynamic modeling and explicit control of a PEM water electrolysis process". In: *Smart and Sustainable Manufacturing Systems* 2.2 (2018), pp. 25–43. DOI: 10.1520/SSMS20180017.

[219] Paolo Colbertaldo, Sonia Laura Gómez Aláez, and Stefano Campanari. "Zero-dimensional dynamic modeling of PEM electrolyzers". In: *Energy Procedia* 142 (2017), pp. 1468–1473. DOI: 10.1016/j.egypro.2017.12.594.

[220] M. Kiaee et al. "Demonstration of the operation and performance of a pressurised alkaline electrolyser operating in the hydrogen fuelling station in Porsgrunn, Norway". In: *Energy Conversion and Management* 94 (2015), pp. 40–50. DOI: https://doi.org/10.1016/j.enconman.2015.01.070.

[221] J. M. Stansberry and J. Brouwer. "Experimental dynamic dispatch of a 60 kW proton exchange membrane electrolyzer in power-to-gas application". In: *International Journal of Hydrogen Energy* 45.16 (2020), pp. 9305–9316. DOI: https://doi.org/10.1016/j.ijhydene.2020.01.228.

[222] Enapter. *Enapter Handbook, AEM Technology*. Web Page. (online). URL: https://handbook.enapter.com/knowledge_base/aem_technology.html.

[223] J. Stansberry et al. "Experimental analysis of photovoltaic integration with a proton exchange membrane electrolysis system for power-to-gas". In: *International Journal of Hydrogen Energy* 42.52 (2017), pp. 30569–30583. DOI: https://doi.org/10.1016/j.ijhydene.2017.10.170.

[224] Siemens. *Datasheet Silyzer300*. Web Page. (online). URL: https://assets.siemens-energy.com/siemens/assets/api/uuid:a193b68f-7ab4-4536-abe2-c23e01d0b526/datasheet-silyzer300.pdf.

[225] B. W. Tuinema et al. "Modelling of large-sized electrolysers for real-time simulation and study of the possibility of frequency support by electrolysers". In: *IET Generation, Transmission & Distribution* 14.10 (2020), pp. 1985–1992. ISSN: 1751-8695. DOI: https://doi.org/10.1049/iet-gtd.2019.1364.

[226] J. Gorre et al. "Cost benefits of optimizing hydrogen storage and methanation capacities for Power-to-Gas plants in dynamic operation". In: *Applied Energy* 257 (2020). DOI: https://doi.org/10.1016/j.apenergy.2019.113967.

[227] C. Chen, Y. Lu, and L. Xing. "Levelling renewable power output using hydrogen-based storage systems: A techno-economic analysis". In: *Journal of Energy Storage* 37 (2021). DOI: https://doi.org/10.1016/j.est.2021.102413.

[228] Feras Alshehri et al. "Modelling and evaluation of PEM hydrogen technologies for frequency ancillary services in future multi-energy sustainable power systems". In: *Heliyon* 5.4 (2019). ISSN: 2405-8440. DOI: https://doi.org/10.1016/j.heliyon.2019.e01396.

[229] NREL. *Champion photovoltaic module efficiency chart*. Web Page. (online). 2022. URL: https://www.nrel.gov/pv/module-efficiency.html.

[230] Mojtaba Fereidooni et al. "A comprehensive evaluation of hydrogen production from photovoltaic power station". In: *Renewable and Sustainable Energy Reviews* 82 (2018), pp. 415–423. DOI: https://doi.org/10.1016/j.rser.2017.09.060.

[231] Armand Fopah-Lele et al. "Solar electricity storage through green hydrogen production: A case study". In: *International Journal of Energy Research* 45.9 (2021), pp. 13007–13021. DOI: https://doi.org/10.1002/er.6630.

[232] M. Reuß et al. "Solar hydrogen production: a bottom-up analysis of different photovoltaic-electrolysis pathways". In: *Sustainable Energy & Fuels* 3 (2019), pp. 801–813. DOI: https://doi.org/10.1039/C9SE00007K.

[233] F. Sayedin et al. "Optimization of photovoltaic electrolyzer hybrid systems; taking into account the effect of climate conditions". In: *Energy Convers. Manag.* 118 (2016), pp. 438–449.

[234] Tuyen Nguyen Duc et al. "Optimization strategy for high efficiency 20 kW-class direct coupled photovoltaic-electrolyzer system based on experimental data". In: *International Journal of Hydrogen Energy* 44.49 (2019), pp. 26741–26752. DOI: https://doi.org/10.1016/j.ijhydene.2019.07.056.

[235] Evangelia Topriska et al. "The Application of Solar-Powered Polymer Electrolyte Membrane (PEM) Electrolysers for the Sustainable Production of Hydrogen Gas as Fuel for Domestic Cooking". In: *Renewable Energy in the Service of Mankind Vol I: Selected Topics from the World Renewable Energy Congress WREC 2014*. Ed. by Ali Sayigh. Cham: Springer International Publishing, 2015, pp. 193–203. DOI: 10.1007/978-3-319-17777-9_18.

[236] Jan Vaculik et al. "Calculation of efficiency of hydrogen storage system at the fuel cells laboratory". In: *Proceedings of the 2014 15th International Scientific Conference on Electric Power Engineering (EPE)*. 2014, pp. 381–384. DOI: 10.1109/EPE.2014.6839440.

[237] A.H. Abdol Rahim et al. "Optimization of Direct Coupling Solar PV Panel and Advanced Alkaline Electrolyzer System". In: *Energy Procedia* 79 (2015). 2015 International Conference on Alternative Energy in Developing Countries and Emerging Economies, pp. 204–211. DOI: https://doi.org/10.1016/j.egypro.2015.11.464.

[238] "Hydrogen Production Using Solar Energy - Technical Analysis". In: *Energy Procedia* 112 (2017). Sustainable Solutions for Energy and Environment, EENVIRO 2016, 26-28 October 2016, Bucharest, Romania, pp. 418–425. DOI: https://doi.org/10.1016/j.egypro.2017.03.1097.

[239] A. Khalilnejad, A. Sundararajan, and A.I. Sarwat. "Performance evaluation of optimal photovoltaic-electrolyzer system with the purpose of maximum Hydrogen storage". In: *2016 IEEE/IAS 52nd Industrial and Commercial Power Systems Technical Conference (I&CPS)*. 2016, pp. 1–9. DOI: 10.1109/ICPS.2016.7490222.

[240] Daniel Węcel et al. "Investigation on System for Renewable Electricity Storage in Small Scale Integrating Photovoltaics, Batteries, and Hydrogen Generator". In: *Energies* 13.22 (2020). DOI: 10.3390/en13226039.

[241] Brahim Laoun et al. "Modeling of solar photovoltaic-polymer electrolyte membrane electrolyzer direct coupling for hydrogen generation". In: *International Journal of Hydrogen Energy* 41.24 (2016), pp. 10120–10135. DOI: https://doi.org/10.1016/j.ijhydene.2016.05.041.

[242] Ziyun Su et al. "Optimization and sensitivity analysis of a photovoltaic-electrolyser direct-coupling system in Beijing". In: *International Journal of Hydrogen Energy* 39.14 (2014), pp. 7202–7215. DOI: https://doi.org/10.1016/j.ijhydene.2014.02.136.

[243] M.L. Ferrari, M. Rivarolo, and A.F. Massardo. "Hydrogen production system from photovoltaic panels: experimental characterization and size optimization". In: *Energy Conversion and Management* 116 (2016), pp. 194–202. DOI: https://doi.org/10.1016/j.enconman.2016.02.081.

[244] Rupsha Bhattacharyya, Apurva Misra, and K.C. Sandeep. "Photovoltaic solar energy conversion for hydrogen production by alkaline water electrolysis: Conceptual design and analysis". In: *Energy Conversion and Management* 133 (2017), pp. 1–13. DOI: https://doi.org/10.1016/j.enconman.2016.11.057.

[245] H. Niaz, H.H. Lakkouraj, and J. Liu. "Techno-economic feasibility evaluation of a standalone solar-powered alkaline water electrolyzer considering the influence of battery energy system: a Korean case study". In: *Korean Journal of Chemical Engineering* 38 (2021), pp. 1617–1630. DOI: https://doi.org/10.1007/s11814-021-0819-z.

[246] S.M.S. Privitera et al. "Highly efficient solar hydrogen production through the use of bifacial photovoltaics and membrane electrolysis". In: *Journal of Power Sources* 473 (2020), p. 228619. DOI: https://doi.org/10.1016/j.jpowsour.2020.228619.

[247] F. Gutiérrez-Martín, Lidia Amodio, and Maurizio Pagano. "Hydrogen production by water electrolysis and off-grid solar PV". In: *International Journal of Hydrogen Energy* 46.57 (2021). HYDROGEN ENERGY SYSTEMS, pp. 29038–29048. DOI: https://doi.org/10.1016/j.ijhydene.2020.09.098.

[248] K.G.U. Wijayatha. *Photoelectrochemical cells for hydrogen generation.* Electronic Book Section. 2012. DOI: https://doi.org/10.1533/9780857096371.1.91.

[249] Vu Minh Phap et al. "Feasibility analysis of hydrogen production potential from rooftop solar power plant for industrial zones in Vietnam". In: *Energy reports* 8 (2022), pp. 14089–14101. DOI: https://doi.org/10.1016/j.egyr.2022.10.337.

[250] Ronald Mas et al. "Genetic algorithms-based size optimization of directly and indirectly coupled photovoltaic-electrolyzer systems". In: *Energy Conversion and Management* 270 (2022), p. 116213. DOI: https://doi.org/10.1016/j.enconman.2022.116213.

[251] Osama Majeed Butt et al. "A predictive approach to optimize a HHO generator coupled with solar PV as a standalone system". In: *Sustainability* 13.21 (2021), p. 12110. DOI: https://doi.org/10.3390/su132112110.

[252] Z. Yang et al. "A New Direct Coupling Method for Photovoltaic Module-PEM Electrolyzer Stack for Hydrogen Production". In: *Fuel Cells* 18.4 (2018), pp. 543–550. DOI: https://doi.org/10.1002/fuce.201700206.

[253] Mourad Frites and Shahed U.M. Khan. "Optimum Conditions for Efficient Hydrogen Generation by Water Electrolysis in an Electrochemical Cell Powered either by Power Supply or Solar Cells". In: *ECS Transactions* 50.49 (Apr. 2013), p. 3. DOI: https://doi.org/10.1149/05049.0003ecst.

[254] Hadi Ganjehsarabi. "Performance assessment of solar-powered high pressure proton exchange membrane electrolyzer: A case study for Erzincan". In: *International Journal of Hydrogen Energy* 44.20 (2019). 9th International Conference on Hydrogen Production (ICH2P-2018), pp. 9701–9707. DOI: https://doi.org/10.1016/j.ijhydene.2018.12.007.

[255] Argonne National Laboratory. *Basic research needs for the hydrogen economy*. (online). 2003.

[256] Office of energy efficiency & Renewable energy. *Hydrogen and fuel cell technologies office multi-year research development and demonstration plan*. (online). 2014.

[257] Nelson A. Kelly. "The coupling factor: A new metric for determining and controlling the efficiency of solar photovoltaic power utilization". In: *International Journal of Hydrogen Energy* 38.5 (2013), pp. 2079–2094. DOI: https://doi.org/10.1016/j.ijhydene.2012.11.105.

[258] R. García-Valverde, N. Espinosa, and A. Urbina. "Optimized method for photovoltaic-water electrolyser direct coupling". In: *International Journal of Hydrogen Energy* 36.17 (2011), pp. 10574–10586. DOI: https://doi.org/10.1016/j.ijhydene.2011.05.179.

[259] N.R. Shriyan. *Modelling of PV-Electrolyzer system for optimum operation*. Thesis. 2020.

[260] Meng Tao et al. "Review-Engineering Challenges in Green Hydrogen Production Systems". In: *Journal of The Electrochemical Society* 169.5 (2022), p. 054503. DOI: https://doi.org/10.1149/1945-7111/ac6983.

[261] Gowri M. Siriramagiri et al. "Computation and assessment of solar electrolyzer field performance: comparing coupling strategies". In: *Sustainable Energy & Fuels* 3 (2019), pp. 422–430. DOI: https://doi.org/10.1039/C8SE00399H.

[262] *System Advisor Model*.

[263] D. Guilbert, Stefania Maria Collura, and Angel Scipioni. "DC/DC converter topologies for electrolyzers: State-of-the-art and remaining key issues". In: *International Journal of Hydrogen Energy* 42.38 (2017), pp. 23966–23985.

[264] Maik Becker, Jörn Brauns, and Thomas Turek. "Battery-Buffered Alkaline Water Electrolysis Powered by Photovoltaics". In: *Chemie Ingenieur Technik* 93.4 (2021), pp. 655–663. DOI: https://doi.org/10.1002/cite.202000151.

[265] B. Gillessen et al. "Hybridization strategies of power-to-gas systems and battery storage using renewable energy". In: *International Journal of Hydrogen Energy* 42.19 (2017), pp. 13554–13567. DOI: https://doi.org/10.1016/j.ijhydene.2017.03.163.

[266] V. Papadopoulos et al. "Improving the utilization factor of a PEM electrolyzer powered by a 15 MW PV park by combining wind power and battery storage – Feasibility study". In: *International Journal of Hydrogen Energy* 43.34 (2018), pp. 16468–16478. ISSN: 0360-3199. DOI: https://doi.org/10.1016/j.ijhydene.2018.07.069.

[267] Michihisa Koyama. "Toward Economically Rational Hydrogen Production from Solar Energy: From Battery Versus Hydrogen to Battery × Hydrogen". In: *Nanostructured Materials for Next-Generation Energy Storage and Conversion: Photovoltaic and Solar Energy*. Ed. by Tulay Aygan Atesin, Sajid Bashir, and Jingbo Louise Liu. Berlin, Heidelberg: Springer Berlin Heidelberg, 2019, pp. 457–470. DOI: https://doi.org/10.1007/978-3-662-59594-7_16.

[268] Narihisa Sako et al. "Techno-economic and life cycle analyses of battery-assisted hydrogen production systems from photovoltaic power". In: *Journal of Cleaner Production* 298 (2021), p. 126809. ISSN: 0959-6526. DOI: https://doi.org/10.1016/j.jclepro.2021.126809.

[269] ChungHyuk Lee et al. "Transient Gas Saturation in Porous Transport Layers of Polymer Electrolyte Membrane Electrolyzers". In: *ECS Transactions* 92.8 (July 2019), p. 821. DOI: https://doi.org/10.1149/09208.0821ecst.

[270] Christian Schnuelle et al. "Dynamic hydrogen production from PV & wind direct electricity supply – Modeling and techno-economic assessment". In: *International Journal of Hydrogen Energy* 45.55 (2020), pp. 29938–29952. ISSN: 0360-3199. DOI: https://doi.org/10.1016/j.ijhydene.2020.08.044.

[271] Jörn Brauns and Thomas Turek. "Alkaline water electrolysis powered by renewable energy: A review". In: *Processes* 8.2 (2020), p. 248. DOI: https://doi.org/10.3390/pr8020248.

[272] Zsolt Dobó and Árpád Bence Palotás. "Impact of the current fluctuation on the efficiency of Alkaline Water Electrolysis". In: *International Journal of Hydrogen Energy* 42.9 (2017), pp. 5649–5656. ISSN: 0360-3199. DOI: https://doi.org/10.1016/j.ijhydene.2016.11.142.

[273] Zsolt Dobó and Árpád Bence Palotás. "Impact of the voltage fluctuation of the power supply on the efficiency of alkaline water electrolysis". In: *International Journal of Hydrogen Energy* 41.28 (2016), pp. 11849–11856. ISSN: 0360-3199. DOI: https://doi.org/10.1016/j.ijhydene.2016.05.141.

[274] F.-W. Speckmann et al. "Alkaline Electrolysis with Overpotential-Reducing Current Profiles". In: *Journal of The Electrochemical Society* 165.7 (May 2018), F456. DOI: 10.1149/2.0511807jes.

[275] L. Allidières et al. "On the ability of pem water electrolysers to provide power grid services". In: *International Journal of Hydrogen Energy* 44.20 (2019). 9th International Conference on Hydrogen Production (ICH2P-2018), pp. 9690–9700. ISSN: 0360-3199. DOI: https://doi.org/10.1016/j.ijhydene.2018.11.186.

[276] Samuel Furfari and Alessandro Clerici. "Green hydrogen: the crucial performance of electrolysers fed by variable and intermittent renewable electricity". In: *The European Physical Journal Plus* 136.5 (2021), p. 509. DOI: https://doi.org/10.1140/epjp/s13360-021-01445-5.

[277] Emanuele Taibi et al. *Green hydrogen cost reduction. Scaling up electrolyzers to meet the 1.5°C climate goal.* Tech. rep. IRENA, 2020.

[278] David Fischer et al. "Real live demonstration of MPC for a power-to-gas plant". In: *Applied Energy* 228 (2018), pp. 833–842. ISSN: 0306-2619. DOI: https://doi.org/10.1016/j.apenergy.2018.06.144.

[279] Mitch Ewan et al. "(Invited) Development of a Hydrogen Energy System as a Grid Frequency Management Tool". In: *ECS Transactions* 75.14 (Aug. 2016), p. 403. DOI: https://doi.org/10.1149/07514.0403ecst.

[280] A. Bergen et al. "Transient electrolyser response in a renewable-regenerative energy system". In: *International Journal of Hydrogen Energy* 34.1 (2009), pp. 64–70. ISSN: 0360-3199. DOI: https://doi.org/10.1016/j.ijhydene.2008.10.007.

[281] O. Schmidt et al. "Future cost and performance of water electrolysis: An expert elicitation study". In: *International Journal of Hydrogen Energy* 42.52 (2017), pp. 30470–30492. ISSN: 0360-3199. DOI: https://doi.org/10.1016/j.ijhydene.2017.10.045.

[282] Jinfeng Wu et al. "A review of PEM fuel cell durability: Degradation mechanisms and mitigation strategies". In: *Journal of Power Sources* 184.1 (2008), pp. 104–119. ISSN: 0378-7753. DOI: https://doi.org/10.1016/j.jpowsour.2008.06.006.

[283] Qi Feng et al. "A review of proton exchange membrane water electrolysis on degradation mechanisms and mitigation strategies". In: *Journal of Power Sources* 366 (2017), pp. 33–55. ISSN: 0378-7753. DOI: https://doi.org/10.1016/j.jpowsour.2017.09.006.

[284] Christoph Rakousky et al. "Polymer electrolyte membrane water electrolysis: Restraining degradation in the presence of fluctuating power". In: *Journal of Power Sources* 342 (2017), pp. 38–47. ISSN: 0378-7753. DOI: https://doi.org/10.1016/j.jpowsour.2016.11.118.

[285] A. Weiß et al. "Impact of Intermittent Operation on Lifetime and Performance of a PEM Water Electrolyzer". In: *Journal of The Electrochemical Society* 166.8 (Apr. 2019), F487. DOI: https://doi.org/10.1149/2.0421908jes.

[286] SA Grigoriev, DG Bessarabov, and VN Fateev. "Degradation mechanisms of MEA characteristics during water electrolysis in solid polymer electrolyte cells". In: *Russian Journal of Electrochemistry* 53 (2017), pp. 318–323. DOI: https://doi.org/10.1134/S1023193517030065.

[287] Pia Aßmann et al. "Toward developing accelerated stress tests for proton exchange membrane electrolyzers". In: *Current Opinion in Electrochemistry* 21 (2020), pp. 225–233. ISSN: 2451-9103. DOI: https://doi.org/10.1016/j.coelec.2020.02.024.

[288] Yosuke Uchino et al. "Relationship between the redox reactions on a bipolar plate and reverse current after alkaline water electrolysis". In: *Electrocatalysis* 9 (2018), pp. 67–74. DOI: https://doi.org/10.1007/s12678-017-0423-5.

[289] Atif Khan Niaz et al. "Effects of the operation mode on the degradation behavior of anion exchange membrane water electrolyzers". In: *Journal of Power Sources* 481 (2021), p. 229093. DOI: https://doi.org/10.1016/j.jpowsour.2020.229093.

[290] S Stucki et al. "PEM water electrolysers: evidence for membrane failure in 100kW demonstration plants". In: *Journal of Applied Electrochemistry* 28.10 (1998), pp. 1041–1049. DOI: https://doi.org/10.1023/A:1003477305336.

[291] M. Chandesris et al. "Membrane degradation in PEM water electrolyzer: Numerical modeling and experimental evidence of the influence of temperature and current density". In: *International Journal of Hydrogen Energy* 40.3 (2015), pp. 1353–1366. ISSN: 0360-3199. DOI: https://doi.org/10.1016/j.ijhydene.2014.11.111.

[292] P. Millet et al. "Cell failure mechanisms in PEM water electrolyzers". In: *International Journal of Hydrogen Energy* 37.22 (2012). HySafe 1, pp. 17478–17487. ISSN: 0360-3199. DOI: https://doi.org/10.1016/j.ijhydene.2012.06.017.

[293] Philipp Lettenmeier et al. "Proton Exchange Membrane Electrolyzer Systems Operating Dynamically at High Current Densities". In: *ECS Transactions* 72.23 (Aug. 2016), p. 11. DOI: https://doi.org/10.1149/07223.0011ecst.

[294] International Energy Agency. *Hydrogen*. Tech. rep. IEA, 2022.

[295] R.García-Valverde, N. Espinosa, and A. Urbina. "Optimized method for photovoltaic-water electrolyser direct coupling". In: *Int. J. Hydrog. Energy* 36 (17 2011), pp. 10574–10586.

[296] R. García-Valverde et al. "Optimized photovoltaic generator-water electrolyser coupling through a controlled DC-DC converter". In: *Int. J. Hydrog. Energy* 33 (20 2018), pp. 5352–5362.

[297] F. Gallardo et al. "Assessing sizing optimality of OFF-GRID AC-linked solar PV-PEM systems for hydrogen production". In: *Int. J. Hydrog. Energy* 47 (64 2022), pp. 27303–27325.

[298] Ozcan Atlam, Frano Barbir, and Dario Bezmalinovic. "A method for optimal sizing of an electrolyzer directly connected to a PV module". In: *Int. J. Hydrog. Energy* 36 (12 2011), pp. 7012–7018.

[299]   Eshan D. Mitra and William S. Hlavacek. "Parameter estimation and uncertainty quantification for systems biology models". In: *Curr. Opin. Syst. Biol.* 18 (2019), pp. 9–18.

[300]   A. Khalilnejad, A. Abbaspour, and A.I. Sarwat. "Multi-level optimization approach for directly coupled photovoltaic-electrolyzer system". In: *Int. J. Hydrog. Energy* 41 (28 2016), pp. 11884–11894.

[301]   Azadeh Maroufmashat, Farid Sayedin, and Sourena Sattari Khavas. "An imperialist competitive algorithm approach for multi-objective optimization of direct coupling photovoltaic-electrolyzer systems". In: *Int. J. Hydrog. Energy* 39.33 (2014), pp. 18743–18757.

[302]   Farid Sayedin et al. "Optimal design and operation of a photovoltaic–electrolyser system using particle swarm optimisation". In: *International Journal of Sustainable Energy* 35.6 (2016), pp. 566–582. DOI: 10.1080/14786451.2014.922974.

[303]   Z. Yang, G. Zhang, and B. Lin. "Performance evaluation and optimum analysis of a photovoltaic-driven electrolyzer system for hydrogen production". In: *Int. J. Hydrog. Energy* 40 (8 2015), pp. 3170–3179.

[304]   R. Boudries et al. "PV system design for powering an industrial unit for hydrogen production". In: *Int. J. Hydrog. Energy* 39.27 (2014), pp. 15188–15195.

[305]   Berrin Karacavus and Kadir Aydin. "Hydrogen production and storage analysis of a system by using TRNSYS". In: *In. J. Hydrog. Energy* 45 (60 2020), pp. 34608–34619.

[306]   Mariana Corengia and Ana I. Torres. "Coupling time varying power sources to production of green-hydrogen: A superstructure based approach for technology selection and optimal design". In: *Chemical Engineering Research and Design* 183 (2022), pp. 235–249. DOI: https://doi.org/10.1016/j.cherd.2022.05.007.

[307]   Davide Pivetta, Chiara Dall'Armi, and Rodolfo Taccani. "Multi-objective optimization of a hydrogen hub for the decarbonization of a port industrial area". In: *J. Mar. Sci. Eng.* 10.2 (2022), p. 231.

[308]   Linus Engstam et al. "Grid-supported electrolytic hydrogen production: Cost and climate impact using dynamic emission factors". In: *Energy Conversion and Management* 293 (2023), p. 117458. DOI: https://doi.org/10.1016/j.enconman.2023.117458.

[309]   Siyu Zhang et al. "Study on the Optimization of System Configuration of Green Hydrogen Projects". In: *2022 7th International Conference on Power and Renewable Energy (ICPRE)*. 2022, pp. 1260–1263. DOI: 10.1109/ICPRE55555.2022.9960360.

[310]   Jonathon Yates et al. "Techno-economic analysis of hydrogen electrolysis from off-grid stand-alone photovoltaics incorporating uncertainty analysis". In: *Cell reports Physical science* 1 (2020), p. 100209. DOI: https://doi.org/10.1016/j.xcrp.2020.100209.

[311] Long Phan Van, Long Hieu Hoang, and Tuyen Nguyen Duc. "A comprehensive review of direct coupled photovoltaic-electrolyser system: Sizing techniques, operating strategies, research progress, current challenges, and future recommendations". In: *International Journal of Hydrogen Energy* (2023). DOI: https://doi.org/10.1016/j.ijhydene.2023.03.257.

[312] Artuso Paola, Zuccari Fabrizio, and Orecchini Fabio. "Techno-economic optimisation of hydrogen production by PV – electrolysis: "RenHydrogen" simulation program". In: *International Journal of Hydrogen Energy* 36.2 (2011), pp. 1371–1381. DOI: https://doi.org/10.1016/j.ijhydene.2010.10.068.

[313] Mathworks. *particleswarm - Particle swarm optimization*. 2022. URL: https://www.mathworks.com/help/gads/particleswarm.html.

[314] Lester James V. Miranda et al. *PYSWARMS - A research toolkit for particle swarm optimization in Python*. 2017. URL: https://pyswarms.readthedocs.io/en/latest/index.html.

[315] Bilal Abderezzak. "2 - Charge Transfer Phenomena". In: *Introduction to Transfer Phenomena in PEM Fuel Cell*. Ed. by Bilal Abderezzak. Elsevier, 2018, pp. 53–83. DOI: 10.1016/B978-1-78548-291-5.50002-0.

[316] P. Fragiacomo and M. Genovese. "Modeling and energy demand analysis of a scalable green hydrogen production system". In: *Int. J. Hydrog. Energy* 44 (57 2019), pp. 30237–30255.

[317] M.J. Moran and H.N. Shapiro. *Fundamentals of Engineering Thermodynamics*. Wiley, 2006.

[318] N. Connor. *What is Isentropic Process - Definition*. 2019. URL: https://www.thermal-engineering.org/what-is-isentropic-process-definition/.

[319] N. Hall, ed. *Isentropic Compression (or expansion)*. 2021. URL: https://www.grc.nasa.gov/www/k-12/airplane/compexp.html.

[320] Wouter Knap. "Basic measurements of radiation at station Cabauw (2013-01)". In: PANGAEA, 2013. DOI: 10.1594/PANGAEA.807193.

[321] Arno Smets et al. *Solar Energy: The Physics and Engineering of Photovoltaic Conversion, Technologies and Systems*. UIT Cambridge, 2016.

[322] James W. Stultz. "Thermal and Other Tests of Photovoltaic Modules Performed in Natural Sunlight". In: *Journal of Energy* 3.6 (1979), pp. 363–372. DOI: https://doi.org/10.2514/3.62445.

[323] TrinaSolar. *The Tallmax M framed 144 layout module (datasheet)*. 2019. URL: https://static.trinasolar.com/sites/default/files/AP_Datasheet_TallmaxM_DE17M.T0(II).pdf.

[324] Mohd Alam et al. "Renewable sources based DC microgrid using hydrogen energy storage: Modeling and experimental analysis". In: *Sustainable Energy Technologies and Assessments* 42 (2020), p. 100840.

[325] J. Kennedy and R. Eberhart. "Particle swarm optimization". In: *Proceedings of ICNN'95 - International Conference on Neural Networks*. Vol. 4. 1995, 1942–1948 vol.4.

[326] Adam Slowik and Halina Kwasnicka. "Nature inspired methods and their industry applications - Swarm intelligence algorithms". In: *IEEE Trans. Indstr. Inform.* 14.3 (2018), pp. 1004–1015.

[327] Farid Sayedin et al. "Evolutionary optimization approaches for direct coupling photovoltaic-electrolyzer systems". In: *2015 International Conference on Industrial Engineering and Operations Management (IEOM)*. 2015, pp. 1–8. DOI: 10.1109/IEOM.2015.7093884.

[328] Fuel Cells and Hydrogen Obervatory. *Levelized Cost of Hydrogen*. 2022. URL: https://www.fchobservatory.eu/observatory/technology-and-market/levelised-cost-of-hydrogen-green-hydrogen-costs.

[329] Mostafa Rezaei, Alexandr Akimov, and Evan MacA. Gray. "Economics of solar-based hydrogen production: Sensitivity to financial and technical factors". In: *International Journal of Hydrogen Energy* 47.65 (2022), pp. 27930–27943. DOI: https://doi.org/10.1016/j.ijhydene.2022.06.116.

[330] TRACTEBEL Engineering and Hinicio. *Study on early business cases for H2 in energy storage and more broadly power to h2 applications*. Tech. rep. Fuel Cells and Hydrogen Joint Undertaking, 2017.

[331] Abdelhamid Mraoui and Abdallah Khellaf. "Optimization of the design of hydrogen production systems based on product cost". In: *J. Sol. Energy Eng.* 142 (4 2020), p. 041003.

[332] Abdulrahman S. Al-Buraiki and Abdullah Al-Sharafi. "Hydrogen production via using excess electric energy of an off-grid hybrid solar/wind system based on a novel performance indicator". In: *Energy Conversion and Management* 254 (2022), p. 115270. DOI: https://doi.org/10.1016/j.enconman.2022.115270.

[333] F.H.Murphy, S. Sen, and A.L.Soyster. "Electric utility capacity expansion planning with uncertain load forecasts". In: *IIE Trans.* 14 (1 1982), pp. 52–59.

[334] Wojciech Uchman and Janusz Kotowicz. "Varying load distribution impacts on the operation of a hydrogen plant". In: *Int. J. Hydrog. Energy* 46 (79 2021), pp. 39095–39107.

[335] Bradley Efron. *The jacknife, the bootstrap, and other resampling plans*. philadelfie, USA: Society for Industrial and applied mathematics, 1982.

[336] Angel Hernández-Gómez, Víctor Ramirez, and Damien Guilbert. "Investigation of PEM electrolyzer modeling: Electrical domain, efficiency, and specific energy consumption". In: *Int. J. Hydrog. Energy* 45 (2020), pp. 14625–14639.

[337] Shivashankar Sukumar et al. "Ramp-rate control smoothing methods to control output power fluctuations from solar photovoltaic (PV) sources—A review". In: *Journal of Energy Storage* 20 (2018), pp. 218–229. DOI: https://doi.org/10.1016/j.est.2018.09.013.

[338] Xiaoyang Chen et al. "Towards the applicability of solar nowcasting: A practice on predictive PV power ramp-rate control". In: *Renewable Energy* 195 (2022), pp. 147–166. DOI: https://doi.org/10.1016/j.renene.2022.05.166.

[339] E. Cirés et al. "The potential of forecasting in reducing the LCOE in PV plants under ramp-rate restrictions". In: *Energy* 188 (2019), p. 116053. DOI: https://doi.org/10.1016/j.energy.2019.116053.

[340] V. A. Martinez Lopez et al. "Dynamic operation of water electrolyzers: A review for applications in photovoltaic systems integration". In: *Renewable and Sustainable Energy Reviews* 182 (2023), p. 113407. DOI: https://doi.org/10.1016/j.rser.2023.113407.

[341] A. Gonzalez-Moreno et al. "a PV ramp-rate control strategy to extend battery lifespan using forecasting". In: *Applied Energy* 323 (2022), p. 119546. DOI: https://doi.org/10.1016/j.apenergy.2022.119546.

[342] Quanyuan Jiang and Haisheng Hong. "Wavelet-Based Capacity Configuration and Coordinated Control of Hybrid Energy Storage System for Smoothing Out Wind Power Fluctuations". In: *IEEE Transactions on Power Systems* 28.2 (2013), pp. 1363–1372. DOI: 10.1109/TPWRS.2012.2212252.

[343] Mojtaba Saleh et al. "Battery-Less Short-Term Smoothing of Photovoltaic Generation Using Sky Camera". In: *IEEE Transactions on Industrial Informatics* 14.2 (2018), pp. 403–414. DOI: 10.1109/TII.2017.2767038.

[344] Xiaoyang Chen et al. "Robust Proactive Power Smoothing Control of PV Systems Based on Deep Reinforcement Learning". In: *IEEE Transactions on Sustainable Energy* 14.3 (2023), pp. 1585–1598. DOI: 10.1109/TSTE.2023.3239852.

[345] V. A. Martinez Lopez et al. "Maximization of PV energy use and performance analysis of a stand-alone PV-hydrogen system". In: *International Journal of Hydrogen Energy* 48.99 (2023), pp. 39298–39314. DOI: https://doi.org/10.1016/j.ijhydene.2023.09.072.

[346] Eugene L. Maxwell. *A Quasi-Physical Model for Converting Hourly Global Horizontal to Direct Normal Insolation*. Tech. rep. SERI/TR-215-3087. Golden, CO: Solar Energy Research Institute, 1987.

[347] Sandia National Laboratories. *PV_LIB Toolbox*. URL: https://pvpmc.sandia.gov/tools/pv%5C_lib-toolbox/.

[348] Kashif Ishaque, Zainal Salam, and Hamed Taheri. "Simple, fast and accurate two-diode model for photovoltaic modules". In: *Solar Energy Materials and Solar Cells* 95.2 (2011), pp. 586–594. DOI: https://doi.org/10.1016/j.solmat.2010.09.023.

[349] D. S. Falcão and A. M. F. R. Pinto. "A review on PEM electrolyzer modelling: Guidelines for beginners". In: *Journal of Cleaner Production* 261 (2020), p. 121184. DOI: https://doi.org/10.1016/j.jclepro.2020.121184.

[350] Chroma. *Solar array simulator DC power supply*. 2023. URL: https://www.chromausa.com/product/solar-array-simulator/.

[351] Imperix. *SiC Power module PEB8024*. 2023. URL: https://imperix.com/products/power/sic-power-module/.

[352] Imperix. *Passive Filters*. 2023. URL: https://imperix.com/products/power/filter-box/.

[353] Imperix. *Rapid prototyping controller B-box RCP*. 2023. URL: https://imperix.com/products/control/rapid-prototyping-controller/.

[354] Ana Cabrera-Tobar et al. "Active power control of a PV generator for large scale photovoltaic power plant without energy storage". In: *2019 IEEE PES Innovative Smart Grid Technologies Conference - Latin America (ISGT Latin America)*. 2019, pp. 1–6. DOI: 10.1109/ISGT-LA.2019.8895469.

[355] CMS Shreder. *cms ASI-16/51*. 2018. URL: http://www.schreder-cms.com/en_pdf/ASI-16_InfoBroch.pdf.

[356] Ricardo Marquez and Carlos F.M. Coimbra. "Intra-hour DNI forecasting based on cloud tracking image analysis". In: *Solar Energy* 91 (2013), pp. 327–336. DOI: https://doi.org/10.1016/j.solener.2012.09.018.

[357] Tensorflow. *Keras applications ResNet50*. 2023. URL: https://www.tensorflow.org/api_docs/python/tf/keras/applications/resnet50/ResNet50.

[358] Lefteri H. Tsoukalas and Robert E. Uhrig. *Fuzzy and neural approaches in engineering*. USA: John Wiley & Sons, Inc., 1997.

[359] Yinghao Chu, Mengying Li, and Carlos F.M. Coimbra. "Sun-tracking imaging system for intra-hour DNI forecasts". In: *Renewable Energy* 96 (2016), pp. 792–799. DOI: https://doi.org/10.1016/j.renene.2016.05.041.

[360] Rebecca Chaplin-Kramer et al. "Global modeling of nature's contributions to people". In: *Science* 366.6462 (2019), pp. 255–258. DOI: 10.1126/science.aaw3372.

[361] Paul W. Taylor. "Environmental Ethics 3". In: Center of environmental philosophy University of North Texas, 1981. Chap. The ethics of respect for Nature.

[362] Aldo Leopold. "A sand county almanac: And sketches here and there". In: Oxford University Press, Inc., 1949. Chap. The land ethic.

[363] Bill Devall and George Sessions. *Deep ecology*. Peregrine Smiths Books, 1985.

[364] Peter Singer. "Ethics and problems of the 21st century". In: ed. by K.E. Goodpaster and K.M. Sayre. University of Notre Dame Press, 1979. Chap. Not for humans only: The place of nonhumans in environmental issues.

ACKNOWLEDGEMENTS

Some years ago I started a two-year journey and adventure of pursuing a Master's degree in the Netherlands, leaving everything behind. The adventure was supposed to last two years. Suddenly, six years and many "I will never do a PhD" later, I find my self writing the final chapter of my PhD dissertation. "A journey well shared is a journey well enjoyed", the saying goes. So this chapter is dedicated to everyone of you who have shared this path and adventure with me, and without whom I could not have reached this far.

To you, my promotors, Olindo and Miro, for believing in me and giving me the opportunity of even starting the program, for the discussions, feedback and points of view. To you, my co-promotor and daily supervisor, Hesan, for those biweekly meetings discussing all kinds of crazy ideas that eventually would give shape to this thesis and for encouraging me to follow them.

To you, the technicians who helped with the setups used in this thesis. For your patiente in having to hear the "this is not working, when can it be fixed?" question more than once, and swiftly attending to help.

To you, my students, who put your trust in me to guide you through your graduation projects. Thank you for the knowledge interchange, for teaching me how to give feedback, support and guidance and overall, for your hard work in your thesis projects. You allowed me to move faster in the PhD trajectory and brought new ideas.

To you, my colleagues of the PVMD group, for taking the time of explaining things to me, from basic knowledge, to discussion of more complex ideas. For helping me to navigate through the academic peer review process, for letting me help you with some tasks, for sharing a coffee break, a celebration cake or simply for asking how I was doing.

To you, my sunny friends, for sharing those sunny lunches, for all the discussions that had nothing to do with work, from silly to deeper ones. For the time spent outside university, whether at a party or a conference. Thank you for spicing and removing the seriousness of academic life with laughter.

To you, my closest friends, for never leaving my side. Either from the distance or in person. You helped me to navigate through the mist and hold the steering wheel when I was getting lost. Thank you for being a strong oak where I could lean; for encouraging me to keep going. For teaching me so much about life, for making me feel at home and for every beautiful moment that we shared together. You made this journey more bearable and enjoyable.

To you, my family, for being with me, even from the distance. Always interested in what I am doing and checking on me every now and then.

To you, Ale, for being my main and strongest supporter. Who pushed me to come to the Netherlands in the first place, who is always cheering me up, for being at my side giving me support, no matter what. "Adventure awaits" we used to say and without you, all this adventure would have never happened.

Finally, to all of you, who crossed my path during these four years, for all the things that I learned from you, either from an academic perspective or in my life itself. All these experiences enriched my journey and helped to shape the person that I am today.

A todos ustedes, por todo esto, y por lo que se le escape a mi memoria ¡muchas gracias!

Victor Arturo Martinez Lopez
Delft, February 2024

LIST OF PUBLICATIONS

PEER-REVIEWED JOURNAL ARTICLES

6. **V.A. Martinez Lopez**, O. Isabella, M. Zeman, H. Ziar, *Battery-less uncertainty-based control of a stand-alone PV-electrolyzer system*, Journal of Power Sources, **614**, (2024).

5. **V.A. Martinez Lopez**, P. Manonukul, O. Isabella, M. Zeman, H. Ziar, *Mapping the suitability of photovoltaic potential in the Netherlands considering environmental impact*, Scientific Reports, under review, (2024).

4. **V.A. Martinez Lopez**, G. van Urk, P.J.F. Doodkorte, M. Zeman, O. Isabella, H. Ziar, *Using sky-classification to improve the short-term prediction of irradiance with sky images and convolutional neural networks*, Solar Energy, **269**, (2024).

3. **V.A. Martinez Lopez**, H.Ziar, M. Zeman and O. Isabella, *Maximization of PV energy use and performance analysis of a stand-alone PV-hydrogen system*, International Journal of Hydrogen Energy, **48**, 99 (2023).

2. **V.A. Martinez Lopez**, H. Ziar, J.W. Haverkort, M. Zeman, O. Isabella, *Dynamic operation of water electrolyzers: A review for application in photovoltaic systems integration*, Renewable and Sustainable Energy Reviews, **182**, 113407, (2023).

1. **V.A. Martinez Lopez**, U. Žindžiūtė, H. Ziar, M. Zeman and O. Isabella, *Study on the Effect of Irradiance Variability on the Efficiency of the Perturb-and-Observe Maximum Power Point Tracking Algorithm*, Energies, **15**, 20 (2022).

CONFERENCES

7. **V.A. Martinez Lopez**, G. van Urk, P.J.F. Doodkorte, M. Zeman, O. Isabella, H. Ziar, Hybrid artificial intelligence-based prediction model for irradiance nowcasting using sky images. 40th European Photovoltaic Solar Energy Conference and Exhibition (2023),Lisbon, Portugal. Oral presentation

6. P. Manonukul, **V.A. Martinez Lopez**, M. Zeman, O. Isabella, H. Ziar. A compatibility index map of the Netherlands for siting new photovoltaic projects. Sunday NL, Ede, the Netherlands (2023). Poster

5. **V.A. Martinez Lopez**, H. Ziar, M. Zeman, O. Isabella. Optimization of a stand-alone PV-electrolysis plant. 33th International Photovoltaic Science and Engineering Conference. Osaka, Japan (2022). Poster

4. **V.A. Martinez Lopez**, H. Ziar, M. Zeman, O. Isabella. Optimal PV configuration for stand-alone hydrogen generation. 8th World Conference on Photovoltaic Energy Conversion. Milan, Italy (2022). Oral presentation

3. **V.A. Martinez Lopez**, P.J.F. Doodkorte, H. Ziar, M. Zeman, O. Isabella. Development of a sky image based model for prediction of irradiance in a minute range horizon. 8th World Conference on Photovoltaic Energy Conversion. Milan, Italy (2022). Poster

2. **V.A. Martinez Lopez**, H. Ziar, M. Zeman, O. Isabella. Optimization of a stand-alone PV system for efficient hydrogen production using an alkaline water electrolyzer. 23rd World Hydrogen Energy Conference, Istanbul, Türkiye (2022). Oral presentation.

1. **V.A. Martinez Lopez**, H. Ziar, M. Zeman, O. Isabella, Methodology for sizing electric storage using solar variability. 38th European Photovoltaic Solar Energy Conference and Exhibition (online, 2021). Oral presentation.

Patents

2. **V.A. Martinez Lopez**, A.L. Romero Olvera, H. Ziar, M. Zeman and O. Isabella, Bioinspired casing for irradiance sensors, No. WO2023/158302, Under revision, (2023).

1. J.C. Ortiz Lizcano, O. Isabella, **V.A. Martinez Lopez**, Miura-ori photovoltaic module, No. WO2021/206542, Under revision, (2021)

CURRICULUM VITÆ

Victor Arturo MARTINEZ LOPEZ

Victor Arturo Martinez Lopez was born in Mexico City, Mexico on the 27th of September 1986. He studied electrical and electronic engineering at the Universidad Nacional Aútonoma de México from which he graduated in 2012. He started his professional career in the renewable energy sector working for Acciona Energía México, a wind energy company, first as a wind farm operator and then in the wind resource assessment department. This practical experience motivated him to pursue a Master's degree at Delft University of Technology in electrical power engineering. His thesis in the Photovoltaic Materials and Devices entitled *Enhancing Solar Energy Integration with Innovative mini-modules* resulted in one patent application. He continued his academic career within the same research group pursuing a PhD in hydrogen production using solar energy. He is now working as a researcher in sustainable energy in agriculture at Wagenigen Research, the Netherlands.